Towards the use of Electrostatic Force Microscopy to study interphases in nanodielectric materials

Diana El Khoury

To cite this version:

Diana El Khoury. Towards the use of Electrostatic Force Microscopy to study interphases in nanodielectric materials. Classical Physics [physics.class-ph]. Université de Montpellier, 2017. English. NNT : . tel-01997985v1

HAL Id: tel-01997985
https://theses.hal.science/tel-01997985v1

Submitted on 29 Jan 2019 (v1), last revised 11 Dec 2018 (v2)

THÈSE POUR OBTENIR LE GRADE DE DOCTEUR DE L'UNIVERSITÉ DE MONTPELLIER

En Électronique

École doctorale Information, Structures, Systèmes

Unité de recherche UMR 5214, Institut d'Électronique et des Systèmes

Towards the use of Electrostatic Force Microscopy to study interphases in nanodielectric materials

Présentée par Diana EL KHOURY
Le 17 Novembre 2017

Sous la direction de Jérôme CASTELLON
et Richard ARINERO

Devant le jury composé de

M. Juan-Martinez VEGA, Professeur, Université Paul Sabatier	Président
M. Alun VAUGHAN, Professeur, University of Southampton	Rapporteur
M. Philippe LECLERE, Maître de recherche, Université de Mons	Rapporteur
Mme Christina VILLENEUVE, Maître de conférences HDR, Université Paul Sabatier	Examinatrice
M. John FOTHERGILL, Professeur émérite, City University London	Examinateur
M. Jérôme CASTELLON, Maître de conférences HDR, Université de Montpellier	Directeur
M. Richard ARINERO, Maître de conférences HDR, Université de Montpellier	Directeur
M. Jean-Charles LAURENTIE, Maître de conférences, Université de Montpellier	Co-encadrant

UNIVERSITÉ
DE MONTPELLIER

“The task is not so much to see what no one has yet seen, but to think what nobody has yet thought about that which everybody sees.” Erwin Schrödinger

TO MY MOTHER, FATHER AND SISTER

Acknowledgments

---

and after all, what matters the most is thanking all of you, who helped me getting to this day…

This PhD work has been performed at the Institute of Electronics and Systems - Energy and Materials Group (IES-GEM), financially supported by the French ministry of education and research and the doctoral school "Information, Structures, Systèmes" (I2S) of the University of Montpellier, within a doctoral contract.

I would first like to thank you Serge AGNEL for receiving me in your group, and for your very positive energy.

I gratefully acknowledge all the jury members, for your presence, your instructive comments and questions, and your appreciation for this work. In particular, Prof. Juan-Martinez VEGA, thank you for accepting to be the jury president. Prof. John FOTHERGIL, I sincerely appreciate your insistency on concretely evaluating this work, in spite of the hard moments you were facing during the defense period. I would also like to acknowledge Dr. Christina VILLENEUVE for your follow-up questions; these have well enhanced the quality of the manuscript. Prof. Alun VAUGHAN, I am grateful to your thorough review of the manuscript and kind opinion, exotic introduction during the defense and your, as usual, interesting comments and questions. Prof. Philippe LECLERE, I am extremely grateful to your very supportive and ample evaluation of the manuscript, as well as your original questions and suggestions for this work.

It is now time to address my word to my beloved supervisors. The three of you provided all the time needed, generosity to transfer your knowledge, adopt the appropriate methods to well supervise this project and introduce me to the research word. I equally acknowledge leaving me a very large space of autonomy. Jerome, I am especially grateful to your confidence, and to always looking after making room for wider future opportunities to me. Richard, beyond your scientific high qualities, I would like to thank you for always being there to listen to me and to afford a caring guidance in many life aspects. Jean-Charles, I greatly acknowledge your valuable contribution through your critical ideas and original advices.

I would like to thank the following people for their support, without whose help this work would never have been possible: Mikhaël, we are indebted to your generosity on keeping the doors of the European Institute of Membranes (IEM) open to all samples preparation. Our collaboration has been one cornerstone for this project. Viktoriia thank you for your valuable time, at the expense of your PhD, spent on preparing at the beginning a large set of samples, and later, teaching me the basics to prepare them. Michel RAMONDA, you know how much I appreciate your availability, technical support, inspiring conversations, and above all, thank you for your distracting sense of humor. Another person who had a major contribution on this thesis is Michel FRÉCHETTE. We acknowledge your observation Michel concerning the importance of model samples. I would also like to thank you, Nadine and Mohammed, for the mechanical characterizations, our collaboration must be sure continued.

I am grateful to all of the GEM members: Odile, Coco (Coralie), Petru, Thierry, Philippe, Olivier, Gilles, Francois, Jean-Jacques. Thank you all for the pleasing work environment you constitute, and Petru I appreciate that you trusted me to teach your courses at the IUT of Béziers. "Mme Katia", Amin and all other administration staff and security guards, thank you for allowing me to write the thesis in the lab at improbable hours.

Above all, what would these three years have been without you my dearest friends-colleagues? Past PhD students - young doctors: Aurel (Aurélien), Phanul (Phanuel), Zahir, Julien, Amjad, Hanoun (Hanan), Ashraf (avec un s), Shuo and you Tarik; Future doctors: Piscini (Lorenzo), Xav (Xavier), Gui (Guillaume), Shakeel, Mourad, Pierre; and Alexandra, Sébastien and Pascal. It would be unreasonable to detail all the amazing, constructive and crazy moments and activities we have experienced together. However, I must point out that you have constituted one amazing family to me, and I will never forget these incredible days. Thank you, and love you guys!

My deepest appreciation also belongs to the doctors and future doctors of the IEM laboratory: Stephanie ROUALDES, Vincent ROUESSAC, Damien VOIRY, Octavio, Mathieu, Aude, Loraine, Bastien, Sara, Maro (Maryline), Joël and Dana, for the useful discussions and your technical help.

My days in Montpellier wouldn't be the same without the blessed and joyful entourage of all the friends of Paroisse Ste Bernadette. I would also like to thank all my friends from the Lebanese University, IES and else, for filling up my days with lots of smiles, experiences and support to my journey, with a special dedication to those who have been able to be present during the defense.

Sabina, my lovely cousin, thank you for your corrections and your presence on the 17th of November, it meant a Lot to me. Douda, your contribution to the success of my years in Montpellier cannot be valued. Thank you "brotha".

I express my gratitude to all the people, friends and family, who through their different kinds of support, I have been able to pursue my education and accomplish the PhD. I would also like to deeply thank one particular person, Mr. Charles-my physics teacher in college: your passionate way of teaching set in me the love for physics. I would also like to add my grateful appreciation to all the professors I had through my entire education, among which my MS supervisors, Roland HABSHI and Ziad ADEM: you too played a key role, although indirectly, to allow me finding this thesis.

These acknowledgments would not be complete without mentioning Renno, my childhood best friend, and Elie… Thank you for your perpetual support, among which, during the hard moments of the PhD.

Last but not least, my most precious words are dedicated to my Everything, to my Family. You Mum, Dad and sister (Dano), you know that you are the main reason that this could be accomplished. I am extremely blessed and grateful for having you (have had you Daddy (Papito), my Forever idol…) in my life. I love you and I hope I would always be able making you proud!

Thank you God for your guidance…

Ready for next missions!

Contents

I - From nanodielectrics to Electrostatic Force Microscopy

II - Introduction to Electrostatic Force Microscopy

III - Theoretical and modeling approach

IV - Samples and experiments description

V - Experimental results

List of Publications

Abstract

Introduction

"God made solids; surfaces were the work of the devil." Wolfgang Pauli

Composite polymeric materials have long revealed improved physical properties owing to a mixing of their constituents' characteristics. Hence, conventional two-phase mixture laws are usually sufficient to clarify and expect the response of microcomposites to an external stimulus. However, surprisingly, for a given concentration, when the filler size is reduced to the nanometer range, nanocomposites exhibit unexpected properties changes. For instance, J. K. Nelson and J. C. Fothergill noticed for the first time in 2004, a decreased dielectric permittivity of the base resin (from 9.99 to 8.49 at 1 kHz for example) with the addition of titanium dioxide nanoparticles, although the latter possess much higher permittivity than the polymeric matrix (> 100 %) [1].

The anomalous behavior of dielectric nanocomposites, constituted by a mixture of nanoparticles in a matrix, also called nanodielectrics [2], has been attributed to the nanometric size of the fillers [3]. At this scale, and for the same weight of material, the ratio of atoms and molecules present at the surface of the nanoparticles regarding the bulk ones increases exponentially compared to microparticles. Moreover, the reactivity of surface molecules of a condensed phase is high. At the contact with another phase, a series of interactions occurs at their mutual interface in order to establish a thermodynamical equilibrium. These interactions are likely to favor the emergence of a region with unique properties, different than the involved phases. As an example, it has been usually postulated that in a nanocomposite, polymer chains rearrange at the interface with the nanoparticles creating an immobilized layer with increased order [4]. The latter is mostly elevated at the particle surface and lowers as it approaches the polymer bulk. This is the so-called interphase, present in high percentage in nanodielectrics and extending from a few angstroms up to a few hundred of nanometers thick. The interphase might thus possess lower permittivity than the polymer in volume, which clarifies the exceptional observed dielectric response in nanodielectrics. Various electrical insulation properties, such as space charge formation, treeing propagation, dielectric breakdown strength etc., have also been promised and proved to improve with nanofiller addition compared to their unfilled and microfilled counterparts [5-7].

Accordingly, at this scale, since interphases start to monitor the final material properties, the local characterization of these nanometric regions becomes undoubtedly fundamental. What are they made of? Where are they really located in the material? What are their properties? How deep is their extension?

In order to answer all these questions, it is simple: "you just look at the thing!", as Richard Feynman mentioned in his famous talk "There's plenty of rooms on the bottom", pointing out the importance of high resolution imaging techniques to make clear many vital scientific questions [8].

Nowadays, the two most developed high resolution imaging methods are Electron Microscopies and Scanning Probe Microscopies (SPM). Contrarily to electron microscopies, SPM systems and particularly Atomic Force Microscopy (AFM) techniques are versatile, easy-to-handle methods, especially appropriate to the study of electrical insulators [9]. In the simplest definition, AFM uses a physical probe with a tip at its end of nanometric apex, providing the nanometric resolution. This near field microscope detects the material with large precision by sensing the field of interaction between the sample and the probe similarly to a hand touching a surface with closed eyes. When interacting electrostatic forces are selectively detected, we speak about Electrostatic Force Microscopy (EFM) [10].

EFM is one of the AFM-derived methods constituting a promising technique to locally characterize interphases owing to its sensitivity to the capacitive response in the presence of the sample [11]. However, due to the probe geometry and the long range nature of electrostatic forces, the actual probed region of the specimen becomes too complex to be defined and EFM signals get easily misinterpreted.

Consequently, the aim of this work is to conduct a search to determine whether EFM is able to detect interphases in nanodielectrics. In other words, the question is how would the interphase presence or absence be manifested on EFM signals? How is it possible to measure its dielectric permittivity and/or dimensions? What are the experimental protocols and signal analysis that allow selecting the intrinsic artifact-free response of the interphase?

In the aim of answering all these questions, firstly, we started by numerically simulating the interaction of the EFM tip with several types of nanostructured samples, to fill up the gaps in the literature concerning EFM response with complex sample geometries and composition. Subsequently, interphase impact on EFM signals was simulated for various types of nanodielectric materials. Nevertheless, this theoretical approach was not enough to allow us at this stage to measure nanodielectrics with unknown interphases. Experimental measurements on reference samples were quickly qualified to be essential for the development of the appropriate experimental methods for future interphase characterization of "real" nanodielectrics. Materials with three distinct dielectric phases were designed and synthesized to electrostatically model a nanodielectric material within an EFM measurement. Experimental tests were hence conducted on those samples to adapt EFM for interphase study. Thereby, several methods have been developed in order to fulfill the issues of this research.

This thesis is structured as follows:

Since our materials of interest are solid dielectrics, we begin in Chapter I by introducing their basic structure and response to an electric field. The motivation for the use of nanodielectrics in electrical engineering insulation systems is detailed next leading to the concept of interphase. Several electrochemical interphase models found in literature are exposed with the usual indirect methods to attest them. A state of the art of currently used high resolution imaging and characterization methods for interphases in composite systems is then displayed. Thereby, the expected appropriateness of EFM for the study of interphases in nanodielectric materials is highlighted.

In Chapter II, we review the most recent electrical scanning probe microscopies explaining the advantage of EFM. After an overview on the basics of AFM, we detail the theory and working principles of EFM with most of its detection modes. A special note is attributed to the resolution, in both classical topographical imaging with AFM and electrical imaging with EFM. Moreover, an overview on noise sources in AFM and their influence on the sensitivity within the detection methods adopted in this work is clarified. We note that the detection of an interphase in a nanodielectric specimen requires the ability at the nanometric scale to both, sense the subsurface composition of the material, and distinguish among the association of several types of dielectric materials. Therefore, we complete this chapter with a literature review on the late advances in electrical scanning probe microscopies in general, and EFM in particular, to study 3D nanometric objects, for subsurface imaging and for multi-layered systems imaging. At last, the few specialized studies on interphases in particulate filled polymeric nanocomposites are reported.

As stated previously, the weakness of previous studies to ascertain the validity of electrical scanning results in the interpretation of interphases and complex dielectric materials constitute the motivation for the simulations presented in Chapter III. In this chapter, we discuss through finite-element simulations, the physics of interaction of an EFM probe and several types of nanostructured dielectric samples, most of which were never investigated individually in the literature. We illustrate our adopted electrostatic model of a nanodielectric possessing an interphase, try to identify how to show the presence of an interphase on EFM signals and point out some ranges of validity of EFM for this issue.

Subsequently, in Chapter IV, we define the constituting materials and the preparation methods of our reference samples chosen to electrostatically model a nanodielectric. We also present the details of our experimental EFM adopted modes in addition to a brief description of other complementary used characterization techniques.

The Chapter V is dedicated to the experimental results obtained over the different sets of model samples. Various EFM modes and comparison methods were used in order to develop appropriate experimental protocols and accurate signal analysis to detect and identify interphases in nanocomposite dielectrics. Experiments have been often confronted to simulations, allowing the extraction of quantitative permittivity values of our nanostructured multilayered materials.

Finally, in the concluding Chapter VI, we outline the key results of simulations and experiments and suggest new research prospects on the covered topics in this work.

References

[1] J. K. Nelson and J. C. Fothergill, "Internal charge behaviour of nanocomposites," *Nanotechnology,* vol. 15, p. 586, 2004.

[2] M. F. Frechette, M. L. Trudeau, H. D. Alamdar, and S. Boily, "Introductory remarks on nanodielectrics," *Dielectrics and Electrical Insulation, IEEE Transactions on,* vol. 11, pp. 808-818, 2004.

[3] T. J. Lewis, "Nanometric dielectrics," *Dielectrics and Electrical Insulation, IEEE Transactions on,* vol. 1, pp. 812-825, 1994.

[4] T. Andritsch, R. Kochetov, P. H. F. Morshuis, and J. J. Smit, "Proposal of the polymer chain alignment model," in *Electrical Insulation and Dielectric Phenomena (CEIDP), 2011 Annual Report Conference on*, 2011, pp. 624-627.

[5] J. K. Nelson, J. C. Fothergill, L. A. Dissado, and W. Peasgood, "Towards an understanding of nanometric dielectrics," in *Annual Report Conference on Electrical Insulation and Dielectric Phenomena*, 2002, pp. 295-298.

[6] Y. Yi, C. Jiong, Y. Jingning, X. Dengming, T. Demin, Y. Rui*, et al.*, "Effect of space charge in nanocomposite of LDPE/TiO2," in *Proceedings of the 7th International Conference on Properties and Applications of Dielectric Materials (Cat. No.03CH37417)*, 2003, pp. 913-916 vol.3.

[7] K. Y. Lau, A. S. Vaughan, and G. Chen, "Nanodielectrics: opportunities and challenges," *IEEE Electrical Insulation Magazine,* vol. 31, pp. 45-54, 2015.

[8] R. P. Feynman, "There's plenty of room at the bottom [data storage]," *Journal of Microelectromechanical Systems,* vol. 1, pp. 60-66, 1992.

[9] G. Binnig, C. F. Quate, and C. Gerber, "Atomic Force Microscope," *Physical Review Letters,* vol. 56, pp. 930-933, 03/03/ 1986.

[10] Y. Martin, C. C. Williams, and H. K. Wickramasinghe, "Atomic force microscope–force mapping and profiling on a sub 100-Å scale," *Journal of Applied Physics,* vol. 61, pp. 4723-4729, 1987/05/15 1987.

[11] S. Peng, Q. Zeng, X. Yang, J. Hu, X. Qiu, and J. He, "Local Dielectric Property Detection of the Interface between Nanoparticle and Polymer in Nanocomposite Dielectrics," *Sci Rep,* vol. 6, p. 38978, Dec 13 2016.

Chapter I

From nanodielectrics to Electrostatic Force Microscopy

Chapter I

“I never see what has been done; I only see what remains to be done.” Marie Curie

1. Introduction

This first chapter begins with an introduction to the physics of dielectrics, and their basic response to an electric field. Afterwards, the contribution of nanodielectrics to electrical engineering applications is outlined. Nanodielectrics properties will be detailed next, leading to the introduction of interphases. Several electrochemical models of the interphase found in literature will be exposed. After a description of current indirect interphase characterization approaches, the need for local interphase study is derived. A state of the art of most developed local interphase characterization techniques, among which scanning probe microscopies, is introduced. To finish, the potentiality of electrostatic force microscopy to study the interphase is addressed.

2. Dielectrics

2.1. Origin

Solid state matter is divided into three main types of materials: metals, semiconductors and insulators. The latter are also called “dielectrics”. These three categories are defined and classified according to their electrical conductivity, or more precisely, to the state of their electron energy bands, and mainly, to the width of the energy gap between their valence and conduction bands.

According to quantum mechanics, an isolated atom presents discrete electron energy levels. When atoms get closer to form a solid, electrons discrete energy states or wave functions start to overlap. Since electrons satisfy Pauli’s exclusion principle, where two fermions (particles with half-integer spin) cannot possess exactly similar quantum numbers, alike energy states degenerate into N different states (N is the number of atoms), separated according to the intensity of interaction between overlapping electrons [1]. The result of superposition and degeneration is the production of energy bands filled with closely separated energy levels that can be assumed as a continuum. Leftover ranges of energy not covered by any band result in band gaps. In the outer shell, the last band gap separates what is called the valence band from the conduction band (Fig. I - 1). Electrons in the conduction band, with the highest energy values, are totally free to move in the material, and are consequently responsible for its electrical conductivity [2].

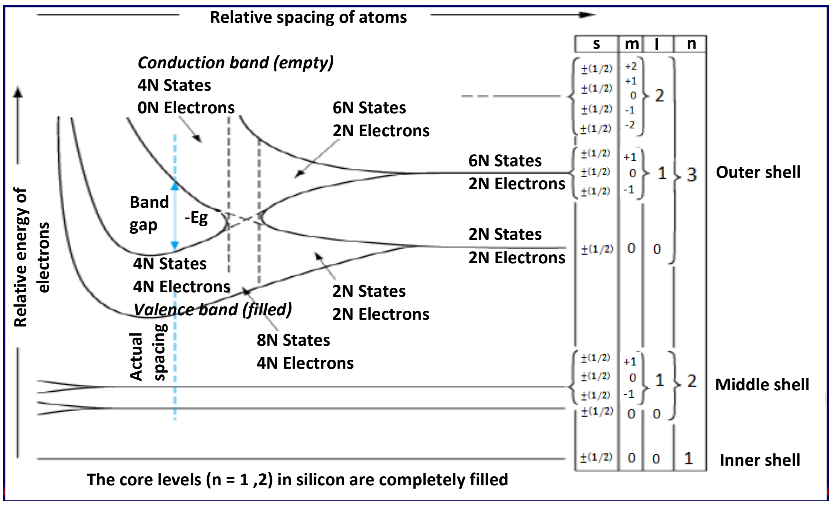

Fig. I - 1 : Representation of electrons energy vs. atoms spacing when 2N silicon atoms are brought together to form a solid.

The excitation of an electron from the valence to the conduction band creates an electron-hole pair into the conduction and valence bands, respectively. The Fermi level E_F is a fictive energy level that separates these two bands (Fig. I - 2) [3]. In a metal, the band gap is almost inexistent as valence and conduction bands can overlap, whereas, semi-conductors and insulators have E_g of the order of electron-volts ($E_g >> K_B T_{amb} \approx 0.026$ eV). Insulators have the largest band gap. Non-crystalline, semi-crystalline and real insulations have, in contrast with Fig. I - 2, a certain density of states around E_F . This figure represents a perfect case, met at 0 K.

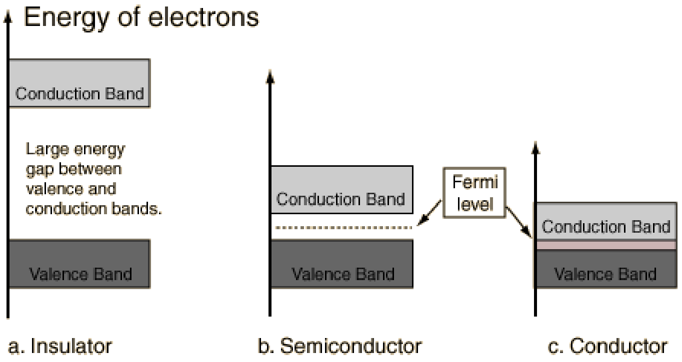

Fig. I - 2 : Schematic diagrams of the energy bands in a perfect: a. insulator, b. semiconductor, and c. conductor: T = 0 K.

2.2. Definition

Dielectric materials are hence at first, and by the simplest definition, electrical insulators whose specific response to an electric field is to create or separate pairs of opposite bound charges. This mechanism called polarization will be explained in the following paragraph. However, the boundary between a dielectric behavior and a conductive one is not absolute. The matter can be somewhat conductive, somewhat insulating, depending on its intrinsic and external conditions. Dielectrics are usually used in power cables to transmit electrical energy, in electronic circuits encapsulation to eliminate and prevent any electrical short-circuit, in capacitors for energy storage [4] etc.

2.3. Dipoles

An electric dipole is created by two punctual charges or by the barycenter of a density of charges q of same value and opposite signs that are separated by a distance l (Fig. I - 3). It is common use to measure the extent of a dipole by its electrical dipolar moment $\boldsymbol{p}$, such as:

$$\boldsymbol{p} = q\boldsymbol{l} \quad (I.1)$$

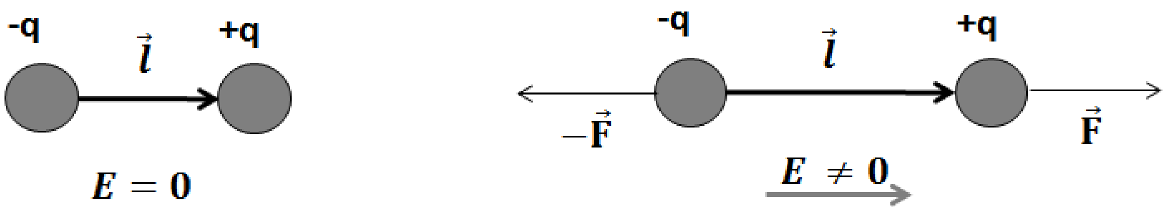

Fig. I - 3 : Schematic illustration of a dipole moment, (left) with no external electric field, (right) under an electric field.

Please note that all bold symbols in the text account for vector quantities.

Dielectric materials can be divided into two groups depending on the total polarity of their molecules in the absence of an electric field. The total polarization $\boldsymbol{P}$ of a material or a molecule is the sum per unit volume of its dielectric moments $\boldsymbol{p}_i$. For a continuous distribution, $\boldsymbol{P}$ writes:

$$\boldsymbol{P} = \int_{v} \boldsymbol{p_i} dv \tag{I.2}$$

v is the volume of the integrated region. Thus, a material can be:

a) Non-Polar: if a molecule possesses a center of symmetry, the barycenters of positive and negative charges overlap in the absence of an electric field. No permanent dipole is hence produced and the material is called non-polar. This is especially the case of solids with metallic bonding and covalent-ionic bonding such as ceramics, like aluminum oxide, zirconium dioxide, zinc oxide, as well as some macromolecules like polyethylene, polyvinyl acetate, polystyrene [5] etc.

b) Polar: molecules that do not possess a center of symmetry present a permanent dipole in the absence of an electric field. These molecules are defined polar. This is the case of some molecules like water H_2O, epoxy function C_2O and macromolecules like polymers with epoxy group etc. However, at ambient temperature, the macroscopic ***P*** of a polar material is null due to the chaotic orientation of its dipoles, cancelling each other.

Hereafter, a general discussion is initiated concerning the response of a dielectric material to an electric field in the case of low-intermediate fields.

2.4. Polarization

2.4.1. Definition

A characteristic of an electric field ***E*** is that it creates a force ***F*** over a charge *q*, proportional to the field intensity and charge value, and collinear to the field (see Fig. I - 3):

$$\boldsymbol{F} = q\boldsymbol{E} \tag{I.3}$$

Consequently, in the case of an electric dipole, ***F*** acts with the same intensity on both poles, with opposite directions. This local displacement of charges, keeping them bonded, is called “polarization”. Different polarization phenomena can be cited depending on the initial state of charges and dipoles in the material.

In a dense dielectric medium, the total electric field acting on a dipole is not only the one resulting from the voltage source, but also from the contribution of the electric field $\boldsymbol{E_{dip}}$ created by surrounding dipoles [6]:

$$\boldsymbol{E_l} = \boldsymbol{E} + \boldsymbol{E_{dip}} \tag{I.4}$$

The local field E_l in the approximation of a cubic lattice region has been evaluated by Lorentz:

$$E_l = E + \frac{P}{3\varepsilon_0} \tag{I.5}$$

2.4.2. Polarization mechanisms

Different types of polarization mechanisms can take place in a dielectric material in response to an external electric field, each requiring a specific establishment time [7]:

a) **Electronic polarization**: it corresponds to the distortion of the electronic cloud of an atom regarding its nucleus. The nucleus stays almost immobile due to the large mass of protons, and consequently, the nucleus versus electrons mass ($m_{nucleus}/m_{electrons} \approx 2000$). The polarization induced in each atom p_{el} is equal to:

$$\boldsymbol{p_{el}} = \alpha_{el}\boldsymbol{E_l} \tag{I.6}$$

The electronic polarizability α_{el} expressed in F.m^2, is generally small and mainly depends on the atom radius. The establishment time of electronic polarization is around 10^{-15} s. In this type of polarization, the delay is due to the necessary time for an electron to acquire the sufficient electric energy from E_l and to get excited to another energy level of the quantized energy states in the atom.

After the displacement of the cloud of electrons due to $\boldsymbol{F}$, a restoring Columbic force takes place in order to bring back electrons to their initial position. The final displacement is therefore reached at equilibrium. Under a sinusoidal external electric field E (ω), the system is similar to a harmonic oscillator, resulting in an α_{el} that becomes equal to the sum of a real part α_{el}' and an imaginary part α_{el}''. The imaginary part represents the loss or delays of the polarization with the field creating energy dissipation.

b) **Ionic polarization:** it is related to the displacement of ionic species in an ionic crystalline lattice due to the electric field. The resulting polarization is:

$$\boldsymbol{P_{io}} = N_{io}\alpha_{io}E_l \tag{I.7}$$

N_{io} is the number of polarizable species per unit volume.

c) **Orientation polarization:** it is encountered in the case of molecules, unit cells of a crystal lattice or the material at a macroscopic level that already possess permanent electric dipoles. According to (I.3), when a dipole is not parallel to the external applied field, the latter creates a couple of forces that act on each pole of the dipole in order to reorient it in the same direction of the field.

According to Langevin theory, the orientation polarization P_{or} can be written for low fields as follows:

$$\boldsymbol{P_{or}} = N_{or}\alpha_{or}\boldsymbol{E_l} = \frac{N_{or}\mu^2}{3K_BT}\boldsymbol{E_l} \tag{I.8}$$

α_{or}, μ, N_{or}, K_B and T are respectively the orientation polarizability, local dipoles, number of polarizable species per unit volume, the Boltzmann constant and the temperature. The temperature dependence is well noted in this type of polarization, causing thermal shocks.

d) **Hopping polarization:** it is the polarization induced by the localized charges that move from one quantum potential well to another well. The hopped charge leaves behind it a positive charge and deposits a negative one at the other site, creating an electric dipole.

e) **Interfacial polarization or space charge polarization:** at the interface of two dielectric media of different dielectric constants (ε_1, ε_2) and conductivities (σ_1, σ_2), whenever $\varepsilon_1\sigma_2 = \varepsilon_2\sigma_1$, an accumulation of virtual charges occurs upon the application of an electric field, creating the interfacial or space charge polarization, also called Maxwell-Wagner-Sillars polarization [8, 9]. In practice, even a homogeneous material is likely to present structural defects creating cracks or voids, and impurities such as solvent and water traces. The impedance of charge carriers migration at the interface creates a space charge and results in a distortion field. This field is observed as an increase in the capacitance of the sample that can be undistinguishable from a real rise of the dielectric constant [10]. The detection of this mechanism can be especially observed at very low frequencies (10^{-5} to 10^2 Hz).

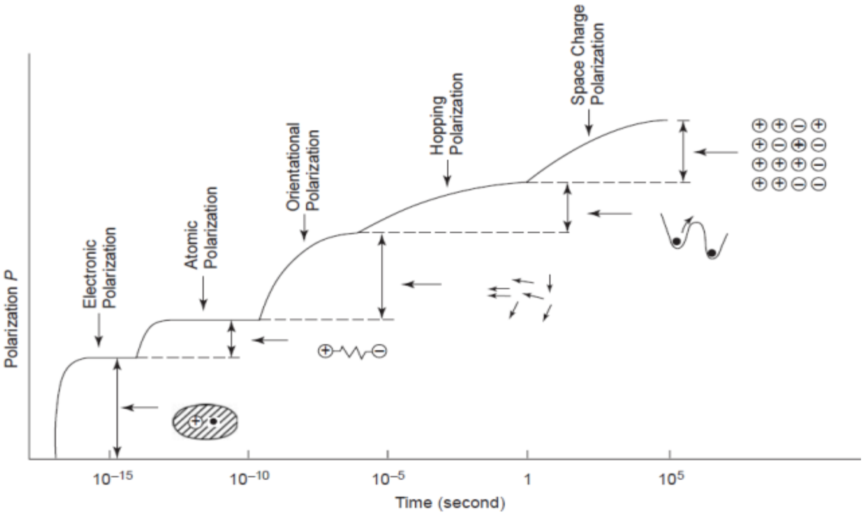

Fig. I - 4 : Variation of different types of polarization with time under a static electric field [11].

As expressed in eq (I.2), the total resulting polarization is the sum of all produced ones. However, each polarization process, regarding its characteristics, has a specific response time to the applied electric field. The above cited polarizations are listed in an ascending order of response time. Consequently, for alternating electric fields, high frequencies can limit the number of polarization processes that can take place. In particular, electronic and atomic polarizations respond almost instantaneously to the applied electric field, without a considerable lag time. Furthermore, in the approximation of harmonic oscillator, when the field has a pulsation equal to the resonance frequency of the ions and electrons inside the molecules and atoms of the material, a resonance phenomenon can take place. These types of polarization are then defined as ''resonance'' processes. For orientation, hopping, or space charge polarization and depolarization induced by an alternating electric field, the required time is quite longer and varies in a wide range depending on the dielectric systems. Generally, such polarization processes are sometimes referred as ''relaxation'' processes. In fact, these types of polarization need a larger relaxation time allowing the system to return to its equilibrium state upon application and removal of the electric field. Resonances and relaxations of a system can be measured with several techniques such as the broadband dielectric spectroscopy (BDS), which will be briefly explained in the next paragraphs.

As long as several polarization phenomena can coexist, their effects can be summed. If the material is considered to be isotropic, or if it presents a cubic symmetry, the local field has the same value for all types of dipoles. Hence, the global polarization has the form:

$$\boldsymbol{P} = \sum_{pol} N_{pol} \alpha_{pol} \boldsymbol{E_{lpol}} \tag{I.9}$$

pol indicates the type of polarization phenomena, N_{pol} is the number of polarizable species under the mechanism *pol*, α_{pol} is the corresponding polarizability and E_{lpol} is the local electric field for *pol* dipoles.

3. Dielectric permittivity

3.1. Definition

The generalization of Gauss law for a volume *v* delimited by a surface *S* containing a dielectric material, considers the charges due to the polarization, and then gives:

$$\oint_S (\varepsilon_0 \boldsymbol{E} + \boldsymbol{P}) d\boldsymbol{S} = \int_v \rho dv \tag{I.10}$$

ε_0 is the vacuum permittivity (8.845 × 10^{-12} F/m). The electric induction ***D*** can be written in terms of:

$$\boldsymbol{D} = \varepsilon_0 \boldsymbol{E} + \boldsymbol{P} \tag{I.11}$$

In the approximation of a homogeneous, linear and isotropic dielectric, ***P*** and ***E*** are directly collinear, and the expression of ***D*** can be expressed with:

$$\boldsymbol{D} = \varepsilon_0 \varepsilon_r \mathbf{E} \tag{I.12}$$

ε_r is the relative permittivity of the dielectric medium, and $\varepsilon = \varepsilon_0 \varepsilon_r$ is its permittivity. However, for simplicity, we referred in this thesis to ε_r with permittivity instead of relative permittivity.

The polarization ***P*** can be also written as:

$$\boldsymbol{P} = \varepsilon_0 (\varepsilon_r - 1) \boldsymbol{E} \tag{I.13}$$

Then ε_r is the coefficient of proportionality between the electric induction and the electric field, as well as the polarization and the electric field. It expresses the extent of the electric field effect on the polarization of the medium and the electric field flux out of the volume surface. Consequently, higher permittivities result in lower electric field penetration into the medium. ε_r can be also called dielectric constant.

3.2. Microscopic to macroscopic relation

It can be noticed that the dielectric permittivity is a macroscopic property of the material. We will try here to correlate it to the microscopic polarization properties of the material expressed through the polarizabilities α_{pol} [12].

Carrying equation (I.5) into (I.9), we get:

$$P = (E + \frac{1}{3\varepsilon_0} P) \sum_i N_{pol} \alpha_{pol} \tag{I.14}$$

Identifying this expression to the one given in (I.13), the following general expression is drawn for the complex dielectric permittivty ε_r* in the sinusoidal regime, while distinguishing the role of the orientation polarization:

$$\frac{\varepsilon_r{}^* - 1}{\varepsilon_r{}^* + 2} = \frac{1}{3\varepsilon_0} \left(\sum_{pol-1} N_{pol-1} \alpha_{pol-1} + \frac{N_o}{1 + j\omega\tau} \frac{p_m{}^2}{3K_B T} \right) \tag{I.15}$$

τ is the delay time (s) and p_m is the magnetic permeability (Henry/m).

This expression is the so-called Clausius-Mossotti relation. A general presentation of the complex dielectric permittivity $\varepsilon^*(\omega)$ can thereby be expressed in the frequency domain by:

$$\varepsilon^*(\omega) = \varepsilon'(\omega) - j\varepsilon''(\omega) = \varepsilon_0 \varepsilon_r{}' - j\varepsilon_0 \varepsilon_r{}'' \tag{I.16}$$

ε_r' and ε_r'' are respectively the real and imaginary relative permittivities, with no unit ($\varepsilon_r' > 1$). The real part represents the polarization response and the imaginary part represents the loss.

Fig. I - 5 shows the general shape of ε_r' and ε_r'' with the frequency of the electric field. Maxima show the resonance of electronic, ionic, orientation and interface polarization mechanisms, starting from the highest frequencies (lowest delay times). The loss part is only minimal when the real permittivity does not vary. The real value becomes more important at low frequencies when several polarization phenomena can take place (Fig. I - 4).

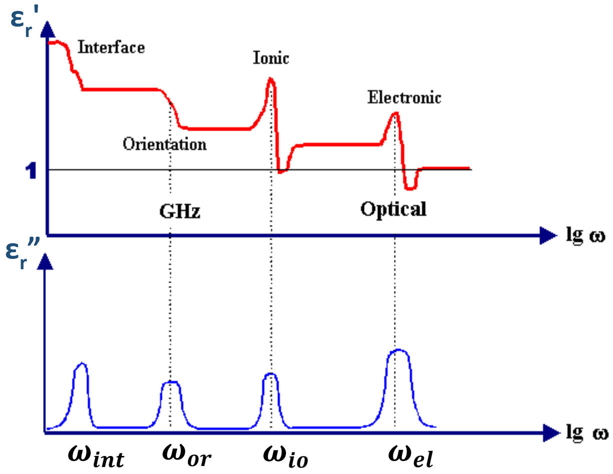

Fig. I - 5 : Frequency dependence of real and imaginary dielectric permittivity.

3.3. Macroscopic measurement technique of the permittivity

Since the above described polarization phenomena are mainly observed at electromagnetic radiations between 10^{-12} and 10^{6} Hz, the measurement of the complex dielectric permittivity can be studied at the macroscopic level with the so-called Broadband Dielectric Spectroscopy (BDS) [13]. This technique uses two planar electrodes of known dimensions, into which the dielectric sample is inserted. The BDS measures with a picoammeter, the total current from which it deduces the corresponding real and imaginary permittivity values.

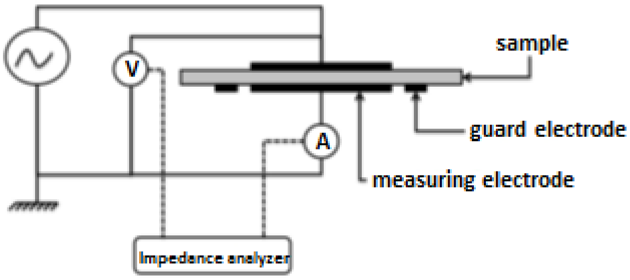

Fig. I - 6 : Schematic diagram of the dielectric spectroscopy measurement setup [14].

Moreover, a temperature sweep can be added and a map of the complex permittivity as a function of frequency and temperature can be obtained. By analyzing BDS results, information about the dynamics of a molecular ensemble can be obtained. It is usual to study either $\varepsilon_r'(\omega)$ or $\varepsilon_r''(\omega)$ because both components contain the same information as they are interrelated by Kramers-Kronig relations [14].

3.4. Electric field outside a dielectric volume

A dielectric volume *v* creates at an external point B placed at a distance *r* far from *v*, an electric potential V_B such as:

$$V_B = \oint_S \frac{\sigma_p dS}{4\pi\varepsilon_0 r} + \int_V \frac{\rho_p dV}{4\pi\varepsilon_0 r} \tag{I.17}$$

with $\sigma_p = \boldsymbol{P}.\boldsymbol{n}$ and $\rho_p = -\nabla.\boldsymbol{P}$. $\boldsymbol{n}$ is the unit normal vector.

An important deduction from this formula is that the dipoles in the volume create at the external region of *v*, the same electric potential, and consequently, the same electric field of a fictive distribution of charges distributed in the volume and on the surface *S* of *v*. The volume density of these charges is ρ_p and the surface one is σ_p. It must be noted that these charges are bound and not free charges [7]. In the absence of free charges in the material, the dielectric is electrically neutral and the sum of σ_p and ρ_p , integrated all over the surface *S* and volume *v*, respectively, is null.

3.5. Limits conditions at the boundary of two dielectric media

In any real insulation, different types of defects or impurities can be present making the material non-perfectly homogeneous. Specifically, this is the case of composite materials, naturally heterogeneous. Hereafter, we will try to deduce the limit conditions of the electric field at the interface between two dielectric media.

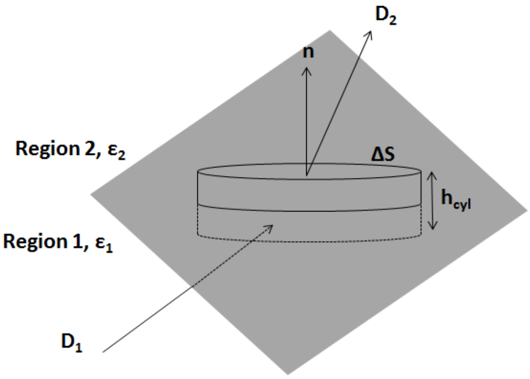

Fig. I - 7 : Discontinuity of electrical induction at the interface of two dielectrics.

Let us consider at the interface between the two media, a little cylinder of negligible height h_{cyl}, on the surface ΔS delimited by the cylinder. In the case where a free charge of surface density σ is present at the interface ($\sigma \neq 0$), with the application of Gauss Law, the following equation is established:

$$D_{n1} - D_{n2} = \sigma \qquad (I.18)$$

This shows the discontinuity of the normal component of the electric displacement, and similarly, the electric field, at the interface between two different media.

When $\sigma = 0$, the following important relation is deduced:

$$\varepsilon_1 E_{n1} = \varepsilon_2 E_{n2} \qquad (I.19)$$

and the tangential components of the electric field can be similarly demonstrated to be continuous:

$$E_{t1} = E_{t2} \qquad (I.20)$$

4. Nanodielectrics

4.1. Definition

“Nanometric dielectrics” [15], later introduced as “Nanodielectrics” in 2004 by M.F. Frechette *et al.* [16], is a nowadays popular term in the dielectrics community used to refer to nanocomposites made by the inclusion of dielectric nanoparticles in a polymeric matrix for dielectric interest [16, 17]. How has interest in nanodielectrics been grown?

First used solid dielectrics were made of natural materials such as glass, silk and ceramics. However, as the need for higher electrical power transmissions continuously increases, usual insulations could not sufficiently cater to demand. Insulators are naturally non-perfect; under certain electrical stresses, they can fail and, inter alia, become conductive. Thus, it was with the development of materials science, and especially the successful introduction of natural and synthetic polymers in several technologies, that new perceptions for better insulators based on polymers started to arise. Hence, new ideas were based on the utilization of materials that have been useful in other domains than electrical insulation applications, and introduce them for insulation fields [4].

As an example, the introduction of inorganic microparticles into a polymeric matrix has commonly shown to improve the mechanical properties of the base polymer, such as its tensile strength and elastic modulus as well as the heat transport. The final microcomposite properties are a combination of both mixing elements properties, usually predictable by general two-phase rules of mixture [18].

Although microcomposites proved to enhance mechanical and thermal behavior compared to the base polymer, contrarily wise, the latter electrical performance has usually degraded [19, 20]. One explanation for the decreased insulation properties is the introduction of defects with the microfillers.

In contrast, the proper incorporation of little nanofillers weight percentage to polymers showed to enhance the dielectric performance while addressing thermal, mechanical and economic requirements [21-24]. This “non-uniform” behavior of nanocomposites has been conferred to the interfacial region between the nanoparticles and the polymer, also called the “interphase”. This region, present in a high percentage at the nanoscale, is supposed to possess different properties than both polymer and filler, which could explain nanodielectrics behavior. A detailed description of interphase models will be presented in next sections.

4.1. Overview on nanodielectrics properties

The first unprecedented experimental work on nanodielectrics has been approached by Henk *et al.* [25] and by J.K. Nelson and J.C. Fothergill on an epoxy system filled with titanium dioxide microparticles compared to nanoparticles [26]. Adding nanoparticles to conventional polymer dielectrics influences the dielectric properties of dielectric materials. Recorded influences are very wide in literature; one can yet notice a certain agreement on several dielectric properties.

An increase in the breakdown strength [26-28] and the time to failure [29], a decrease in the trap controlled-mobility [29] and in space charge accumulation at medium fields [30] and an influence over accumulated charges type, homo or heterocharges, have been commonly noticed upon the introduction of nano-sized fillers to insulating polymers. In order to explain these effects, Tanaka et al. proposed for example that partial discharges take a zigzag path towards weak regions, the matrix, avoiding the filler [22]. Similar mechanisms have been suggested for the retardation of electrical trees propagation observed in nanodielectrics [31-33]. T. Andritsch *et al.* considered the interphase region as a recombination center [34].

4.2. Nanodielectrics permittivity

In addition to the above mentioned changes in nanocomposites, dielectric spectroscopy measurements at low frequencies revealed a less pronounced interfacial polarization in nanodielectrics (see Fig. I - 8) [26].

More surprisingly, although the filler usually possesses a higher permittivity than the polymer (inorganic fillers), the resulting nanofiller mixture in the matrix has been reported to present, at low nanofiller concentrations, a dielectric constant lower than both mixture components (Fig. I - 8 and Fig. I - 9) [14, 26, 35, 36]. This behavior contradicts common two-phase mixture laws, which predict total composite properties that are a compromise between its basic constituents. This can be due to the very small size of the particles giving rise to limited cooperative movements of dipoles reorientation within them [26]. However, scientists mostly agree that the surface interaction of the nano-inclusions with the host polymer rearranges polymer chains and reduces their mobility at the interface [26, 36, 37]. The reduction in mobility can lower polar polymer permittivity, and thereby, that of the interphase. Moreover, other researchers reported water absorption at the interface [38-40]. Water molecules within the interphase increase its effective dielectric constant, which can justify unexpectidly high nanocomposite permittivities.

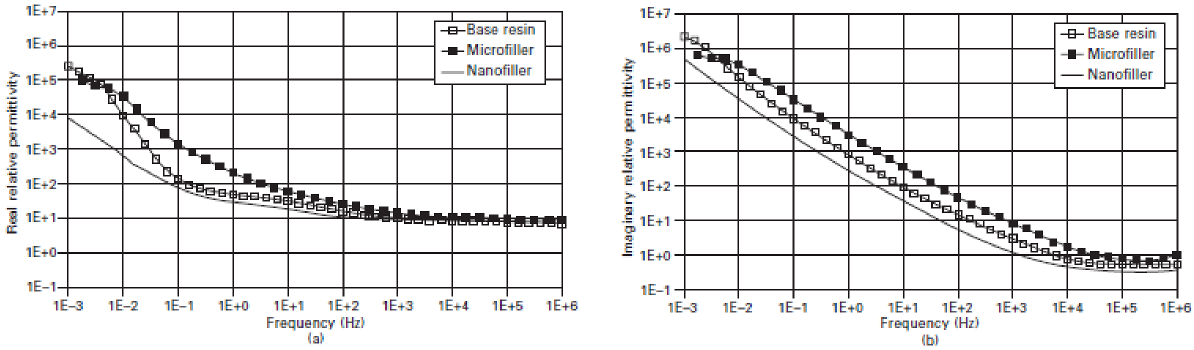

Fig. I - 8 : Response spectra at 393 K as revealed in the dielectric spectroscopy experiment for 10 wt. % titania in epoxy: a. real permittivity for the unfilled resin and micro and nanocomposites, b. imaginary (loss) permittivity [41].

Furthermore, from Fig. I - 9, it can be noticed that exceeding a certain nanofiller weight percentage (wt. %) starts increasing the real permittivity regarding filler content [14, 35-37]. Authors explain that at low filler loadings (or small particle diameters), the interphase volume increases with filler content, thus, increasing its influence on the material. However, at a certain critical loading, an overlap of interphases can occur, decreasing then the interphase effects and making room for particle bulk properties.

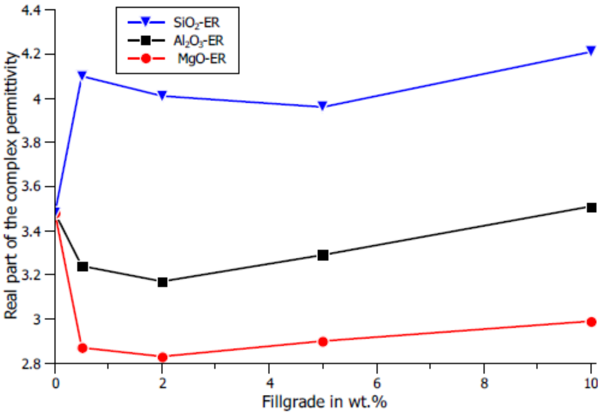

Fig. I - 9 : Relative permittivity of aluminum oxide (Al_2O_3), magnesium oxide (MgO) and silicon dioxide (SiO_2) filled epoxy resin nanodielectrics for 1.15 kHz at 293 K as a function of fillgrade [36].

5. Interphase

5.1. Interphase role in nanocomposites

At the nanometric level, the behavior of any material becomes predominantly monitored by the properties of its interface with the surroundings [42]. In fact, as the size of a spherical particle, for example, is reduced, the number of atoms and molecules present at its surface increases exponentially compared to the ones present in its volume (see Fig. I - 10) [23]. Consequently, the state of surface molecules will tailor the physical properties of the particle, if it is used alone, or of the composite, if it is mixed with another material. The properties of the surface differ from the volume since surface molecules and atoms of a condensed phase exhibit lower number of bondings with the bulk phase, increasing their reactivity [43]. At very low dimensions, quantum mechanical effects can also arise, changing casual bulk particle properties [44].

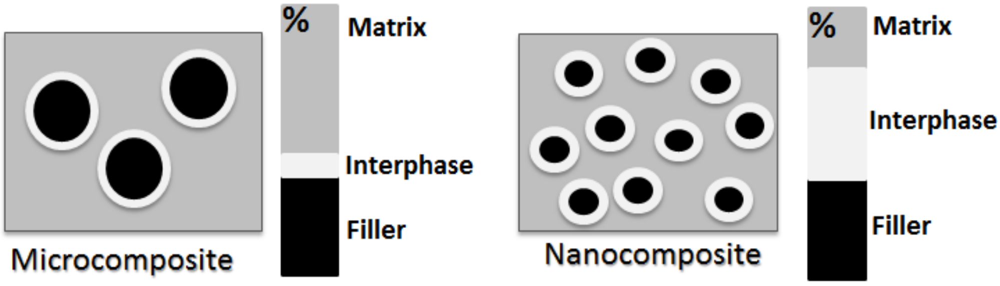

Fig. I - 10 : Sketch illustrating the percentage of interfacial regions for the same amount of filler in a composite, for micron-sized particles compared to nano-sized particles.

In the same way, since nanodielectrics are composed of nano-sized fillers embedded into the polymer matrix, the regions at the interface between particle and matrix possess special intrinsic properties and occupy a high volume in the material. As a consequence, these interfacial zones result in a new phase in the material that is commonly called the interphase. The interphase properties in nanocomposites are of the utmost importance, explaining most of their macroscopic behaviors; mainly, their electrical properties.

The physico-chemical state of interfaces in composites has been first characterized by indirect spectroscopic techniques such as the Fourier transform infrared spectroscopy, Raman spectroscopy and X-ray photoelectron spectroscopy, which lead to several interphase models [45].

Hereafter, a description of different interphase models set in order to describe this nanometric region in nanodielectrics is presented.

5.2. Interphase models

5.2.1. Intensity model

A classical description of interfacial zones has been explained with the intensity model. Each atom or molecule interacts at the interface with its environment according to different types of long and short range forces. Thus, the intensity of each physical or chemical property, associated with these forces, changes over a finite distance of a few nanometers, over the interphase (Fig. I - 11) [46]. The thickness of the interfacial zone may be less than a nanometer when only low range forces exist, and reaches 10 nm and more regarding long range forces, as is the case with electrically charged surfaces.

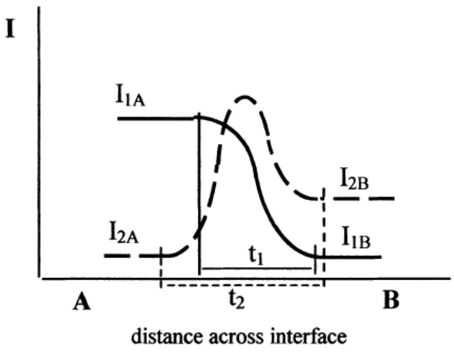

Fig. I - 11 : The interface between two phases A and B defined by the intensities I_1 and I_2 of properties 1 and 2 as they vary over effective distances t_1 and t_2 between A and B. t_1 and t_2 will be of nanometric dimension [46].

5.2.2. Lewis model of electrical double layer

According to Helmholtz, an electric double layer is formed between a solid and a liquid where the liquid represents a mobile phase [47]. In the case of a nanocomposite, the solid phase is made of nanoparticles and the amorphous polymer matrix is approximated to represent the mobile phase. In fact, the chains in a polymer can slightly move, in contrast to the ceramic filler structures.

Lewis's model of electrical double layer is encountered when a part or the whole surface of the nanoparticles is electrically charged [21]. In response to this charge, the matrix creates a shielding layer against the surface charge. Lewis defines the two layers of this model as the following:

a) The first is named Stern layer of molecular thickness. It mainly contains oppositely charged ions regarding the particle surface (counter-ions) at high densities and of rigid binding with the surface through strong forces. The intensity of these forces makes the ions in this layer almost immobile in the normal direction to the charged surface.
b) The second layer is named Gouy-Chapman layer, which is less dense than the first layer (diffuse layer). Gouy-Chapman layer is connected to the surface by Columbic forces. Stiffness and thickness of this layer are inversely proportional to the conductivity of the matrix.

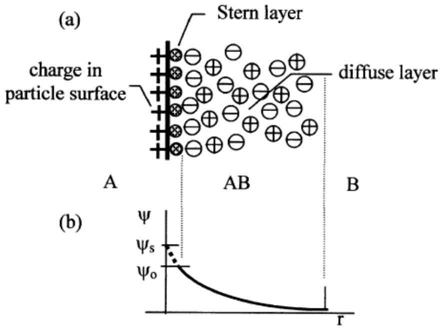

Fig. I - 12 : a. The diffuse electrical double layer produced by a charged particle A in a matrix B containing mobile ions, and b. the resulting electrical potential distribution $\Psi(r)$ [21].

5.2.3. Tsagaropoulos model

Tsagaropoulos model consists of two basic layers around the nanoparticle. The first contains the channels of the polymer that are strongly related to the particle, and the second is the least bonded layer [48]. A third layer of unaffected polymeric chains has been later added to the model [49].

The movement of polymers is restricted in the first layer and becomes suspicious in the second to become almost free in the third. The morphology of polymer chains was used in order to explain the two glass transition temperatures (T_g) sometimes measured in nanodielectrics [48]. The second T_g

has been found to correspond to the more restricted polymer chains of the loose layer created by sufficiently close particles at appropriate filler content.

5.2.4. Multicore model

The multicore model of T. Tanaka *et al.* considers the interface between an inorganic nanoparticle and a polymeric organic matrix as divided into three layers, overlapped by a Gouy-Chapman diffuse layer [22]:

a) Bonded layer: this is the layer that firmly connects the inorganic nanoparticle to the matrix. This bonding is usually provided by coupling agents added to the surface such as silane coupling agents. The thickness of this layer is about ~ 1 nm.

b) Bounded layer: this is the part of the interphase that consists of polymer chains in strong bonding and/or interaction with the first layer and the inorganic particle. The thickness of the bounded layer is of a few nanometers depending on the intensity of the present forces.

c) Loose layer: this is the layer that follows the first two layers and that reacts loosely with the bounded layer. Its corresponding polymer chains are generally considered to have different conformations, mobility and even free volume or crystallinity from the organic bulk. It can also consist of a less stoichiomerically cross-linked layer. The thickness of the loose layer is of the order of a few tens of nanometers.

Furthermore, Columbic forces superimpose the above chemical layers. When the particle is charged, an electrical double layer thus overlaps the three layers. This model also states that polymer chains order diminishes with the transition from the first to the third layer. Hence, charge carrier traps can be deep in the first ordered layers, and superficial in the rest. Moreover, this model has been used to explain the previously mentioned decrease in the dielectric permittivity of nanofilled polymers. Authors explain that by the decrease of chains mobility in the second layer, and the decrease of free volume in the third [22].

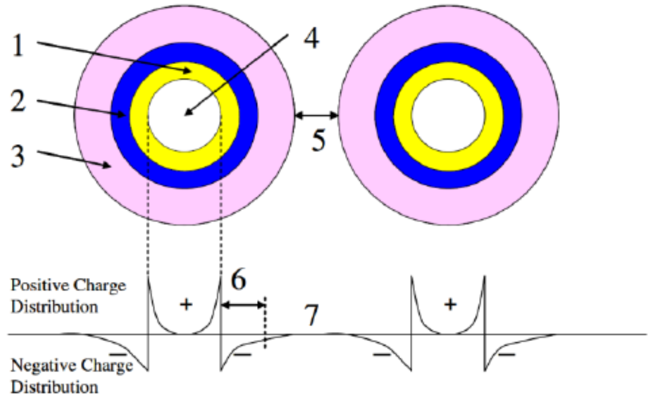

1: The first layer with mutual tight binding: several nm
2: The second layer with deep traps: about 10 nm
3: The third layer with large local free volume as ion traps and shallow electronic traps: several tens nm
4: Nano-particles: 20 to 50 nm in diameter
5: Interparticle distance (surface to surface): 40 to 100 nm
6: Debye yielding distance: up to about 100 nm
7: Possible overlapping of the third layers and charge tails of nano-particles

Fig. I - 13 : Tanaka's model of three layers interphase overlapped by a Gouy-Chapman layer [22].

5.2.5. Water shell model

C. Zhou *et al.* [38] further developed past models in order to explain the observed behaviors of dielectric materials in the presence of humidity. Based on the characterization results of an epoxy nanocomposite system, authors assume that three types of water shells surround the nanoparticle, which itself plays the role of a "core":

a) The first one is made of a few water monolayers molecules (~ 5) firmly bound to the nanofiller.

b) The second one contains water molecules that are loosely bound by Van Der Waals forces. In this second layer, the concentration of water may be sufficient to make it conductive. These first two layers are likely to provide channels to charges and carriers, and overlapping water shells can result in a conduction path to charge carriers.

c) The third and last layer also includes water molecules which are however “free” and present in the bulk of the matrix.

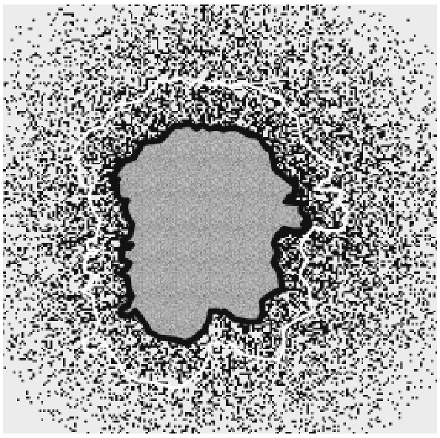

Fig. I - 14 : Schematic of a water shell surrounding a particle. The first layer with the highest concentration of water molecules is drawn in black, followed by the second layer with a lower concentration and thicker extension and finally the third layer with the least big water concentration [38].

5.2.6. Interphase volume model

The interphase volume model aims at giving the dependency of the interphase volume fraction regarding filler weight percentage [50]. The model assumes that an interphase region surrounds the particles of any diameter, and which satisfies three suppositions:

a) Particles are homogeneously dispersed in the matrix.
b) They are all spherical.
c) Their disposition is similar to a face centered cubic lattice.

Four cases of interphase neighboring particles are taken into consideration: not overlapped, overlapped, highly overlapped and absolutely overlapped (Fig. I - 15). Each case mainly depends on the distance between particles center, which is dependent on the filler content or the interphase thickness.

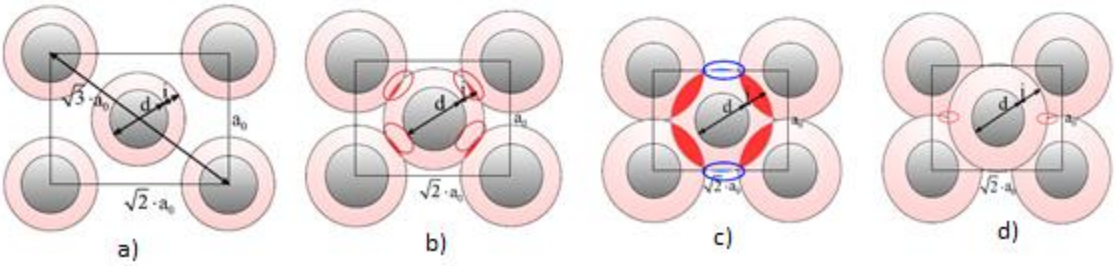

Fig. I - 15 : View on the body diagonal: a. interphases do not overlap; b. interphases of the nearest neighboring particles do overlap, c. interphases of the neighboring center particles do overlap, and d. triple points reached: the whole material is only consisting of interphase and particle volume [50].

Ratio percentages of the interphase volume over the particle volume have been found to be linearly depending on the filler content with decreasing steepness after overlaps. Thus, interphase range thickness is estimated to be approximately between 20-40 nm in the case of high particle-matrix interaction, in accordance with Tanaka’s model [22].

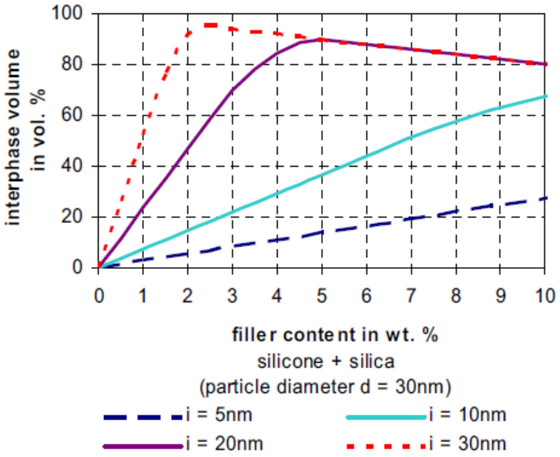

Fig. I - 16 : Interphase content according to the interphase volume model for a silicone matrix with SiO_2 nanoparticles and interphase thicknesses i, for a particle diameter d = 30 nm [50].

Optimal nanocomposite properties are supposed to be achieved at maximum interphase volume percentage reached at specific filler concentrations. Consequently, characterizing the best weight percentage, scientists referred to the above graph (Fig. I - 16) to deduce hypothetic values for interphase thickness [51].

5.2.7. Polymer chain alignment model

The polymer chain alignment model [34] is especially influenced by Tanaka’s model and interphase volume model. It considers the strong dependency of the material pre- and post- processing operations on the interphase. When coupling agents are used to connect organic chains to the inorganic surface, this connection can result in a restructuring of the surrounding host matrix. A layer of perpendicularly aligned polymer chains is then formed around the particle surface that is modified by a curing agent. This layer forms a rigid polymer structure (Fig. I - 17).

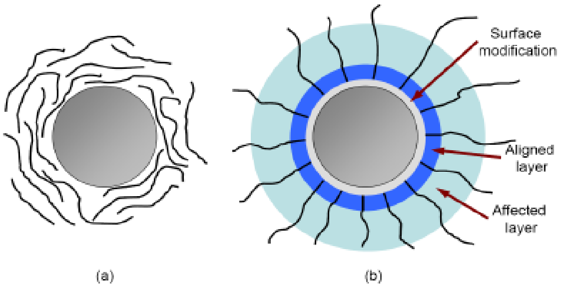

Fig. I - 17 : a. Particle without surface modification and thus only weak interaction with the host, and b. particle with layer of surface modification, resulting layer of aligned polymer chains, further affecting the surrounding area thus restructuring the polymer [34].

The alignment is also extended beyond this layer since polymers often consist of long chains. Furthermore, an interpenetrating polymer network can be formed between polymer chains leading to physical properties unlike those of particle or host. Thus, an illustration of the obtained system is given in Fig. I - 18. The order decreases gradually with the distance from the filler depending on the particle surface shape. Dimensions of these regions can be predicted with the equations present in ref [34].

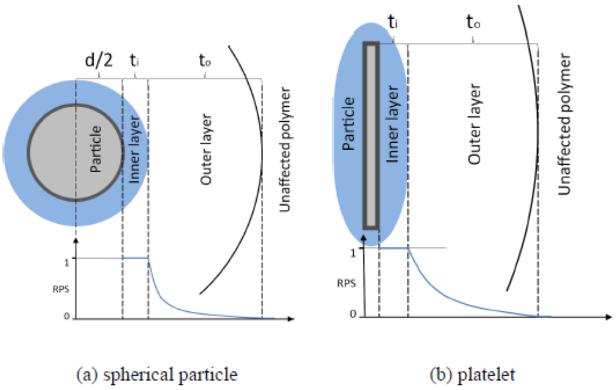

Fig. I - 18 : Illustration of how rigid polymer structure can change from, a. spherical particle or, b. platelet to surrounding polymer [34].

5.2.8. Other nanocomposites models

In some cases, the higher breakdown strength of nanodielectrics, the electrical tree growth and surface discharge phenomena have been attributed to the nanoparticles themselves acting as barriers to the flow of current between electrodes [11, 31, 52, 53]. More recently, T. Tanaka presented a new model for nanodielectrics explaining several of their electrical behaviors [54]. In this model, nanoparticles are represented as quantum dots. Since quantum dots possess negative dielectric permittivity, the author notes that this can simply explain the commonly observed permittivity decrease in nanocomposites.

5.3. Indirect interphase characterization

As it has been noted earlier in this chapter, interphases play a substantial role in the final properties of a nanocomposite. In fact, in order to predict the behavior of the dielectric permittivity of nanodielectrics, general two-phase mixture laws failed to predict the inconsistent behavior of nanocomposites regarding filler content and mixture components properties. Thus, these casual “power-laws” have been modified into “interphase power-laws”, so the interphase is included as a third phase in the material, with different properties than filler and matrix [55]. Furthermore, in order to account for the non-uniformity regarding particles wt. % explained by overlapped interphase layers, I. Preda *et al.* added an overlapping factor into the interphase power-law [56].

Consequently, we deduce the importance of interphase characterization in nanocomposites in order to both, understand their macroscopic behavior, and tailor them by optimizing the rules that link mixture component properties to the final material. To date, scientists commonly used semi-phenomenological methods to gain insight into interphase properties.

In ref [57], an electrostatic three layers model was considered for the filler-polymer interface in which an exponential charge distribution through a diffuse layer was taken into account (Fig. I - 19). Each layer permittivity was calculated with simplified chemical methods. The predicted effective permittivities showed a good correlation with the experimental results of permittivities at low frequencies (Fig. I - 20).

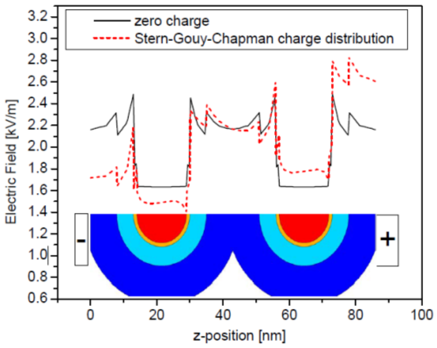

Fig. I - 19 : Electric field variation along a line perpendicular to armatures passing through nanoparticles, for 5 wt. % SiO_2 [57].

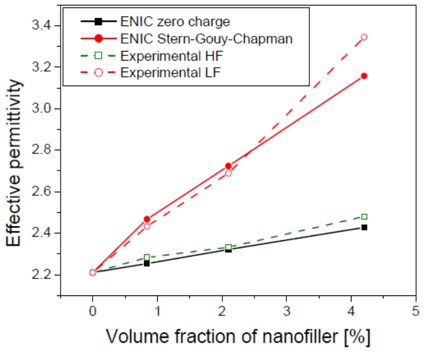

Fig. I - 20 : Comparison of the simulated effective permittivity with experimental results obtained at 10^{-2} Hz (LF: low frequency) and at 10^{6} Hz (HF: high frequency) [57].

Another model found in literature inspired by ref [58] and [56], calculates the interphase with an exponential formula, identifying an overlapping factor for very small particles and high filler contents (Fig. I - 21) [59].

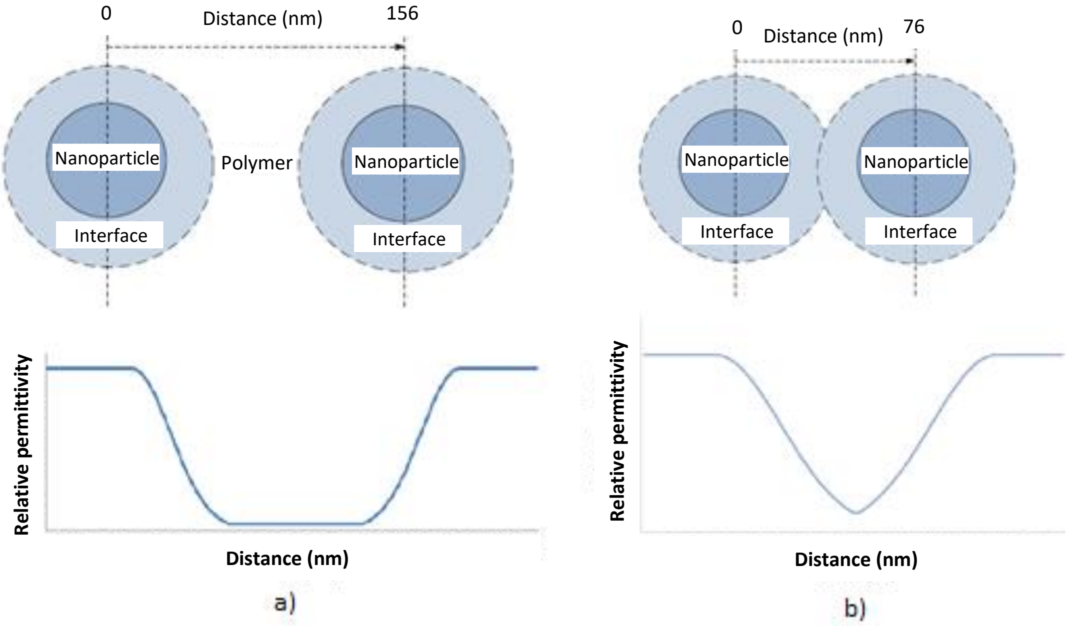

a) b)

Fig. I - 21 : Relative permittivity distribution between the centers of two identical neighboring TiO_2 nanoparticles with: a) 50 nm diameter and b) 26 nm diameter embedded in epoxy resin, without overlapped interphases [59].

Recently, J.C. Pandey and N. Gupta estimated the thickness of the interphase by modifying the interphase volume model [60]. Contrarily to the previous model, authors consider, in this modified version, a material with non-perfect dispersion of particles. In conjunction with experiments, an approximate thickness of 200 nm of the interphase in an epoxy resin with aluminum oxide of 50 nm radius has been calculated.

In conclusion, although interphases are supposed to be the key to understand nanodielectrics interesting electrical performances, up until now, only semi-phenomenological hypotheses on interphase properties have been addressed. As we can see from above studies, in order to explain global nanocomposite behavior, macroscopic characterizations are associated to theoretical interphase models. However, since special dielectric changes are occurring at the nanometric level, these indirect methods reach a certain limit of accuracy and deep understanding of real phenomena. The following question is hence brought up: why not probing locally the interphase?

6. Local interphase characterization

Local measurement of interphases is nowadays mainly addressed by two imaging and characterization methods of high resolution: electron microscopies and scanning probe microscopies. Scanning probe microscopy has been used as a novel alternative method to the equally well used techniques: nano-indentation and nano-scratch. All of these techniques probe different interphase properties in order to differentiate it from initial material components. A brief description of these techniques and their recent advances in interphase study of variously filled composites will be developed in the following paragraphs.

6.1. Electron and ion microscopies

6.1.1. Definition

Electron microscopies use a beam of charged particles or electrons that are accelerated with a high voltage in a vacuum chamber, and focused with electromagnetic or electrostatic lenses. Due to the wave-particle duality, at 10 kV for example, the wavelength of the electrons reaches 12.5 pm. Such low wavelengths permit to electron microscopies to differentiate between features as small as one angstrom, typically an individual atom.

Electron microscopies can be divided into four main types: Transmission Electron Microscopy (TEM), Scanning Electron Microscopy (SEM), Scanning Transmission Electron Microscopy (STEM), Focused Ion Beam and DualBeam microscopy (FIB). Briefly, in a SEM the signal is obtained from the surface of the sample that has been bombarded with the beam, in contrary to the TEM where the transmitted signal is detected from the opposite surface of the beam direction. The STEM is the combination of SEM and TEM, and FIB is similar to SEM except that a beam of ions replaces electrons and provides higher resolution imaging. Several informations can be derived out of the signal depending on the type of electron beam-sample interaction, among which, density contrasts, cristallinity, chemical elemental composition etc.

6.1.2. Interface characterization state of the art

TEM has been widely used to study the interphase of coated ceramic fibers in a ceramic matrix [61], the interphase in carbon reinforced composites [62, 63] and ceramic fiber reinforced polymers [64].

A gradient variation in the structure at the interfacial region has been reported in ref [62]. Later, authors studied the effect of three types of sample preparation on the accuracy of interphase study with TEM: Focused Ion Beam (FIB), Ion Beam etching (IB) and Ultramicrotomy (UM) [63]. According to the analysis of bonding states of FIB prepared specimens, an interphase of 200 nm thickness has been estimated (Fig. I - 22), through which the quantity of oxygen increases gradually from the carbon fiber to the matrix (Fig. I - 23). Ion beam prepared cross-sections showed that the interphase is a transition region from crystalline states to amorphous ones.

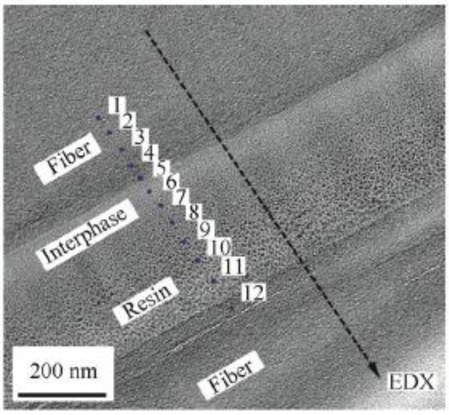

Fig. I - 22 : STEM image showing the identified fiber, interphase and resin matrix regions [63].

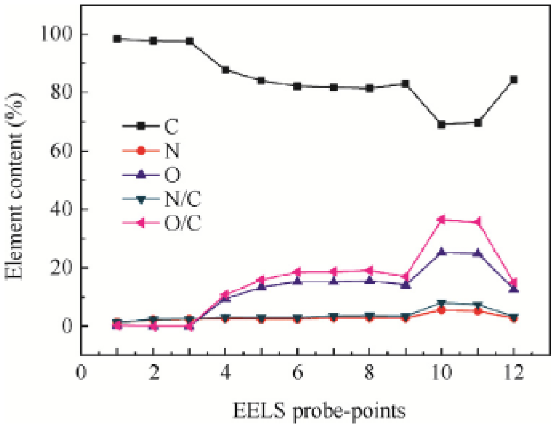

Fig. I - 23 : Variation of element contents at electron energy loss spectroscopy (EELS) probe-points of Fig. I - 22 [63].

A recent paper reports TEM measurements of the interphase in two types of glass fiber reinforced polymers containing nanocellulose at fibers surface [64]. Authors proved that FIB is the most appropriate method for TEM lamella preparation, limiting the deformation of the interphase of investigated samples.

6.1.3. Limitations

Electron microscopy limits are due to the easily deflected or stopped electron beam in the matter. This explains the necessity to work under low pressure and the requirement of very thin samples especially for TEM measurements (< few hundreds of nanometers). However, thinning preparation techniques face several challenges to preserve the specimen bulk properties. Scientists commonly studied suitable sample preparation methods for interphase study [63, 64]. An example of obtained results for carbon-fiber epoxy composites is presented in Fig. I - 24. Therefore, specimen preparation is a science by itself, requiring too much care to preserve the interphase original properties.

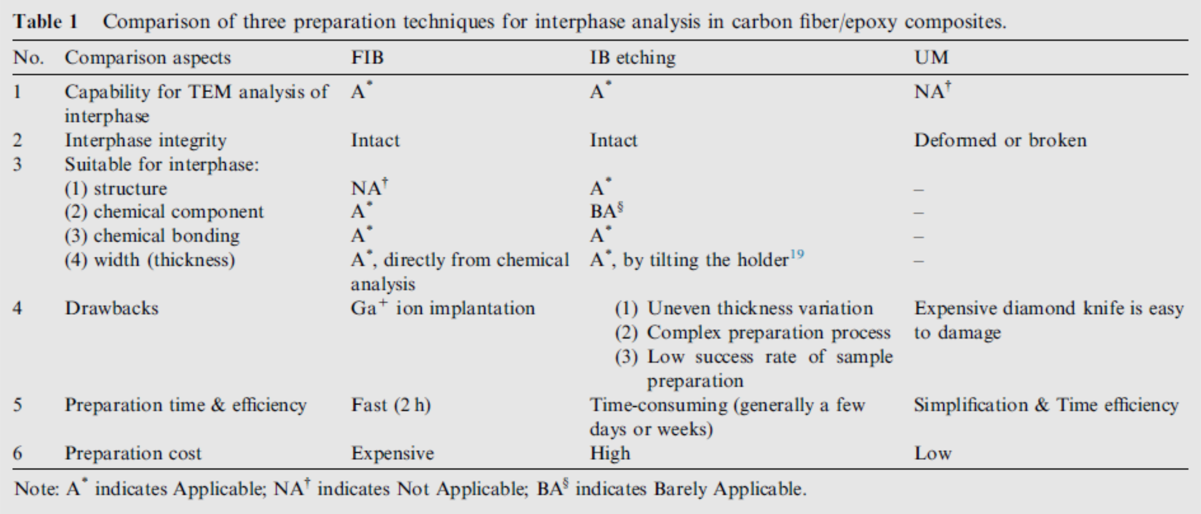

Table 1 Comparison of three preparation techniques for interphase analysis in carbon fiber/epoxy composites.

No.	Comparison aspects	FIB	IB etching	UM
1	Capability for TEM analysis of interphase	A*	A*	NA†
2	Interphase integrity	Intact	Intact	Deformed or broken
3	Suitable for interphase:			
	(1) structure	NA†	A*	–
	(2) chemical component	A*	BA§	–
	(3) chemical bonding	A*	A*	–
	(4) width (thickness)	A*, directly from chemical analysis	A*, by tilting the holder[19]	–
4	Drawbacks	Ga^+ ion implantation	(1) Uneven thickness variation (2) Complex preparation process (3) Low success rate of sample preparation	Expensive diamond knife is easy to damage
5	Preparation time & efficiency	Fast (2 h)	Time-consuming (generally a few days or weeks)	Simplification & Time efficiency
6	Preparation cost	Expensive	High	Low

Note: A* indicates Applicable; NA† indicates Not Applicable; BA§ indicates Barely Applicable.

Fig. I - 24 : Comparison of three preparation techniques for interphase analysis in carbon-fiber epoxy composites [63].

Moreover, when used to study electrical insulations, electron microscopies resolution is reduced and image artifacts can appear due to charging effects [65-69]. Specimens are usually coated with a metal layer to suppress charging. However, the additional layer decreases the resolution of non-flat samples.

6.2. Nano-indentation and Nano-scratch

As interphases affect the global physical properties of composites, their macroscopic mechanical behavior has also been shown to be correlated to the quality of the interface between the filler and the matrix [70]. Hence, several local mechanical techniques have been used, going from micro-bond and micro-droplet test methods for fracture toughness and interfacial shear stress measurements [71, 72], to the most accurate ones with nano-indentation, nano-scratch and ultimately, AFM nanomechanical methods . In the following, a brief description of nano-indentation, nano-scratch and AFM mechanical methods and their corresponding state of the art for interphase study will be addressed.

6.2.1. Definition

The nano-indentation method uses an indenter that is pressed into the material while recording loading-hold-unloading cycles in function of the displacement [73]. Calibrating the indenter geometry and assuming a linear elastic behavior on the onset of loading, the hardness and quasi-static elastic modulus can be derived [74]. On the other hand, nano-scratch tests also use a characteristic tip of calibrated geometry but placed in contact with the sample. The latter is moved below the tip creating linear scratches.

6.2.2. Interphase characterization state of the art

Nano-indentation and nano-scratching methods have been used to study interfaces in several types of composites, among which, glass-reinforced polymers [75-78] and single-wall-carbon-nanotubes [79]. Similarly to SEM, these types of composites have been investigated in cross-sectioned specimen. Authors have been able to show the diffusion into the interphase of water molecules due to water ageing [78], and the dissolution of silane coupling agents in the interphase [77]. The interphase widens with water ageing and silane coupling agents concentration. Interfacial regions in fiber-reinforced composites frequently show a gradual change in hardness and stiffness between matrix and filler [79]. The reported interphase thickness values are very different, varying from 0.1 - 1.5 µm for example [76, 80, 81], to 2 - 6 µm [75, 78]. The measured width depends on the type of material components, as well as the specific measured property with the corresponding adopted experiment.

6.2.3. Limitations

Although these techniques have shown to be useful for interphase study, they are however limited in resolution. They might be applicable to microfilled composites, possible to be cross-sectioned, but they quickly reach limitations for nanofilled polymers. Moreover, even on microcomposite samples, it has been widely discussed that the measured variations in the mechanical properties of the interphase are mostly created by the used technique rather than an actual material property [81-84].

6.3. Nanomechanical atomic force microscopy

As a novel approach for nanomechanical characterization, atomic force microscopy, adapted to mechanical testing, has emerged to study composite materials that present extremely narrow interphase regions and/or nanometric fillers, difficult to be distinguished in casual mechanical techniques.

6.3.1. Definition

The Atomic Force Microscope (AFM) uses a physical probe in the form of a micrometric cantilever with a very sharp tip at its end. The probe senses interaction forces with the sample while placed either in contact (contact mode) or at few nanometers from the surface (non-contact or tapping mode). Several operational methods can be adopted in order to investigate numerous material properties according to the physical nature of the tip-sample interaction and to the mechanism of signal extraction. High lateral resolutions (atomic scale) and sensitivities (< 10 pN) can be achieved with AFM on almost all kinds of surfaces with minimal treatment in many environments, contrarily to SEM. The high resolution mainly relies on the precise and accurate motions provided by piezoelectric devices. A detailed description of AFM will be presented in Chapter II. Commonly used nanomechanical AFM techniques are Contact Resonance [85], PeakForce Tapping [86] and Tapping phase [87].

6.3.2. Interphase characterization state of the art

The nanomechanical modes of AFM are the most widely used and developed modes of scanning probe microscopies for interphase investigation in composite materials. An extensive state of the art can be found for several types of polymeric composites where their interphase has been studied with nanomechanical AFM.

Researchers used AFM tapping mode phase signal, nano-indentation mode with low scanning force, force volume mode etc. to characterize the transition region in carbon and glass fiber-reinforced polymers of micrometric diameter [88-95] as well as in confined polymers to substrates surface [96]. Studying cross-sectioned specimens, authors reported an interphase either with higher stiffness than the bulk matrix [90], or a lower one [90, 91]. When the interphase thickness exceeded the AFM resolution, measurements were sensitive to thicknesses going from 100 nm to 800 nm depending on material composition, fillers surface modification, temperature, water ageing [84, 90, 93, 95] etc.

Until now, whether with electron microscopies or local mechanical techniques, we have only mentioned interphase investigation in materials where the cross-section gives direct access to the interfacial zone (e.g: fiber reinforced polymers). However, as mentioned earlier, in the framework of this thesis, we are mostly concerned about composites with 3D nanometric fillers, such as nanoparticles. In this case, cross sectioning is not too probable to reveal the interphase. Nevertheless, unlike electron microscopies and past mechanical methods, some advances in the study of nanoparticles filled composites have been achieved with nanomechanical AFM.

S. Chang e*t al.* tried to measure the interphase in a silicon dioxide (SiO_2) filled glassy polymer nanocomposite [97]. Through the combination of the nanoscale Contact Resonance AFM results to the macroscopic Brillouin light scattering ones, authors found an interphase of 3 nm approximately. The interphase showed higher elastic modulus than bulk polymer in accordance to authors previous broadband spectroscopy study [98]. The higher modulus of the interfacial layer has been attributed to polymer chains stretching, despite the lower dense segmental packing of the interfacial region compared to the bulk polymer. Authors used the following hypothesis on the sample configuration to analyze their results (see inset Fig. I - 25.b):

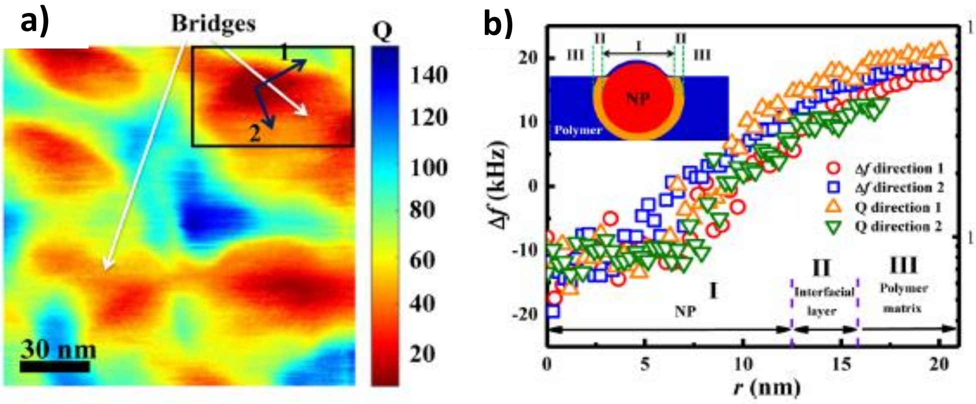

Fig. I - 25 : AFM images of the SiO_2 nanocomposite: a. *Q*-factor (quality factor-see Chapter II) of the cantilever map of the surface, b. the spatial resonance frequency shifts (Δf_0-due to changes in mechanical properties) and *Q* profile for a single nanoparticle framed by the black boxes in panel (a.). The inset shows schematic positioning of the nanoparticle in the polymer matrix and demonstrates three regions associated with different changes in Δf_0 and *Q* [97].

N. Lahoud *et al.* used PeakForce Tapping-Quantitative Nanomechanical Mapping in order to study the profile of Young's modulus over boron nitride nanoparticles in a polyimide matrix [99]. Authors measured a 23 nm approximately wide region of transitional Young's modulus from the particle to the matrix. This region has been affected to the interphase.

More recently, H. Huang *et al.* performed an AFM nanomechanical study for the interphase in SiO_2 nanoparticles filled polymer matrix [100]. SiO_2 particles diameter in matrix has been estimated to 40 nm from topography surface profile. Authors found a gradient in the stiffness on a region between the particle and the matrix that was ascribed to the interphase. The interphase width has been measured from the distance of the supposed-to-be the real tip apex position when it finishes scanning the particle, and the point where the stiffness becomes equal to the bulk matrix one. The glass transition of the interphase has been measured locally and found to be higher than the bulk polymer. The interphase thickness has been supposed to increase with temperature, inversely to previous works [101, 102]. However, authors mention clearly the possibility of having measured artifacts with increasing temperature. A model of the interphase chemistry has been also hypothesized. Authors suppose the following arrangement of particle-interphase-matrix (inset Fig. I - 26):

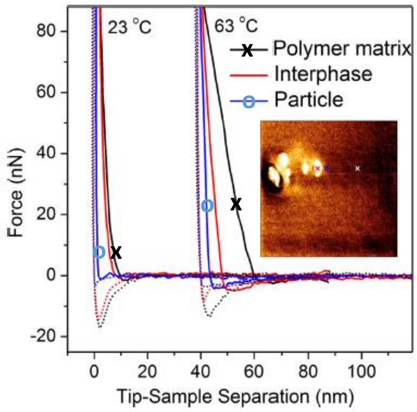

Fig. I - 26 : AFM force-distance curves recorded between the tip and (x) the polymer matrix, (-) the interphase region and (o) on top of a hydrophobized silica particle located at the nanocomposite surface. The curves were recorded in force mapping spectroscopy mode at 23°C and 63°C, respectively, at the positions marked with crosses on the image. The force curves measured at 63 °C have been displaced on the x-axis for clarity. Measurements on approach and retraction are shown as solid and dotted lines, respectively [100].

6.3.3. Limitations

From the above AFM overview, it can be noticed that the measured thickness range of the interphase in microcomposites generally exceeds that of nanocomposites. Moreover, for the current studies performed on nanocomposites, the thickness of the interphase varies considerably between different studies. This can be attributed at the first sight to the different composites compositions and thereby, physico-chemical interfacial interactions. However, this is also highly related to the scanned property, and most importantly, to possible scanning artifacts. In fact, while some studies consider tip convolution in AFM images [100], others do not seem to do so [97, 99]. Furthermore, AFM tip interaction with non-planar samples is not fully understood yet [103]. Understanding the underlying physics of the probe interaction with each type of sample configuration and then, quantifying measurement resolution in each specific scanning mode, is substantially important. Additionally, authors suppose certain assumptions on the subsurface composition of the probed region, on which they have based their interpretations of the interphase. However, there is no direct evidence for the consistency of these speculations. For instance, if other configurations constitute the probed specimen, different analysis must be performed, that might draw different conclusions on the interphase.

6.4. Electrostatic force microscopy for interphases…?

In addition to the current limitations concerning SEM and nanomechanical methods for interphase measurement, in this work, due to the electrical application of nanodielectrics, we have been interested in the dielectric polarization properties of these materials. Since the permittivity of the interphase is supposed to be different than mixing components as described in the previous sections, this characteristic is thereby going to be the property of interest for interphase characterization. Thus, the necessity of both local and dielectric characterization method can be provided by Electrostatic Force microscopy (EFM), an AFM variant adapted to electrostatic forces detection.

In the following chapter, we will present the state of the art of all scanning probe microscopies electrical methods and EFM in particular. Moreover, the advances in those techniques in the fields of material investigation that are needed to solve the problem of interphase study in nanocomposite systems will be reported.

7. Conclusion

In this first chapter, a review on the basics of electrical insulators, or dielectrics, and their response to electric fields has been stated. An electric field can either separate superposed opposite charges to create an electric dipole, or reorient a permanent dipole. This is the so-called “polarization” phenomena, which can be divided into several types with specific establishment time. As electrical insulations are often prone to failure, new versatile insulating materials are always needed.

Nanodielectrics, a combination of nanoparticles in a polymeric matrix, seem to cater to demand: mechanical, thermal and insulating properties have often been improved, contrarily to their microcomposite counterparts. The explanation behind the special properties in nanodielectrics is usually attributed to the interfacial zone between filler and matrix: the interphase. As interfacial interactions can lead to regions in the interphase that are characterized with unique properties compared to both nanoparticles and polymer, and due to the high percentage of interfaces at the nanoscale, the interphase intrinsic properties are of the utmost importance. For example, the prediction of nanodielectrics macroscopic dielectric constant could only be afforded by using modified mixture laws that include the interphase: its volume and permittivity. At low particles concentration, the permittivity of nanodielectrics can present values that are either higher or lower than both filler and matrix. Several physico-chemical interphase models have been established to understand electrical experimental results. All of them agree on the fact that the interphase is a region around nanoparticles, where the interactions between particles surface and polymer chains can rearrange polymer chains, which can explain lower interphase permittivities. Water molecules have been also reported to adsorb and accumulate in the interfacial region, clarifying the macroscopic increased permittivities.

Insight into the interphase has been usually addressed through macroscopic characterizations. In particular, scientists used to correlate macroscopic permittivity measurements to theoretical models such as the modified mixture laws, to speculate interphase thickness and dielectric constant. However, the task is doubly complicated since theoretical models may not be appropriate, as well as interphase properties are unknown. Consequently, a local characterization of the interphase becomes essential. Mostly used methods to study the interphase at the nanometric level are electron microscopies and nanomechanical characterizations techniques, such as classical nano-indentation and nano-scratch methods that have evolved recently towards nanomechanical atomic force microscopy. These methods proved to resolve interphases in composites with simple geometries, like fiber fillers, where the interphase becomes easily exposed to the surface after cross-sectioning, which is not likely for nanoparticles filled polymers. Moreover, these techniques present some limitations, such as sample preparation complexity for TEM measurements in addition to imaging artifacts. Interphases in nanocomposite materials have been particularly investigated with AFM nanomechanical techniques. The measured interphase thickness importantly varies in literature. This is mainly due to the nature of composite components, measuring technique and most importantly, results interpretation.

In this thesis, the dielectric permittivity of the interphase is going to be used as its signature. Consequently, the electrostatic force microscope will be utilized as a potential technique for both local and dielectric characterization method with the aim of interfacial zones detection. In the following chapter, an introduction to EFM basic principle will be presented.

8. References

[1] P. Robert, *Matériaux de l'électrotechnique*: Dunod, 1979.

[2] M. C. Petty, "Electrical Conductivity," in *Molecular Electronics*, ed: John Wiley & Sons, Ltd, 2007, pp. 65-128.

[3] L. A. Dissado and J. C. Fothergill, *Electrical degradation and breakdown in polymers*: The institution of Engineering and Technology, 1992.

[4] E. Tuncer and I. Sauers, "Industrial Applications Perspective of Nanodielectrics," in *Dielectric Polymer Nanocomposites*, J. K. Nelson, Ed., ed: Springer US, 2010, pp. 321-338.

[5] G. Blaise and D. Treheux, "Physics of Dielectrics," in *Dielectric Materials for Electrical Engineering*, ed: John Wiley & Sons, Inc., 2013, pp. 1-16.

[6] M. Mario and D. Rodolphe, "Matériaux diélectriques," *Techniques de l'ingénieur Propriétés électriques et électrochimiques,* vol. base documentaire : TIB336DUO, 2010.

[7] F. Robert, *Les isolants en électrotechnique*: EYROLLES, 1986.

[8] K. Wagner, "Erklärung der dielektrischen Nachwirkungsvorgänge auf Grund Maxwellscher Vorstellungen," *Archiv für Elektrotechnik,* vol. 2, pp. 371-387, 1914/09/01 1914.

[9] R. W. Sillars, "The properties of a dielectric containing semiconducting particles of various shapes," *Electrical Engineers, Journal of the Institution of,* vol. 80, pp. 378-394, 1937.

[10] K. C. Kao, "2 - Electric Polarization and Relaxation," in *Dielectric Phenomena in Solids*, K. C. Kao, Ed., ed San Diego: Academic Press, 2004, pp. 41-114.

[11] S. Singha and M. J. Thomas, "Permittivity and tan delta characteristics of epoxy nanocomposites in the frequency range of 1 MHz-1 GHz," *IEEE Transactions on Dielectrics and Electrical Insulation,* vol. 15, pp. 2-11, 2008.

[12] R. Coelho and B. Aladenize, *Les diélectriques : Propriétés diélectriques des matériaux isolants*: HERMES, 1993.

[13] F.Kremer and A. Schönhals, *Broadband Dielectric Spectroscopy*: Springer, 2002.

[14] I. A. Preda, "Modeling and characterization of nanocomposite materials using dielectric methods," PhD, Université Montpellier 2, 2013.

[15] T. J. Lewis, "Nanometric dielectrics," *Dielectrics and Electrical Insulation, IEEE Transactions on,* vol. 1, pp. 812-825, 1994.

[16] M. F. Frechette, M. L. Trudeau, H. D. Alamdar, and S. Boily, "Introductory remarks on nanodielectrics," *Dielectrics and Electrical Insulation, IEEE Transactions on,* vol. 11, pp. 808-818, 2004.

[17] G. C. Psarras, "Nanodielectrics: an emerging sector of polymer nanocomposites," *eXPRESS Polymer Letters,* 2008.

[18] Wiley-VCH, *Ullmann's Polymers and Plastics, 4 Volume Set: Products and Processes*: Wiley, 2016.

[19] C. Mayoux, "Degradation of insulating materials under electrical stress," *IEEE Transactions on Dielectrics and Electrical Insulation,* vol. 7, pp. 590-601, 2000.

[20] Y. Cao, P. C. Irwin, and K. Younsi, "The future of nanodielectrics in the electrical power industry," *IEEE Transactions on Dielectrics and Electrical Insulation,* vol. 11, pp. 797-807, 2004.

[21] T. J. Lewis, "Interfaces are the dominant feature of dielectrics at the nanometric level," *Dielectrics and Electrical Insulation, IEEE Transactions on,* vol. 11, pp. 739-753, 2004.

[22] T. Tanaka, M. Kozako, N. Fuse, and Y. Ohki, "Proposal of a multi-core model for polymer nanocomposite dielectrics," *Dielectrics and Electrical Insulation, IEEE Transactions on,* vol. 12, pp. 669-681, 2005.

[23] J. K. Nelson, "Overview of nanodielectrics: Insulating materials of the future," in *2007 Electrical Insulation Conference and Electrical Manufacturing Expo*, 2007, pp. 229-235.

[24] S. Hishukawa, S. Okada, T. Imai, and T. Shimizu, "Thermal and Mechanical Performance of Nanocomposite Insulating Materials," in *Advanced Nanodielectrics: Fundamentals and Applications*, T. I. Toshikatsu Tanaka, Ed., ed Penthouse Level, Suntec Tower 3, 8 Temasek Boulevard, Singapore 038988: Pan Stanford Publishing Pte. Ltd., 2017.

[25] P. O. Henk, T. W. Kortsen, and T. Kvarts, "Increasing the Electrical Discharge Endurance of Acid Anhydride Cured DGEBA Epoxy Resin by Dispersion of Nanoparticle Silica," *High Performance Polymers,* vol. 11, pp. 281-296, 1999.

[26] J. K. Nelson, Y. Hu, and J. Thiticharoenpong, "Electrical properties of TiO2 nanocomposites," in *2003 Annual Report Conference on Electrical Insulation and Dielectric Phenomena*, 2003, pp. 719-722.

[27] M. Dongling, A. H. Treese, W. S. Richard, C. Anna, M. Eva, Ö. Carina*, et al.*, "Influence of nanoparticle surface modification on the electrical behaviour of polyethylene nanocomposites," *Nanotechnology,* vol. 16, p. 724, 2005.

[28] S. Li, G. Yin, G. Chen, J. Li, S. Bai, L. Zhong*, et al.*, "Short-term breakdown and long-term failure in nanodielectrics: a review," *IEEE Transactions on Dielectrics and Electrical Insulation,* vol. 17, pp. 1523-1535, 2010.

[29] R. C. Smith, C. Liang, M. Landry, J. K. Nelson, and L. S. Schadler, "The mechanisms leading to the useful electrical properties of polymer nanodielectrics," *Dielectrics and Electrical Insulation, IEEE Transactions on,* vol. 15, pp. 187-196, 2008.

[30] R. C. Smith, J. K. Nelson, and L. S. Schadler, "3 - Electrical behavior of particle-filled polymer nanocomposites," in *Physical Properties and Applications of Polymer Nanocomposites*, S. C. Tjong and Y. W. Mai, Eds., ed: Woodhead Publishing, 2010, pp. 70-107.

[31] A. B. M. Danikas, R. Sarathi, A. Basri Bin Abd Ghani, "A Review of Two Nanocomposite Insulating Materials Models: Lewis' Contribution in the Development of the Models, their Differences, their Similarities and Future Challenges," *Engineering, Technology & Applied Science Research,* vol. 4, pp. 636-643, 2014.

[32] D. Pitsa, G. E. Vardakis, and M. G. Danikas, "Effect of nanoparticles loading on electrical tree propagation in polymer nanocomposites," in *Proceedings of 2011 International Symposium on Electrical Insulating Materials*, 2011, pp. 9-11.

[33] D. Pitsa, M. G. Danikas, G. E. Vardakis, and T. Tanaka, "Influence of homocharges and nanoparticles in electrical tree propagation under DC voltage application," *Electrical Engineering,* vol. 94, pp. 81-88, June 01 2012.

[34] T. Andritsch, R. Kochetov, P. H. F. Morshuis, and J. J. Smit, "Proposal of the polymer chain alignment model," in *Electrical Insulation and Dielectric Phenomena (CEIDP), 2011 Annual Report Conference on*, 2011, pp. 624-627.

[35] R. Kochetov, T. Andritsch, P. H. F. Morshuis, and J. J. Smit, "Anomalous behaviour of the dielectric spectroscopy response of nanocomposites," *IEEE Transactions on Dielectrics and Electrical Insulation,* vol. 19, pp. 107-117, 2012.

[36] T. Andritsh, "Epoxy based nanocomposites for high voltage DC applications - Synthesis, Dielectric Properties and Space Charge Dynamics," PhD, Technische Universiteit Delft, 2010.

[37] R. Kochetov, "Thermal and Electrical Properties of Nanocomposites, Including Material Processing," PhD, Technische Universiteit Delft, 2012.

[38] C. Zou, J. C. Fothergill, and S. W. Rowe, "The effect of water absorption on the dielectric properties of epoxy nanocomposites," *IEEE Transactions on Dielectrics and Electrical Insulation,* vol. 15, pp. 106-117, 2008.

[39] C. Zhang and G. C. Stevens, "The Dielectric Response of Polar and Non-Polar Nanodielectrics," *IEEE Transactions on Dielectrics and Electrical Insulation,* vol. 15, pp. 606-617, 2008.

[40] D. Fabiani, G. C. Montanari, and L. Testa, "Effect of aspect ratio and water contamination on the electric properties of nanostructured insulating materials," *IEEE Transactions on Dielectrics and Electrical Insulation,* vol. 17, pp. 221-230, 2010.

[41] J. K. Nelson and J. C. Fothergill, "Internal charge behaviour of nanocomposites," *Nanotechnology,* vol. 15, p. 586, 2004.

[42] Y. Li, Y. Huang, T. Krentz, B. Natarajan, T. Neely, and L. S. Schadler, "Polymer Nanocomposite Interfaces: The Hidden Lever for Optimizing Performance in Spherical Nanofilled Polymers," in *Interface/Interphase in Polymer Nanocomposites*, ed: John Wiley & Sons, Inc., 2016, pp. 1-69.

[43] G. Meier, *Thermodynamics of Surfaces and Interfaces: Concepts in Inorganic Materials*. Cambridge: Cambridge University Press, 2014.

[44] S. K. Saha, "Observation of giant dielectric constant in an assembly of ultrafine Ag particles," *Physical Review B,* vol. 69, p. 125416, 03/26/ 2004.

[45] M. Stamm, "Polymer Surface and Interface Characterization Techniques," in *Polymer Surfaces and Interfaces: Characterization, Modification and Applications*, M. Stamm, Ed., ed Berlin, Heidelberg: Springer Berlin Heidelberg, 2008, pp. 1-16.

[46] A. I. Rusanov, "Recent Investigations on the Thickness of Surface Layers," in *Progress in Surface and Membrane Science*. vol. Volume 4, M. D. R. J.F. Danielli and C. D.A, Eds., ed: Elsevier, 1971, pp. 57-114.

[47] H. Helmholtz, "Ueber einige Gesetze der Vertheilung elektrischer Ströme in körperlichen Leitern mit Anwendung auf die thierisch-elektrischen Versuche," *Annalen der Physik,* vol. 165, pp. 211-233, 1853.

[48] G. Tsagaropoulos and A. Eisenberg, "Dynamic Mechanical Study of the Factors Affecting the Two Glass Transition Behavior of Filled Polymers. Similarities and Differences with Random Ionomers," *Macromolecules,* vol. 28, pp. 6067-6077, 1995/08/01 1995.

[49] V. Arrighi, I. J. McEwen, H. Qian, and M. B. Serrano Prieto, "The glass transition and interfacial layer in styrene-butadiene rubber containing silica nanofiller," *Polymer,* vol. 44, pp. 6259-6266, 9// 2003.

[50] S. Raetzke and J. Kindersberger, "Role of interphase on the resistance to high-voltage arcing, on tracking and erosion of silicone/SiO2 nanocomposites," *IEEE Transactions on Dielectrics and Electrical Insulation,* vol. 17, pp. 607-614, 2010.

[51] J. Seiler and J. Kindersberger, "Insight into the interphase in polymer nanocomposites," *Dielectrics and Electrical Insulation, IEEE Transactions on,* vol. 21, pp. 537-547, 2014.

[52] P. Preetha and M. J. Thomas, "AC breakdown characteristics of epoxy nanocomposites," *IEEE Transactions on Dielectrics and Electrical Insulation,* vol. 18, pp. 1526-1534, 2011.

[53] D. Pitsa and M. G. Danikas, "Interfaces features in polymer nanocomposites: a review of proposed models," *Nano,* vol. 06, pp. 497-508, 2011.

[54] T. Tanaka, "A novel concept for electronic transport in nanoscale spaces formed by islandic multi-cored nanoparticles," in *2016 IEEE International Conference on Dielectrics (ICD)*, 2016, pp. 23-26.

[55] M. G. Todd and F. G. Shi, "Complex permittivity of composite systems: a comprehensive interphase approach," *Dielectrics and Electrical Insulation, IEEE Transactions on,* vol. 12, pp. 601-611, 2005.

[56] I. Preda, J. Castellon, M. Frechette, and S. Agnel, "Modelling the dielectric permittivity of nanocomposites - the overlap model," in *Electrical Insulating Materials (ISEIM), Proceedings of 2014 International Symposium on*, 2014, pp. 17-21.

[57] F. Ciuprina, L. Andrei, F. M. G. Tomescu, I. Plesa, and T. Zaharescu, "Electrostatic model of LDPE-SiO2 nanodielectrics," in *Solid Dielectrics (ICSD), 2013 IEEE International Conference on*, 2013, pp. 876-879.

[58] W. J. L. Li, J. Zheqiang, L. Xuguang, and Y. Yi,, "Finite element simulation of LDPE/SiO2 Nanocomposite," in *Int. Symp. on Electrical Insulating Materials*, 2011, pp. 366-369.

[59] D. Pitsa and M. G. Danikas, "Modeling relative permittivity and electrical treeing in polymer nanocomposites," in *Solid Dielectrics (ICSD), 2013 IEEE International Conference on*, 2013, pp. 832-835.

[60] J. C. Pandey and N. Gupta, "Estimation of interphase thickness of epoxy-based nanocomposites," *IEEE Transactions on Dielectrics and Electrical Insulation,* vol. 23, pp. 2747-2756, 2016.

[61] O. Dugne, S. Prouhet, A. Guette, R. Naslain, and J. Sevely, "Interface Characterisation by Transmission Electron Microscopy and Auger Electron Spectroscopy in Tough SiC Fiber (Nicalon)-SiC Matrix Composite with a Boron Nitride Interphase," in *Developments in the Science and Technology of Composite Materials: ECCM3 Third European Conference on Composite Materials 20.23 March 1989 Bordeaux-France*, A. R. Bunsell, P. Lamicq, and A. Massiah, Eds., ed Dordrecht: Springer Netherlands, 1989, pp. 129-135.

[62] Q. Wu, M. Li, Y. Gu, Y. Li, and Z. Zhang, "Nano-analysis on the structure and chemical composition of the interphase region in carbon fiber composite," *Composites Part A: Applied Science and Manufacturing,* vol. 56, pp. 143-149, 2014/01/01/ 2014.

[63] Q. Wu, M. Li, Y. Gu, S. Wang, and Z. Zhang, "Imaging the interphase of carbon fiber composites using transmission electron microscopy: Preparations by focused ion beam, ion beam etching, and ultramicrotomy," *Chinese Journal of Aeronautics,* vol. 28, pp. 1529-1538, 2015/10/01/ 2015.

[64] B. E. B. Uribe and J. R. Tarpani, "Interphase analysis of hierarchical composites via transmission electron microscopy," *Composite Interfaces,* vol. 24, pp. 849-859, 2017/11/22 2017.

[65] D. R. Clarke and P. R. Stuart, "An anomalous contrast effect in the scanning electron microscope," *Journal of Physics E: Scientific Instruments,* vol. 3, p. 705, 1970.

[66] M. A. Stevens Kalceff, M. R. Phillips, and A. R. Moon, "Electron irradiation-induced changes in the surface topography of silicon dioxide," *Journal of Applied Physics,* vol. 80, pp. 4308-4314, 1996/10/15 1996.

[67] D. C. Joy, "Control of charging in low-voltage SEM," *Scanning,* vol. 11, pp. 1-4, 1989.

[68] M. Belhaj, S. Odof, K. Msellak, and O. Jbara, "Time-dependent measurement of the trapped charge in electron irradiated insulators: Application to Al2O3–sapphire," *Journal of Applied Physics,* vol. 88, pp. 2289-2294, 2000/09/01 2000.

[69] S. Fakhfakh, O. Jbara, M. Belhaj, Z. Fakhfakh, A. Kallel, and E. I. Rau, "An experimental approach for dynamic investigation of the trapping properties of glass-ceramic under electron beam irradiation from a scanning electron microscope," *Eur. Phys. J. AP,* vol. 21, pp. 137-146, 2003.

[70] D. A. Jesson and J. F. Watts, "The Interface and Interphase in Polymer Matrix Composites: Effect on Mechanical Properties and Methods for Identification," *Polymer Reviews,* vol. 52, pp. 321-354, 2012/07/01 2012.

[71] D. Shiqiang, Y. Lin, and Y.-W. Mai, "Measurement of interfacial shear strength of carbon fibre/epoxy composites using a single fibre pull-out test," *Advanced Composite Materials,* vol. 7, pp. 169-182, 1998/01/01 1998.

[72] M. Rodríguez, J. M. Molina-Aldareguía, C. González, and J. Llorca, "A methodology to measure the interface shear strength by means of the fiber push-in test," *Composites Science and Technology,* vol. 72, pp. 1924-1932, 2012/10/12/ 2012.

[73] J.-K. Kim and A. Hodzic, "Nanoscale characterisation of thickness and properties of interphase in polymer matrix composites," *The Journal of Adhesion,* vol. 79, pp. 383-414, 2003/04/01 2003.

[74] O. W. and P. G., "An improved technique for determining hardness and elastic modulus using load and displacement sensing indentation experiments," *Journal of Materials Research,* vol. 7, pp. 1564-1583, 1992.

[75] A. Hodzic, Z. H. Stachurski, and J. K. Kim, "Nano-indentation of polymer–glass interfaces Part I. Experimental and mechanical analysis," *Polymer,* vol. 41, pp. 6895-6905, 2000/08/01/ 2000.

[76] A. Hodzic, S. Kalyanasundaram, J. K. Kim, A. E. Lowe, and Z. H. Stachurski, "Application of nano-indentation, nano-scratch and single fibre tests in investigation of interphases in composite materials," *Micron,* vol. 32, pp. 765-775, 2001.

[77] J.-K. Kim, M.-L. Sham, and J. Wu, "Nanoscale characterisation of interphase in silane treated glass fibre composites," *Composites Part A: Applied Science and Manufacturing,* vol. 32, pp. 607-618, 2001/05/01/ 2001.

[78] A. Hodzic, J. K. Kim, A. E. Lowe, and Z. H. Stachurski, "The effects of water aging on the interphase region and interlaminar fracture toughness in polymer–glass composites," *Composites Science and Technology,* vol. 64, pp. 2185-2195, 2004/10/01/ 2004.

[79] A. M. Díez-Pascual, M. A. Gómez-Fatou, F. Ania, and A. Flores, "Nanoindentation Assessment of the Interphase in Carbon Nanotube-Based Hierarchical Composites," *The Journal of Physical Chemistry C,* vol. 116, pp. 24193-24200, 2012/11/15 2012.

[80] E. Mäder, S.-L. Gao, and J.-K. Kim, "New Nano-Scale Characterization Techniques for Interphases," in *Interface Controlled Materials*, ed: Wiley-VCH Verlag GmbH & Co. KGaA, 2005, pp. 237-242.

[81] S. B. Yedla, M. Kalukanimuttam, R. M. Winter, and S. K. Khanna, "Effect of Shape of the Tip in Determining Interphase Properties in Fiber Reinforced Plastic Composites Using Nanoindentation," *Journal of Engineering Materials and Technology,* vol. 130, pp. 041010-041010-15, 2008.

[82] T. D. Downing, R. Kumar, W. M. Cross, L. Kjerengtroen, and J. J. Kellar, "Determining the interphase thickness and properties in polymer matrix composites using phase imaging atomic force microscopy and nanoindentation," *Journal of Adhesion Science and Technology,* vol. 14, pp. 1801-1812, 2000/01/01 2000.

[83] R. Kumar, W. M. Cross, L. Kjerengtroen, and J. J. Kellar, "Fiber bias in nanoindentation of polymer matrix composites," *Composite Interfaces,* vol. 11, pp. 431-440, 2004/01/01 2004.

[84] W. M. Cross, W. M. Cross, L. Kjerengtroen, and J. J. Kellar, "Interphase variation in silane-treated glass-fiber-reinforced epoxy composites," *Journal of Adhesion Science and Technology,* vol. 19, pp. 279-290, 2005/01/01 2005.

[85] R. Arinero, "Microscopie à force atomique en mode contact vibrant et application à l'étude des propriétés élastiques à l'échelle nanométrique," PhD, Milieux Dense et Matériaux, Université de Montpellier 2, 2003.

[86] B. Pittenger, N. Erina, and C. Su, "Mechanical Property Mapping at the Nanoscale Using PeakForce QNM Scanning Probe Technique," in *Nanomechanical Analysis of High Performance Materials*, A. Tiwari, Ed., ed Dordrecht: Springer Netherlands, 2014, pp. 31-51.

[87] P. Leclère, P. Viville, M. Jeusette, J.-P. Aimé, and R. Lazzaroni, "Scanning Probe Microscopy of Complex Polymer Systems: Beyond Imaging their Morphology," in *Scanning Probe Microscopies Beyond Imaging*, ed: Wiley-VCH Verlag GmbH & Co. KGaA, 2006, pp. 175-207.

[88] M. R. VanLandingham, R. R. Dagastine, R. F. Eduljee, R. L. McCullough, and J. W. Gillespie, "Characterization of nanoscale property variations in polymer composite systems: 1. Experimental results," *Composites Part A: Applied Science and Manufacturing,* vol. 30, pp. 75-83, 1999/01/01/ 1999.

[89] T. A. Bogetti, T. Wang, M. R. VanLandingham, and J. W. Gillespie Jr, "Characterization of nanoscale property variations in polymer composite systems: 2. Numerical modeling," *Composites Part A: Applied Science and Manufacturing,* vol. 30, pp. 85-94, 1999.

[90] S.-L. Gao and E. Mäder, "Characterisation of interphase nanoscale property variations in glass fibre reinforced polypropylene and epoxy resin composites," *Composites Part A: Applied Science and Manufacturing,* vol. 33, pp. 559-576, 2002.

[91] S.-L. Gao, E. Mäder, and S. F. Zhandarov, "Carbon fibers and composites with epoxy resins: Topography, fractography and interphases," *Carbon,* vol. 42, pp. 515-529, 2004.

[92] T. J. Young, M. Monclus, W. R. Broughton, S. L. Ogin, and P. A. Smith, "Observations on interphase characterisation in polymer composites by nanoscale indentation and use of AFM cantilever torsion to identify measurement artefacts," *Plastics, Rubber and Composites,* vol. 41, pp. 240-246, 2012/07/01 2012.

[93] Y. Gu, M. Li, J. Wang, and Z. Zhang, "Characterization of the interphase in carbon fiber/polymer composites using a nanoscale dynamic mechanical imaging technique," *Carbon,* vol. 48, pp. 3229-3235, 2010/09/01/ 2010.

[94] M. A. Monclus, T. J. Young, and D. Di Maio, "AFM indentation method used for elastic modulus characterization of interfaces and thin layers," *Journal of Materials Science,* vol. 45, pp. 3190-3197, 2010/06/01 2010.

[95] V. Cech, E. Palesch, and J. Lukes, "The glass fiber–polymer matrix interface/interphase characterized by nanoscale imaging techniques," *Composites Science and Technology,* vol. 83, pp. 22-26, 2013/06/28/ 2013.

[96] X. Cheng, K. W. Putz, C. D. Wood, and L. C. Brinson, "Characterization of local elastic modulus in confined polymer films via AFM indentation," *Macromol Rapid Commun,* vol. 36, pp. 391-7, Feb 2015.

[97] S. Cheng, V. Bocharova, A. Belianinov, S. Xiong, A. Kisliuk, S. Somnath*, et al.*, "Unraveling the Mechanism of Nanoscale Mechanical Reinforcement in Glassy Polymer Nanocomposites," *Nano Letters,* vol. 16, pp. 3630-3637, 2016/06/08 2016.

[98] S. Cheng, A. P. Holt, H. Wang, F. Fan, V. Bocharova, H. Martin*, et al.*, "Unexpected Molecular Weight Effect in Polymer Nanocomposites," *Physical Review Letters,* vol. 116, p. 038302, 01/22/ 2016.

[99] N. Lahoud-Dignat, M. N. Hidayatullah, F. Saysouk, M. L. Locatelli, and S. Diaham, "Using the Atomic Force Microscopy for nanocomposites local mechanical characterization: Towards the interphase measurement," in *2016 IEEE International Conference on Dielectrics (ICD)*, 2016, pp. 64-67.

[100] H. Huang, I. Dobryden, N. Ihrner, M. Johansson, H. Ma, J. Pan*, et al.*, "Temperature-dependent surface nanomechanical properties of a thermoplastic nanocomposite," *Journal of Colloid and Interface Science,* vol. 494, pp. 204-214, 5/15/ 2017.

[101] S. Gong, Q. Chen, J. F. Moll, S. K. Kumar, and R. H. Colby, "Segmental Dynamics of Polymer Melts with Spherical Nanoparticles," *ACS Macro Letters,* vol. 3, pp. 773-777, 2014/08/19 2014.

[102] C. D. Wood, A. Ajdari, C. W. Burkhart, K. W. Putz, and L. C. Brinson, "Understanding competing mechanisms for glass transition changes in filled elastomers," *Composites Science and Technology,* vol. 127, pp. 88-94, 2016/04/28/ 2016.

[103] G. Stan and R. F. Cook, "Mapping the elastic properties of granular Au films by contact resonance atomic force microscopy," *Nanotechnology,* vol. 19, p. 235701, 2008.

Chapter II

Introduction to Electrostatic Force Microscopy

Chapter II

"We have to remember that what we observe is not nature in itself, but nature exposed to our method of questioning." Werner Heisenberg

1. Introduction

The principle of scanning force microscopies for the imaging process is the use of a physical probe in the form of a cantilever with a sharp tip at its end, which allows high resolutions, and a feedback mechanism controlling tip movement. The family of scanning force microscopies started in 1982 with the scanning tunneling microscope (STM) invented by G. Binnig and H. Rohrer [1]. STM works by controlling the tunneling current flowing between a metallic tip and a conductive or semi-conductive surface in a vacuum atmosphere by monitoring the distance of the probe from the surface. The change in probe position can basically reflect sample topography. However, STM reached limitations to image poorly conductive materials such as biomolecules that also need a specific atmosphere. Those limitations served as a motivation for G. Binnig *et al.* to invent later in 1986, the atomic force microscope (AFM) with much higher process versatility [2]. The probe motion in an AFM is altered by the interaction forces with the sample at close proximity. According to the nature of the force and the usage of appropriate feedback mechanism, several physico-chemical properties can be deduced. Thereby, since its first development, an impressive number of AFM modes have been developed giving the capability of probing, in addition to the topography of different kinds of materials, their electrical, magnetic, chemical, thermal and optical properties at the nanoscale.

In the following, an overview of recent electrical scanning probe microscopies is presented to proceed, in the next part of this chapter, to the detailed description of Electrostatic Force Microscopy (EFM). Moreover, a review on the advances of electrical scanning probe microscopies in the study of complex nanostructured materials and the interphase in nanocomposites is included.

2. Overview on local electrical characterization methods

In addition to STM that can measure electron density and the conductivity of conductive and semi-conductive materials [1, 3], several scanning probe microscopies (SPM) electrical characterization techniques have been developed giving access to numerous electrical properties. These methods can be mainly divided into two categories:

a) Current detection techniques: the electric current flowing from substrate to tip is measured and used to obtain the targeted electrical property.
b) Force or force gradient detection techniques: the electric force acting on the probe is detected and used to probe the property of interest.

Fig. II - 1 summarizes the most commonly used current and force detection electrical microscopies:

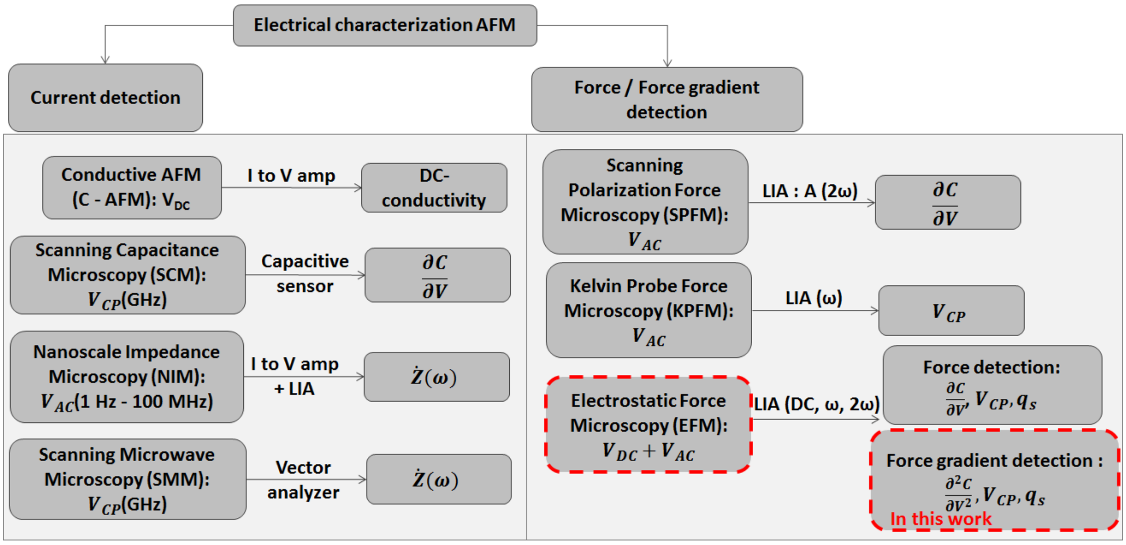

Fig. II - 1 : Summary of commonly used AFM electrical characterization techniques, arrows in boxes refer to the basic detection system, and point out the measured parameter, LIA: lock-in amplifier. Signal processing is not detailed here (see [4, 5] for further explanation).

Most of current detection methods use the tip in contact mode with the sample to maintain the electrical contact for current measurement [6, 7]. Moreover, although in Nanoscale Impedance Microscopy or Scanning Microwave Microscopy, for example, it is possible to perform measurements in non-contact mode if desired, AC voltages introduce some noise [8-10]. The signal is highly influenced by the stray capacitance originating from the chip and non-screened cables that highly reduces the sensitivity.

In contrast, force and force gradient detection methods are usually performed in non-contact mode, allowing for topography and electrical images to be obtained separately [11-13]. Higher sensitivities are achieved since the capacitive coupling is reduced by the physics of interaction, including capacitance first or second derivatives instead of raw capacitance. Furthermore, several information about the capacitance, surface voltages and charges, can be accessed with little changes in the experimental set up and protocol. A more detailed review of electrical AFM methods can be found elsewhere [4, 5].

3. EFM definition

The EFM, first introduced by Y. Martin *et al.* [11, 14] detects weak but long range electrostatic forces. The system making up the EFM, in which it differs from a conventional AFM is:

a) a conductive probe acting as an upper electrode,
b) a metallic sample holder used as a counter-electrode, creating together an equivalent of a capacitor (Figure 5.12).

The probe can be excited with a DC and/or AC electrical voltage, and lock-in amplifiers can be used in order to detect signals at specific frequencies (see below sections).

AFM tip, cantilever and probe support are usually made of monocrystalline silicon or silicon nitride prepared by microfabrication techniques [15-17]. Due to their monocrystalline nature, AFM tips possess a high mechanical and thermal stability. Diamond tips can be also used for even larger durability.

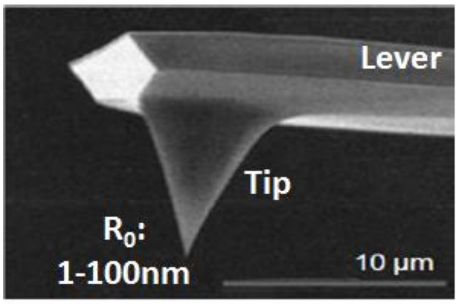

Fig. II - 2 : Scanning electron image of a typical AFM probe with a conical tip.

For EFM measurements, in order to make the probe sensitive to electrostatic interactions, the cantilever and the tip are metallized through the deposition of a thin metal film on their surface, such as: chromium, chromium-gold, platinum-iridium, titanium-platinum, carbide Tungsten, titanium nitride etc. The deposited thickness is of the order of 25 nm, which increases the tip radius of curvature and correspondingly, reduces the lateral resolution for the topography. It must be noticed that metal covered tips become more prone to wear and hence, more prone to imaging artifacts, in addition to the fact that EFM signal variation is highly influenced by the radius of the apex. Thus, highly doped silicon or diamond probes are sometimes utilized. Their electrical conductivity is usually convenient to EFM measurements while keeping a sharp tip end (highly doped silicon probes) or better mechanical properties (silicon and diamond coated probes) [18].

4. Set up

Since EFM is one variant of AFM, we start by presenting a brief description of AFM basic system and working principles, followed by the specificities of EFM detection mechanism.

4.1. AFM basics

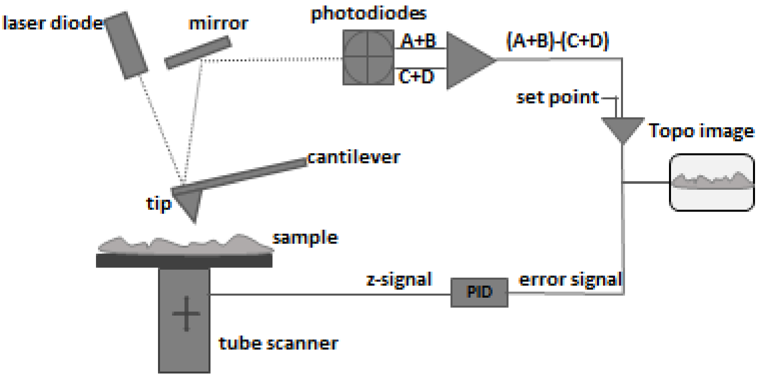

Fig. II - 3 : A simplified schematic diagram of basic Atomic Force Microscopy components (in static mode).

AFM works by scanning a probe over a sample surface in the three dimensions of space, monitored with three high precision piezoelectric tubes. Either the tip or the sample can be displaced. The probe is a nanometric tip maintained below a cantilever fixed at one end and free from the other one. The movement of the probe is usually followed optically by the reflection of a laser beam from the back side of the cantilever. Reflected beams are collected on a four segment photodiode (A, B, C, D), an optical position sensitive detection system (PSD). The variation of vertical tip movement is computed as the signal: (A+B) - (C+D), and lateral one as: (A+C) - (B+D). The collected signal is compared to a set point signal. With a proportional-integral-derivative controller (PID), the resulting error signal is used to feed a retroaction system that maintains one characteristic of probe movement (deflection, torsion, vibration etc.). According to the physical property of interest, the nature of the excitation of the probe and the action of feedback controls are going to be selected.

The mapping process is forwarded by the establishment and detection of interacting forces between the tip and the sample. Involved forces are very wide, however having in common the dependency to the tip-sample distance *z*. A common way to describe the interaction between the sensor and the specimen is by the approximation of the interaction of two neutral atoms (or molecules) with Lenard-Jones potential. As presented in Fig. II - 4a., the latter shows the important variation of the force intensity with the distance, in addition to the distinction between attractive and repulsive forces [19]. At large distances, attractive forces occur such as: Van der Waals forces (VdW), capillary forces due to the water meniscus between tip and sample surface in air environment, long range electrostatic forces due to differences in sample and probe work functions, or permanent surface charges on the sample or capacitive charges, magnetic forces etc. At short separations, roughly approximated to start at the minimum of the curve ($\leq$ 5 Å interatomic distance), repulsive forces arise due to the overlap of electron orbitals of tip and sample according to Pauli's exclusion principle [20]. At these separations, the two bodies are considered to be in contact.

In order to obtain the topography, the tip is usually placed at appropriate close distances from the surface to allow VdW forces to dominate. As the force is a decreasing function of the distance, for a fixed tip position, surface asperities will modify the force field around the tip. Force variation is detected through the induced change in the cantilever movement such as its flexion, or its torsion in the case of lateral mapping [21].

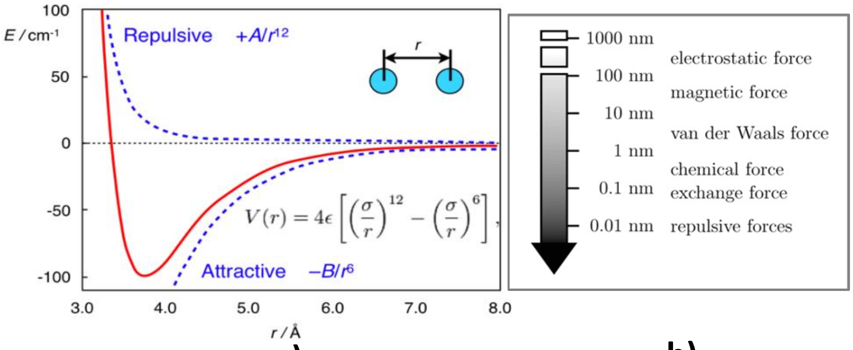

a) b)

Fig. II - 4 : a. Lennard Jones potential describing the interaction between two neutral atoms or molecules regarding their mutual separation r, and b. Nature of interaction forces and their range, brightest color corresponds to the higher force magnitude [22].

In EFM, electrical information is obtained from the detection of long range electrostatic forces while minimizing VdW ones.

4.2. EFM Lift mode

Within the framework of this thesis, EFM measurements have been conducted in a double-pass, also called double-scan, configuration [23]. During the first scan, the surface topography is acquired using Tapping Mode$^{\text{TM}}$, while electrical data are collected at the second scan with the so-called Lift Mode$^{\text{LM}}$. In the following, a description of each scan is explained separately.

4.2.1. 1st pass: Dynamic modes - Tapping mode

4.2.1.1. Spring - mass model

In order to predict cantilever motion in a force field, the cantilever-sample interaction is roughly modeled as a point mass spring oscillator. The forces acting on the cantilever are considered as the point mass pushing the spring to extend (or retract) according to its stiffness *K*. *K* depends on the geometry, the density and the Young's modulus of the cantilever. The restoring force is derived from Hooke's law, and in the static case, it can be simply expressed as (see Fig. II - 5) [19]:

$$F(z) = K\Delta z \qquad \text{(II.1)}$$

Δz is the probe deflection from initial position. Among possible methods to measure *K* [24-26], a widespread and simple calculation of the normal spring constant with the assumption of a rectangular cantilever shape is based on the use of the following theoretical formula [24]:

$$K = \frac{E_Y W t^3}{4L^3} \qquad \text{(II.2)}$$

E_Y is the Young's modulus of the cantilever, *W*, *t* and *L* are its width, thickness and length, respectively. The additional mass introduced by the tip is usually not considered since it is negligible with respect to the mass of the cantilever. The tip deflection is either positive or negative for attractive or repulsive interactions with sample surface, respectively.

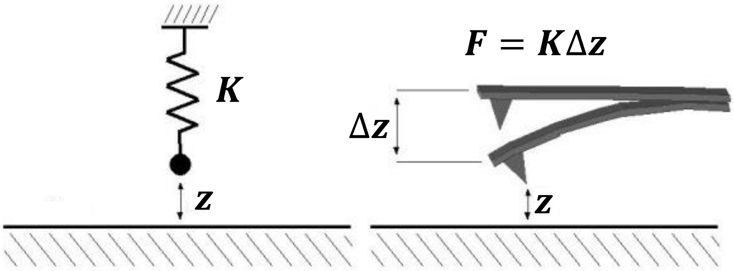

Fig. II - 5 : Spring-mass model of the cantilever-tip interaction with the sample.

4.2.1.2. Tip oscillation in dynamic mode

AFM has in general two main operating modes, contact and Tapping Mode™. The latter is a variant of non-contact imaging methods. In EFM measurements, we used tapping mode, which forms the basis for most of SPM force and force gradient electrical detection modes [27].

In a tapping scan, the tip is excited in the z direction by a bimorph piezoelectric actuator at a frequency close or equal to its first eigenmode resonance frequency. The mean tip-surface distance and amplitude of vibration are wisely chosen to stay out of contact in the majority of the oscillation cycle so that the tip hits the surface only briefly at the end of one vibration period (Fig. II - 6). The interaction with the sample modifies the amplitude and phase of oscillation. Those quantities are used for the regulation process and thereby for imaging. In order to follow the tip vibration and its dependency to the sensed forces, we will extend next the dynamics of oscillation, when 1) no interaction with the sample is present, and 2) an interaction force is detected by the tip.

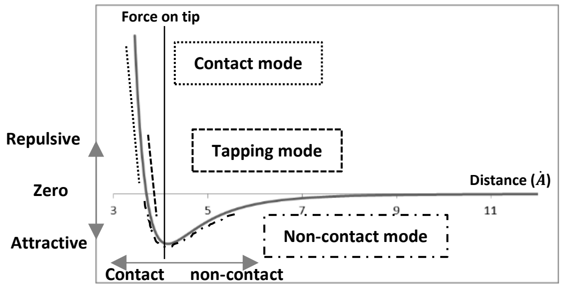

Fig. II - 6 : Position on Lennard-Jones potential curve of scanning modes working distances.

4.2.1.3. No tip-sample interaction

At sufficiently far distances from the sample surface where no interaction is present, when the tip is only subjected to a sinusoidal excitation, the motion of the tip along the z direction is described by a second order differential equation [28]:

$$m_e\ddot{z} = -\Upsilon\dot{z} - Kz + F_d\cos(\omega_c t) \qquad \text{(II.3)}$$

F_d and ω_c are respectively the amplitude and the angular frequency of the driving force of the cantilever. m_e and Υ are respectively the effective mass of the cantilever and the attenuation coefficient. It is usually advisable to consider an effective mass of the probe $m_e = 0.24\,m$ [21] (m is the real mass of the cantilever at rest), and to take into account the fact that the mass of the cantilever is distributed over its entire length. The components of the above equation represent the sum of all forces acting on the tip-cantilever system that are from the left to the right, the friction force, the restoring force and the driving force (here, of the actuator).

The angular resonance frequency is hence calculated from:

$$\omega_0 = \sqrt{\frac{K}{m_e}} \qquad \text{(II.4)}$$

The solution to the tip equation of motion is that of a harmonic oscillator with damping:

$$z(t) = A_c\cos(\omega_c t - \phi_c) + Bexp(-t/\tau)\cos(\omega_D t + \beta) \qquad \text{(II.5)}$$

A_c is the resulting amplitude of the cantilever oscillation, ϕ_c is the phase difference between the driving force and the cantilever oscillation, ω_D is the resonance frequency of the cantilever influenced by the damping effect, τ is a time constant characterizing the decay of the damping effect (damping is reduced by *1/e* after *τ; e* is the exponential constant). The first term of the equation of motion is a steady solution and the second term is a transient one.

In order to define *τ*, the quality factor *Q* must be inevitably introduced. *Q* describes the ratio between the energy stored per oscillation cycle on the work provided per cycle.

For a lightly damped harmonic oscillator, *Q* is written as [29]:

$$Q = \frac{{\omega_c}^2 + {\omega_0}^2}{2\gamma\omega_c} \qquad \text{(II.6)}$$

and is simplified at resonance ($\omega_c = \omega_0$) to:

$$Q = \frac{\omega_0}{\gamma} \qquad \text{(II.7)}$$

When an external force is applied temporarily, the viscous friction of the cantilever in the air is at the origin of the transient regime. This is also the cause for example when the probe encounters a physical obstacle or a steep force change on the surface during sweeping. The characteristic time for the oscillating probe to reach equilibrium is related to the attenuation factor and consequently, to the quality factor by the relation:

$$\tau = \frac{2}{\gamma} = \frac{2Q}{\omega_0} = \frac{2Q}{\sqrt{K/m_e}} \tag{II.8}$$

The resonance frequency of the cantilever, reflecting its stiffness, together with the quality factor, influences damping time. Hence, these parameters determine the required scan rate to obtain faithful images. It is considered that it is necessary to wait for a typical time of 3τ before reaching equilibrium. Common manufactured AFM cantilevers have quality factors of a few hundred in air. For a typical probe used in this thesis with Q = 220 and resonance frequency f_0 = 60 kHz, the time required to reach steady state is thus about 3.5 ms. For an image resolution with 512 × 512 pixels, around 15 minutes will be necessary. However, in ultra-high vacuum, Q is multiplied by 100 and imaging time becomes unreasonable. That is why higher harmonics are usually used in vacuum in order to compensate the quality factor increase (eq. II.8) assuming an unchanged effective mass with flexural mode order [23, 30]. Thus, cantilevers of relatively high stiffness are required for tapping mode AFM, even if this is at the expense of the sensitivity. An “artificial” modification of the quality factor (the so-called Q control) is sometimes performed in order to enhance tapping speed [31].

When the transient motion fades out, the sinusoidal oscillation of the cantilever is characterized by:

$$A_c = \frac{F_d}{m_e[{\omega_0}^2 - {\omega_c}^2 + (\omega_0\omega_c/Q)^2]^{1/2}} \tag{II.9}$$

$$\tan(\phi_c) = \frac{\omega\omega_0}{Q({\omega_0}^2 - {\omega_c}^2)} \tag{II.10}$$

The expression of the amplitude is a Lorentzian function centered on the resonance frequency of the oscillator of the studied harmonic mode (see Fig. II - 8 free cantilever case). The quality factor can be determined graphically from the amplitude curve using:

$$Q = \frac{\omega_{c2} - \omega_{c1}}{\omega_0} \tag{II.11}$$

ω_{c1} and ω_{c2} are the pulsations at the $\sqrt{2}$ ratio of the maximum oscillation amplitude.

At ω_0, the phase is centered at π/2. Importantly, in this fully linear treatment of the problem, the amplitude of the exciting force F_d has no effect on the general shape of the resonance curve.

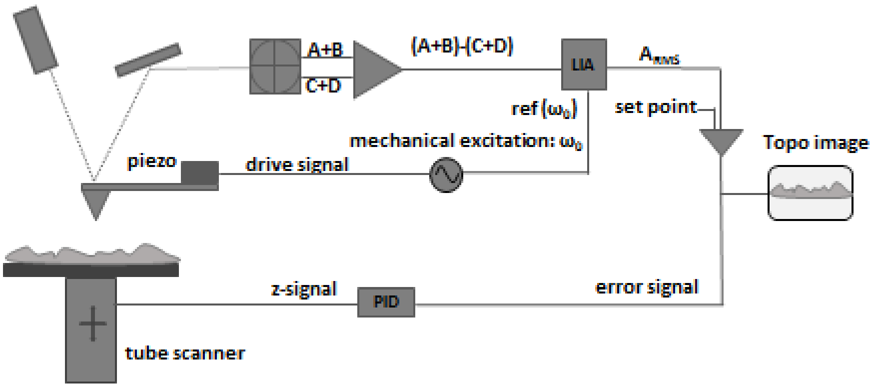

Fig. II - 7 : Simplified block-diagram of tapping mode during topography acquisition.

4.2.1.4. Presence of tip-sample interaction force

When the probe is placed in the vicinity of the surface, or when the tip is conditioned in a way that a force field is created due to tip-sample interaction, an additional force F_{ts} must be added to equation (II.3). If we do not know the dependency of F_{ts} with z, this equation is a priori not soluble. However, for small oscillations, or small displacements around average z scanning position, z_0, F_{ts} can be expressed as a first order Taylor development around z_0 [28]:

$$F_{ts}(z) \approx F_{ts}(z_0) + z\left(\frac{\partial F_{ts}}{\partial z}\right)_{z_0} \tag{II.12}$$

so equation (II.3) becomes:

$$m_e\ddot{z} = -\frac{m_e\omega_0}{Q}\dot{z} - \left(K - \left(\frac{\partial F_{ts}}{\partial z}\right)_{z_0}\right)z + F_{ts}(z_0) + F_d\cos(\omega_c t) \tag{II.13}$$

The term $F_d(z_0)$ is independent of time, which only creates a static deflection of the cantilever that has no influence on the coming process. However, from the comparison of the second terms at the right hand side of (II.3) and (II.13), it can be noticed that when subjected to an interaction force with the sample, force gradients modify the effective stiffness of the probe, K_{eff}, which writes:

$$K_{eff} = K - \left(\frac{\partial F_{ts}}{\partial z}\right)_{z_0} \tag{II.14}$$

The new cantilever pulsation is then given by:

$$\omega_{eff} = \left(\frac{K - \frac{\partial F_{ts}}{\partial z}}{m_e}\right)^{1/2} = \left(\frac{K}{m_e} - \frac{1}{m_e}\frac{\partial F_{ts}}{\partial z}\right)^{1/2} = \omega_0\left(1 - \frac{1}{K}\frac{\partial F_{ts}}{\partial z}\right)^{1/2} \tag{II.15}$$

For small displacements, the average force gradient is small compared to the spring constant of the cantilever: $\left(\frac{\partial F_{ts}}{\partial z}\right)_{z_0} \ll K$. Consequently, the Taylor series of equation (II.15) concludes that the frequency shift Δf_0 of the probe resonance frequency for a weakly perturbed oscillator is proportional to the force gradient of the interaction:

$$\Delta\omega_0 = \omega_{eff} - \omega_0 \cong -\frac{1}{2}\frac{\omega_0}{K}\frac{\partial F_{ts}}{\partial z} \tag{II.16}$$

$$\Delta f_0 \cong -\frac{f_0}{2K}\frac{\partial F_{ts}}{\partial z} \tag{II.17}$$

Furthermore, for static force gradients, the mechanical phase shift can be expressed as [30, 32]:

$$\Delta\phi_c \cong -\frac{Q}{K}\frac{\partial F_{ts}}{\partial z} \qquad \text{(II.18)}$$

Thus, from equations (II.17) and (II.18) it can be deduced that force gradients can be detected by either measuring the frequency shifts or the phase shifts, respectively. Even so, measuring the frequency shifts is preferred to avoid phase saturation observed at high voltages for example (> 10 V) [33]. Amplitude shift signal can be also used to measure indirectly the frequency shifts. A further description of signal modulation for each of the three cases will be presented in the next paragraph.

However, the main conclusion of this section is that tip-sample interaction forces modify the oscillation of the cantilever. Attractive force gradients decrease the effective stiffness of tip motion, which decreases its resonance frequency, and vice versa for repulsive ones. Positive force gradients are usually generated when the cantilever is relatively far from the sample (Fig. II - 8), and negative ones are produced at relatively close distances. The resonance amplitude and phase curves of the tip are consequently shifted to be centered on a new effective resonance frequency while keeping a similar shape of the curve.

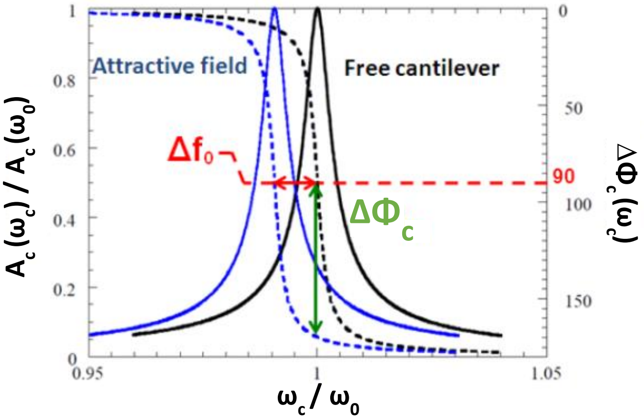

Fig. II - 8 : Amplitude (line) and phase (dotted line) of the free cantilever (black) and in the presence of an attractive force gradient (blue) at fixed drive frequency: curves are shifted to lower frequencies [33].

4.2.2. 2nd pass: Force and Force gradient detection - DC + AC excitation

As mentioned previously, during the second pass, EFM measurements have been performed with Lift Mode^{LM}, a sub-mode of non-contact scanning. For each scan line over the probed region, the topography is obtained with tapping mode, and collected on the height image of the AFM software. The tip is then retracted to a higher distance from the surface (~ 100 nm) in order to detach it from any possible water meniscus with the sample, and then dropped back to a certain level chosen by the user [33, 34]. The latter additional distance is the so-called “lift”. The reference origin for the lift is the position of the probe during the first scan *z* (x, y), which reflects the topography of the sample. The consequent movement of the tip at the second scan is to retrace the topography at a higher separation from the surface. At this stage, the tip-to-substrate system is usually electrically biased to develop capacitive electrostatic forces on the probe (Fig. II - 9).

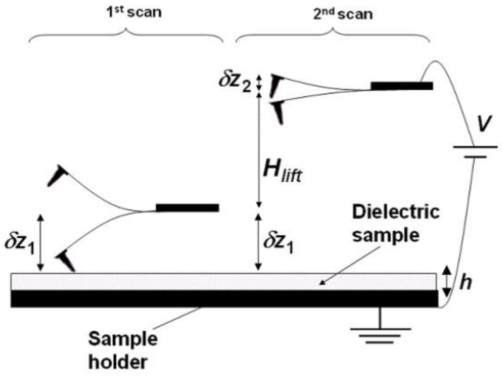

Fig. II - 9 : Principle of the double-pass method [33].

For force gradient measurements, which are the case in this work, electrical data acquisition is also performed in dynamic mode. However, importantly, the drive amplitude is typically reduced to the third of the oscillation amplitude used for topography measurement [33]. This allows the use of very low lifts without crushing the tip, and to stay out of the interval of distances of short range forces such as VdW ones. Moreover, small oscillations are required to stay in the linear regime, a mandatory condition to extract quantitative solutions with casual methods. In fact, as sketched in Fig. II - 9, at the first scan, and in the nonlinear approximation, the tip-sample distance is approximated to be equivalent to the oscillation amplitude [35]. Hence, during the second scan, even at 0 nm lift, if the oscillation amplitude is reduced, the tip is more likely to stay out of contact from the surface.

It must be noted that the decorrelation of long range forces from short range ones stems from the variation of VdW and electrostatic forces with *z*. In fact, the power law dependency with *z* is $(\sim\frac{1}{z^6})$ and $(\sim\frac{1}{z^2})$ for VdW and electrostatic forces, respectively. These relations show the predominance of short range forces at low distances, in contrast to high distances. Nonetheless, when the sample possesses exceptionally strong surface or volume charges, scientists often measured topography artifacts produced by the resulting permanent high electric field [36-38].

4.2.2.1. Physics governing EFM tip-sample interaction

The interaction between an EFM sensor and an insulator is a combination of an attractive Columbic force between induced charges on electrodes due to the capacitance *C* of the probed region (capacitive force), and a Columbic force between local surface charges q_s (if present) and their image charges on the tip - q_s [21, 23, 39]. The image charge in the counter electrode is neglected. The total tip-sample voltage is due to externally applied voltages, DC and/or AC voltages, as well as those due to the existing tip-to-sample work function difference (well known as surface or contact potential difference V_{CP}). Other externally induced voltages can be added to V_{CP} such as those resulting from polarization, illumination, mechanical stress, etc (see Fig. II - 10).

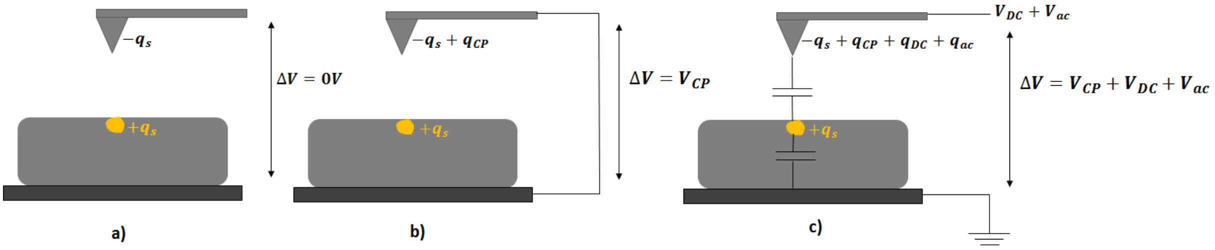

Fig. II - 10 : Schematic of the electrostatic interactions of an insulator possessing a permanent surface charge when: a. electrodes are disconnected, b. electrodes are connected, and c. electrodes are biased with a DC and AC voltage.

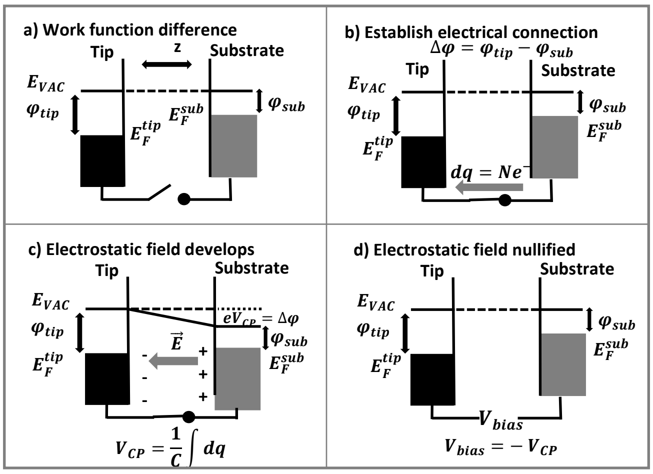

Fig. II - 11 : Schematic of the origin of contact potential difference between two metals, namely, the conductive EFM tip and the metallic sample holder: a. Fermi levels before contact, b. electrons flow upon connection, c. contact potential establishment at equilibrium, d. electrostatic field nullification with a bias opposite to the contact potential difference: general principle of Kelvin Probe Force Microscopy.

The general equation of the force *F* that describes these interactions, for large tip-surface distances compared to atomic dimensions, is defined as follows:

$$F = \frac{1}{2}\frac{\partial C}{\partial z}\Delta V^2 + \frac{q_s q_t}{4\pi\varepsilon_0 z^2} \tag{II.19}$$

z is the instantaneous distance between the tip apex and the sample surface, q_t is the sum of all charges interacting with the surface static charges q_s, and the total voltage difference ΔV writes:

$$\Delta V = V_{DC} + V_{AC}\sin(\omega t) + V_{CP} \tag{II.20}$$

V_{DC} and $V_{AC}\sin\omega t$ are the DC and AC externally applied voltages, respectively. ω is the pulsation of the AC voltage. V_{CP} is usually measured with Kelvin Probe Force Microscopy (KPFM) [12]. Fig. II - 11 presents a schematic of the origin of V_{CP} at the electrical contact between the metallic tip and the electrode, as well as the basic process to deduce it with KPFM Fig. II - 11d. An overview of KPFM working principles will be given in the following sections. In the case of a perfect insulator and perfect dielectric-metal contact, V_{CP} mostly corresponds to the difference in the work functions between the metals constituting the tip and the substrate [33, 40] [40, 41]. Note that the other external voltages mentioned before are neglected, or can be included within V_{CP}.

q_t is expressed as follows:

$$q_t = q_s + q_{DC} + q_{ac} + q_{CP} \tag{II.21}$$

where $q_{DC} = CV_{DC}$, $q_{ac} = CV_{AC}\sin\omega t$ and $q_{CP} = CV_{CP}$ are the capacitive charges due to V_{DC}, $V_{AC}\sin\omega t$ and V_{CP} respectively. We remind that *C* is the equivalent capacitance of the EFM sensor including the air gap and the dielectric sample (Fig. II - 10).

At low electric fields, the tip-sample capacitance and its derivatives are generally assumed to remain unchanged upon addition of external voltages for common samples. The following relationships for electrostatic forces and their gradients can thus be derived. The force acting on the tip becomes equal to:

$$F = \frac{q_s(q_s + CV_{DC} + CV_{AC}\sin\omega t + CV_{CP})}{4\pi\varepsilon_0 z^2} + \frac{1}{2}C'(V_{DC} + V_{AC}\sin\omega t + V_{CP})^2 \tag{II.22}$$

The development of this expression shows that it can be expressed as the sum of *DC*, *ω* and *2ω* components:

$$F = F_{DC} + F_{\omega} + F_{2\omega} \tag{II.23}$$

$$\begin{aligned} F_{DC} = {} & \frac{1}{2}C'{V_{DC}}^2 + \left(\frac{Cq_s}{4\pi\varepsilon_0 z^2} + C'V_{CP}\right)V_{DC} + \frac{1}{4}C'{V_{AC}}^2 + \frac{{q_s}^2}{4\pi\varepsilon_0 z^2} + \frac{Cq_sV_{CP}}{4\pi\varepsilon_0 z^2} \\ & + \frac{1}{2}C'{V_{CP}}^2 \end{aligned} \tag{II.24}$$

$$F_{\omega} = \left[\frac{q_s}{4\pi\varepsilon_0}\frac{C}{z^2} + C'(V_{DC} + V_{CP})\right]V_{AC}\sin\omega t \tag{II.25}$$

$$F_{2\omega} = -\frac{1}{4}C'{V_{AC}}^2\cos 2\omega t \tag{II.26}$$

At this stage, it can be noted that similar information about sample properties can be carried out either by force detection, or force gradient detection. However, the force gradient detection method is expected to offer higher resolution as will be discussed in the following sections.

Accordingly, the force gradient $G = \frac{\partial F}{\partial z}$ is deduced from previous expressions and becomes similarly to the force, the sum of three components:

$$G = G_{DC} + G_{\omega} + G_{2\omega} \tag{II.27}$$

$$\begin{aligned} G_{DC} = {} & \frac{1}{2}C''{V_{DC}}^2 + \left(\frac{q_s}{4\pi\varepsilon_0}\frac{C'z^2 - 2Cz}{z^4} + C''V_{CP}\right)V_{DC} + \frac{1}{2}C''{V_{CP}}^2 \\ & + \frac{q_s}{4\pi\varepsilon_0}\frac{C'z^2 - 2Cz}{z^4}\,V_{CP} + \frac{1}{4}C''{V_{AC}}^2 - \frac{2{q_s}^2}{4\pi\varepsilon_0 z^3} \end{aligned} \tag{II.28}$$

$$G_{\omega} = [\frac{q_s}{4\pi\varepsilon_0}\frac{C'z^2 - 2Cz}{z^4}V_{AC} + C''(V_{DC} + V_{CP})]V_{AC}\sin\omega t \tag{II.29}$$

$$G_{2\omega} = -\frac{1}{4}C''{V_{AC}}^2\cos 2\omega t \tag{II.30}$$

As already explained for tapping mode, the force gradients sensed by the probe shift its resonance frequency.

In other terms, during the second scan, the tip is excited mechanically at the resonance frequency of its first mode (ω_0), and is electrically biased with a DC and/or AC voltage (*ω*). The latter induces perturbating electrostatic forces with varying frequencies (*0*, *ω* and *2ω*). In this case, these electrical forces between the tip and the sample constitute the F_{ts} of equation (II.12), F_{ts} is then mainly composed of three components oscillating at different frequencies. When no interferences are present, everything happens as if the tip is excited independently at three excitations each influencing the mechanical vibration with specific periods: a static modification due to the DC gradient, a *ω* varying vibration and a *2ω* one.

Note that when the external mechanical drive is stopped, these electrostatic forces become equal to the main driving force F_d of eq (II.12) also varying at $\omega_C = 0$, *ω* and *2ω*, and $F_{ts} = 0$. Thus, eq (II.12) returns in this case equivalent to (II.3).

Since each of the above force and force gradient spectral components depend differently on the system capacitance, surface charges and contact potential, it becomes ingenious to monitor them independently, and thereby deduce specific electrical properties with different ways. Lock-in amplifiers (LIA) are used for this aim as they demodulate the signal at the desired frequencies. Moreover, a LIA suppresses all the noises and electrical responses that are not at the frequency of interest, and hence, do not contribute to the researched property [36]. Subsequently, the extracted signal is either imaged directly on an independent EFM image, or used as a feedback signal to control and extract a specific property. Next, a description and discussion of force mode detection versus force gradient mode is presented.

4.2.2.2. Electrostatic force detection

During the second scan, when the electrostatic force is measured, the external mechanical excitation can be switched off. Here, the electrical stimulus oscillates the tip at three spectral components as it has been deduced above. Consequently, the measure of the amplitude of oscillation at ω_i pulsation ($\omega_i = 0$, ω or 2ω) determines the force researched following the below equation, deduced from the combination of equation (II.23) into (II.9) with $F_d = F_{\omega i}$ [42]:

$$F_{\omega_i} = KH(\omega_i)A_c(\omega_i) \tag{II.31}$$

with $H(\omega_i)$:

$$H(\omega_i) = \left[\left(1 - \left(\frac{\omega_i}{\omega_0}\right)^2\right)^2 + \frac{\omega_i}{Q\omega_0}\right]^{1/2} \tag{II.32}$$

Note that when F_{DC} is measured, the static amplitude is equivalent to the static deflection of the probe and eq (II.31) becomes equivalent to eq (II.1) [43]. In Fig. II - 13, A_{RMS} extraction shows an illustration of this measurement mode.

Care must be taken using this mode to keep the amplitude of electrical oscillation much lower than the mean tip-sample separation. Otherwise, sensor movements become not appropriate to be treated with the linear regime hypothesis.

Consequently, the equalization of (II.31) with (II.26) can give access to C', V_{CP} and q_s, depending on the chosen spectral component.

Electrostatic force detection is commonly used in the literature to study dielectric metal-oxides [43-46], polymers [42, 44, 45], bio-membranes [47, 48], viruses [46] and bacteria [49]. However, since the electrostatic force is proportional to the first derivative of the probe-to-stage capacitance, stray capacitances from the cantilever and the chip highly contribute to the signal. That being so, the locality of the measurement is altered [36, 50]. In order to overcome this problem, for each measurement, researchers subtracted the signal over the sample for a certain lift, to that over the bare substrate at a reference distance from the surface. This calculation step is also added to simulations when a quantitative study is desired [45, 46, 49]. Nonetheless, another method to directly reduce the non-locality is detecting instead electrostatic force gradients.

4.2.2.3. Electrostatic force gradient detection

Contrarily to force measurements, force gradients are acquired keeping the mechanical drive during the second scan. As it has been shown earlier in this chapter, force gradients change the effective resonance frequency of the sensor (eq (II.17)). Fig. II - 8 illustrates the resulting decrease of the effective resonance frequency for a given attractive force field, which is the case of capacitive forces.

Consequently, when the drive frequency is locked at ω_0, resonance frequency shifts will decrease the amplitude and the phase of the oscillating cantilever. As a result, force gradients can be detected by three dynamic methods: amplitude, phase and frequency shifts detection. A simplified block diagram of EFM for these three detection modes is illustrated in Fig. II - 13.

a) Amplitude shift detection

According to eq (II.9) plotted on Fig. II - 8, an indirect measurement of force gradients is to collect changes in the cantilever amplitude at fixed drive frequency (see Fig. II - 13, ΔA_{RMS} extraction).

However, both amplitude and amplitude shifts measurement methods, for respectively force and force gradient study, are not recommended due to the probable appearance on EFM images of laser interference artifacts. If the laser is not correctly aligned at the back of the cantilever, spreads over the edges reflect at the surface of a reflective sample and interfere with the reflected beam from the cantilever. Constructive and destructive interferences induce periodic stripes on the EFM image [51]. An example of an EFM image with laser interference artifacts is presented on Fig. II - 12. The image can be misleading as it reveals features similar to the subsurface composition of the sample (Fig. II - 12 c. versus e.).

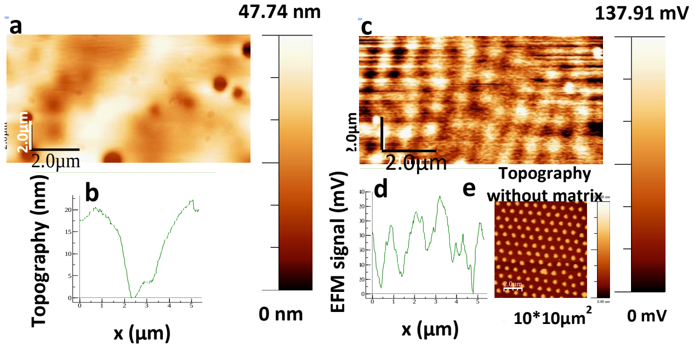

Fig. II - 12 : EFM image artifacts obtained on the $A_{2\omega}$ signal for a sample composed of particles placed at the substrate and covered by a polymer layer. (PVAc film of ~ 1.5 µm thickness covering PS particles + 60 nm Al_2O_3 shell), a. topography image; c. $A_{2\omega}$ amplitude image with V_{AC} = 7.5 V and f_0 = 10 kHz at z = 21 nm; b. and d. cross-sectional profiles along the blue line of a. and c., respectively; e. sample topography without matrix. It can be noticed the misleading match between the subsurface and electrical image, however, verified to be due to laser interference.

Contrariwise, laser interference is not detectable on the phase or frequency signals channel. Therefore, a second alternative method to extract force gradients is phase shift detection.

b) Phase shift detection

Here, similarly to amplitude shift detection, the phase of the signal at the photodiodes is extracted first with a LIA locked at the drive mechanical frequency ω_0. The latter phase shift is either directly collected on an EFM image for *DC* phase shifts measurement, or fed back into a LIA locked at the electrical frequency to extract ω and 2ω components (see Fig. II - 13, $\Delta\Phi_c$ extraction). Note that as the phase drive signal is centered at the resonance frequency, the measured signal is thereby equal to the phase lag between the drive and the cantilever response. Consequently, the phase shifts can be correlated to the electrical force gradients as follows [32]:

$$\Delta\phi_c\,(\omega_i) \cong -\frac{Q}{K}g(\omega_i)G(\omega_i) \tag{II.33}$$

where $g\,(\omega_i)$:

$$g(\omega_i) = \frac{1}{\sqrt{1+2(Q\frac{\omega_i}{\omega_0})^2}} \tag{II.34}$$

$\omega_i = 0$, ω or 2ω and $g(\omega_i)$ is an attenuation coefficient < 1. In fact, the response of the phase shift versus ω_i has been found to exhibit a low-pass like filter behavior [32]. Thus, $g(0) = 1$ for *DC*-phase shifts, and $g(2\omega) \cong 2$ in the frame of our experiments ($Q \cong 220$, $\omega_0 \cong 120\pi$ rad/s and $\omega = 200\pi$ rad/s).

c) Frequency shift detection

During frequency shift detection, the phase shifts are measured similarly to the previous phase shift method. However, those signals are used here as feedback parameter to vary the drive frequency in order to keep a zero phase shift (see Fig. II - 13, $\Delta f_0(DC)$ extraction). According to eq (II.17), frequency shifts are generally related to force gradients with the following equation:

$$\Delta f_0\,(\omega_i) \cong -\frac{f_0}{2k} G(\omega_i) \tag{II.35}$$

Nevertheless, due to a lack in our system set-up, in our case, this method is only applicable for *DC* frequency shift measurements. An alternative method to obtain *AC* frequency shifts (i.e. AC gradients) is to convert *AC* phase shifts into frequency shifts with the following relation, from the combination of equations (II.33) and (II.35):

$$\Delta f_0(\omega_i) = \frac{f_0}{2Qg(\omega_i)} \Delta\phi(\omega_i) \tag{II.36}$$

It can be concluded that EFM can be employed using DC and/or AC electrical excitation, for either force or force gradients detection. Force measurements are performed with turned off mechanical excitation. On the other hand, force gradient detection requires a dynamic excitation of the sensor. The detection can be implemented by three methods: amplitude, phase and frequency shifts detection. Phase and frequency signals measurement are the most advisable methods. Frequency shift detection has been used in our work for DC measurements, and 2ω phase shift detection for AC ones. Here also, force gradients detection requires low mechanical and electrical oscillation amplitudes, lower than the mean tip-to-sample distance.

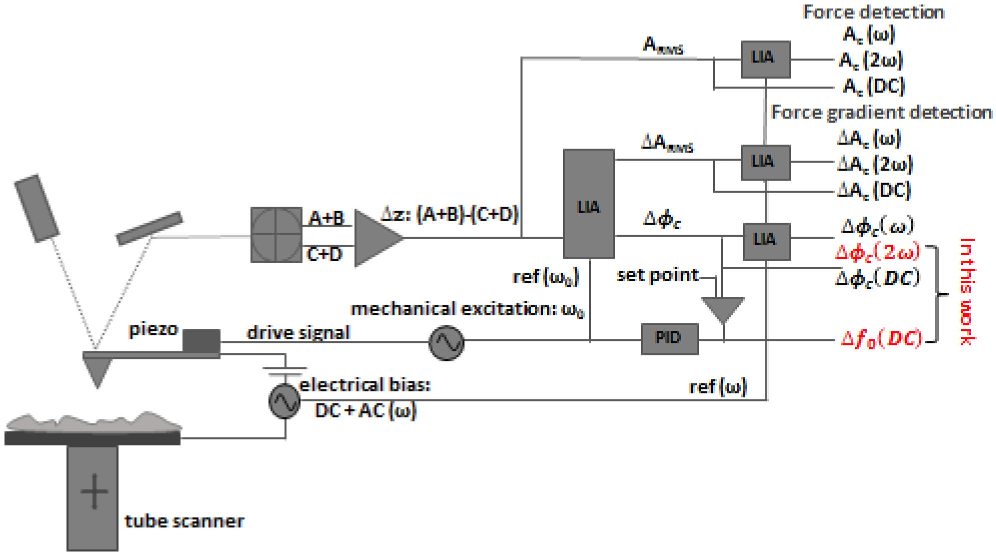

Fig. II - 13 : Simplified block-diagram of EFM electrical measurements showing signal extraction with the methods described above; for force detection: A_c and force gradient detection: ΔA_c, $\Delta\Phi_c$ and Δf_0.

d) Options to extract electrical properties

A summary of possible electrical parameters extraction with force and force gradient measurements at DC and AC excitation modes is presented in Table II - 1**.**

i. **Capacitive response:** In the framework of this thesis, we have been mostly interested in the measurement of the pure capacitive response of the system. Hence, as it can be seen from equations (II.26) and (II.30), the 2ω components are the only ones that reflect the capacitive response without V_{CP} and q_s effects. Nevertheless, in Chapter IV, we will present an alternative method that we have developed to extract accurate information on the capacitive response by using simple DC measurements.

ii. **Contact potential:** The contact potential V_{CP} is however commonly measured with KPFM that can be considered to be derived from EFM [12]. In KPFM, a low AC voltage, with ω near the cantilever resonance frequency, excites the cantilever in order to induce the vibration of the probe at ω and 2ω. Since $F(\omega)$ and $G(\omega)$ are both proportional to ($V + V_{CP}$), feedback controls are used to change the applied DC-bias intensity so it nullifies the signal (either amplitude or phase) at ω. The magnitude of supplied bias is in principle a measure of V_{CP}. Another method to measure V_{CP} in DC and AC at ω with an open loop on the supplementary applied voltage is to obtain $\Delta f_0(V)$ curves. In the assumption of zero surface charge ($q_S = 0$), the shift in the V axis from 0 V is equal to V_{CP} according to (II.24, II.25) and (II.28, II.29).

iii. **Surface charges:** Similarly to V_{CP}, surface charges can be measured from the *DC* and ω component of the signal [34]. Charge measurement with KPFM requires however to properly model the capacitance in order to get accurate estimation of q_s. In our past work, we have developed a method to extract surface charges from *DC* measurements without the need to model the capacitance [39]. This method has been used later to measure surface charge difference above nanocomposites at particles and polymer regions [52].

Table II - 1 : Table of comparison of the information extracted with force vs. force gradient detection methods in DC and AC electrical excitation, R_0 and θ are tip apex radius and cone half-angle, respectively; and ε and h are respectively the sample dielectric constant and thickness.

	Force detection		**Force gradient detection**	
	Component	Information	Component	Information
DC	F_{DC}	$C'(\varepsilon, h, R_0, \theta), q_s, V_{CP}$	G_{DC}	$C''(\varepsilon, h, R_0, \theta), q_s, V_{CP}$
AC	F_{ω}	$C'(\varepsilon, h, R_0, \theta), q_s, V_{CP}$	G_{ω}	$C''(\varepsilon, h, R_0, \theta), q_s, V_{CP}$
	$F_{2\omega}$	$C'(\varepsilon,h)$	$G_{2\omega}$	$C''(\varepsilon,h)$

5. Spatial resolution

The research for resolution enhancement is one of the principle aims of AFM techniques. The resolution depends on the accuracy of the interaction area between the tip and the sample. Probe dimensions are of the utmost importance in determining the spatial resolution in most AFM variants. In the next paragraphs, we develop the main factors conditioning topography and EFM signal resolution.

5.1. Topography resolution

Topography images can be mainly influenced in intermittent contact measurements by profile broadening artifacts due to tip geometry. However, according to the relative dimension of the tip radius R_0 in regard to the particle to be measured, some analytical equations can be used in an attempt to reconstruct the true geometry of the sample. Two common cases are discussed for a feature of particle curvature radius r_p, and the resolution limit is subsequently extracted [53]:

a) Tip radius $R_0 << $ particle radius r_p:

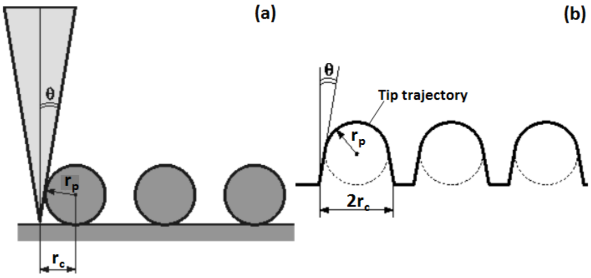

Fig. II - 14 : a. Schematic of the studied object and the AFM probe for $R_0 << r_p$, b. the resulting AFM image profile [53] .

For this case analysis, the height of the object remains the same, but its radius is broadened from r_p to r_c. r_c is related to the probe cone half-angle θ as follows :

$$r_c = r_p\left(\cos\theta + \sqrt{\cos^2\theta + (1+\sin\theta)\left(-1+\frac{\tan\theta}{\cos\theta}\right) + \tan^2\theta}\right) \tag{II.37}$$

b) Tip radius $R_0 \approx$ particule radius r_p :

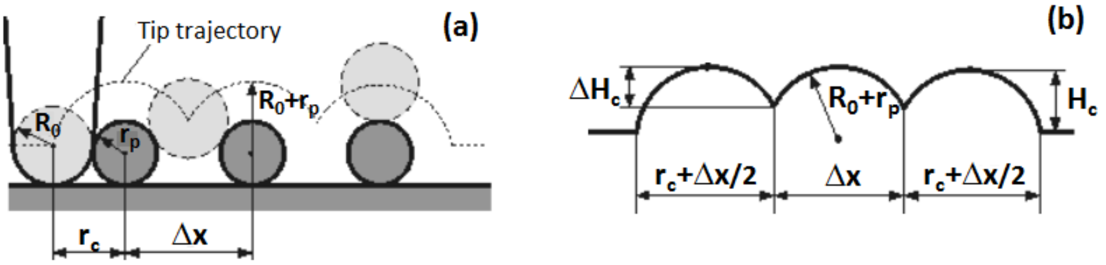

Fig. II - 15 : a. Schematic of the studied object and the probe for $R_0 \approx r_p$, b. the resulting AFM image profile [53].

When the tip apex radius is close to the one of the object, close particles appear with a relative change in their height from $2r_p$ to H_c, in addition to their apparent radius r_c. The probe is approximated to its apex, and elementary calculations result in the following relations:

$$r_c = 2\sqrt{R_0 r_p} \tag{II.38}$$

$$H_c = r_p\left[1 - \sqrt{1 - \frac{{r_c}^2}{\left(R_0 + r_p\right)^2}}\right] \tag{II.39}$$

Moreover, when the distance between objects is less than particle diameter ($\Delta x < 2R_0$), during scanning, the tip will only be able to penetrate between them up to the distance ΔH_c and thus, particle height will be underestimated:

$$\Delta H_c = r\left[1 - \sqrt{1 - \frac{(\Delta x/2)^2}{\left(R_0 + r_p\right)^2}}\right] \tag{II.40}$$

c) Optimum resolution:

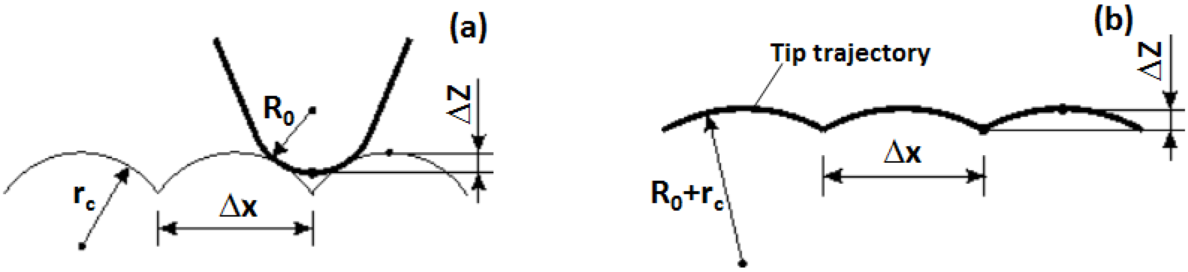

Fig. II - 16 : a. Schematic of the studied object and the probe, b. the resulting AFM image profile [53].

In general, the optimal resolution $\Delta_{Topo} = \Delta x$ is conditioned by the vertical resolution ΔZ, which is the minimum detectable z change within the instrument noise. For the case presented in Fig. II - 16 a., geometrical calculations lead to the following expression for Δ_{Topo}:

$$\Delta_{Topo} = \Delta x \cong \sqrt{8\left(R_0 + r_p\right)\Delta Z} \tag{II.41}$$

Since the resolution must be a characteristic of the instrument independent of the scanned object, a point approximation of the particles ($r_p = 0$) can be used to define the lateral resolution limit Δ_{Topo} obtained for the two constants, tip curvature radius R_0 and vertical resolution limit ΔZ:

$$\Delta_{Topo} = \sqrt{8R_0\Delta Z} \tag{II.42}$$

5.2. EFM resolution

Similarly to topography resolution, EFM lateral resolution Δ_{EFM} is conditioned by the effective radius of interaction R_{int} with the sample [54]. Since EFM measurements are usually performed out of contact with the sample, and due to the long range nature of these forces, the effective radius of interaction with the sample can quickly exceed the real physical radius of the tip [54]. An approximate expression for the effective tip radius in an EFM measurement over a metallic surface can be found in [36]:

$$\Delta_{EFM} = R_{int} = R_0\left[\cos\theta + \left(1 - \sin\theta + \frac{z}{R_0}\right)\left(\frac{1}{\cos\theta} - \tan\theta\right)\right] \tag{II.43}$$

Another generally agreed analytical expression for the spatial resolution at low tip-sample distances z (for $z < 0.5\,R_0$) writes [36, 55-57]:

$$\Delta_{EFM} = b\sqrt{R_0 z} \tag{II.44}$$

while b coefficient being larger in force measurements, compared to gradient measurement techniques ($b_{gradient} \cong 0.7 b_{force}$).

A simple method to understand the difference in force and force gradient resolutions is described in ref [36] : at close tip-sample separations, the electrostatic force is roughly approximated to that between a sphere of radius R_0 and a plane (II.45), as well as to that between two disks of radii equal to the radius of interaction R_{int} (II.46).

$$F = -\pi\varepsilon_0 \frac{R_0}{z} V^2 \tag{II.45}$$

$$F = -\frac{\pi\varepsilon_0}{2} \frac{{R_{int}}^2}{z^2} V^2 \tag{II.46}$$

From the equalization of these two force expressions, the disk interaction radius for force measurements becomes $\Delta_{EFM\ F} = R_{int\ F} \cong \sqrt{2}\sqrt{R_0 z}$. In the same way, the equality for force gradient expressions gives $\Delta_{EFM\ G} = R_{int\ G} \cong \sqrt{R_0 z}$. The lateral resolution is consequently enhanced in gradient detection mode.

With force gradient detection, sufficiently correct local electrical measurements are thereby obtained at intermediate working distances, suitable for ambient conditions. In general, since force gradients are proportional to the second derivative of the capacitance, and since tip-sides contributions are slowly varying functions with respect to *z* [58], at experimental working distances, their contribution becomes negligible. The advantage of force gradient measurements over force measurements have already been accepted by many authors [36, 59, 60]. This further supports our choice for force gradient measurements in this work.

Some attempts to improve the spatial resolution are to use highly sharp tips such as the grafting of carbon nanotubes at the end of the tip. These tips have shown improved spatial resolutions [61, 62]. However, although the apex and cone aperture have been highly reduced, the nanotube large length can be also problematic [59].

Electrostatically coupled regions can also affect the accuracy of measured surface contact potential in KPFM [36, 63, 64]. Nevertheless, high spatial resolutions have still been able to be reached with KPFM especially under vacuum [63, 65-69] and in air with different methods [70-73].

In fact, in addition to tip geometry and working distance effects, the spatial resolution depends on the quality, precision and the nature of the used detection mode. Better sensitivities improve the resolution. The sensitivity in AFM will be detailed in the following paragraph.

As a conclusion, the main idea for enhancing the resolution is to favor the apex interaction compared to the cone and cantilever ones [59]. At low distances compared to tip radius, this is achievable for lower apex radii. However, although counter-intuitive, a bigger apex radius can enhance the resolution at higher distances as it increases the contribution of the end of the tip compared to its sides. Force gradient detection benefits from better spatial resolutions.

6. Sensitivity

The sensitivity or the vertical resolution is primarily determined by the resolution of the piezo tube used for *z* displacements, of the order of a few angstroms. However, the sensitivity is strongly deteriorated by the system noise, which will condition the minimum detectable force and force gradient. The deflection noise density versus noise frequency *f* shows generally an 1/*f* dependence for low frequencies, and a constant white noise above the so-called 1/*f* corner frequency (f_c) (see Fig. II - 17) [74]. Consequently, due to the 1/*f* dependence, static measurements are highly altered by the noise compared to dynamic AFM. In fact, for the latter case, measurements are performed around the resonance frequency of the cantilever f_0. When f_0 is higher than f_c, a bandpass filter is sufficient to only integrate the white noise in the bandpass bandwidth. Among ambient noise sources, we enumerate three cases:

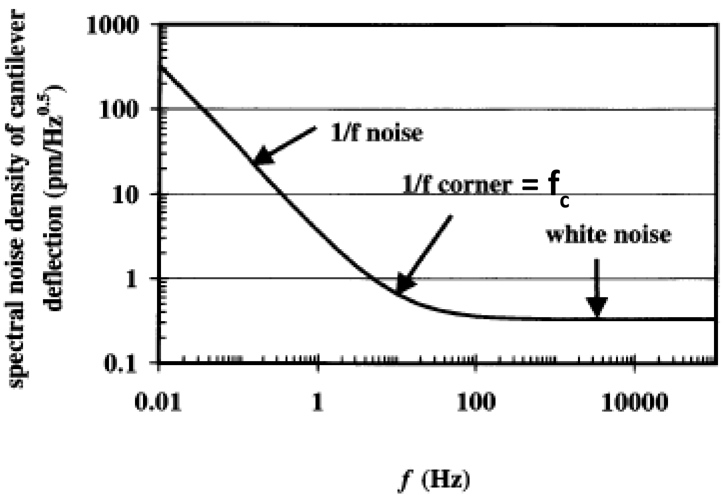

Fig. II - 17 : Schematic view of spectral noise density of AFM cantilever deflection in regard to the frequency [74].

6.1. Electronic noise

Electronic noise, such as Johnson-Nyquist noise, is introduced by means of conditioning electronics (preamplifier, proportional and integral gains…) [34, 75]. It mostly appears at low frequencies, thus, altering considerably static AFM measurements.

6.2. Optical detection system noise

Optical noises can be classified into two categories [76]:

a) Classical noise: like the laser fluctuation in intensity or beam direction. This noise can be reduced by a proper experimentation.
b) Quantum noise: like photons shot noise at the detector and the back action of the light on the cantilever. Back light action, or the reflected light can be neglected because the force created by a 1 mW laser is of the order of pico Newton. However, shot noise is unavoidable. It is considered as white noise, and it depends on the optical beam deflection system. A typical value of the optical beam deflection system (OBD) precision is 100 $\mathrm{fm}/\sqrt{\mathrm{Hz}}$.

A recent study of B. Potier and L. Bellon reported a method to decrease the instrumental noise of a casual OBD [75]. This method allows a “noiseless” thermal noise measurement of AFM cantilevers (see paragraph 6.3). The study of the thermal spectral vibrations is commonly used to calibrate the cantilever stiffness [77, 78].

6.3. Cantilever fluctuations: thermal noise

The thermal noise is caused by the Brownian motion of the gas in which the probe is immersed (the air in our case), which induces random fluctuations of the cantilever. It is considered as a white noise and can play a potential limiting factor.

According to the equipartition principle, it is supposed that the energy stored in the cantilever, approximated by a spring, is on average equal to the thermal energy and thus [28]:

$$\frac{1}{2}K_B T = \frac{1}{2}K\langle\Delta z^2\rangle \qquad \text{(II.47)}$$

The fluctuation-dissipation theorem, which relates the response of equilibrium systems to small external perturbations and their response functions, is used to deduce the power spectral density *S(ω)* of cantilever fluctuations caused by thermal noise [79]:

$$S(\omega) = \frac{K_B T {\omega_0}^3}{\pi Q K \left[({\omega_0}^2 - {\omega_c}^2)^2 + \frac{{\omega_c}^2 {\omega_0}^2}{Q^2} \right]} \tag{II.48}$$

The average fluctuation of the sensor η is calculated as:

$$\eta = \sqrt{4\pi B S(\omega)} \tag{II.49}$$

with B the bandwidth of the measurement. This expression is simplified according to whether one is working on or off-resonance:

$$\eta \approx \frac{4K_B TQB}{K\omega_0} \quad \text{On-resonance} \tag{II.50}$$

$$\eta \approx \frac{4K_B TB}{K\omega_0 Q} \quad \text{Off-resonance} \tag{II.51}$$

The minimum detectable force and force gradients are those for which the amplitude of oscillation is equal to the average thermal fluctuation of the cantilever [11]. It follows that:

$$F_{min} = K\eta \tag{II.52}$$

At resonance, the amplitude derivative in regard to the frequency of excitation is calculated as [34]:

$$\frac{dA}{d\omega_c} = \pm A_m \frac{4Q}{3\sqrt{3}\omega_0} \tag{II.53}$$

with A_m the maximum amplitude of the oscillator. From relation (II.54), a small amplitude variation will be connected to the force gradient by the expression:

$$\Delta A = \frac{dA}{d\omega_c} \Delta\omega_c = A_m \frac{2Q}{3\sqrt{3}K} \left| \frac{\partial F}{\partial z}(z_0) \right|_{min} \tag{II.54}$$

Hence, from the equalization of (II.54) and (II.50), the following expression of the minimum force gradient at resonance is deduced:

$$G_{min} = \left| \frac{\partial F}{\partial z}(z_0) \right|_{min} = \frac{1}{A_m} \sqrt{\frac{27K_B TBK}{\omega_0 Q}} \tag{II.55}$$

The thermal noise is consequently highly dependent on the tip stiffness, resonance frequency and quality factor in addition to the temperature and measurement bandwidth. Note that eq (II.55) is also valid for other vibration modes of the sensor.

In the next chapter, a detailed study of EFM signal variation versus sample properties will be discussed. The rate at which the signal changes with a corresponding property conditions the sensitivity of EFM. We will show that, in addition to the above experimental limiting factors, EFM sensitivity and resolution depend interestingly on the material itself.

7. Recent advances

As we have concluded in the first chapter, we can deduct from the literature an agreed dielectric model for a nanocomposite: it is made of nanoparticles surrounded by an interphase layer of different properties than the nanocomposite initial elements, such as its dielectric permittivity, with the assembly embedded within a matrix. Thus, to have access to the interphase with SPM in general, and EFM in particular, several imaging problems raise including:

a) Subsurface imaging, as the interphase is usually present below a matrix layer;
b) Capability to distinguish the composition of multilayered materials, as the interphase is usually a subphase of three superposed materials: particle-interphase-matrix (this is a subcase of subsurface sensitivity);
c) Both above criteria must be also possible for nanometric geometries in the three dimensions, as commonly used nanocomposites are nano-particulate filled.

7.1. 3D nano-subsurface imaging

In order to detect subsurface nano-features in a material, the AFM generated wave or field must be disturbed by the buried object with a relevantly measurable intensity. For this purpose, various advantageous interaction fields have been proposed. One approach uses AFM to detect ultrasonic waves scattered by subsurface features (ultrasonic-AFM) [80, 81], or nano-mechanical modulation of the surface contact stiffness due to buried objects (Contact Resonance-AFM or CR-AFM) [82-86]. However, ultrasonic exact imaging mechanism has not been fully understood yet [87, 88] and CR-AFM can also present important topographic cross-talks [89].

Electrically coupled SPM have shown to be able to gather information beneath the surface. In ref [90], three techniques have been investigated through the study of test samples specifically designed to verify their subsurface imaging capabilities. Authors show and discuss the aptitude of Scanning Microwave Microscopy (SMM) to image the capacitance of buried metal lines, KPFM to image the electric potential of buried metal lines, and EFM phase imaging to see buried interface surface roughness [90]. Metal lines under 2 micrometers of surface oxide could be resolved with SMM [91]. A phase difference has been measured between metal surfaces covered with 800 nm oxide thickness, compared to 2200 nm covering layer.

SMM has also been indicated to achieve nanoscale tomography of metals to detect defects [92]. More recently, [93] SMM has been reported to detect atomically thin regions of dopant atoms patterned on silicon substrate and placed below another silicon layer. Authors have been able to extract dopants concentration.

Concerning nanocomposites, scientists also tried different EFM derived methods to perform subsurface imaging of carbon nanotubes composites [94-98]. So far, they have found that the extraction of the *2ω* component of the electrostatic force was the most robust one.

In ref [94], DC amplitude modulation-EFM (AM-EFM) with single pass scanning has been used to achieve high resolution, and penetration sensitivity going from 10 to 100 nm. The physical nature of EFM contrast in carbon-nanotubes filled composites has been attributed to Joule heating and not to local variations of effective dielectric constants.

E. Castaneda-Uribe *et al.* combined KPFM and AM-EFM force detection of the 2ω component [97]. This technique has reached penetration depths for Single Wall Carbon Nanotubes (SWCN) layer with increasing matrix coverage up to 450 nm. They have also used numerical simulations to estimate the depth of SWCN in a nanocomposite.

In ref [89], the authors addressed a comparative study between two key tools for subsurface imaging: KPFM and CR-AFM. A list of the advantages and limitations of each technique has been deduced for SWCN composites, in conjunction with numerical simulations for the underlying physical phenomena.

7.2. 3D nano-multilayered materials imaging

A breakthrough work concerning nano-objects characterization with EFM has been published in 2012 by L. Fumagalli *et al.* [46]. The authors utilized low stiffness cantilevers, and using the *2ω* electrostatic force detection, sub-piconewton sensitivity was attainable. The dielectric constants of SiO_2, PS and Al_2O_3 nanoparticles of close radii have been quantified with the conjunction of experiments to Comsol® numerical simulations. Furthermore, EFM has been able to distinguish nanoparticles with similar external shell and different inner composition. A discrimination of empty from DNA-containing virus capsids was possible, as well as an estimation of the filled-virus core dielectric constant (Fig. II - 18). Later, within the same research group, D. Esteban-Ferrer *et al.* quantified the effective dielectric constant of four types of single bacterial cells under dry and air conditions [49]. An increase in the dielectric constant under ambient humidity has been noticed. Another similar study of the dielectric permittivity of bacterial cells has been also addressed with SMM [99]. Moreover, in ref [99] M. Chiara Biagi *et al.* introduced topography "cross-talk" removal from electrical signals.

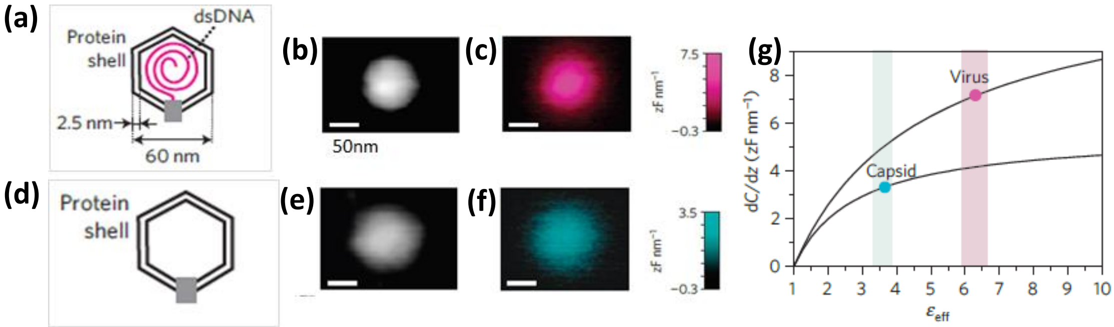

Fig. II - 18 : Dielectric constant measurement and material identification of a. the bacteriophage T7 virus and d. capsid ; b. and e. measured topography, and c. and f. dielectric images at constant height of the bacteriophage T7 and its capsid (scan height 49 nm and 36 ± 0.5 nm, respectively) taken on graphite substrates in air, c. f. phase images show that the icosahedral shape and coat-protein pattern of the shell are preserved, and g. matching the maximum dielectric signals (symbols) with calculations using a homogeneous oblate-spheroid model gives the effective dielectric constants 6.3 ± 0.17 and 3.65 ± 0.15 [46].

7.3. Interphase investigation

J. Seiler and J. Kindersberger tried a radius comparison method with EFM to show the existence of an interphase around SiO_2 nanofilled composites [100]. Authors measured the EFM average radius of the nanoparticles before and after embedding them into the polymer matrix, and used a topography deconvolution equation from [101] in the aim of deconvoluting tip geometry effect out of EFM images. Before mixing with the polymer, electrical measurements were obtained with biased cantilever-to-stage system at - 5 V. However, after insertion into the matrix, particle size has been obtained from EFM images at 0 V. An increased particle radius has been obtained, which was explained by the interphase presence around the particle.

Despite the qualitative confirmation of interphase thickness calculations with authors previous work on the same samples [102], care must be taken to interpret those results. Comparisons have been addressed at different measurements conditions (V_{DC} = - 5 and 0 V), thus, at different origins of EFM response. Moreover, the highly probable presence of a matrix layer over the particles in the nanocomposite has been ignored. The matrix above the nanoparticles can obviously broaden particles apparent size and explain obtained results. Furthermore, topographic tip deconvolution application on EFM measurements is supposed to be insufficiently appropriate [54].

Later in ref [52], based on the method introduced in ref [39] to measure model free surface charges, the authors studied the existence of surface charges on particles in a nanocomposite.

J. Deschler *et al*. hypothesized the presence of an electric double layer around the particles, at the interfacial region. Here also, any presence of matrix layer above the particles has been neglected.

In similar perspectives, a recently developed EFM technique, the intermodulation EFM (ImEFM) [103] has been reported to probe the injection and extraction of charges around individual surface modified aluminum oxide nanoparticles embedded in a low-density polyethylene matrix [104]. Localized energy states close to the conduction band have been reported to exist in the vicinity of the nanoparticles.

Another interesting paper, published at the end of 2016, used EFM to show the presence of the interphase in low density polyethylene nanocomposite with titanium dioxide nanoparticles of 50 nm radius [105]. Authors studied thin sectioned parts of the bulk composite. Through the extraction of the *2ω*-phase shift EFM component, three areas of different composition have been distinguished: the matrix alone, a particle exposed at the surface of the sample and matrix bump due to the nanoparticle underneath the surface. After the interpretation of phase shifts values at these regions, and through the corroboration with numerical simulations, authors declare an interphase around the nanoparticles. The signal at the bump position could not be explained through simulations unless an interfacial layer of lower permittivity than the bulk polymer is present. Typical dielectric permittivity and thickness of the interphase have been found to be 1.6 and 20 nm, respectively.

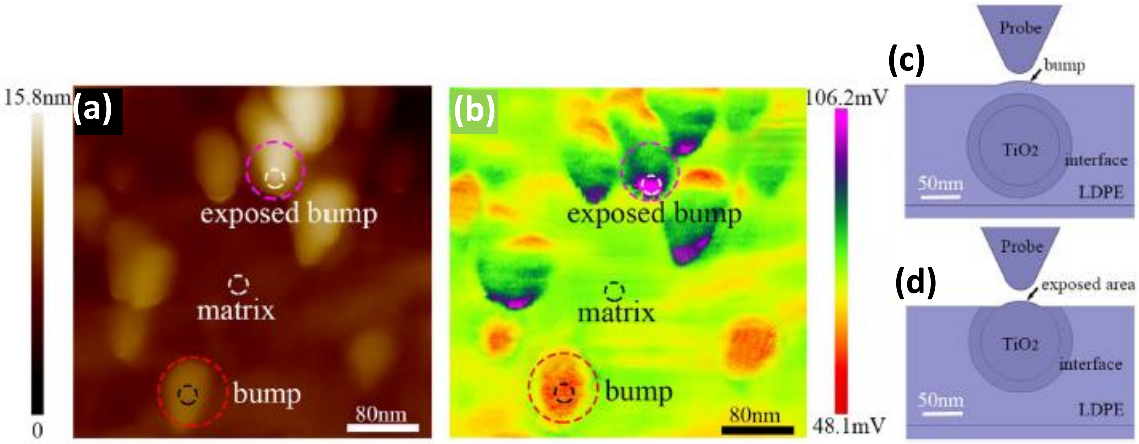

Fig. II - 19 : The results of local dielectric property detection: a. topography image, and b. $|\Delta\phi_c\ (2\omega)|$ signals amplified by the LIA. c. and d. present the local finite models corresponding to two cases with interface: "bump" and "exposed bump" [105].

8. Conclusion

In this second chapter, AFM basic working principles have been defined. An overview of electrical AFM methods has been reviewed briefly to get to the introduction of the main technique of interest of this thesis, Electrostatic Force Microscopy (EFM). As a general definition, an EFM tip-sample-stage system is similar to a capacitor: the tip and sample holder being both metallic, with the possibility to be electrically biased. The EFM sensor detects the electrostatic forces between capacitive charges, local static charges with their image charge on the tip and charges caused by differences in work functions. In this work, the double-pass method has been used with oscillating probe, where topography is acquired on a first scan and EFM measurements during the second one. For the second pass, the tip is retracted to a larger separation from the surface and retraces the corresponding topography.

The polarization of the system with DC and AC voltages at an electrical frequency ω induces three spectral components for both the electrostatic force and force gradients: *DC*, ω and 2ω. Each component depends differently on the electrical properties of the system such as the capacitance, surface charges, and contact potential. Consequently, to extract and monitor each part of the signal of interest separately, making use of lock-in amplifiers, and eventually feedback loops, leads to the ingenious extraction of the property of interest. In our work, we have been mainly interested by the extraction of the pure capacitive response. The latter can be directly measured from the 2ω component or in the *DC* one with a special experimental protocol that will be exposed in Chapter IV. Furthermore, EFM experiments can be carried out either in force, or force gradient detection methods. The main difference in the obtained physical properties is the capacitance derivative: the former method is proportional to the first capacitance derivative, and the latter method to its second derivative. This explains the increased spatial resolution of force gradient EFM mode compared to force mode.

The tip-sample interaction is approximated in the simplest way by a point-mass spring. Once subjected to a sinusoidal excitation, such as the driving oscillation used in dynamic mode, the resulting motion of the probe is similar to a harmonic oscillator. In the linear approximation, the additional electrostatic interaction force gradients change the effective resonance frequency of the sensor. Force and force gradients can thereby be extracted in several ways. Forces are measured with the mechanical excitation turned off, from the cantilever amplitude of vibration generated by the electrical stimulus. However, force gradients are conventionally only measured in dynamic mode. The response to mechanical drive oscillation is altered by electrostatic gradients. The latter are measured by cantilever amplitude, phase or frequency shifts detection. In the framework of this thesis, we measured the frequency shifts: 1) directly, by regulating the drive frequency to nullify the phase signal, or 2) indirectly, by converting detected phase shifts to frequency shifts. This choice has been made owing to the widely renowned benefits of force gradient measurement, in addition to the accuracy of phase and frequency signals to amplitude extraction.

Concerning the limits of the technique, a discussion on spatial and vertical resolutions has been reported. The main determining factors for the spatial resolution are the tip geometry and working distance, and for the sensitivity, are optical shot noise and thermal noise, also dependent on the sensor stiffness, quality factor, resonance frequency, vibration mode etc. The resolution and the sensitivity are also influenced by the sample itself as it will be detailed in the following chapter.

Afterwards, a state of the art on the advances either directly or indirectly related to the interphase detection in nanocomposites has been reviewed. Subsurface imaging and 3D-multilayered structures study have achieved some advances for specific type of materials. However, the precise characterization of the interphase in nanocomposites, although attempted by a few scientists, has not been fully established yet. Either EFM measurements analysis or comparisons were not sufficiently addressed in an accurate way, or nanoscale measurements have not been correlated to macroscopic ones to show consistency with SPM results. Nonetheless, one common point found in all previous works with electrical AFM methods, and EFM in particular, can be highlighted: the exact source of the measured signal is not totally identified, thus, the measurement of complex materials stays a big challenge. The following questions naturally arise: what are the main factors influencing EFM signal intensity, width, shape, variation? What are the capabilities of EFM?

In order to investigate the physics of an EFM measurement, simulations over each specific type of complex material must be addressed, in addition to the calibration with test samples of known properties. Both theoretical studies and well-defined structured test samples will help understanding the operation and limitations of EFM. In this thesis, we have adopted these steps in order to investigate EFM capabilities to study interphases in nanodielectrics. Our results, presented and discussed later, are also applicable on heterogeneous multilayered nano-materials with similar configurations as nanodielectrics.

9. References

[1] G. Binnig, H. Rohrer, C. Gerber, and E. Weibel, "Surface Studies by Scanning Tunneling Microscopy," *Physical Review Letters,* vol. 49, pp. 57-61, 07/05/ 1982.

[2] G. Binnig, C. F. Quate, and C. Gerber, "Atomic Force Microscope," *Physical Review Letters,* vol. 56, pp. 930-933, 03/03/ 1986.

[3] G. Binnig, K. H. Frank, H. Fuchs, N. Garcia, B. Reihl, H. Rohrer*, et al.*, "Tunneling Spectroscopy and Inverse Photoemission: Image and Field States," *Physical Review Letters,* vol. 55, pp. 991-994, 08/26/ 1985.

[4] A. O. Rachel, "Advances in AFM for the electrical characterization of semiconductors," *Reports on Progress in Physics,* vol. 71, p. 076501, 2008.

[5] G. Gramse, "Dielectric constant of supported biomembranes measured in air and liquid environment," PhD, Universitat De Barcelona, Electronic departement, 2012.

[6] T. Hantschel, P. Niedermann, T. Trenkler, and W. Vandervorst, "Highly conductive diamond probes for scanning spreading resistance microscopy," *Applied Physics Letters,* vol. 76, pp. 1603-1605, 2000/03/20 2000.

[7] R. C. Barrett and C. F. Quate, "Charge storage in a nitride ‐ oxide ‐ silicon medium by scanning capacitance microscopy," *Journal of Applied Physics,* vol. 70, pp. 2725-2733, 1991/09/01 1991.

[8] G. Ferrari and M. Sampietro, "Wide bandwidth transimpedance amplifier for extremely high sensitivity continuous measurements," *Review of Scientific Instruments,* vol. 78, p. 094703, 2007/09/01 2007.

[9] L. Fumagalli, G. Ferrari, M. Sampietro, and G. Gomila, "Quantitative Nanoscale Dielectric Microscopy of Single-Layer Supported Biomembranes," *Nano Letters,* vol. 9, pp. 1604-1608, 2009/04/08 2009.

[10] K. Lai, M. B. Ji, N. Leindecker, M. A. Kelly, and Z. X. Shen, "Atomic-force-microscope-compatible near-field scanning microwave microscope with separated excitation and sensing probes," *Review of Scientific Instruments,* vol. 78, p. 063702, 2007/06/01 2007.

[11] Y. Martin, C. C. Williams, and H. K. Wickramasinghe, "Atomic force microscope–force mapping and profiling on a sub 100 ‐ Å scale," *Journal of Applied Physics,* vol. 61, pp. 4723-4729, 1987/05/15 1987.

[12] M. Nonnenmacher, M. P. O'Boyle, and H. K. Wickramasinghe, "Kelvin probe force microscopy," *Applied Physics Letters,* vol. 58, pp. 2921-2923, 1991/06/24 1991.

[13] J. Hu, X. D. Xiao, and M. Salmeron, "Scanning polarization force microscopy: A technique for imaging liquids and weakly adsorbed layers," *Applied Physics Letters,* vol. 67, pp. 476-478, 1995/07/24 1995.

[14] Y. Martin, D. W. Abraham, and H. K. Wickramasinghe, "High ‐ resolution capacitance measurement and potentiometry by force microscopy," *Applied Physics Letters,* vol. 52, pp. 1103-1105, 1988/03/28 1988.

[15] G. Binnig, G. Ch, E. Stoll, T. R. Albrecht, and C. F. Quate, "Atomic Resolution with Atomic Force Microscope," *EPL (Europhysics Letters),* vol. 3, p. 1281, 1987.

[16] T. R. Albrecht, S. Akamine, T. E. Carver, and C. F. Quate, "Microfabrication of cantilever styli for the atomic force microscope," *Journal of Vacuum Science & Technology A: Vacuum, Surfaces, and Films,* vol. 8, pp. 3386-3396, 1990/07/01 1990.

[17] O. Wolter, T. Bayer, and J. Greschner, "Micromachined silicon sensors for scanning force microscopy," *Journal of Vacuum Science & Technology B: Microelectronics and Nanometer Structures Processing, Measurement, and Phenomena,* vol. 9, pp. 1353-1357, 1991/03/01 1991.

[18] L. Fumagalli, M. A. Edwards, and G. Gomila, "Quantitative electrostatic force microscopy with sharp silicon tips," *Nanotechnology,* vol. 25, p. 495701, 2014.

[19] L. Nony, "Analyse de la microscopie de force dynamique : application à l'étude de l'A.D.N.," PhD, Université Bordeaux I, 2000.

[20] S. Yongho and J. Wonho, "Atomic force microscopy and spectroscopy," *Reports on Progress in Physics,* vol. 71, p. 016101, 2008.

[21] D. Sarid, *Scanning Force Microscopy with Applications to Electric, Magnetic and Atomic Forces* New York: OXFORD UNIVERSITY PRESS, 1994.

[22] Jennarocca. (2016, 9/18/2017). *Lennard Jones Potential Equation* [Free web image]. Available: http://www.cambridgemedchemconsulting.com/resources/molecular_interactions_files/ljp.png

[23] P. Girard and A. N. Titkov, "Electrostatic Force and Force Gradient Microscopy: Principles, Points of Interest and Application to Characterisation of Semiconductor Materials and Devices," in *Applied Scanning Probe Methods II: Scanning Probe Microscopy Techniques*, B. Bhushan and H. Fuchs, Eds., ed Berlin, Heidelberg: Springer Berlin Heidelberg, 2006, pp. 283-320.

[24] J. E. Sader, I. Larson, P. Mulvaney, and L. R. White, "Method for the calibration of atomic force microscope cantilevers," *Review of Scientific Instruments,* vol. 66, pp. 3789-3798, 1995/07/01 1995.

[25] J. E. Sader, J. W. M. Chon, and P. Mulvaney, "Calibration of rectangular atomic force microscope cantilevers," *Review of Scientific Instruments,* vol. 70, pp. 3967-3969, 1999/10/01 1999.

[26] M. A. Poggi, A. W. McFarland, J. S. Colton, and L. A. Bottomley, "A Method for Calculating the Spring Constant of Atomic Force Microscopy Cantilevers with a Nonrectangular Cross Section," *Analytical Chemistry,* vol. 77, pp. 1192-1195, 2005/02/01 2005.

[27] Q. Zhong, D. Inniss, K. Kjoller, and V. B. Elings, "Fractured polymer/silica fiber surface studied by tapping mode atomic force microscopy," *Surface Science,* vol. 290, pp. L688-L692, 1993/06/10/ 1993.

[28] R. García and R. Pérez, "Dynamic atomic force microscopy methods," *Surface Science Reports,* vol. 47, pp. 197-301, 2002/09/01/ 2002.

[29] D. K. Jha, *Text Book Of Simple Harmonic Motion And Wave Theory*: Discovery Publishing House Pvt. Limited, 2005.

[30] L. Portes, P. Girard, R. Arinero, and M. Ramonda, "Force gradient detection under vacuum on the basis of a double pass method," *Review of Scientific Instruments,* vol. 77, p. 096101, 2006/09/01 2006.

[31] M. W. Fairbairn, S. O. R. Moheimani, and A. J. Fleming, "Q Control of an Atomic Force Microscope Microcantilever: A Sensorless Approach," *Journal of Microelectromechanical Systems,* vol. 20, pp. 1372-1381, 2011.

[32] L. Portes, M. Ramonda, R. Arinero, and P. Girard, "New method for electrostatic force gradient microscopy observations and Kelvin measurements under vacuum," *Ultramicroscopy,* vol. 107, pp. 1027-1032, 2007/10/01/ 2007.

[33] C. Riedel, "Dielectric and Mechanical Properties of Polymers at Macro and Nanoscale " PhD, Université Montpellier 2, 2010.

[34] R. Dianoux, "Injection et détection de charges dans des nanostructures semiconductrices par Microscopie à Force Atomique," PhD, Université Joseph-Fourier - Grenoble I, 2004.

[35] R. R. A. Bugacov, C. Baur, N. Montoya, K. Woronowicz, A. Papson, B. E. Koel, A. A. G. Requicha and P. Will, "Measuring the tip-sample separation in dynamic force microscopy," *Probe Microscopy,* vol. 1, pp. 345-354, 1999.

[36] B. Bhushan and H. Fuchs, *Applied Scanning Probe Methods II-Scanning Probe Microscopy Techniques*. Germany: Springer, 2006.

[37] A. L. Tolstikhina, R. V. Gaĭnutdinov, M. L. Zanaveskin, K. L. Sorokina, N. V. Belugina, and Y. V. Grishchenko, "Particular artifacts of topographic images of dielectrics in atomic-force microscopy," *Crystallography Reports,* vol. 52, pp. 894-900, 2007/09/01 2007.

[38] C. Carlos A. R., L. Evandro M., P. Maria H. O., G. Fernando, and D. Christoph, "AFM topography artifacts resulting from electrostatic force," in *Technical memorandum*, ed, 2014.

[39] D. El Khoury, R. Arinero, J. C. Laurentie, and J. Castellon, "Nanoscale surface charge detection in epoxy resin materials using electrostatic force spectroscopy," *AIP Advances,* vol. 6, p. 035318, 2016/03/01 2016.

[40] F. A. Vick, "Theory of contact electrification," *British Journal of Applied Physics,* vol. 4, p. S1, 1953.

[41] C. Riedel, "Dielectric and mechanical properties of polymers and macro and nanoscale," Institut d'électronique et des systèmes, University of Montpellier, 2010.

[42] M. J. Cadena, S. H. Sung, B. W. Boudouris, R. Reifenberger, and A. Raman, "Nanoscale Mapping of Dielectric Properties of Nanomaterials from Kilohertz to Megahertz Using Ultrasmall Cantilevers," *ACS Nano,* vol. 10, pp. 4062-4071, 2016/04/26 2016.

[43] G. Gramse, I. Casuso, J. Toset, L. Fumagalli, and G. Gomila, "Quantitative dielectric constant measurement of thin films by DC electrostatic force microscopy," *Nanotechnology,* vol. 20, p. 395702, 2009.

[44] R. I. Revilla, X.-J. Li, Y.-L. Yang, and C. Wang, "Comparative Method To Quantify Dielectric Constant at Nanoscale Using Atomic Force Microscopy," *The Journal of Physical Chemistry C,* vol. 118, pp. 5556-5562, 2014/03/13 2014.

[45] G. Gramse, G. Gomila, and L. Fumagalli, "Quantifying the dielectric constant of thick insulators by electrostatic force microscopy: effects of the microscopic parts of the probe," *Nanotechnology,* vol. 23, p. 205703, 2012.

[46] L. Fumagalli, D. Esteban-Ferrer, A. Cuervo, J. L. Carrascosa, and G. Gomila, "Label-free identification of single dielectric nanoparticles and viruses with ultraweak polarization forces," *Nat Mater,* vol. 11, pp. 808-816, 2012.

[47] A. Dols-Perez, G. Gramse, A. Calo, G. Gomila, and L. Fumagalli, "Nanoscale electric polarizability of ultrathin biolayers on insulating substrates by electrostatic force microscopy," *Nanoscale,* vol. 7, pp. 18327-36, Nov 21 2015.

[48] G. Gramse, A. Dols-Perez, M. A. Edwards, L. Fumagalli, and G. Gomila, "Nanoscale Measurement of the Dielectric Constant of Supported Lipid Bilayers in Aqueous Solutions with Electrostatic Force Microscopy," *Biophysical Journal,* vol. 104, pp. 1257-1262, 2013/03/19/ 2013.

[49] D. Esteban-Ferrer, M. A. Edwards, L. Fumagalli, A. Juárez, and G. Gomila, "Electric Polarization Properties of Single Bacteria Measured with Electrostatic Force Microscopy," *ACS Nano,* vol. 8, pp. 9843-9849, 2014/10/28 2014.

[50] M. M. Kummali, L. A. Miccio, G. A. Schwartz, A. Alegría, J. Colmenero, J. Otegui*, et al.*, "Local mechanical and dielectric behavior of the interacting polymer layer in silica nano-particles filled SBR by means of AFM-based methods," *Polymer,* vol. 54, pp. 4980-4986, 2013/08/16/ 2013.

[51] A. Méndez-Vilas, M. L. González-Martín, and M. J. Nuevo, "Optical interference artifacts in contact atomic force microscopy images," *Ultramicroscopy,* vol. 92, pp. 243-250, 2002/08/01/ 2002.

[52] J. Deschler, J. Seiler, and J. Kindersberger, "Detection of charges at the interphase of polymeric nanocomposites," *IEEE Transactions on Dielectrics and Electrical Insulation,* vol. 24, pp. 1027-1037, 2017.

[53] NT-MDT. (26/7/2017). [Web page]. Available: https://www.ntmdt-si.com/spm-basics/view/effect-tip-radius-cone-angle

[54] E. Tevaarwerk, D. G. Keppel, P. Rugheimer, M. G. Lagally, and M. A. Eriksson, "Quantitative analysis of electric force microscopy: The role of sample geometry," *Review of Scientific Instruments,* vol. 76, p. 053707, 2005.

[55] S. Belaidi, F. Lebon, P. Girard, G. Leveque, and S. Pagano, "Finite element simulations of the resolution in electrostatic force microscopy," *Applied Physics A,* vol. 66, pp. S239-S243, March 01 1998.

[56] S. Gómez-Moñivas, L. S. Froufe, R. Carminati, J. J. Greffet, and J. J. Sáenz, "Tip-shape effects on electrostatic force microscopy resolution," *Nanotechnology,* vol. 12, p. 496, 2001.

[57] G. Lévêque, P. Cadet, and R. Arinero, "Sensitivity and resolution in noncontact electrostatic force microscopy in the case of a constant potential," *Physical Review B,* vol. 71, p. 205419, 05/27/ 2005.

[58] S. Belaidi, P. Girard, and G. Leveque, "Electrostatic forces acting on the tip in atomic force microscopy: Modelization and comparison with analytic expressions," *Journal of Applied Physics,* vol. 81, pp. 1023-1030, 1997/02/01 1997.

[59] J. Colchero, A. Gil, and A. M. Baró, "Resolution enhancement and improved data interpretation in electrostatic force microscopy," *Physical Review B,* vol. 64, p. 245403, 11/28/ 2001.

[60] C. Riedel, A. Alegría, G. A. Schwartz, R. Arinero, J. Colmenero, and J. J. Sáenz, "On the use of electrostatic force microscopy as a quantitative subsurface characterization technique: A numerical study," *Applied Physics Letters,* vol. 99, p. 023101, 2011/07/11 2011.

[61] S. B. Arnason, A. G. Rinzler, Q. Hudspeth, and A. F. Hebard, "Carbon nanotube-modified cantilevers for improved spatial resolution in electrostatic force microscopy," *Applied Physics Letters,* vol. 75, pp. 2842-2844, 1999.

[62] N. R. Wilson and J. V. Macpherson, "Enhanced resolution electric force microscopy with single-wall carbon nanotube tips," *Journal of Applied Physics,* vol. 96, pp. 3565-3567, 2004.

[63] F. Bocquet, L. Nony, C. Loppacher, and T. Glatzel, "Analytical approach to the local contact potential difference on (001) ionic surfaces: Implications for Kelvin probe force microscopy," *Physical Review B,* vol. 78, p. 035410, 07/07/ 2008.

[64] I. Alhossen, C. Villeneuve-Faure, F. Baudoin, F. Bugarin, and S. Segonds, "Sensitivity analysis of the electrostatic force distance curve using Sobol's method and design of experiments," *Journal of Physics D: Applied Physics,* vol. 50, p. 035304, 2017.

[65] U. Zerweck, L. Ch, T. Otto, S. Grafström, and L. M. Eng, "Kelvin probe force microscopy of C 60 on metal substrates: towards molecular resolution," *Nanotechnology,* vol. 18, p. 084006, 2007.

[66] S. Kawai, T. Glatzel, H. J. Hug, and E. Meyer, "Atomic contact potential variations of Si(111)-7 x 7 analyzed by Kelvin probe force microscopy," *Nanotechnology,* vol. 21, p. 245704, Jun 18 2010.

[67] T. Eguchi, Y. Fujikawa, K. Akiyama, T. An, M. Ono, T. Hashimoto*, et al.*, "Imaging of all Dangling Bonds and their Potential on the Surface by Noncontact Atomic Force Microscopy," *Physical Review Letters,* vol. 93, p. 266102, 12/20/ 2004.

[68] S. Sadewasser, P. Jelinek, C.-K. Fang, O. Custance, Y. Yamada, Y. Sugimoto*, et al.*, "New Insights on Atomic-Resolution Frequency-Modulation Kelvin-Probe Force-Microscopy Imaging of Semiconductors," *Physical Review Letters,* vol. 103, p. 266103, 12/28/ 2009.

[69] G. H. Enevoldsen, T. Glatzel, M. C. Christensen, J. V. Lauritsen, and F. Besenbacher, "Atomic Scale Kelvin Probe Force Microscopy Studies of the Surface Potential Variations on the TiO2 (110) Surface," *Physical Review Letters,* vol. 100, p. 236104, 06/13/ 2008.

[70] A. K. Sinensky and A. M. Belcher, "Label-free and high-resolution protein DNA nanoarray analysis using Kelvin probe force microscopy," *Nat Nano,* vol. 2, pp. 653-659, 2007.

[71] E. Palacios-Lidón, B. Pérez-García, and J. Colchero, "Enhancing dynamic scanning force microscopy in air: as close as possible," *Nanotechnology,* vol. 20, p. 085707, 2009.

[72] X. D. Ding, J. An, J. B. Xu, C. Li, and R. Y. Zeng, "Improving lateral resolution of electrostatic force microscopy by multifrequency method under ambient conditions," *Applied Physics Letters,* vol. 94, p. 223109, 2009.

[73] D. Liu, X. Ding, H. Xu, G. Lin, and D. Chen, "Improving lateral resolution of ambient electrostatic force microscopy by intermittent contact method," *Integrated Ferroelectrics,* vol. 169, pp. 96-106, 2016/02/12 2016.

[74] F. J. Giessibl, "Principle of NC-AFM," in *Noncontact Atomic Force Microscopy*, S. Morita, R. Wiesendanger, and E. Meyer, Eds., ed Berlin, Heidelberg: Springer Berlin Heidelberg, 2002, pp. 11-46.

[75] B. Pottier and L. Bellon, "“Noiseless” thermal noise measurement of atomic force microscopy cantilevers," *Applied Physics Letters,* vol. 110, p. 094105, 2017/02/27 2017.

[76] D. P. E. Smith, "Limits of force microscopy," *Review of Scientific Instruments,* vol. 66, pp. 3191-3195, 1995/05/01 1995.

[77] J. L. Hutter and J. Bechhoefer, "Calibration of atomic ‐ force microscope tips," *Review of Scientific Instruments,* vol. 64, pp. 1868-1873, 1993/07/01 1993.

[78] H. J. Butt and M. Jaschke, "Calculation of thermal noise in atomic force microscopy," *Nanotechnology,* vol. 6, p. 1, 1995.

[79] S. Rast, C. Wattinger, U. Gysin, and E. Meyer, "The noise of cantilevers," *Nanotechnology,* vol. 11, p. 169, 2000.

[80] S. A. Cantrell, J. H. Cantrell, and P. T. Lillehei, "Nanoscale subsurface imaging via resonant difference-frequency atomic force ultrasonic microscopy," *Journal of Applied Physics,* vol. 101, p. 114324, 2007/06/01 2007.

[81] A. Striegler, B. Koehler, B. Bendjus, M. Roellig, M. Kopycinska-Mueller, and N. Meyendorf, "Detection of buried reference structures by use of atomic force acoustic microscopy," *Ultramicroscopy,* vol. 111, pp. 1405-16, Jul 2011.

[82] Z. Parlak and F. Levent Degertekin, "Contact stiffness of finite size subsurface defects for atomic force microscopy: Three-dimensional finite element modeling and experimental verification," *Journal of Applied Physics,* vol. 103, p. 114910, 2008/06/01 2008.

[83] P. K. Jason, Y. K. Jennifer, M. S. Christopher, J. F. Michael, and C. H. Donna, "Quantitative subsurface contact resonance force microscopy of model polymer nanocomposites," *Nanotechnology,* vol. 22, p. 175706, 2011.

[84] E.-C. Spitzner, C. Riesch, and R. Magerle, "Subsurface Imaging of Soft Polymeric Materials with Nanoscale Resolution," *ACS Nano,* vol. 5, pp. 315-320, 2011/01/25 2011.

[85] D. Ebeling, B. Eslami, and S. D. J. Solares, "Visualizing the Subsurface of Soft Matter: Simultaneous Topographical Imaging, Depth Modulation, and Compositional Mapping with Triple Frequency Atomic Force Microscopy," *ACS Nano,* vol. 7, pp. 10387-10396, 2013/11/26 2013.

[86] K. Kimura, K. Kobayashi, K. Matsushige, and H. Yamada, "Imaging of Au nanoparticles deeply buried in polymer matrix by various atomic force microscopy techniques," *Ultramicroscopy,* vol. 133, pp. 41-9, Oct 2013.

[87] G. J. Verbiest, J. N. Simon, T. H. Oosterkamp, and M. J. Rost, "Subsurface atomic force microscopy: towards a quantitative understanding," *Nanotechnology,* vol. 23, p. 145704, 2012.

[88] H. J. Sharahi, G. Shekhawat, V. Dravid, S. Park, P. Egberts, and S. Kim, "Contrast mechanisms on nanoscale subsurface imaging in ultrasonic AFM: scattering of ultrasonic waves and contact stiffness of the tip-sample," *Nanoscale,* vol. 9, pp. 2330-2339, 2017.

[89] M. J. Cadena, Y. Chen, R. G. Reifenberger, and A. Raman, "Sub-surface AFM imaging using tip generated stress and electric fields," *Applied Physics Letters,* vol. 110, p. 123108, 2017/03/20 2017.

[90] J. J. Kopanski, L. You, J. Li, J. J. Ahn, and Y. S. Obeng, "(Invited) Characterization of Buried Interfaces with Scanning Probe Microscopes," *Meeting Abstracts,* vol. MA2016-01, p. 997, April 1, 2016 2016.

[91] Y. Lin, A. Jung-Joon, S. O. Yaw, and J. K. Joseph, "Subsurface imaging of metal lines embedded in a dielectric with a scanning microwave microscope," *Journal of Physics D: Applied Physics,* vol. 49, p. 045502, 2016.

[92] J. Rossignol, C. Plassard, E. Bourillot, O. Calonne, M. Foucault, and E. Lesniewska, "Non-destructive technique to detect local buried defects in metal sample by scanning microwave microscopy," *Sensors and Actuators A: Physical,* vol. 186, pp. 219-222, 2012/10/01/ 2012.

[93] G. Gramse, A. Kölker, T. Lim, T. J. Z. Stock, H. Solanki, S. R. Schofield*, et al.*, "Nondestructive imaging of atomically thin nanostructures buried in silicon," *Science Advances,* vol. 3, 2017.

[94] H. T. Thompson, F. Barroso-Bujans, J. G. Herrero, R. Reifenberger, and A. Raman, "Subsurface imaging of carbon nanotube networks in polymers with DC-biased multifrequency dynamic atomic force microscopy," *Nanotechnology,* vol. 24, p. 135701, Apr 05 2013.

[95] M. J. Cadena, R. Misiego, K. C. Smith, A. Avila, B. Pipes, R. Reifenberger*, et al.*, "Sub-surface imaging of carbon nanotube-polymer composites using dynamic AFM methods," *Nanotechnology,* vol. 24, p. 135706, Apr 5 2013.

[96] M. J. Cadena, S. H. Sung, B. W. Boudouris, R. Reifenberger, and A. Raman, "Nanoscale Mapping of Dielectric Properties of Nanomaterials from Kilohertz to Megahertz Using Ultrasmall Cantilevers," *ACS Nano,* vol. 10, pp. 4062-71, Apr 26 2016.

[97] O. A. Castañeda-Uribe, R. Reifenberger, A. Raman, and A. Avila, "Depth-Sensitive Subsurface Imaging of Polymer Nanocomposites Using Second Harmonic Kelvin Probe Force Microscopy," *ACS Nano,* vol. 9, pp. 2938-2947, 2015/03/24 2015.

[98] T. S. Jespersen and J. Nygård, "Mapping of individual carbon nanotubes in polymer/nanotube composites using electrostatic force microscopy," *Applied Physics Letters,* vol. 90, p. 183108, 2007.

[99] M. C. Biagi, R. Fabregas, G. Gramse, M. Van Der Hofstadt, A. Juárez, F. Kienberger*, et al.*, "Nanoscale Electric Permittivity of Single Bacterial Cells at Gigahertz Frequencies by Scanning Microwave Microscopy," *ACS Nano,* vol. 10, pp. 280-288, 2016/01/26 2016.

[100] J. Seiler and J. Kindersberger, "Insight into the interphase in polymer nanocomposites," *IEEE Transactions on Dielectrics and Electrical Insulation,* vol. 21, pp. 537-547, 2014.

[101] L. C. Sawyer, D. T. Grubb, and G. F. Meyers, *Polymer microscopy*. New York: Sringer, 2008.

[102] S. Raetzke and J. Kindersberger, "Role of interphase on the resistance to high-voltage arcing, on tracking and erosion of silicone/SiO2 nanocomposites," *IEEE Transactions on Dielectrics and Electrical Insulation,* vol. 17, pp. 607-614, 2010.

[103] R. Borgani, D. Forchheimer, J. Bergqvist, P.-A. Thorén, O. Inganäs, and D. B. Haviland, "Intermodulation electrostatic force microscopy for imaging surface photo-voltage," *Applied Physics Letters,* vol. 105, p. 143113, 2014/10/06 2014.

[104] R. Borgani, L. K. H. Pallon, M. S. Hedenqvist, U. W. Gedde, and D. B. Haviland, "Local Charge Injection and Extraction on Surface-Modified Al2O3 Nanoparticles in LDPE," *Nano Letters,* vol. 16, pp. 5934-5937, 2016/09/14 2016.

[105] S. Peng, Q. Zeng, X. Yang, J. Hu, X. Qiu, and J. He, "Local Dielectric Property Detection of the Interface between Nanoparticle and Polymer in Nanocomposite Dielectrics," *Sci Rep,* vol. 6, p. 38978, Dec 13 2016.

Chapter III

Theoretical and modeling approach

Chapter III

"Beware of false knowledge; it is more dangerous than ignorance."
George Bernard Shaw

1. Introduction

This chapter aims at discussing the interaction between an EFM probe and different types of dielectric samples, to be finally applied to the specific case of a nanodielectric material. For each class of sample geometry and composition, we start by presenting the corresponding state of the art associated to our own numerical simulations performed with Comsol® Multiphysics software. The model adopted in the thesis for a nanodielectric within the frame of an EFM measurement is first presented, followed by a detailed description of our numerical model. Then, the influence on the signal of the probe geometry and scanning parameters without a dielectric sample is reviewed and simulated. Afterwards, we investigate the effect of several sample configurations whose constitution represents potentially that of existent materials in nanoscience. Later, in the section of tip-nanodielectric interaction modeling, an existing analytical model that assumes no restrictions of EFM spatial resolution is firstly adapted to our system. Secondly, this interaction is modeled in a more realistic way through numerical simulations, so we try to understand how to attest the presence of the interphase with EFM and discuss the benefits and limitations of this technique.

2. Tip-sample interaction: numerical modeling description

The interpretation and quantification of the interaction between an EFM probe and a sample has been the subject of several research works since the first implementation of EFM [1]. The accurate analysis of the microscope electrical signals is not obvious since electrostatic signals are long range forces, not always confined to the supposed-to-be probed region. EFM response strongly depends on the shape and dimensions of the probe and the sample, as well as the intrinsic properties of the sample. The probe geometry is complex and specimen dimensions can vary from few nanometers up to hundreds of micrometers, and can sometimes contain differently shaped heterogeneities of various electrical nature. Therefore, one must resort to adequate models in order to explain EFM results.

Since a few decades, many models have been proposed. Those models covered principally the EFM tip interaction with the metal electrode, with a planar homogeneous thin and thick dielectric film and with punctual charges. However, we can rarely find appropriate models for more complicated samples such as superposed dielectric materials, nanoparticles… and to our knowledge, no detailed simulations for EFM signal above a nanodielectric material presenting an interphase.

Hereafter, the adopted model of a nanodielectric material and the numerical model definition are presented.

2.1. Adopted electrostatic model of a nanodielectric

In the first chapter, we saw that in the literature the composition dependence of the real dielectric permittivity of nanodielectrics has revealed at low nanofiller concentrations lower values than filler as well as matrix permittivities [2-4]. This macroscopic behavior has been explained by the need to reconsider the presence of the interphase, occupying a considerable volume in nanocomposites and exhibiting a dielectric permittivity lower than both filler and matrix. Moreover, it has been indicated that water absorption at the interfacial particle-matrix region is commonly reported [5, 6]. Water molecules within the interphase rise its effective dielectric constant showing the possibility of obtaining a high interphase permittivity. Moreover, concerning interphase thickness, the latter has been reported to vary from few nanometers [7, 8], up to 200 nm [9].

In our work, we are mainly interested in the characterization of the interphase with EFM. The latter is an electrostatic force detector, which depends on the first or second derivative (with respect to the distance) of the probe-sample capacitance. Consequently, EFM signal is altered by sample dimensions and dielectric permittivity.

Accordingly, we model a nanodielectric as an association of three dielectric materials distinguished and characterized by their dielectric permittivity, geometry and dimensions. The first one is the nanoparticle with a spherical shape; the second one is the interphase surrounding the particle and the third one is the matrix containing both, the particle and the interphase. In Fig. III - 1, a transverse sketch of one studied region of the nanodielectric model is presented, where ε_p, ε_i and ε_m are the relative dielectric constants of the particle, interphase and matrix, respectively. r_p, t_i and h are respectively the particle radius, interphase thickness and matrix height. The particle is buried at a certain depth d, from the matrix upper and lower surfaces.

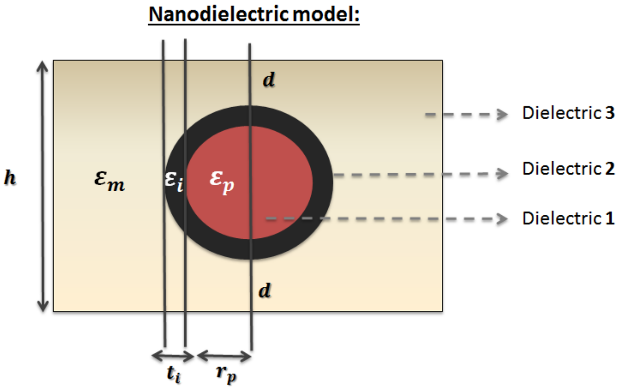

Fig. III - 1 : Adopted model of a nanodielectric measured with an electrostatic force microscope: particle-shell-matrix association represented as three dielectric materials distinguished by their dielectric constants, geometries, dimensions and disposition.

2.2. EFM probe model

As it has been shown in the above paragraph, our sample geometry and structure are relatively complicated. To date, no analytical model can describe the interaction between an EFM tip and a similar type of material. In the next sections, the present analytical models will be reviewed in details and their limits analyzed. Moreover, not all numerical methods can be adapted to simulate our system [10]. One appropriate numerical solution is the finite-element method to simulate EFM signals accounting for the exact geometry of the tip and the sample. In this thesis, Comsol® Multiphysics software has been used to study the interaction between an AFM conductive probe and different types of dielectric samples.

The interacting system is mainly composed by the force detector represented by the EFM probe, and the sample which is placed on a conductive planar counter-electrode. In the present chapter, we modeled the tip according to the geometry of standard EFM tips, namely, as a solid truncated cone of height H = 10 µm and half-angle θ = 10 ° with a spherical apex at its end, of radius R_0 = 25 nm [11]. Within our modeling conditions, the truncated cone-plane geometry includes all the components of the probe that effectively contribute to the electrostatic interaction with the sample. In fact, this geometry has proved accurate quantification of the dielectric constant of both ultrathin (< 10 - 50 nm) [12-14] and intermediate thick dielectric films (< 10 µm) [15], corresponding to the range of thicknesses studied in the thesis (≤ 1 µm). We placed the tip at a commonly used EFM working distance z = 20 nm from the top of the sample, which is deposited on a metallic substrate. Note that our experimental EFM measurements have been performed in the force gradient detection mode, which further localizes the interaction to the nanometric parts of the probe [16, 17]. A more detailed explanation of the localization of the electrostatic force interaction and probe modeling range of validity will be explained in more details in the following sections.

The substrate was modeled as a disk of 20 µm diameter, which allows taking into account finite-size lateral effects. In fact, as discussed in ref [18], for a tip of 10 µm cone height and samples of 1 µm maximum thickness, 20 µm disk is sufficient to neglect substrate borders effects (see figure 3 (b) of ref [18]).

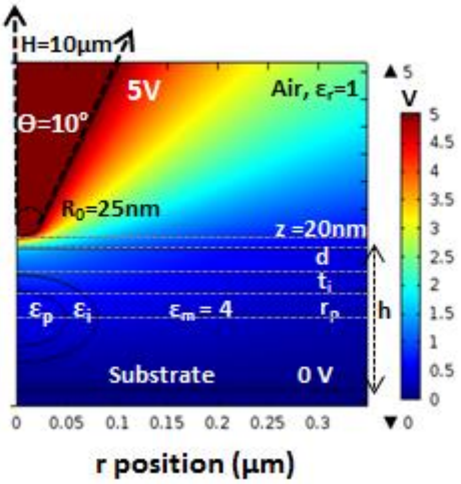

Fig. III - 2 : Electric potential map resulting from the EFM modeled tip during simulations above a model nanodielectric.

We modeled the air in the EFM enclosure as an empty space of relative permittivity $\varepsilon_r = 1$. For 2D axisymmetric calculations, spherical geometry coordinates and a spherical shape for the simulation box were chosen. The box was divided into two spherical regions to model the infinite extension of the space surrounding the probe-sample system: the inner region of 30 µm radius and the outer one of 32 µm radius. We applied the built-in infinite elements transformations to the outer region in order to avoid box geometry and dimensions influence. An automated extremely fine physics-controlled meshing was used to the whole simulation box. Meshing domains have the form of free triangles in 2D (and free tetrahedrals in 3D), with a minimum size of 1.28 nm and maximum size of 640 nm. We verified that, within these conditions of simulation box extension and resulting mesh size and form, our results are sufficiently correct (< 5 % variation with larger boxes and/or smaller mesh size). For 2D calculations, keeping the same model dimensions, square boxes were defined for computation region and cylindrical coordinates were used. Infinite elements transformations were not applied for 2D simulations. However, the negligible influence of border effects was also verified (< 10 % variation with larger boxes).

2.3. AC-DC electrostatics physics interface

The problem consists in determining the electrostatic interaction between the EFM sensor and the metallic substrate, with or without the presence of a specific dielectric sample. During conventional EFM measurements, electrostatic force detection, and/or force gradient detection can be analyzed. In this chapter, we calculated the electrostatic force as a basic theoretical study of EFM signals. Moreover, the used software provides direct force measurements; whereas, to study the force gradient, we have adopted an additional procedure, detailed in the Chapter V of the thesis.

2.3.1. Domain equations

To model the force acting on an EFM probe, the AC-DC module (Electrostatics physics interface) of Comsol® Multiphysics software was used. This finite-element method based software solves the Poisson's equation for the tip-sample system (III.1), maps the electrostatic potential *V* (*r*, z) distribution, and then calculates the Maxwell stress tensor (III.2). The integration of the Maxwell stress tensor around the tip surface gives the resulting electrostatic force at each position of the scan-line (III.3). To shift from 2D calculations to 3D ones, the system includes the perimeter *2πx* factor in (III.3) where *r* is the distance from the 2D probe surface to the axis of symmetry.

The domain equations used in the Electrostatics-Physics interface are detailed in the following:

The electric scalar potential, *V*, satisfies the space charge free Poisson's equation (Laplace equation):

$$\boldsymbol{\nabla} D = \mathbf{0} \tag{III.1}$$

where $\boldsymbol{D} = \varepsilon_0\varepsilon_r\boldsymbol{E}$, is the electric displacement vector and $\boldsymbol{E} = -\boldsymbol{\nabla} V$, is the electric field vector (see Chapter 1). We remind that bold symbols represent vector quantities.

The Maxwell stress tensor T_M appropriate to our problem is expressed by**:**

$$T_M = -\frac{1}{2}\varepsilon_0 E^2 \tag{III.2}$$

The resulting electrostatic force ***F*** reads:

$$\boldsymbol{F} = 2\pi r \int T\boldsymbol{n}dS \tag{III.3}$$

2.3.2. Boundary conditions

As introduced in Chapter I, the continuity conditions at the sample material interfaces (material 1: $\boldsymbol{D}_1$ - material 2: $\boldsymbol{D}_2$) and interior simulation box boundaries can be expressed by:

$$\boldsymbol{n}.\boldsymbol{D_1} = \boldsymbol{n}\,.\boldsymbol{D_2} \tag{III.4}$$

The space charge density in the system has been considered to be negligible, which explains the zero in the right hand side of eq (III.1).

System external boundaries, applied on external box edges, have been set to insulators by:

$$\boldsymbol{n}.\boldsymbol{D} = 0 \tag{III.5}$$

Note that these conditions are ensured by the natural boundary conditions of the program.

When measuring the force at the top of particle-interphase assembly, our system is axisymmetric. We calculated then the system in 2D axisymmetric dimensions, which is faster and more accurate than 3D calculations that are performed within a reasonable time of computation. Moreover, when the tip is placed over the matrix alone, relatively far from the particle as well as film boundaries, we verified that the tip is not influenced by the particle. The system is thus similar to an EFM tip over the matrix without the inclusion. In this case, our measurements have been performed in axisymmetric dimensions as well. However, for the calculations of the force on a scan line, 2D geometry was used.

The probe was biased, whereas the substrate was grounded. We fixed the potential to 5 V and 0 V respectively on the tip and the substrate boundaries for 2D axisymmetric calculations, and on their surface for 2D ones.

Since during EFM experiments the probe is only driven to oscillate in the z direction, the *z* component of the electrostatic force *F* has been studied, similarly to previous EFM models [19].

Although an eventual Guy-Chapman layer might be present on material interfaces, and thereby in the interphase, we did not consider it during our simulations. In fact, a region with free charges presents a conductive behavior, which can be seen with EFM as a region of higher dielectric constant [20]. Moreover, as described in Chapter II, if AC-EFM measurements are used, the detection of the 2ω component allows the unique sensitivity to the intrinsic capacitance of the system without the influence of surface space charges. For a study focusing on the distinction of materials through their intrinsic dielectric constant, our hypothesis of zero space charge can be considered sufficiently valid.

In the following paragraphs, a detailed state of the art of the models used in literature to understand the interaction between an EFM probe and different types of samples will be discussed. In parallel, the results of our simulations will be presented, extending past models and studying missing sample configurations of the literature. Afterwards, the results for the specific case of EFM tip interacting with a nanodielectric material will be reported.

3. Tip-Metallic substrate

3.1. State of the art

The electrostatic force acting on an AFM conductive probe above a bare metallic substrate has been widely studied in the past. Many methods, mainly divided into sets of analytical and numerical models, have been established.

Concerning analytical models, the earliest model goes to Y. Martin *et al.* with their first paper on the possibility of electrostatic force measurements with AFM [1]. Authors assumed a geometrical approximation to the probe considering it as a plane electrode, and the system as a plane-plane capacitor. Hence, approximating the capacitance of the system, a theoretical estimation of the force has been derived. Similarly, other approximations followed such as the sphere-plane models whose expressions depend on the separation distance range (table Fig. III - 3). Another analytical model is the conical-sphere ended tip-plane where authors added the contribution from the cone [21]. The latter has been expected to play an important role at larger distances than those considered in the sphere-plane models. H. W. Hao *et al*. derived the expression for the total interaction force by replacing the equipotential lines around the tip, with their equivalent image charges. At small angles, authors replaced the cone by a line of charge and the apex of the tip by an extra charge at the end of the line.

In the Knife-edge model, the tip geometry has been considered as an infinite plane in the z axis with a similar width to that of the counter-electrode [22]. The resulting expression of the force does not include the value of the width due to the translation symmetry of the problem.

Later, an exact three dimensional solution for the potential between two hyperboloid electrodes surfaces in the presence of a free charge has been derived [23]. Authors modeled the system in the prolate-spheroidal coordinates to extract the corresponding electric field. The force could be obtained by the integration of the electrostatic pressure exerted on the plane facing the tip. The interaction force has also been calculated as the one derived from a single point charge that produces equipotential lines similar to those produced by a sphere electrode [24]. This model is valid when the distance between the single charge and the sample surface is much larger than the radius of the sphere. Nevertheless, the hyperboloid model can be also verified for lower distances if the equivalent charge is placed at an appropriate separation to result in a curvature of the first equipotential line, touching the surface.

Afterwards, S. Hudlet *et al.* modeled the electric field between an axially symmetric concave tip and a plane electrode [19]. The tip surface was approximated by a superposition of infinitesimal surfaces obtained by faceting. The electric field between each part and the plane electrode was approximated to the one obtained for a dihedral capacitor with the same relative orientation between its facets to that of between the tip and the sample. The infinitesimal surface charge density was thus obtained, from which the capacitance was then calculated since the tip and the electrode are in close influence. The total force could thereby be derived. Although the approximation for the electric field source is significant, this model revealed little errors compared to previous ones. The main advantage of S. Hudlet *et al.* model is its possible application for any working distance with an axisymmetric tip. A brief summary of the analytical expressions of described models is presented in Fig. III - 3.

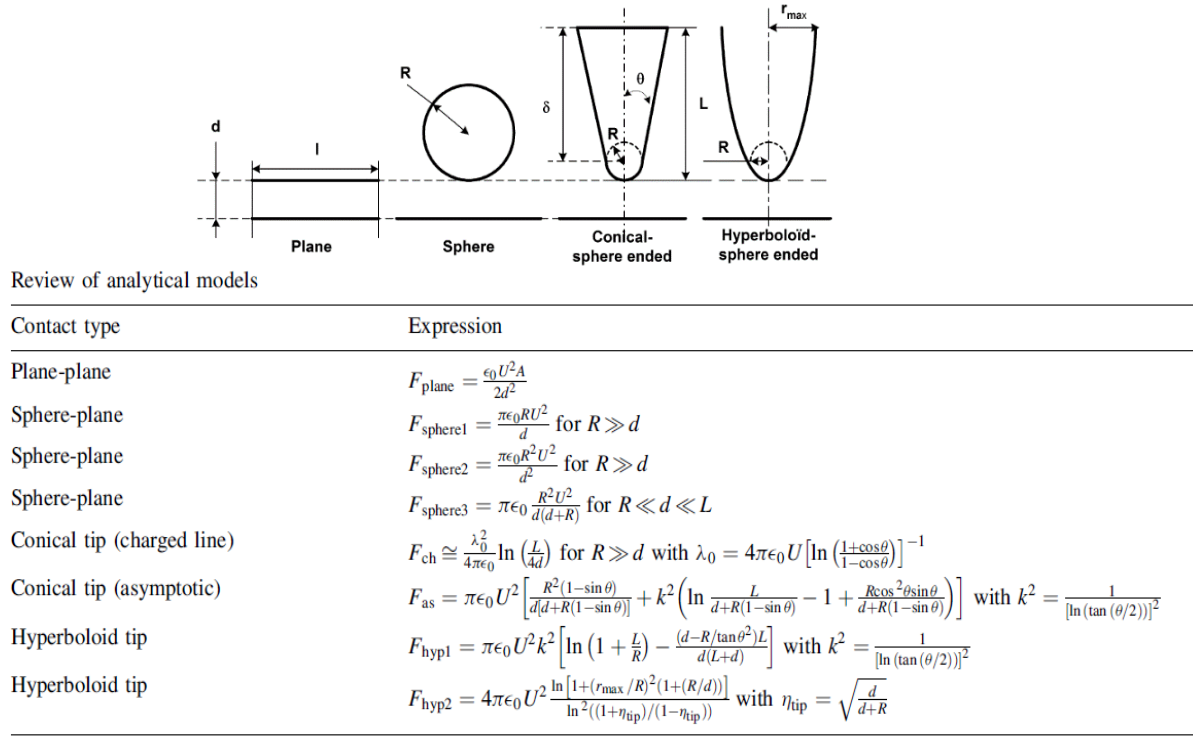

Review of analytical models

Contact type	Expression
Plane-plane	$F_{\text{plane}} = \frac{\epsilon_0 U^2 A}{2d^2}$
Sphere-plane	$F_{\text{sphere1}} = \frac{\pi\epsilon_0 R U^2}{d}$ for $R \gg d$
Sphere-plane	$F_{\text{sphere2}} = \frac{\pi\epsilon_0 R^2 U^2}{d^2}$ for $R \gg d$
Sphere-plane	$F_{\text{sphere3}} = \pi\epsilon_0 \frac{R^2 U^2}{d(d+R)}$ for $R \ll d \ll L$
Conical tip (charged line)	$F_{\text{ch}} \cong \frac{\lambda_0^2}{4\pi\epsilon_0} \ln\left(\frac{L}{4d}\right)$ for $R \gg d$ with $\lambda_0 = 4\pi\epsilon_0 U \left[\ln\left(\frac{1+\cos\theta}{1-\cos\theta}\right)\right]^{-1}$
Conical tip (asymptotic)	$F_{\text{as}} = \pi\epsilon_0 U^2 \left[\frac{R^2(1-\sin\theta)}{d[d+R(1-\sin\theta)]} + k^2\left(\ln\frac{L}{d+R(1-\sin\theta)} - 1 + \frac{R\cos^2\theta\sin\theta}{d+R(1-\sin\theta)}\right)\right]$ with $k^2 = \frac{1}{[\ln(\tan(\theta/2))]^2}$
Hyperboloid tip	$F_{\text{hyp1}} = \pi\epsilon_0 U^2 k^2 \left[\ln\left(1+\frac{L}{R}\right) - \frac{(d-R/\tan\theta^2)L}{d(L+d)}\right]$ with $k^2 = \frac{1}{[\ln(\tan(\theta/2))]^2}$
Hyperboloid tip	$F_{\text{hyp2}} = 4\pi\epsilon_0 U^2 \frac{\ln\left[1+(r_{\max}/R)^2(1+(R/d))\right]}{\ln^2((1+\eta_{\text{tip}})/(1-\eta_{\text{tip}}))}$ with $\eta_{\text{tip}} = \sqrt{\frac{d}{d+R}}$

Fig. III - 3 : Representation of usual geometries for the EFM tip with a review on analytical models expressions [25].

Another set of models can be mentioned which are based on the Image Method (IM) [26]. In ref [27], authors called this method the Image Charge Method (ICM) that has been extended later to the Generalized Image Charge Method (GICM) [10], and finally known as the Equivalent Charge Method (ECM) [28-30]. This set of numerical models is based on replacing the electrodes (surface charge density) and the sample, by a series of punctual charges and/or linear charges as “image” charges, in the tip. The latter are adjusted in order to recreate the desired potential at the surface boundaries that restores the same shape of the tip. S. Belaidi *et al.* used ECM to verify the validity of several analytical models, derived the constants in the models, suggested some empirical laws of different range of validity, and extended the simulations for the study of EFM tip interaction with the presence of surface charges and potential steps [28]. Later, the self-consistent method incorporated the technique of Green’s function and ICM in order to evaluate the interaction with the tip at different *z* distance, cubic sample size, permittivity etc [31].

Recently, finite-difference methods [32] and finite-element methods [12, 18, 33] have been extensively used to model EFM probe-sample interaction. The main advantage of these models is their ability to take into account the exact geometries of the probe and the sample. However, this type of numerical modeling still requires high computation capabilities due to the large dimension differences between the probe parts and the sample, from micrometric to nanometric ones. This explains the reason why authors usually keep on performing some approximations of the system symmetry and probe geometry during such simulations.

3.2. Modeling results

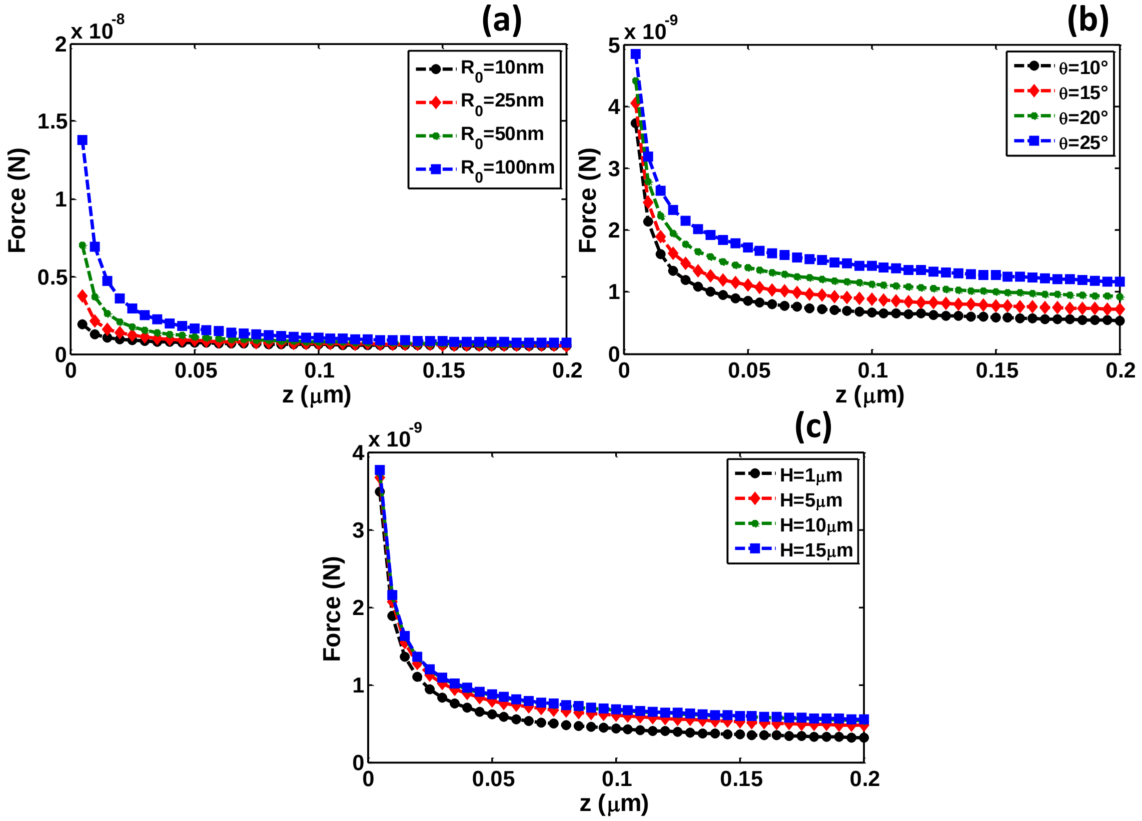

Fig. III - 4 : 2D-axisymmetric electrostatic force vs. tip-sample distance for, a. different tip radii with a cone height *H* = 10 µm, b. different cone half-angles with *H* = 10 µm and R_0 = 25 nm, c. different cone heights with a tip radius R_0 = 25nm.

The first step to understand the interaction with an EFM tip is to study the effect of probe geometry without a sample. In order to verify the validity of our model with previous literature results, we present in Fig. III - 4 the electrostatic force between an EFM tip and a bare metallic substrate versus tip-sample distance *z* for various tip apex radii (a), cone half-angle (b) and cone height (c). As expected, we find that the force is a decreasing function of the distance that tends to saturate at large *z*. Moreover, a larger tip radius, cone half-angle or cone height, enhances the signal. This is explained by the larger interaction surface obtained with bigger tips. Furthermore, we investigate the effect of tip parameters on the sensitivity to *z* [1]. When the radius of the tip-apex is doubled, changing from 25 nm to 50 nm, the difference between the force obtained at a tip-sample distance of 5 nm and the one obtained at 200 nm, increases from 3.19 nN to 6.42nN, respectively. Similarly, when the tip cone half-angle varies from 10 ° to 20 °, the difference between the force obtained at 5 nm and the one obtained at 200 nm, rises from 3.19 nN to 3.49 nN, respectively. However, an enlargement of cone height from 1 µm to 5 µm induces force differences from 3.18 nN to 3.2 nN. Hence, a 100 % increase of tip radius modifies the sensitivity to *z* by almost the same amount, and a 100% increase of cone half-angle changes the sensitivity by 9 %. However, 10 times taller tips do not modify the sensitivity by more than 0.6 %. This shows the sensitivity level in this range of distances to the tip apex, in terms of tip radius and cone opening. Taking into account these simulations, in this range of parameters, a fixed cone height to 10 µm is justified.

4. Tip-Dielectric sample

4.1. One homogeneous film

4.1.1. State of the art

In the above section, we reviewed and evaluated the effect of the distance between the EFM probe and the metallic substrate for various tip dimensions. Since no dielectric layer is present, tip-sample distance is equivalent to the tip and counter-electrode separation, simplifying the problem. However, when a dielectric film is present, the origin of the interaction becomes a little more complex. Nevertheless, EFM tip-dielectric film interaction has also been studied in literature. A precise modeling of this interaction is essential in order to quantify the dielectric permittivity and the thickness of the film.

Using nanoscale capacitance microscopy (NCM) [34], I. Casuso *et al.* measured electrically the thickness of a 5 nm biological layer (purple membranes) [35]. The quantification of the thickness has been estimated using the expression of the electrostatic force derived by G. M. Sacha *et al.*, to get the capacitance gradient of the tip in close proximity to a thin dielectric layer [10]. The obtained expression only takes into account the tip apex contribution (eq. (III.6). At relatively small distances, the electrostatic interaction over thin films has been reported to be concentrated on the tip apex.

$$C_{apex}'(z) = \frac{2\pi\varepsilon_0 {R_0}^2(1-\sin\theta)}{(z+\frac{h}{\varepsilon_r})(z+\frac{h}{\varepsilon_r}+R_0\sin\theta)} \tag{III.6}$$

L. Fumagalli *et al.* used this analytical expression (eq (III.6)) combined to NCM measurements to extract the permittivity of thin SiO_2 patches [14].

Subsequently, G. Gomila *et al.* reported a theoretical assessment of the origin and range of applicability of eq (III.6) [12]. After confronting the analytical model to numerical simulations, they found that this expression relevantly expresses the interaction with a thin sample (< 100 nm) of relative dielectric permittivity below 100, an apex radius between 30 and 200 nm, a cone half-angle between 10 ° and 45 ° and a tip-sample distance z range going from contact to 100 nm.

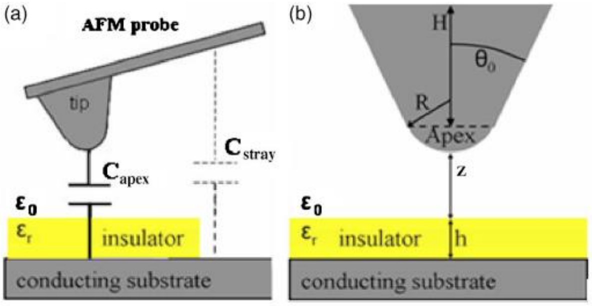

Fig. III - 5 : Schematic representation of: a. nanoscale capacitance measurement and b. the tip-sample system as modeled in the numerical calculations [12].

Later in ref [18], G. Gomila *et al.* extended their analytical model for ultrathin-films (< 20 – 50 nm) to a broader range of applicability by adding to eq (III.6) the contribution of the cone. The latter cannot be neglected for $R_0 < 50$ nm, and $z + h/\varepsilon_r < 100$ nm. Hence, generalizing the expressions for probe-metal interaction [19], authors derived the expression for tip-cone capacitance gradient:

$$C_{cone}'(z) = \frac{2\pi\varepsilon_0}{\ln(\tan\frac{\theta}{2})^2} \times \left[ln\left(\frac{H}{z+\frac{h}{\varepsilon_r}}\right) - 1 + \frac{R_0 \, cos^2\theta \, / \sin\theta}{z + \frac{h}{\varepsilon_r} + R_0(1-\sin\theta)} \right] \tag{III.7}$$

The total capacitance gradient becomes equal to the sum of both apex and cone contributions:

$$C' = C'_{apex} + C'_{cone} \tag{III.8}$$

Earlier in ref [10], Sacha *et al.* compared the force acting on an EFM probe in the presence of a thin film ($h \approx 0.5\ R_0$) calculated with GICM, to that derived from the generalization of the force for tip-metallic substrate introduced by S. Hudlet *et al.* [19]. A good agreement between the analytical model and GICM forces was obtained. In other works [30, 36], C. Riedel *et al.* quantified the dielectric constant of unmixable polymer blend of polyvinyl acetate particles in a polystyrene matrix. The authors performed experimental measurements with DC-force gradient detection in lift-mode. The obtained results were correlated to an ECM model for a truncated cone tip facing a dielectric film in order to extract the best fit for polymers permittivity.

Thus, we remark that thin films dielectric characterization has been commonly demonstrated assisted by analytical models, as well as numerical simulations, within an appropriate range of measurement setup and parameters. However, quantitative measurements of thick films have been much less reported. For thick films, quantifying the dielectric permittivity becomes more difficult since the signal-to-noise ratio decreases and the micrometric parts of the tip actively influence the electrostatic interaction [37]. A precise modeling of the probe has to be done.

In ref [15], L. Fumagalli *et al.* performed AC force measurements ($F_{2\omega}$) correlated to numerical simulations in order to extract the dielectric constant of thick polymer films. The tip was modeled as a solid truncated cone with a spherical apex. The geometry was introduced with caution, using SEM results for cone height, and approach curves fit with simulations to calibrate tip radius and cone half-angle. Moreover, beyond 100 µm thick films, the signal loses sensitivity to film thickness, which was deduced to simplify the simulations for the extraction of thick films permittivity.

Later, G. Gramse *et al.* discussed the influence of the specific geometry of the probe on the signal over thick films [37]. They introduced the cantilever contribution by a disk at the top of the cone as presented in Fig. III - 6. The disk contribution decreases when increasing cone height. However, in all cases, the effective radius of the cantilever disk was found to be much smaller than the effective physical cantilever width. Moreover, authors showed the possibility of dielectric permittivity measurement of any thick film without the knowledge of the microscopic tip dimensions if a preliminary calibration step is performed on a reference material of known permittivity.

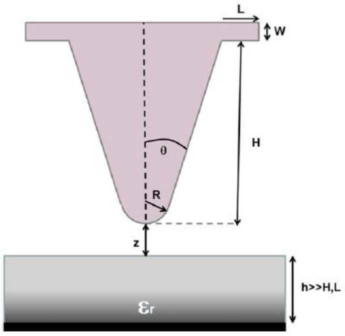

Fig. III - 6 : **Schematic representation of 2D dimensional finite-element numerical modeling of the probe-thick insulator system [37]. Cantilever effects are presented by a disk over the cone.**

Recently, L. A. Miccio *et al*. considered all the parts of the probe in the total force during nanodielectric spectroscopy measurements for thin and thick films [38]. The effective capacitance between the probe and the lower electrode was defined by the addition of the cantilever, cone and apex capacitances (Fig. III - 7). The electrical interaction between the electrodes was modeled by using the equivalent circuit shown in Fig. III - 7, where capacitors 1 and 2 represent the cantilever-air and cantilever-polymer systems; capacitors 3 and 4 for the cone-air and cone-polymer systems; and capacitor 5 for the apex-polymer system. The corresponding analytical expressions can be found in the main publication [38].

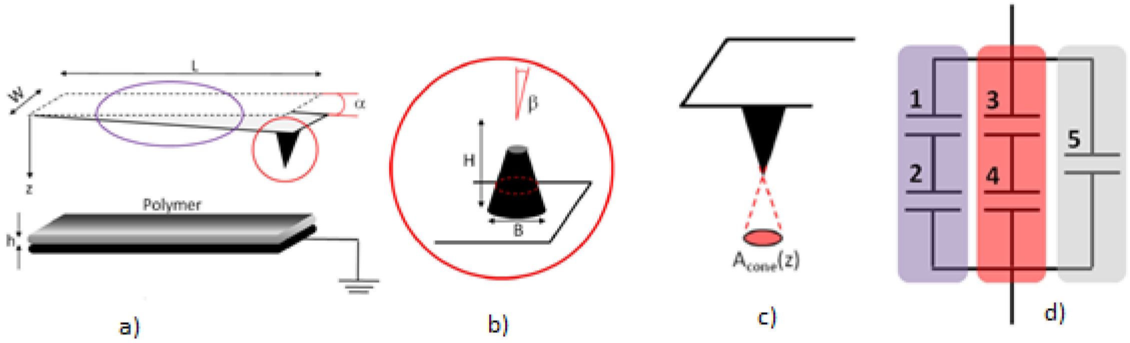

Fig. III - 7 : Geometry of the cantilever-cone-apex/sample system for AFM based dielectric spectroscopy: a. general scheme; b. zoom of the cone; c. projected cone area and d. equivalent circuit model in nanodielectric spectroscopy [38].

4.1.2. Modeling results

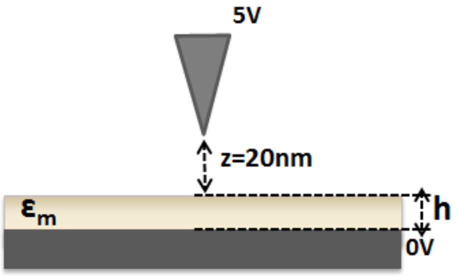

Fig. III - 8 : Sketch of EFM modeled tip facing a homogeneous dielectric film. Note that all thesis descriptive sketches are not to scale.

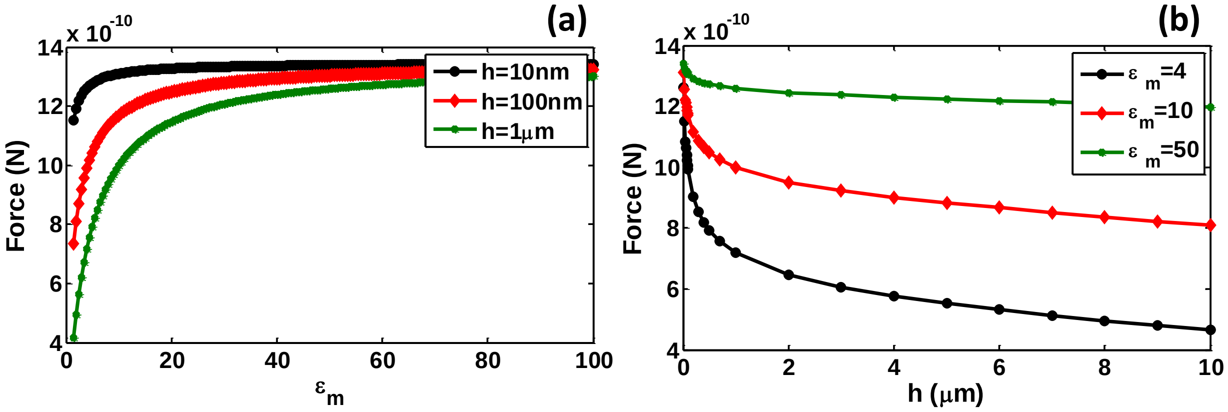

Fig. III - 9 : Electrostatic force acting on the tip in the z direction, over a homogeneous dielectric film, a. vs. film dielectric permittivity for three different thicknesses, b. vs. film thickness for 3 different permittivities.

Now, the addition of a homogeneous thin dielectric film on the metallic substrate is considered in our simulations as shown in Fig. III - 8. The curves of Fig. III - 9a. present the calculated variation of the electrostatic force with the permittivity of the film for three thicknesses: 10 nm, 100 nm and 1 µm. The capacitive force increases with the dielectric permittivity of the homogeneous film [14, 30, 33]. The slope of the curve becomes steeper, and hence, the sensitivity to the dielectric constant decreases at high permittivities and at low film thicknesses. Similarly, we study in Fig. III - 9b., the variation of the force with the film thickness for three dielectric constants: 4, 10 and 50. The interaction is found to decrease with the film thickness, and the variation becomes less pronounced at high thicknesses [15, 37]. Lower dielectric permittivity films decrease the slope of the curve and consequently, enhance the sensitivity to the film thickness.

From these results, we can deduce that depending on the researched film information, certain material properties might be preferred. For example, if we are interested in the detectability of a dielectric film on a metallic substrate (e.g.: oxide layer developed on a metallic substrate), the highest possible permittivity of the film and the lowest thickness are more convenient. However, if we are interested in the distinction of the material dielectric permittivity, less polarizable materials and thicker films are preferred. Moreover, the distinction of the film thickness is more likely for films with low permittivity and thickness.

4.2. Two homogeneous superposed films

As we have reviewed in the above paragraph, a great amount of data can be found for laterally infinite homogeneous films studied with EFM, either theoretically or experimentally. However, there is a lack of works dealing with multilayered films and the influence of their relative properties on the global signal.

4.2.1. State of the art

E. Castellano-Hernandez and G. M. Sacha studied with the artificial neural network algorithm, the interaction between an EFM probe and a thin film over a semi-infinite dielectric substrate [39]. The direct application of such a system has concerned single and few layer graphene (FLG) placed on insulator substrates for planar device architectures applications. Authors replaced the thin film and the substrate with one semi-infinite dielectric film of an equivalent effective permittivity ε_{eff}. Studying a certain range of permittivities and thicknesses, namely, for thin films permittivities ε_1 higher than the dielectric substrate ε_2, they deduced an analytical expression for ε_{eff}:

$$kh\varepsilon_{eff} = \left(\frac{\varepsilon_{eff} - \varepsilon_2}{\varepsilon_1 - \varepsilon_{eff}}\right)^A \tag{III.9}$$

where *k* is a constant depending on the tip geometry, *h* is the film thickness, and *A* is equal to 3/2 for all analyzed geometries. The authors showed that the extremely high dielectric permittivity of ultra-thin films becomes distinguishable, provided that a substrate of lower permittivity is present under the film. This result has been explained by the small thickness of the film that allows the electric field to penetrate inside the substrate. It must be noted that this result has been obtained for the specific case of thin permittivity ε_1 much bigger than substrate permittivity ε_2.

Later in ref [40], authors presented numerical calculations with GICM for an insulating film over a dielectric substrate placed on a metallic electrode, similarly to ref [39]. This configuration is equivalent to the study of two superposed films. Authors fixed the upper thin film dielectric permittivity ε_1 to 20 and measured the force and the force gradient sensed by the tip for substrate permittivities ε_2 below 20 and possessing several thicknesses. The sensitivity of the signal to changes in the dielectric constant of the upper thin film has been also investigated. In conclusion, they found within their range of studied dielectric constants, that *F* and *G* absolute values rise with both ε_2 and h_1. Moreover, the sensitivity to ε_1 was reported to decrease with ε_2 for any h_1, and to increase with h_1, far from certain limits: very low ε_2 and very high h_1.

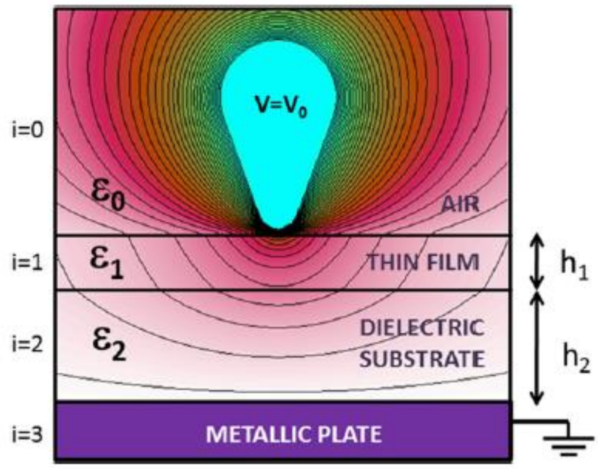

Fig. III - 10 : Equipotential distribution between an EFM tip and a three layered sample in air: thin film, dielectric substrate and grounded metallic plate [40].

In a subsequent work, W. Castellano-Hernandez and G. M. Sacha considered indirectly the effect of two superposed films on the signal [20]. The authors investigated the case of a non-perfect dielectric film with finite conductivity. This study concerns the characterization of thin films in ambient air where water molecules adsorption and condensation creates ad-ions within the insulating sample and hence, change its surface conductivity. The finite conductivity is also encountered in the case of a thin conductive film containing no enough free charges to compensate the external electric field. A change in the sample conductivity is also expected at regions with surface defects implying the presence of surface charges. The sample conductivity has been included through a linearized Thomas-Fermi (Debby-Huckel) approximation. In the presence of electrical conductivity, the tip-sample interaction was derived with GICM. The system was approximated by a superposition of a thin film with a thickness equal to the screening length and a substrate with infinite length, both with the same dielectric constant. A small amount of free charges within the film has been found to reduce the electric field inside the sample, similarly to a thin film with increased permittivity. Different combinations of dielectric constant and screening length have been found to be able to give the same electrostatic force under a specific tip-sample distance, although the effect on the electric field distribution is different. The latter variation explains the dissimilar behavior regarding the tip-sample distance. This can be used to distinguish the physical phenomena involved in the EFM signal, whether it is due to the conductivity or to the dielectric constant. Namely, significant amplification in the apparent permittivity of the sample at two working distances can indicate the presence of a finite conductivity in the sample.

The effect of a dielectric substrate below a thin film has been mentioned briefly elsewhere in the literature. For instance, G. Gomila *et al.* studied the effect of the film width on the EFM signal [18]. They defined a critical diameter above which the signal reaches 90 % of its maximum. The authors showed that a dielectric substrate with a relative permittivity equals to 6 affects the critical diameter for a film with a given dielectric constant of 4.

4.2.2. Modeling results

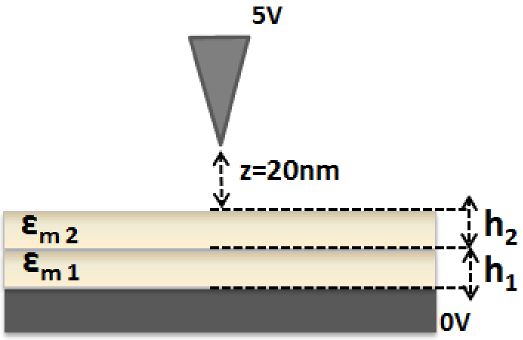

Fig. III - 11 : Sketch of the modeled EFM tip facing two superposed dielectric films (not to scale).

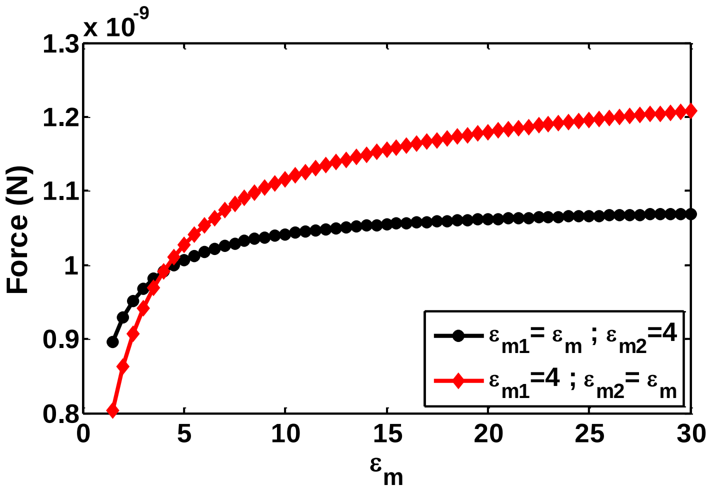

Fig. III - 12 : Electrostatic force over two superposed dielectric films of 50 nm thickness each, a. $\varepsilon_{m1} = 4$, variable $\varepsilon_{m2} = \varepsilon_m$; b. variable $\varepsilon_{m1} = \varepsilon_m$, $\varepsilon_{m2} = 4$. Note that matrix 1 and matrix 2 correspond respectively to film 2 and film 1 of Fig. III - 10 of ref [40].

In this paragraph, the case of two general superposed dielectric films, represented in Fig. III - 11, is studied in details. Modeling results for two superposed dielectric thin films, of 50 nm thick each, are reported in Fig. III - 12. On the black curve (disk like symbols), we fixed the dielectric permittivity of the top layer $\varepsilon_{m2} = 4$, and simulated the force for variable dielectric permittivities of the bottom layer ($\varepsilon_{m1} = \varepsilon_m$, with ε_m is a variable value). The resulting force grows with ε_{m1}. Then, on the red curve (diamond like symbols), we fixed $\varepsilon_{m1} = 4$, and simulated the force for variable ε_{m2}. The resulting force also increases with increasing matrix permittivity (with ε_{m2} in this case). However, the two curves do not superimpose. It can be deduced that the force over two different superposed dielectric films is not conserved for an inversed order of dielectric films position in the vertical direction. Moreover, although the absolute value of the force always increases with any intensification of films permittivity, the gap between the two configurations is not constant, but becomes more important with distinct permittivity values of the superposed films. It can be also noticed that the force divergence from the corresponding value at $\varepsilon_{m1} = \varepsilon_{m2}$ is more significant for ε_{m2} variations rather than ε_{m1} variations. The probe is consequently more sensitive to the permittivity of the top layer. Hence, the absolute value highly increases (or decreases) when the upper film possesses a higher (or lower) permittivity than the bottom one. Except for very low distances and very thin films, this behavior can be explained by the fact that the capacitor configuration in an EFM measurement is far from a plane-plane interaction as we have seen in previous sections. Thus, the electric field is not constant between the electrodes. It decreases gradually in the depth of the material [41], which explains a higher sensitivity to upper layer properties.

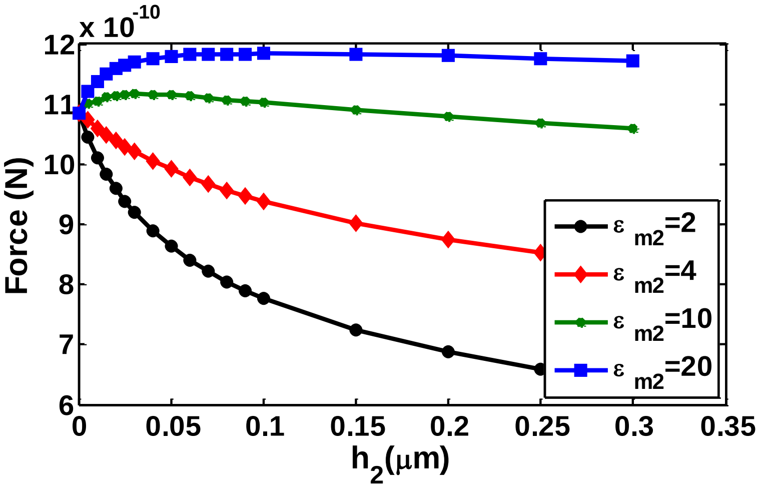

Fig. III - 13 : Electrostatic force over two superposed dielectric films with $\varepsilon_{m1} = 4$, $h_1 = 50$ nm, vs. top film thickness, for top film permittivity inferior ($\varepsilon_{m2} = 2$), equal ($\varepsilon_{m2} = 4$) and superior ($\varepsilon_{m2} = 10, 20$) to the bottom film permittivity.

We study now EFM signal variation regarding top layer thickness, h_2, for a fixed bottom layer height $h_1 = 50$ nm and fixed ε_{m1} and ε_{m2}. With bottom layer permittivity $\varepsilon_{m1} = 4$, we simulated the force for a top layer dielectric constant ε_{m2}: inferior to ε_{m1} ($\varepsilon_{m2} = 2$), equal to ε_{m1} ($\varepsilon_{m2} = 4$) and superior to ε_{m1} ($\varepsilon_{m2} = 10$ and 20). It can be interestingly observed that the signal profile is not the same for all studied ε_{m2} cases (Fig. III - 13). For $\varepsilon_{m2} \leq \varepsilon_{m1}$, the signal decreases with the top layer thickness. However, for $\varepsilon_{m2} > \varepsilon_{m1}$, the signal rises first with the film thickness and then, after a certain value of h_2 ($\approx$ 100 nm), the trend changes and the signal starts to decrease. In Fig. III - 14a., the trend for the case of $\varepsilon_{m2} > \varepsilon_{m1}$ is more clearly presented.

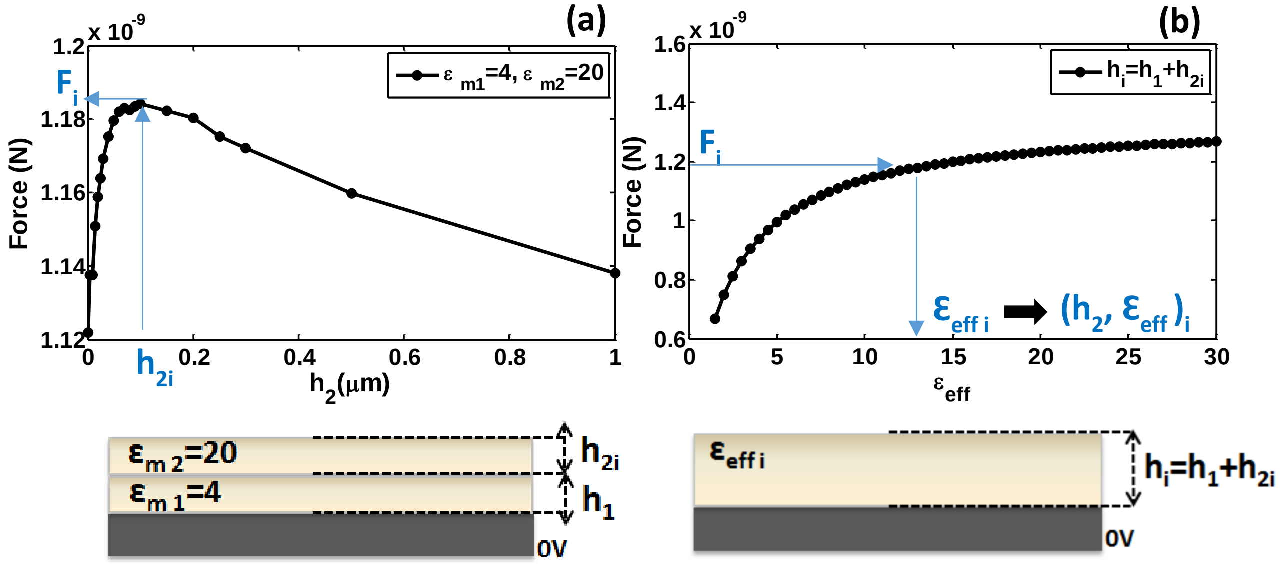

Fig. III - 14 : Force variation vs. upper film thickness for ε_{m2} = 20 (inset a.), and calculated force over a dielectric film with similar dimensions as the association of films 1 and 2 of inset a. (inset b.), for variable film permittivity.

As introduced previously, it has been found in ref [40] that the electrostatic interaction with the probe is sensitive to an effective permittivity of the probed region. Hence, in order to explain the results obtained in Fig. III - 13, we computed the variation of the force for a homogeneous dielectric film with a thickness $h = h_1 + h_2$, and a relative dielectric permittivity ε_{eff}. For each value of h_2, called h_{2i}, we simulated the force corresponding to a total film thickness $h_i = h_1 + h_{2i}$, for several ε_{eff}, called each $\varepsilon_{eff\,i}$. In order to extract the effective permittivity ε_{eff} for the corresponding films association, we noted the force F_i obtained for the studied case of the superposed films with a certain h_{2i} (see Fig. III - 14 a.); and conversely, we extracted the value of the effective permittivity $\varepsilon_{eff\,i}$ obtained on the film of total thickness h_i, which gives the same force value F_i (see Fig. III - 14 b.). This way, we deduced the effective permittivity sensed by the EFM probe facing the superposed dielectric layers for the corresponding layers thicknesses and permittivities. The same procedure has been adopted for all studied film 2 thicknesses and for the following second case of film 2 dielectric permittivity lower than the bottom layer.

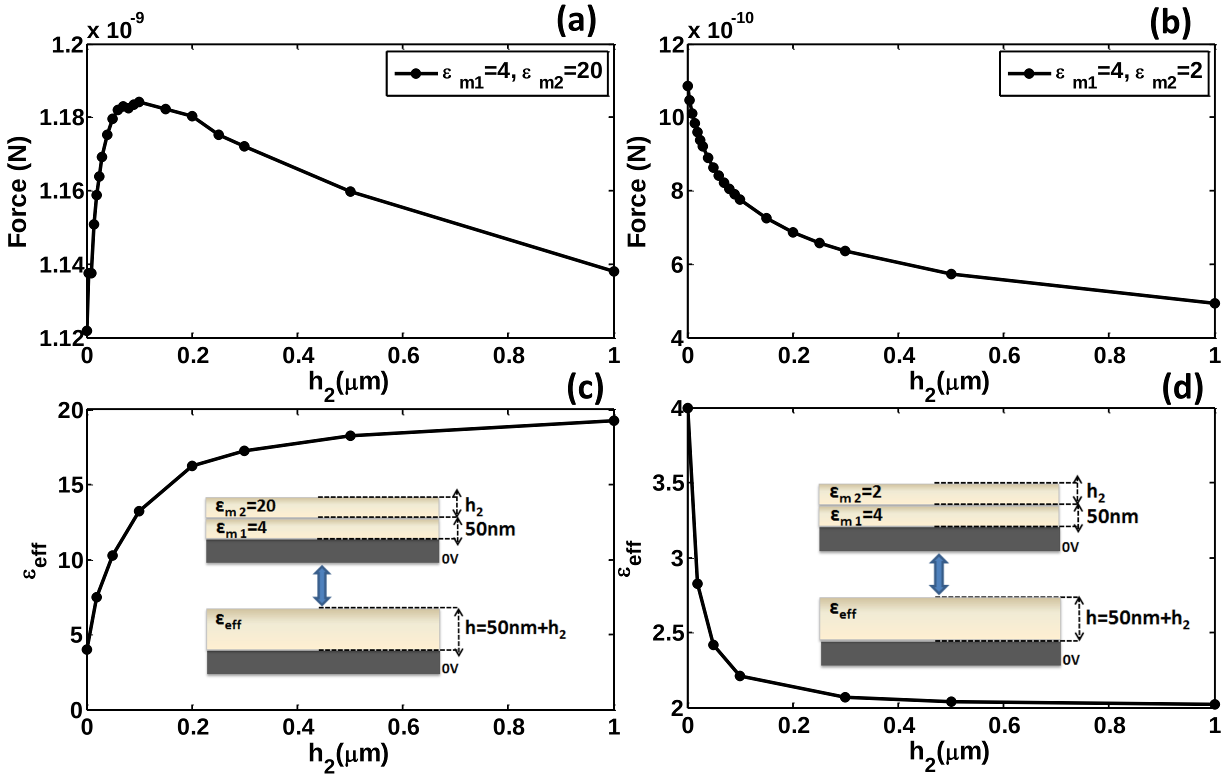

Fig. III - 15: Force variation vs. upper film thickness, a. with ε_{m2} = 20, higher than lower film permittivity ε_{m1} = 4, b. with ε_{m2} = 2, lower than the lower film permittivity; and the calculated equivalent dielectric permittivity for a dielectric film with the same dimensions as the association of films 1 and 2 of Fig. III - 11 (inset), c. for case a. and d. for case b.

We present in Fig. III - 15a. and b. the force versus h_2 for ε_{m2} = 20 > ε_{m1} (same as Fig. III - 14a.) and ε_{m2} = 2 < ε_{m1}, respectively. We present in Fig. III - 15c. and d. the corresponding values of the effective permittivity measured with EFM for a film with similar dimensions to the superposed films (see inset Fig. III - 15c. and d).

For ε_{m2} = 20 > ε_{m1}, we find that the addition of a layer with the highest permittivity amplifies the effective permittivity of the resulting matrix, going from $\varepsilon_{eff} = \varepsilon_{m1}$ at h_{2i} = 0 nm and tending towards ε_{m2} at higher thicknesses. However, the effective improvement is not monotonous and starts to decrease after $h_2 \approx 0.1$ µm. The permittivity steep increase below h_2 = 0.1 µm explains the rised signal obtained in the first branch of the force versus h_2 curve. We interpret this trend by the sensitivity of the system to the global enhanced polarization, which sufficiently intensifies the system equivalent capacitance, compensating the effect of the increased distance between electrodes. As a matter of fact, larger interelectrode distance reduces the capacitance. However, for h_2 > 0.1 µm, the smooth change in ε_{eff} becomes insufficient to counteract geometrical effects and the signal starts to decrease similarly to the case of a homogeneous film with an increasing thickness (Fig. III - 15b.).

For ε_{m2} = 2 < ε_{m1}, we find that the addition of the layer with a lower permittivity decreases the effective permittivity of the resulting matrix (Fig. III - 15b.). It goes from $\varepsilon_{eff} = \varepsilon_{m1}$ at h_{2i} = 0 and tends towards ε_{m2} at higher thicknesses. Here also, the effective regression is not monotonous and starts to slow down after $h_2 \approx 0.1$ µm. The steep decrease of the permittivity explains the decreased signal observed in the first branch of the force versus h_2 curve. The sensitivity to the decreased polarization reduces the capacitance of the system, adding up to the effect of greater interelectrode distances. For h_2 > 0.1 µm, the smooth change in ε_{eff} reduces the decay due to the permittivity. Hence, the signal keeps on smoothly decreasing, similarly to the case of a homogeneous film with a growing thickness (Fig. III - 9b.).

These results suggest paying deep attention when analyzing EFM signals over thin films. An increasing signal of the same laterally infinite film, might lead to misconceptions. For instance, one might think that the film thickness is being reduced, which is not necessarily the case. As we have seen, it can also be due to an increasing thickness when the film is present on a substrate with relatively lower permittivity. We also expect a similar behavior for the inversed case: h_2 fixed, and h_1 changing. However, the rate of change of ε_{eff}, and consequently, the measured force, regarding h_1, must be slower since it corresponds to the bottom layer.

In order to deeper our understanding of this behavior, we compared simulations to the simplistic analytical expression of ε_{eff}, corresponding to a plane-plane capacitor filled with two dielectric layers. From the calculation of the equivalent capacitance for two capacitors in series, we deduce the following analytical expression:

$$\varepsilon_{eff} = \frac{h_1 + h_2}{\frac{h_1}{\varepsilon_1} + \frac{h_2}{\varepsilon_2}} \tag{III.10}$$

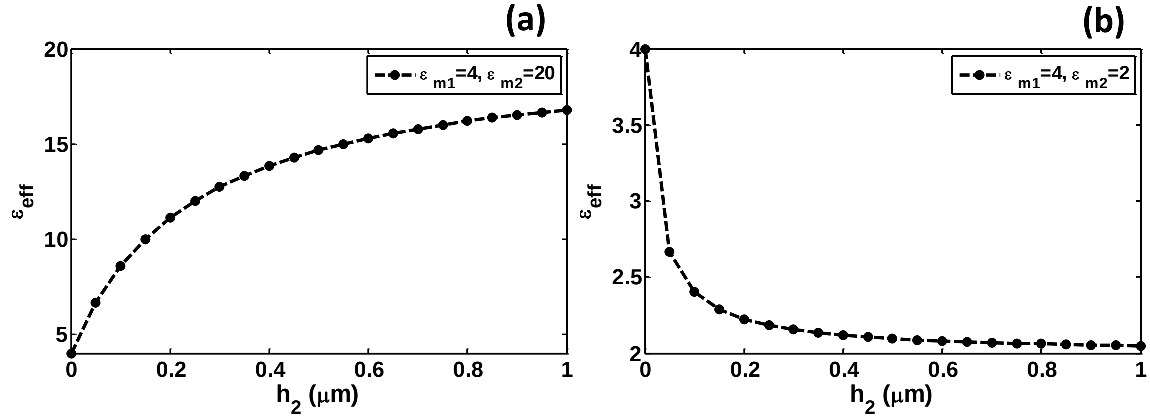

Fig. III - 16 : Calculated equivalent or effective dielectric permittivity of two dielectric films with same dimensions and permittivities of Fig. III - 14, using the plane-plane capacitor model of eq (III.10), a. $\varepsilon_{m2} = 20 > \varepsilon_{m1} = 4$, b. $\varepsilon_{m2} = 2 < \varepsilon_{m1} = 4$.

Similarly to simulations, the effective permittivity grows with h_2 from $\varepsilon_{eff} = \varepsilon_{m1}$ at $h_{2i} = 0$ nm towards ε_{m2} at higher thicknesses. This simple analytical model explains to a good extent the interaction of the EFM probe with two superposed dielectric thin films. The thickness of the dielectric film in a capacitor affects the impact of its dielectric permittivity on the effective permittivity by influencing charge accumulation at the electrodes. However, we notice that ε_{eff} rate change with h_2 is slightly lower than the one obtained with numerical modeling results. In Fig. III - 16, with 1 µm h_2 increase, ε_{eff} goes from 4 to 16.8 with analytical calculations versus 4 to 19.25 with numerical simulations. Moreover, the numerically simulated curves tend to saturate more rapidly. This can be understood by the geometry of the tip which does not allow a conventional polarization response from the system as in the case of a plane-plane capacitor. Probe geometry effect on the electric field between electrodes strengthens the sensitivity to the upper film, increasing ε_{eff} influence to the top film.

One must note that these conclusions can be extrapolated for multi-layered samples. In fact, any association of films can be interpreted with one equivalent permittivity, and be compared to the remaining film, or remaining film association, to be studied.

Our results elucidate the reason behind the observed intensification in literature of the sensitivity to the permittivity of high dielectric constant thin films when placed over dielectric substrates [40]. In fact, the studied film possesses the highest permittivity regarding the substrate.

Hence, according to what it has been concluded earlier, the effective permittivity of the thin film is decreased when placed on the low permittivity substrate. Since the sensitivity to ε generally increases for low sample permittivities, this explains the gain in the sensitivity to the studied high dielectric constant thin films.

In the experimental results of Chapter V, similar signal variations will be verified on real multilayered samples, and the conclusions of this section will be used to study the sensitivity to different dielectric layers, covering nanoparticles.

4.3. Finite-size effects

In the above sections, we treated the case of planar films with an infinite lateral extension relatively to the probe geometry and working conditions. However, the interaction between an EFM tip and a 2D and especially a 3D nanometric sample is much more complicated. In the case of nanoparticles, the electric field is highly non-uniform due to the tip geometry and working distance, as well as it is strongly dependent on the size and shape of the particle, complicating the sensitivity to its intrinsic permittivity.

4.3.1. State of the art

Y-Z Li *et a*l. have investigated the effect of the size of a squared sample on the electrostatic force when presenting the self-consistent method in ref [31]. The response versus sample side-length at different tip-sample distances has shown non-monotonous tendencies. The authors introduced the influence of small sample widths on the coupling with the substrate. The latter effect explained the decrease of the signal at small widths due to a high coupling of the probe with the separated substrate. Moreover, the authors explained that larger samples favor the coupling with the sample instead of the substrate, clarifying the enhanced signal.

More recently, G. Gomila *et al.* studied numerically and analytically the electrostatic force acting on an EFM tip over an oblate nanoparticle [42]. Based on the model developed in ref [43], the authors derived an expression of the capacitance gradient while performing the following approximation on the force origin: the polarization force acting on the tip is equal to the force between the induced electric dipole in the nanoparticle and its image dipole within the tip. The induced electric dipole is considered to be generated by a uniform electric field, independent from the nanoparticle. Comparing to finite-element numerical simulations of the real system, they showed that this approximation only holds for small eccentricity particles (1 to 2) and small dielectric constants (1 to 10). Otherwise, the particle width strongly affects the field lines and the problem must be solved numerically. Authors have also expanded the signal dependence to the shape and dimensions of the particle. In particular, for a fixed particle height, the signal has been found to augment with the width of a nanoparticle of fixed height (or with its eccentricity), impacting then the extracted effective dielectric constant of the sphere, regardless of the tip geometry. Moreover, the dielectric constant of the particle also intensifies the electrostatic force acting on the tip with an increased sensitivity for wider particles.

However, the signal contrast tends to saturate at high eccentricities, and it saturates more rapidly for particles of high dielectric permittivity. The authors explain those signal saturations at high eccentricities to be due to the localized polarization in an EFM interaction. Moreover, the induced dipole gets highly reduced, which lowers the influence of other parameters such as the width. Numerically, in order to understand better these dependencies, they generalized the phenomenological expression of the capacitance-gradient contrast for a spherical nanoparticle introduced in ref [33], to the case of a non-spheroidal one:

$$\Delta C_{non-spher}'(z, \varepsilon_p) = \left(c_0 \frac{(R_0 + r_0)(h_p - d_2)}{(z - h_p)^2 + d_1(h_p - d_2)} \right) (1 + u(ecc - 1)) \log \varepsilon_p \qquad \text{(III.11)}$$

where h_p is the non-spheroidal particle height, *ecc* is its eccentricity factor and $u \approx$ 1-1.4 for $1 < \varepsilon_p < 10$. $c_0 \approx$ 2.22 zF/nm and $r_0 \approx$ 11 nm are phenomenological constants, while $d_0 = d_0\,(R_0) \approx$ 8 - 10 nm, $d_1 = d_1\,(R_0, \varepsilon_p) \approx$ 2-3 nm and $d_2 = d_2\,(R_0, \varepsilon_r) \approx$ 0-12 nm are smooth functions of the tip radius R_0 and particle dielectric constant ε_p. The explicit expressions can be found in the supplementary information of ref [33] and [42].

The dependency of the signal on particle diameter is present in this phenomenological equation, but it was not particularly discussed in these papers. In the supplementary information of ref [33], the authors studied signal contrast variation for only some particular cases.

Another work dealing with finite-size effects of the same research group has been published in [18]. The authors studied the capacitance gradient contrast for dielectric films with variable width. They calculated the capacitance gradient contrast as the difference between the signal at the position of interest and the bare substrate signal for a fixed reference distance, to avoid non-local contributions. The contrast was found to saturate after a certain film width at which the film approaches an infinite plane. They called it critical diameter (D_c). D_c increases with the film thickness. For ultrathin film thicknesses (< 10 nm), D_c depends on the nanometric parts of the tip, and it is not influenced by the dielectric constant of the film. At intermediate thicknesses (> 10 nm and < 1 µm), D_c depends on the nanometric parts of the tip, along with the dielectric constant of the sample. Finally, at higher thicknesses (> 1 µm), it only depends on the film dielectric constant. It has been also verified for all cases that there is no effect of the micrometric parts of the tip on the critical diameter. Furthermore, authors explained the dependency on the film thickness by presenting electric potential drop maps for an intermediate thick film of different widths. The potential highly drops in the depth of the sample for low width films contrarily to large films where the potential is concentrated in the center (see Fig. III - 17). This effect has been explained by the fact that for small widths, the lateral surfaces are majorly exposed to the tip where the potential is not null. A potential drop is thus going to occur in order to reach the zero potential at the substrate boundary. At the opposite, for large films, the lateral surface is more close to the substrate zero potential than the interacting region close to the tip, which explains the decreased effect of the width (Fig. III - 17).

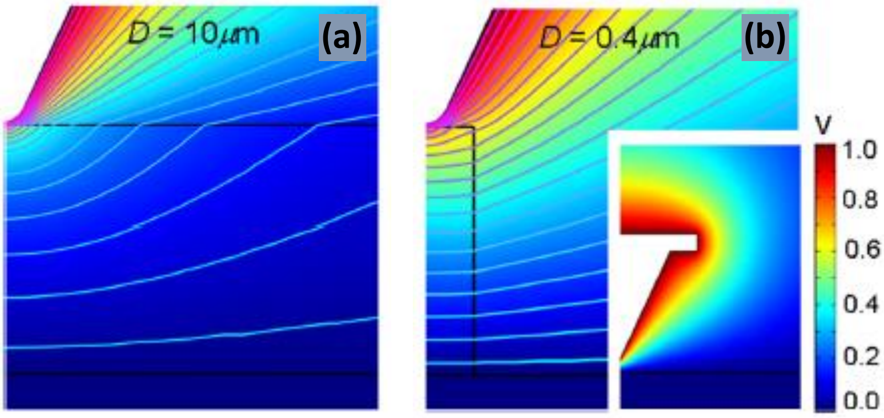

Fig. III - 17 : Zoomed view of the calculated electric potential distribution for the case of a probe with 12.5 µm cone height, 3 µm cantilever radius, 2 µm cantilever thickness, 25 ° cone half-angle, 100 nm apex radius, and an insulating film with 1 µm thickness , dielectric constant ε_m= 4, and diameter a. *D* = 10 µm and b. *D* = 0.4 µm. Inset: global view of the calculated electric potential [18].

C. Riedel *et al.* have used ECM to quantify the dielectric constant of polyvinyl acetate particles embedded in a polystyrene matrix [30, 36]. Although the authors have not accounted for the spherical geometry of the particles in their model, as they considered each point as infinite plane film, reasonable dielectric constants have been measured for the corresponding polymers.

Hence, we deduce that the interaction between a nanoparticle or any 2D nanometric object and an EFM tip cannot be solved analytically, and one has to resort to numerical simulations for the specific studied system including the exact sample geometry.

In this section, we will show the detailed effect of nanoparticle radius and dielectric constant on the electrical signal, compared to an infinitely wide dielectric film with similar height. A study of the nanoparticle radius combines both particle height and width effects in 3D, compared to other studies treating eccentricity change alone, or the diameter for only some particular planar samples [31, 33]. Then, we will study the case of different diameters or depth positions of the particle in the matrix for several constituent dielectric constants. Finally, we will consider the case of two adjacent particles in the matrix with different spacings, for several material properties as well. An insight into the lateral force acting on the tip and its effect on the probe motion will also be reported.

4.3.2. Particle versus film

From the literature and previous simulations sections, it can be deduced that the nanoparticle geometry and dielectric constant, tip dimensions and tip-substrate distance, affect altogether the measured EFM signal. However, the radius has been found to have a particularly complicated influence on the signal. Nevertheless, to our knowledge, particle radius effect was never investigated before individually.

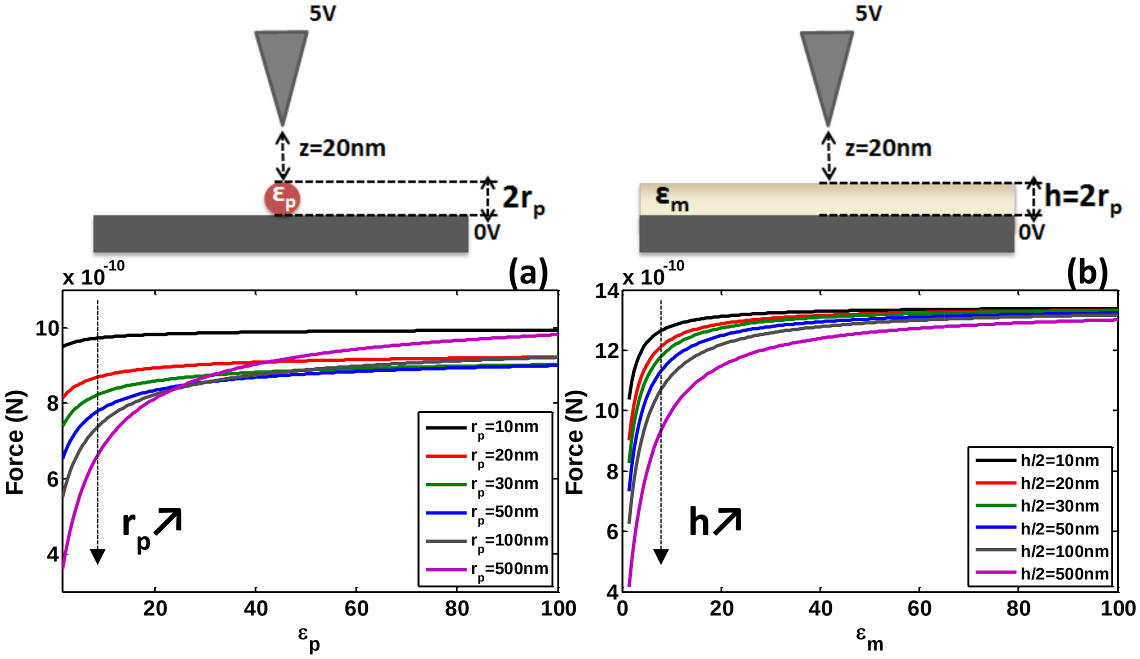

Fig. III - 18 : Electrostatic force vs. sample permittivity for: a. a nanoparticle of different radius (inset a) and b. a dielectric homogeneous laterally dielectric infinite film (inset b).

To gain a deeper insight into the influence of all those co-existing parameters, and especially the radius, we start by presenting in Fig. III - 18a. the absolute electrostatic force change at the particle center with the particle dielectric constant for several diameters. The dielectric constant rises the signal, as expected from Fig. III - 9a., with an increased sensitivity for bigger particles, in accordance with [42]. However, it can be noticed that the tendency versus particle diameter at a fixed permittivity is not the same for all dielectric constants. The signal does not decrease monotonously compared to a laterally homogeneous infinite dielectric film with the same height, as it is calculated in parallel in Fig. III - 18b. This highlights the effect of the geometry of the particle on the signal. Moreover, the absolute value of the force is not the same for a nanoparticle compared to a matrix with the same height [18].

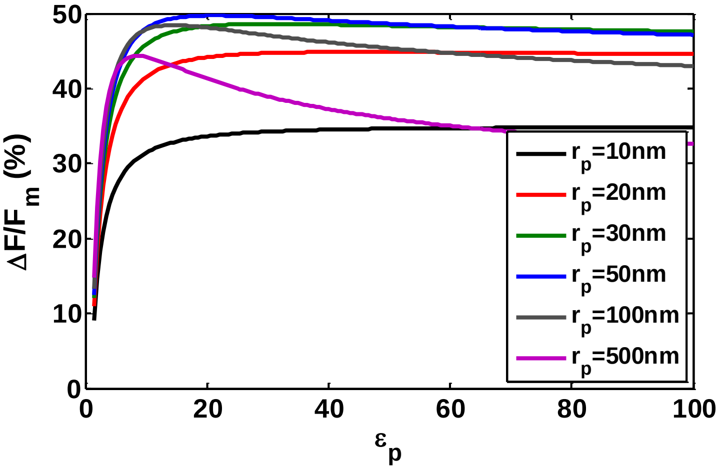

Fig. III - 19 : Force difference percentage between the value at the center of a nanoparticle (Fig. III - 18 a.) and that of the matrix regarding the matrix (Fig. III - 18 b.) at same tip-sample distance, for the same parameters: $\varepsilon_p = \varepsilon_m$ and h = 2r_p.

In Fig. III - 19, the force difference between the signal at the particle center and above a matrix with the same height is calculated, normalized to the corresponding signal above the matrix. Two main behaviors regarding the dielectric constant can be distinguished. At low permittivities, and for all measured particles radii (10-500 nm), the disparity enlarges with the sample dielectric permittivity. The difference of tip interaction with a particle and a matrix with the same height becomes more important, up to a certain permittivity, where the difference either saturates for low diameters or starts decreasing for higher ones. As a consequence, it seems that the influence of particle geometry is less pronounced either for small particles, or relatively big ones with high permittivities.

Nevertheless, at low permittivities, sample polarization is weak and the charge distribution on electrodes gets only slightly modified. Hence, the material is almost not detected and no difference is perceived between a nanoparticle and a matrix at fixed tip-sample distance, when both possess the same height. However, as the permittivity gets more important, the detectability augments, and the material intrinsic contribution increases, so the difference in the lateral geometry becomes more noticeable. That explains the highest force differences with greater permittivities.

However, we remind that the general sensitivity to the permittivity decreases with the permittivity as it can be seen from Fig. III - 9a. and b. where the slope of the curves declines at high permittivities. The decreased sensitivity is more pronounced for thin samples. As a consequence, the difference between the signals becomes almost constant for small particle diameters.

Furthermore, in order to follow more clearly the non-monotonous behavior regarding ε_p for different r_p, noticed in Fig. III - 18 and developed in Fig. III - 19., we present in Fig. III - 20 the variation of the force versus particle radius at four representative permittivities.

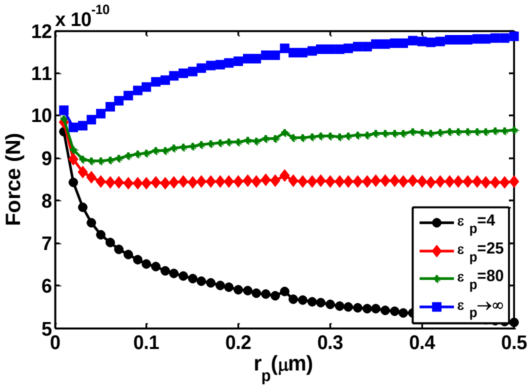

Fig. III - 20 : Electrostatic force over the center of a nanoparticle vs. particle radius for four representative permittivities: ε_p = 4, 25, 80 and infinite.

From Fig. III - 20, two trends for low and high dielectric permittivities at fixed tip geometry and tip-sample distance can be defined. We find that at low particle permittivities, the signal continuously decreases with particle diameter. However, as long as the permittivity increases, signal decay slows down until a certain radius, before the force tendency changes, and the force starts to increase gradually with the particle radius [31].

In order to interpret this behavior, one must note that the change in particle radius involves several effects that co-act on the charge distribution and hence, the electrostatic force sensed by the tip. We mention two main effects:

a) Particle height increase: it enlarges the distance between electrodes that tends normally to decrease the signal at a constant tip-particle distance z;
b) Surface increase: it expands the surface of the sample interacting with the probe that, alone, is supposed to rise the signal [18, 42].

As mentioned previously, a semi-phenomenological model has been reported by L. Fumagalli *et al.* that demonstrates the cooperative dependency of the signal on particle size and permittivity, working distance and tip geometry (eq (III.11)) [33]. Nevertheless, this model is limited to a certain range of parameters. It is consequently insufficient to analytically model the critical-like behavior of particle radius.

On the other hand, our results are in accordance with previous force tendencies versus the dielectric size, observed on cubic samples [31]. Unlike our study, Z. Y. Li *et al.* however indicated sample size effect at different tip-sample distances and for a fixed permittivity.

Therefore, for a nanoparticle, the interpretation of the observed non-monotonous signal tendencies regarding particle radius and permittivity is the following:

a) At low permittivities (Fig. III - 20, ε_p = 4), as mentioned earlier, the sample does not greatly alter the created electric field produced by the applied voltage difference. Hence, the expansion of interelectrode separation is the paramount parameter that describes how the signal decays when the radius broadens. The contribution of particle polarization response and surface widening are insufficient to compensate the decreased capacitance induced by the separated electrodes.
b) However, at high permittivities (Fig. III - 20, ε_p > 4), and exceeding a critical r_p, the important dipolar polarization effect on the capacitance compensates the change due to tip-substrate height increase, and avoids the signal from decreasing. As a consequence, the height change is no longer influential, and particle surface increase starts to dominate and contribute to the augmenting signal.

c) Moreover, concerning the interaction decrease at low radii met at all ε_p (Fig. III - 20), this behavior must be due to the proximity of the electrodes for small particles. In this case, the tip-substrate distance predominates over the material intrinsic polarization response. As the former increases with the radius, it explains the signal drop for relatively small r_p. This interpretation agrees with that provided by Y-Z Li *et al*. for small cubic samples [31].

4.3.3. Particle in a matrix

4.3.3.1. Zero depth

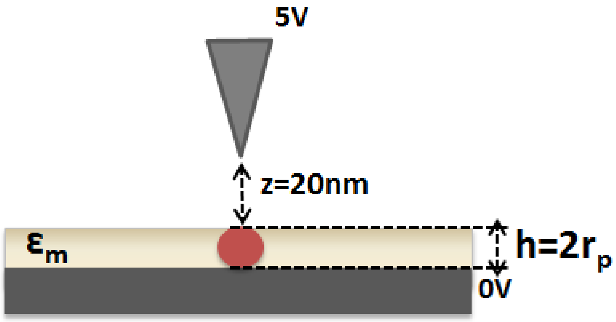

Fig. III - 21 : EFM modeled tip facing a nanocomposite composed of a nanoparticle of radius r_p placed in a matrix of height *h* at zero depth from upper and lower surfaces.

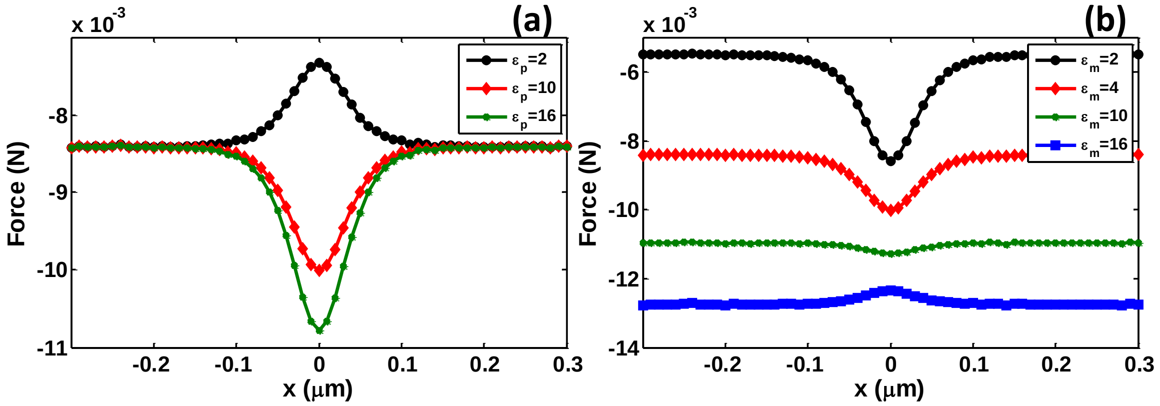

Fig. III - 22 : 2D electrostatic force raw values on a scan line over a nanocomposite of h = 50 nm (Fig. III - 21) for: a. fixed matrix permittivity, ε_m = 4, and variable particle one, ε_p = 2, 10, 16; b. fixed particle permittivity, ε_p = 10, and variable particle one: ε_m = 2, 4, 10. Note that all forces calculated in 2D geometry overestimate the value of the effective 3D force, here measured in 2D axisymmetric geometry (10^{-3} N vs. 10^{-10} N). The accuracy of 2D signal tendencies have been however confirmed to be consistent with 3D ones.

In this section, the EFM signal in front of a nanoparticle placed within a matrix is studied. Fig. III - 22a. presents the force variation on a 2D scan at fixed *z* around the particle center for ε_m = 4, $h = 2r_p$ = 50 nm and ε_p = 2, 10 and 16. The Gaussian like signal shows a maximum at the center of the particle and possesses a certain half-width at half-maximum (HWHM), relatively larger than the particle radius. We find that the signal intensity at the center increases with particle permittivity, thus, changing the contrast. A contrast inversion is obtained as the particle permittivity goes from a higher to a lower permittivity regarding the matrix.

We present in Fig. III - 22b. the force obtained for the same system as in Fig. III - 22a., with a fixed particle permittivity ε_p = 10 and variable matrix permittivity ε_m= 4, 6, 8. We find that for a fixed ε_p, ε_m affects the signal contrast, the force value at matrix regions and the force value at the center of the particle.

From previous results, above a nanoparticle, the signal has been inferred to divert from that corresponding to the similar matrix with the same height, due to the finite resolution of the system (see Fig. III - 18). Hence, the influence of the matrix permittivity on the signal over the particle is not surprising. Similarly to superposed dielectric films interpretation, one can expect a collective effect of the system capacitance from the whole probed region. Hence, since no geometrical parameter is changing, the interaction region from the matrix changes the effective permittivity of the probed zone. It gets larger for ε_m higher than ε_p.

Moreover, as shown in Fig. III - 22a., the decreased contrast observed in Fig. III - 22b. can be explained by the decreased permittivity differences between the inclusion and the matrix reducing the corresponding EFM contrast. The signal contrast and HBWM are found to be inversely proportional. This infers that the measured particle diameter with EFM can change for the same physical particle dimensions. The apparent EFM diameter (particle diameter on EFM signal ≈ EFM signal HBWM) becomes tighter or wider, depending on particle and matrix permittivities ratio closer or distant to 1, respectively.

This shows that EFM resolution in nanocomposite studies depends on the relative dielectric constants of their heterogeneities. When there is a high dielectric contrast with the matrix, the particle detectability increases and its corresponding measured diameter in EFM approaches its real one. This resolution definition is not similar to metal-tip cases which has been defined as only proportional to tip radius and tip-sample distance [17]. This work also extends the study of the resolution performed on planar samples in ref [16]. Authors studied the EFM response function on a scan line using the potential and electric field trace variation on the scan axis. Moreover, our results suggest the need for a meticulous interpretation of the HBWM when used as a proof for interphase presence. For instance, filler EFM apparent diameter would directly change in a matrix, since the dielectric contrast with a common polymeric matrix is less important than that obtained in air. Consequently, it is not sufficiently accurate for example to compare nanofillers size before and after incorporation into the polymer as adopted in a previous study [8].

4.3.3.2. Lateral forces

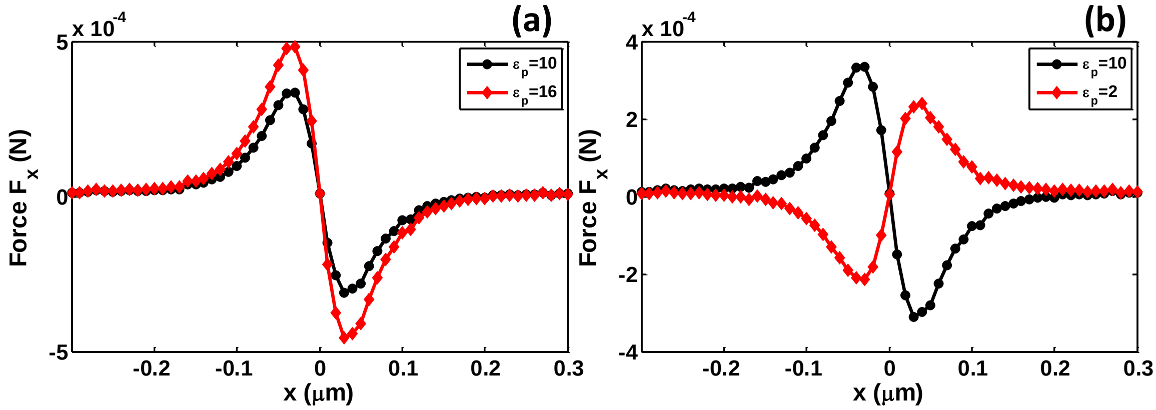

Fig. III - 23 : 2D lateral electrostatic force values on a scan around the center of a nanocomposite (Fig. III - 21) of fixed matrix permittivity $\varepsilon_m = 4$, and: a. particle permittivities $\varepsilon_p = 10$ and 16, increasing permittivities higher than ε_m; b. particle permittivities $\varepsilon_p = 10$ and 2, higher and lower permittivities than ε_m; $r_p = 25$ nm.

In the whole thesis, we studied the normal force acting on the tip, that we have called the total force *F*. This force represents indeed the total force acting on the tip in the case of a perfect symmetry at the probing region and when no local charges are present. This condition is totally verified at any position of a laterally infinite homogeneous film, as well as above the center of a nanoparticle, embedded or not into a matrix, when it is placed at the center of the film with no surface charges. However, when getting away from the center, lateral forces start to appear.

We present in Fig. III - 23 the lateral component of the force F_x, obtained on a scan line over the system sketched in Fig. III - 21. In Fig. III - 23a., the case of two particle permittivities $\varepsilon_p = 10$ and 16, higher than the permittivity of the matrix fixed to $\varepsilon_m = 4$, are compared. Moreover, the signals of $\varepsilon_p = 10$ and $\varepsilon_p = 2$, higher and lower than $\varepsilon_m = 4$, respectively, are studied in Fig. III - 23b.

For $\varepsilon_p > \varepsilon_m$, as the tip approaches the center, we notice that it measures a positive lateral force, and a negative one as it goes away from the particle. A positive lateral force represents a force in the x positive direction, from the left to the right, as considered in our model. Hence, the tip is more attracted towards the particle for $\varepsilon_p > \varepsilon_m$ when it is approaching it. The attraction starts to rise gradually, not too far from the particle (depending on the interaction radius), until it reaches a maximum of attraction at a certain distance (around 300 nm from the center in this case), then it gradually starts decreasing until it reaches a zero value at the particle center. The reverse phenomenon occurs as the tip goes away from the center. A negative sign implies that the attraction is in the opposite x direction.

For $\varepsilon_p < \varepsilon_m$, opposite lateral force directions occur. The tip is more attracted to the matrix when it approaches the particle, until a certain separation, then the intensity of attraction decreases as the tip becomes close to the center. The reverse behavior also occurs as the scan continues.

Electrostatic lateral forces are due to the dissymmetry of electrostatic normal forces acting on the tip, as already underlined in the literature [44-46]. In fact, for $\varepsilon_p > \varepsilon_m$ for example, the normal force is higher in the direction of the particle than that of the matrix as we have seen in Fig. III - 22. Hence, the tip will undergo a more important attraction towards the particle when it approaches the center, which later lowers as it gets closer to the center. Around the center, the equilibrium of forces from both tip sides starts to establish, and force dissymmetry lowers. Whereas, when the scan continues, the tip start again to become more attracted towards the material with the higher permittivity, here, the particle.

The lateral force component within all studied case conditions has been however found to be at least one order of magnitude lower than the normal force. It can still be neglected for more dissymmetric geometries, with some precautions.

4.3.3.3. Different depths

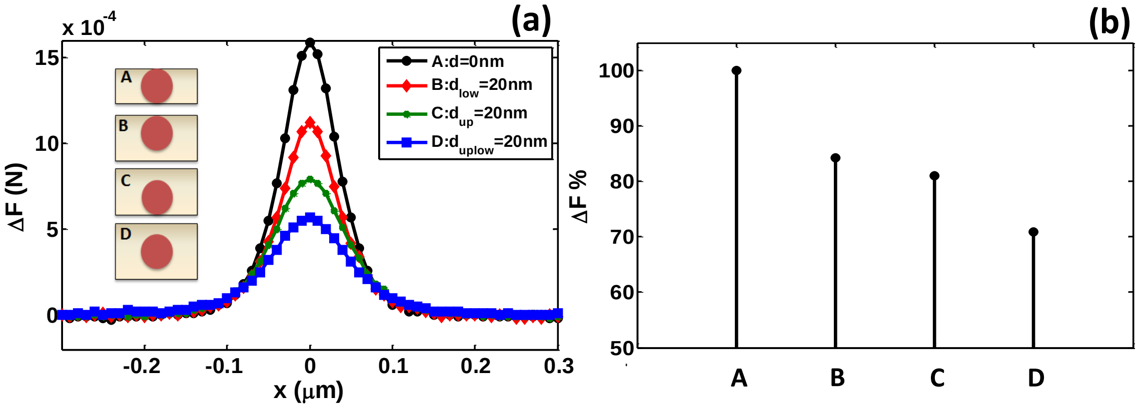

Fig. III - 24 : a. Simulated 2D force contrasts on 0.6 µm scans over a nanocomposite with a spherical filler of $r_p = 25$ nm, $\varepsilon_p = 10$ and a matrix of $\varepsilon_m = 4$ at different depths from upper and/or lower surfaces (inset a.); b. the corresponding normalized absolute force values to zero depth value.

Fig. III - 24 shows the force contrast simulated for a particle located at 0 nm depth (inset A) and with 20 nm of matrix layer below (inset B), above (inset C) and both above and below the particle (inset D). The curves have been obtained by the normalization of the measured signal in each case, to the corresponding one at the matrix region. We find that the presence of a matrix layer always reduces the contrast and rise the apparent diameter of the inclusion. The general decrease in the contrast for fixed matrix permittivity and increased depth can be explained by the change in the effective permittivity of the central region. In fact, these cases are comparable to an association of dielectric layers. In the center, the parts corresponding to the matrix dominate at high depths, and modify the effective dielectric constant of this region to a permittivity closer to the matrix one. Since the difference between the apparent permittivity of the central region and that of the matrix gets smaller, this can explain contrasts reduction in (B), (C) and (D) compared to (A).

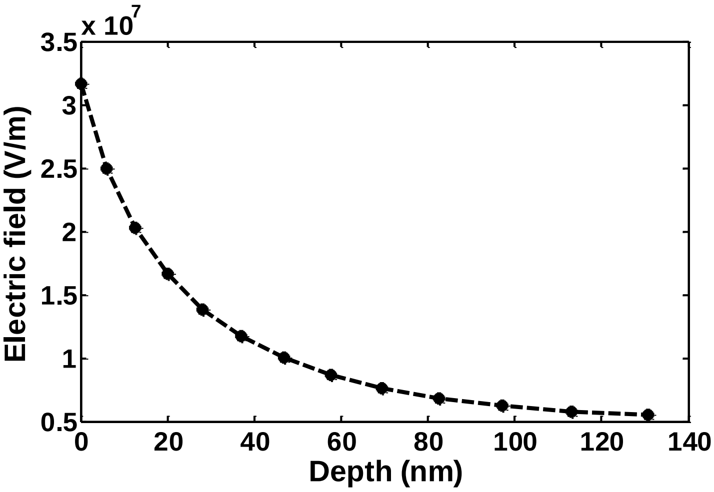

Fig. III - 25 : Electric field intensity into a planar dielectric sample of 150 nm thickness and a relative permittivity that is equal to 4, within an EFM set up.

Furthermore, we notice that the effect of the depth from the upper surface, d_{up}, is the most pronounced. This difference can be explained by the decrease in electric field intensity versus insulation depth in an EFM configuration, as shown in Fig. III - 25. The electric field is characterized by its penetration depth commonly defined as the distance at which the signal is equal to $E(0)/e$, with $E(0)$ the field at the surface and e the exponential constant. The penetration depth has already been reported to be strongly dependent on the probe and sample geometries, measurement parameters, and sample dielectric permittivity [41]. It has been also found to decrease with z [1]. Hence, for a homogeneous sample, it is supposed to increase with sample thickness as well. However, at an equivalent distance from the top surface, the electric field intensity is lower for thicker films. Consequently, the decrease of the electric field in the depth of the sample explains signal differences of case (B) versus (C). Furthermore, the decreased amplitude of the electric field at similar distances from the surface for thicker samples can explain the lowest signal of (D) compared to (C).

4.3.3.4. Several particles

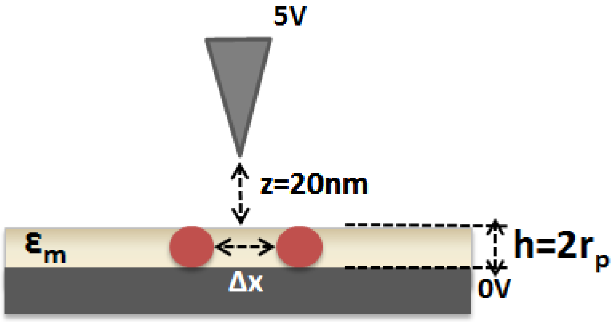

Fig. III - 26 : Sketch of modeled adjacent particles in a matrix at zero depth.

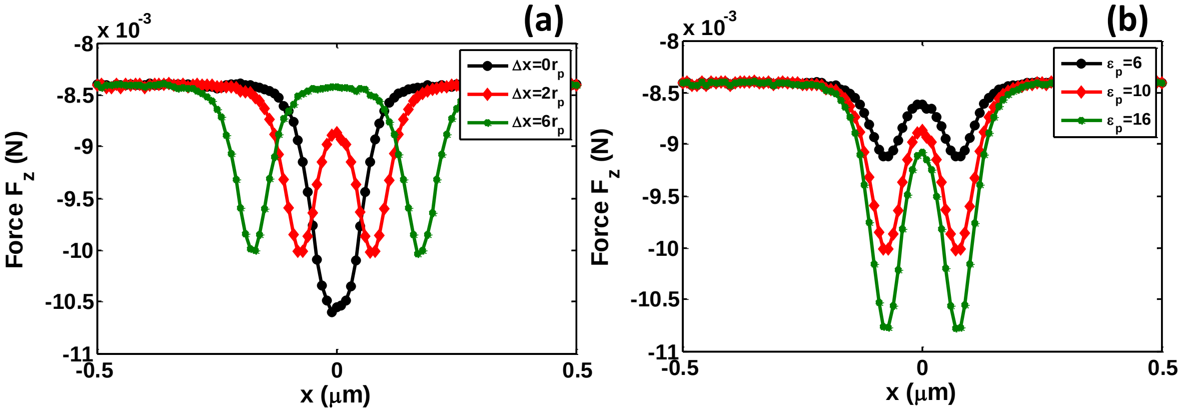

Fig. III - 27 : Electrostatic raw force values (*z* component) on a scan-line: a. over two particles ε_p = 10 in a matrix ε_m = 4, for several inter-particles distance *Δx*, and b. over two particles of fixed inter-particles distance *Δx* = 2r$_p$ and ε_m = 4 for ε_p = 6, 10 and 16; r_p = 25 nm.

Fig. III - 27a. presents the computed normal component of the electrostatic force on a scan line over a matrix containing two particles at different inter-particles distance Δ*x* (see Fig. III - 26). We notice that particles located at different Δ*x* lead to different EFM responses, disrupted by the ambient electrical surrounding at each position. Signals from both particles overlap gradually as they get closer. On one hand, overlapping affects the final form and the HWHM of the response function, which modifies the apparent diameter of the inclusions. On the other hand, signal intensity is also affected by the relative position between the inclusions.

For low spacings (*Δx* = 0 µm), much lower than measurement resolution that is theoretically equal to 22 nm for metals according to Chapter II [17], a total overlapping occur. The sample behaves as if only one particle is placed in the matrix (Fig. III - 22a.). Moreover, when the particle permittivity is higher than the matrix one, we find that approaching particles enhance the signal intensity in the region containing the inclusions. The inverse behavior (decreasing signal) results for $\varepsilon_p < \varepsilon_m$ (not shown here).

At intermediate spacings ($\Delta x = 2r_p$), the two particles can be detected due to the double maxima in the curve. However, the signal at the center of the particles is influenced by neighbor inclusions.

Finally, at large spacings ($\Delta x = 6r_p$), total discrimination of the two particles is observed. The signal in the middle becomes equivalent to that on borders, and that in the center of each particle is hence the intrinsic one relative to its presence in the corresponding matrix.

We deduce that although in a nanocomposite, particles might turn up to be resolved in the signal, their measured dimensions and electrostatic signal can be misleading for inter-particles distances close to the resolution of the measurement. At fixed nanocomposite properties, as well as particles depth, the diameter can appear lower than the expected one, only due to particles spacings.

According to EFM apparent diameter calculus for a nanoparticle within a matrix, we found that the resolution depends on their relative dielectric constants. In Fig. III - 27b., a study of the resolution between two particles has been also addressed regarding their permittivity ratio with the matrix. We find that particles with higher dielectric contrast get resolved at lower spacings. This proves the conclusion derived from Fig. III - 22, stating that the dielectric contrast of sample heterogeneities enhances the resolution. Thus, the latter is not a fixed value of EFM probe and measurements parameters, but depends on the measured material intrinsic properties.

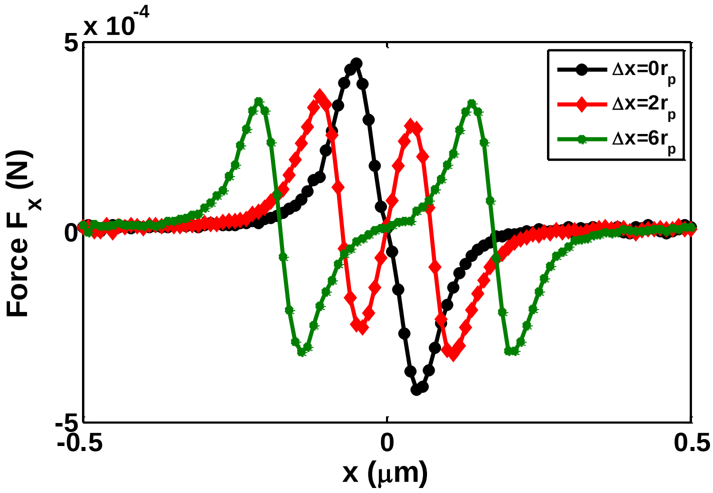

Fig. III - 28 : Lateral electrostatic raw force values on a scan-line over two particles in a matrix for several particles x spacings.

In addition to the effect of particles spacing on the normal component, the impact on the lateral electrostatic force is studied in Fig. III - 28. The expected signal above one nanoparticle ($\varepsilon_p > \varepsilon_m$) has been determined in Fig. III - 23. It is characterized by two branches, one representing an more attractive region towards the particle (left hand side), and towards the matrix (right hand side), characterized by a positive and a negative force, respectively. Thereby, similarly to the normal force interpretation, signals above particles tend to overlap at low spacings (Fig. III - 28). Particles can only be distinguished at intermediate distances. Moreover, when interparticle distance decreases, we notice that the maximum of the attractive part increases, inversely to the repulsive part that decays. Hence, for $\varepsilon_p > \varepsilon_m$, the lateral attraction of the tip towards the inclusions is enhanced at higher inclusions surface density.

This result can be explained by the increasing normal component of the force over the particle for $\varepsilon_p > \varepsilon_m$ as previously explained, enhancing the attraction towards the particles regarding the matrix. However, as the tip moves away from the center of the first particle, it is subjected to a force originating from the matrix, as well as the second particle. The force contrast and the friction are then decreased. The same behavior and interpretation apply for $\varepsilon_p < \varepsilon_m$ with opposite force branches sign. A higher attraction towards the matrix at the curve left hand side is obtained, compared to a reduced attraction at the right hand side (not shown here). Note that in all modeled cases, the lateral force value at the center of the particles remains equal to 0.

5. Tip-Nanodielectric

In the following section, we apply the conclusions and signal interpretations of the previous paragraphs to specifically study the signal above a nanodielectric material. First, an analytical study assuming no restrictions on the spatial resolution is presented. Then, a further investigation of EFM response in a more realistic model is forwarded through numerical simulations.

5.1. Analytical signal preview at perfect spatial resolution

As a first step towards the understanding of EFM-nanodielectric interaction, we considered our material as a superposition of three types of infinite planar dielectric films that correspond to the matrix, particle and interphase. The thickness of each film depends on the position of the probe above the sample as we move from the matrix to the particle. In this case, the model proposed by G. Gomila *et al.* can be adapted to our system in order to calculate the signal at different positions [18]. We studied the case of a particle of r_p = 25 nm and ε_p = 10, an interphase of t_i = 20 nm, and a matrix layer of d = 20 nm above and below the particle-interphase assembly. As described in the beginning of this chapter, the tip was modeled in accordance to commonly used EFM probes with an apex radius R_0 = 25 nm and a cone half-angle θ = 10 ° placed at z = 20 nm above the sample surface. Within this range of material and tip dimensions, both tip apex and cone contributions must be considered into the measured electrostatic force. Moreover, the cantilever contribution to the total capacitance gradient of the probe-sample system was reported to be negligible for comparable sample thicknesses to our nanodielectric model [37].

We adapted the analytical expression for the capacitance gradient of the apex in the limit of infinite planar films of [12], introduced in eq (III. 6), by substituting $\left(\frac{h}{\varepsilon_r}\right)$ by $\left(\frac{h_p}{\varepsilon_p}+\frac{h_i}{\varepsilon_i}+\frac{h_m}{\varepsilon_m}\right)$:

$$C_{apex}{}'(x) = \frac{2\pi\varepsilon_0 {R_0}^2(1-\sin\theta)}{\left(z+\frac{h_p(x)}{\varepsilon_p}+\frac{h_i(x)}{\varepsilon_i}+\frac{h_m(x)}{\varepsilon_m}\right)\left(z+\frac{h_p(x)}{\varepsilon_p}+\frac{h_i(x)}{\varepsilon_i}+\frac{h_m(x)}{\varepsilon_m}+R_0\sin\theta\right)} \tag{III.12}$$

where *z,* the tip-sample distance, represents the thickness of the air layer, modeled with a relative permittivity equals to one. h_p, h_i and h_m are the total thickness of the particle, interphase and matrix at each x position, respectively (see Fig. III - 29).

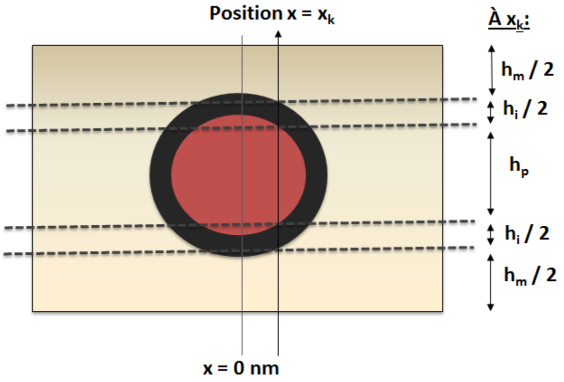

Fig. III - 29 : Illustration of nanodielectric model geometry with the corresponding materials thickness at each lateral x position (x_k) used in our analytical model in eq (III.12) and eq (III.13).

For the cone contribution, we also adapted the analytical expression of ref [18] to our system:

$$C_{cone}{}'(x) = \frac{2\pi\varepsilon_0}{\ln(\tan\frac{\theta}{2})^2} \times \left[ln\left(\frac{H}{z+\frac{h_p(x)}{\varepsilon_p}+\frac{h_i(x)}{\varepsilon_i}+\frac{h_m(x)}{\varepsilon_m}}\right) - 1 + \frac{R_0\, cos^2\theta\,/\sin\theta}{z+\frac{h_p(x)}{\varepsilon_p}+\frac{h_i(x)}{\varepsilon_i}+\frac{h_m(x)}{\varepsilon_m}+R_0(1-\sin\theta)}\right] \tag{III.13}$$

and since $F = -\frac{1}{2}\frac{\partial C}{\partial z}{V_{DC}}^2$, the total electrostatic force writes:

$$F = \frac{1}{2}\left({C_{apex}}' + {C_{cone}}'\right){V_{DC}}^2 \qquad \text{(III.14)}$$

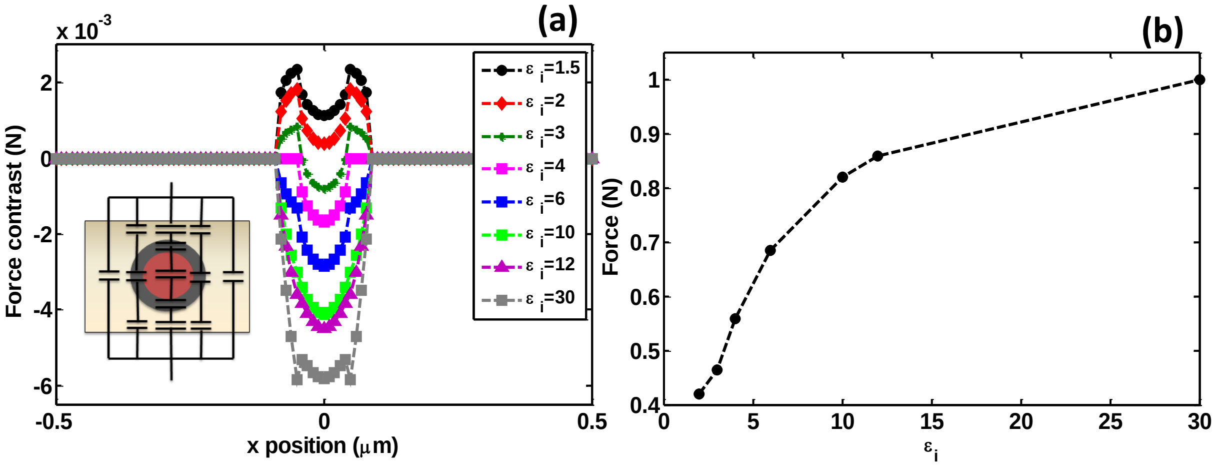

Fig. III - 30 : Analytical model: a. Force calculation on a 1 µm region using the nanodielectric model for a particle of ε_p = 10 and r_p = 25 nm, interphase thickness t_i = 20 nm in a matrix of ε_m = 4 and at 20 nm depth from upper and lower surfaces; b. Force values of Fig. III - 30a. at the center (x = 0 µm) for different interphase permittivities.

We present in Fig. III - 30a. the calculated electrostatic force contrast sensed by the tip for a scan of 1 µm around the nanodielectric central region for different interphase permittivities. We notice that with a perfect resolution, the signal changes in a non-monotonous way when the tip moves away from the center, and it becomes static once the tip is located above the matrix alone. Specifically, for interphase permittivities below 4, which corresponds to the matrix permittivity, or higher than 10, which corresponds to the particle permittivity, the signal contrast changes at two interfaces: particle-interphase and interphase-matrix.

In order to analyze these contrasts, our system can be further simplified to an association of capacitors in series divided into three main lateral regions between the center and extreme borders (see inset Fig. III - 30 a.):

a) The center composed by particle, interphase and matrix sections;
b) The interphase borders composed by interphase and matrix sections;
c) The matrix alone.

As we have seen in above paragraphs, depending on the permittivity and the thickness of the films at each position, the effective permittivity of the multilayered regions changes. Then, the interaction for the nanodielectric model properties, at different regions, can differ. Moreover, the interphase acts on both regions a) and b), either by increasing, or decreasing their resulting force. It can also be noticed that sufficiently high interphase permittivities yield to more gradual signal change between the center and the matrix regions. This can be explained by the predominance of the interphase on the signal for high permittivities.

Fig. III - 30b. presents normalized absolute force values at the center. The force strengthens with interphase permittivity for fixed particle and matrix properties. Here also, the rising intensity can be explained by the increased equivalent permittivity, and consequently, the equivalent capacitance at the central region.

However, this analytical expression does not take into account the position in the *z* direction of the film. As we have seen in Fig. III - 12, the film position regarding the upper surface is crucial. This approximation also neglects the contribution of the electrostatically coupled region. Hence, a more realistic modeling must be forwarded.

Note that in addition to electrostatic force measurements, we have performed the same type of calculations for the force gradient after the integration of equations (III.12) and (III.13). Similar tendencies for the force gradient compared to those obtained for the force presented in Fig. III - 30 were obtained. Hence, as we present hereafter numerical simulations of the electrostatic force; the same conclusions will be supposed to be appropriate for force gradient signals.

5.2. Numerical simulations of EFM tip-nanodielectric interaction

Numerical modeling in general and finite-element simulation in particular is an accurate method to study the interaction between an EFM probe and sophisticated geometries such as those encountered in a nanodielectric model. As we have described in above sections, to present, analytical models have been only suitable for laterally homogeneous dielectrics. Moreover, most analytical models have been focusing on dielectric thin and thick films but rarely on superposed dielectric films. Hence, there is no analytical method to completely model our system that is laterally inhomogeneous at the nanoscale and composed of several superposed materials. In this thesis, we chose finite-element modeling with Comsol® Multiphysics package for all simulations of tip-sample interactions, including nanodielectrics.

The probed region of the nanodielectric model consists of a nanoparticle surrounded by an interphase placed in a matrix. The polymer matrix is represented as a disk of 20 µm diameter, thickness *h*, and dielectric constant ε_m. Similarly to the description of the adopted model of a nanodielectric at the beginning of this chapter, we modeled the nanoparticle as a solid sphere of radius r_p and dielectric constant ε_p. The particle is buried at a certain depth *d*, from the top and the bottom of the matrix. The interphase around the nanoparticle was modeled as a spherical shell of thickness t_i and dielectric constant ε_i (Fig. III - 2).

5.2.1. EFM signal over a nanodielectric: particle-interphase-matrix

5.2.1.1. Force contrast versus interphase permittivity

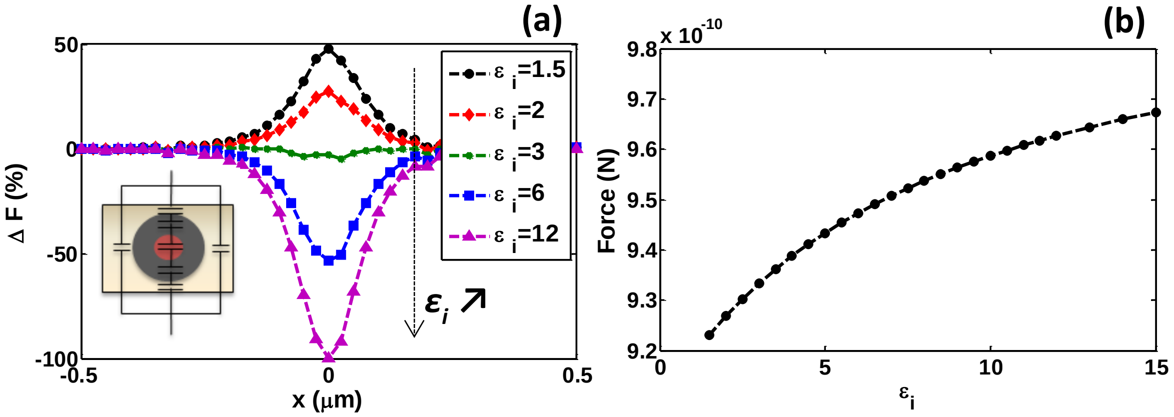

Fig. III - 31 : Numerical simulations: a. EFM normalized signal contrast on a 1 µm scan over a nanodielectric of ε_m = 4, ε_p = 10, r_p = 25 nm, t_i = 20 nm and at 20 nm from upper and lower surfaces, inset: capacitance model of the nanodielectric comparing center to border scan line regions; b. Force value at the center of the same system presented in Fig. III - 31a. calculated in 2D axisymmetric dimensions at the center (*x* = 0 µm) for different interphase permittivities.

We present in Fig. III - 31 a. the result of 2D calculations of the force on a scan line over the nanodielectric probed region for different interphase permittivities. We show that although the probe encounters basically three main regions of different capacitances (Fig. III - 30), the expected signal with numerical modeling of the system is characterized by one maximum and a certain HWHM, similarly to the case of one homogeneous particle in a matrix. The force contrast and HWHM depend on the interphase permittivity; both can either increase or decrease, and the sign of the force contrast can even change. This behavior can be explained by the fact that EFM detects the particle-interphase assembly as one apparent particle with one effective permittivity having a diameter $D_{eff} = 2(r_p + t_i)$. This type of explanation concerning the effective change in permittivity and equivalent diameter of a particle surrounded by a shell (without a matrix) has been already proposed in ref [33]. In the assumption of a uniform electric field within the particle, L. Fumagalli *et al.* used the model given in ref [47] correlated to numerical simulations, to detect the core of a virus through effective permittivity change of its core-shell composition form preserving the same dimensions. That work is however performed in air, and not in a matrix.

Therefore, a further explicit explanation of these numerical model results can be obtained by assimilating our system to an association of capacitors in series, this time, at two main regions (see inset Fig. III - 31 a.):

a) The center composed of particle, interphase and matrix;
b) The matrix alone.

The apparent permittivity becomes higher or lower than matrix one, depending on the relative permittivities and dimensions of the different material components, which explains contrast variations. A unique contrast is observed due to the approximate detection of a probed region wider than that of perfect resolution analytical study. Besides force contrasts, we show in Fig. III - 31 b. the absolute force values change at the central region for the same parameters of Fig. III - 30. We find that the signal increases together with the interphase permittivity. This result is in accordance with Fig. III - 9a.: the force intensifies regarding the dielectric permittivity of a dielectric film, and tends to saturate at high permittivities.

The behavior of force values at the center is also in accordance with what we have seen in the approximate analytical simulation presented in Fig. III - 30b. The analytical equation reflects the response provided by all material components at a specific lateral position as a combination of capacitors in series. This confirms that the EFM tip is sensitive to a general response of the connected materials in a nanodielectric model.

5.2.1.2. Force contrast versus interphase thickness

In Fig. III - 32 a. and b., the changes in force contrasts for a fixed interphase permittivity of $\varepsilon_i = 2$ and 12, respectively, is shown for different interphase thicknesses. Keeping same depths from upper and lower surfaces, the contrast is amplified regarding the interphase thickness in both cases. Similarly to Fig. III - 31, we explain this result by the effective permittivity of the particle-interphase assembly, which, as long as it diverts from matrix permittivity, presents higher contrasts.

Furthermore, the corresponding absolute force values at the sample center are traced in Fig. III - 33. The absolute value of the central force decreases with t_i for both simulated cases of ε_i. This signal tendency is similar to that obtained over a homogeneous film of increasing thickness. It is also similar to the signal change over multilayered samples presenting a varying geometry, contributing to an effective permittivity decrease. Since our system is composed of several superposed materials, the second interpretation must be selected. It is indeed verified for the case of $\varepsilon_i = 2$ lower than both matrix and particle permittivities. However, for $\varepsilon_i = 12$, this interpretation is inconsistent unless the increase in interphase thickness effect on electrode separations is faster than the contribution to the effective permittivity.

Moreover, we notice from Fig. III - 31 and Fig. III - 32 that for certain critical interphase permittivities and thicknesses, the force contrast can greatly decrease and hence, reach the detectability limit of EFM. This indicates that certain conditions might not allow detecting the interphase with EFM even if it is physically present. Consequently, in the following sections, discussions and simulations about interphase detectability within characteristic EFM limits are forwarded.

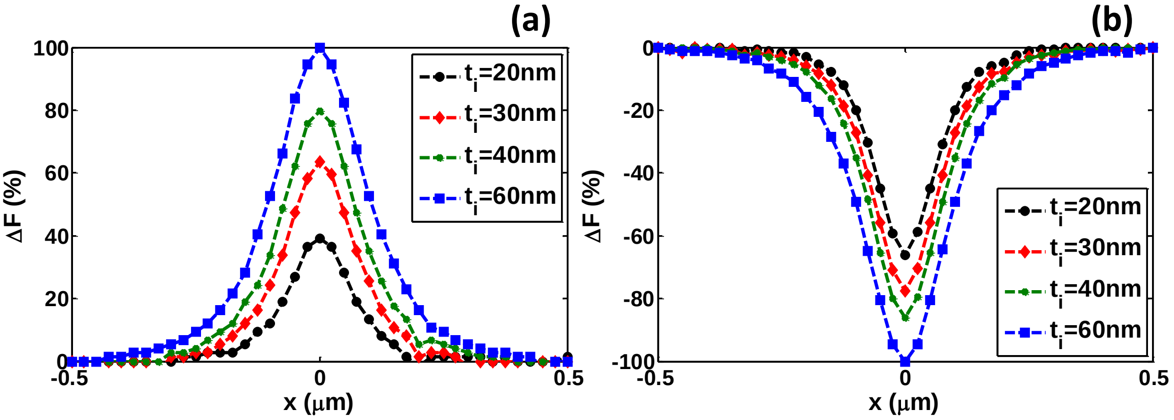

Fig. III - 32 : Normalized force percentage regarding the matrix force value, on a 1 µm scan over a nanodielectric for different interphase thicknesses for $\varepsilon_m = 4$, $r_p = 25$ nm, $\varepsilon_p = 10$, 20 nm from upper and lower surfaces and a. $\varepsilon_i = 2$ and b. $\varepsilon_i = 12$.

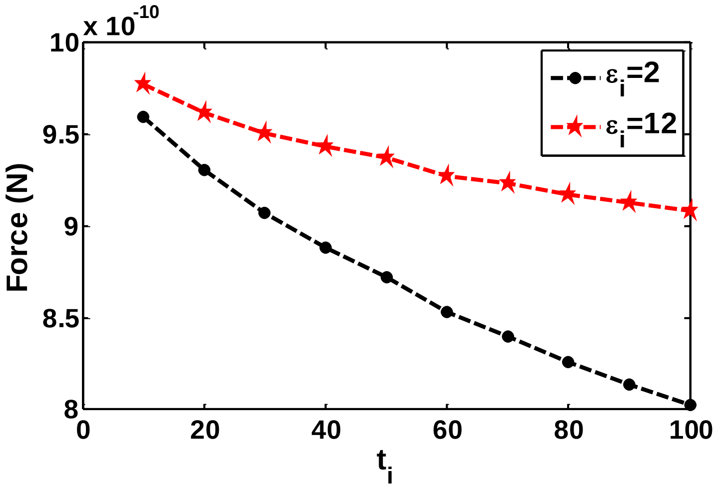

Fig. III - 33 : Raw force intensities corresponding to the samples of Fig. III – 5 a. and b. at the center ($x = 0$ µm), for different interphase thicknesses.

5.2.2. Interphase detectability limits

5.2.2.1. No matrix above and below the particle

a) Interphase detectability conditions

In order to detect the interphase, two main conditions should be accomplished. The first one is to localize the particle-interphase assembly completely embedded within the matrix, and the second one is to identify a difference between the presence and the absence of the interphase. Note that sometimes the particle-interphase below the matrix can still be perceived on the surface topography. In such cases, the first condition is no more mandatory.

In order to accomplish the first condition, the force contrast *ΔF* between the matrix and particle-interphase assembly must be detectable. Thus, Δ*F* should be higher than the noise that we considered to be equal to 10 pN, typically [48].

As an example, Fig. III - 34 presents two cases for particle permittivities, $\varepsilon_p = 10$ and $\varepsilon_p = 4$, both possessing a radius $r_p = 25$ nm and placed within a matrix of permittivity $\varepsilon_m = 4$. The permittivity $\varepsilon_p = 10$ can model aluminum oxide nanofillers, and $\varepsilon_p = 4$, silicon dioxide nanofillers. The curve A of Fig. III - 34a. shows for an aluminum oxide nanofiller the variation of the absolute values of the force contrast Δ*F* versus interphase permittivity ε_i for an interphase thickness $t_i = 20$ nm (inset A). Thus, the interval of critical permittivities ε_{ic}^A for which the assembly is undetectable with these values of r_p and t_i is deduced (see annotations on Fig. III - 34a.).

Then, to accomplish the second condition, we present on the curve B of Fig. III - 34 a., the force difference between presence and absence of interphase (inset B). This difference must also exceed the detectability limit, which is verified for interphase permittivities outside the interval ε_{ic}^B (see Fig. III - 34a.).

The final right condition is the combination of these two intervals, which goes in the case of aluminum oxide, from the minimum of the first one to the maximum of the second one.

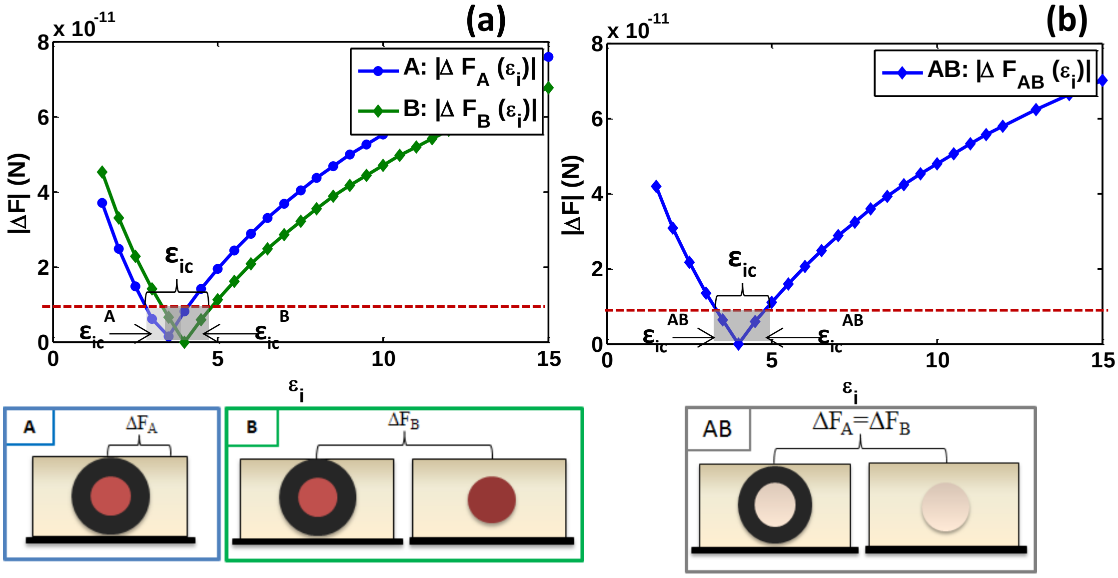

Fig. III - 34 : Force contrast absolute values between particle-interphase assembly and matrix, for a nanoparticle of 25 nm radius and 20 nm interphase thickness; a. for an $\varepsilon_p = 10$, inset A: particle-interphase assembly detection, inset B: interphase detection (assembly compared to particle alone); and b. for an $\varepsilon_p = 4$, inset: same conditions for particle-interphase detection and interphase detection.

In the case of silicone dioxide particles of $\varepsilon_p = 4$, having an equal permittivity to the matrix one, as presented in Fig. III - 34 b., both conditions become similar. In fact, ΔF_A becomes equal to ΔF_B and critical interphase permittivities are directly deduced from the unique curve $|\Delta F_{AB}|$.

b) Critical interphase permittivities

Fig. III - 35 a. and b. show the obtained critical interphase permittivities ε_{ic} at different interphase thicknesses for two radii, $r_p = 25$ and 50 nm of aluminum oxide and silicon dioxide nanoparticles, respectively. For both types of particles, we notice that the area between lower and higher ε_{ic} curves decreases with the thickness of the interphase. Thus, higher interphase thicknesses seem to reduce the width of undetectable interphase permittivities.

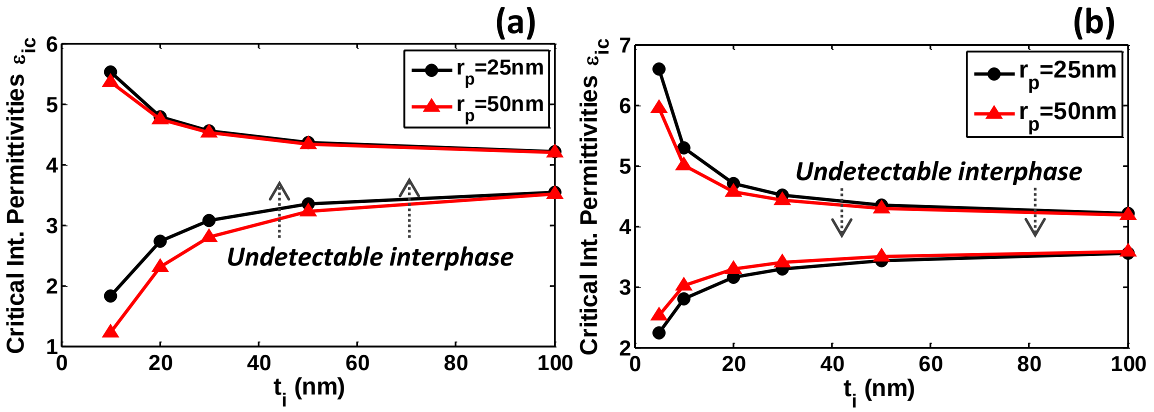

Fig. III - 35 : Final critical combination ε_{ic} values, $[\varepsilon_{i\,Min}, \varepsilon_{i\,Max}]$, at different t_i for interphase detection of a nanoparticle of: a. $\varepsilon_p = 10$, and b. $\varepsilon_p = 4$, having a 25 nm and 50 nm radii in a matrix of $\varepsilon_m = 4$ at zero depth.

c) Critical width of interphase permittivity intervals versus particle permittivity

In Fig. III - 36, we present the width variation of ε_{ic} intervals corresponding to a particle radius $r_p = 50$ nm, for $\varepsilon_p = 2$, 4 and 10, that correspond respectively to a particle of permittivity, lower, equal and higher than the matrix. The width has been measured by subtracting for each t_i case, its corresponding upper and lower ε_{ic} values (($\varepsilon_{ic\,Min} - \varepsilon_{ic\,Max}$) of Fig. III - 35a.). It can be clearly noticed that the intervals width decreases with interphase thickness for the three cases of particle permittivities, in accordance to the observations of above paragraph. Moreover, whatever the thickness t_i is, the lowest critical permittivity interval widths correspond to the case where particle and matrix permittivities are equal. This result appears logical, since in this case, any perceived EFM contrast must be due to the interphase creating the dielectric difference with the matrix. Thus, we conclude that higher interphase thickness, and closer particle and matrix permittivities seem to improve the probability of interphase detection. The investigation of the interphase in EFM is then more likely in nanocomposites with comparable filler and matrix permittivities.

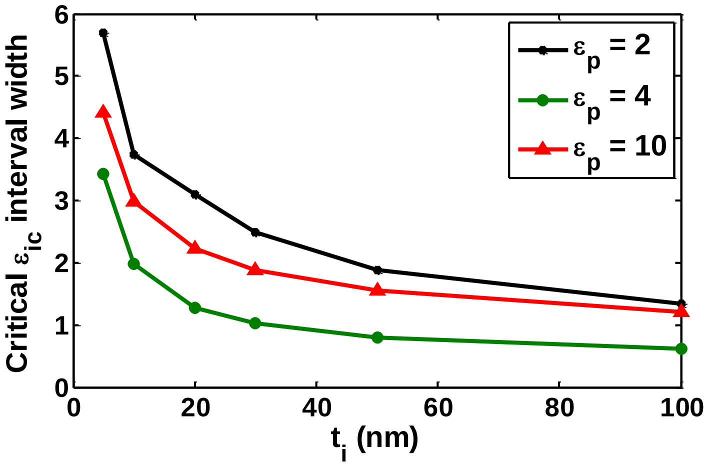

Fig. III - 36 : Width of critical interphase intervals for a particle of 50 nm radius for different particle permittivities below ($\varepsilon_p = 2$), equal to ($\varepsilon_p = 4$) and higher ($\varepsilon_p = 10$) than that of the matrix ($\varepsilon_m = 4$).

5.2.2.2. Matrix layer above and below the particle

a) Force contrast at several particle-interphase depths

In reality, a thin layer of the unchanged polymer matrix should probably exist over and below the particle due to a non-perfectly controlled cutting process of the bulk material when preparing thin sample slices for EFM studies. Therefore, Fig. III - 37 examines the force contrast with 0 nm matrix above and below particle-interphase assembly (inset A), with 20 nm of matrix layer above (inset B), below (inset C) and both above and below the particle-interphase assembly (inset D). The curves were obtained normalizing the measured signal in each case, to the corresponding one at the matrix region. In accordance to the case of a nanocomposite without an interphase (Fig. III - 24), for a nanodielectric model sample, we also found that the addition of a matrix layer simultaneously decreases the contrast and increases the apparent measured EFM diameter of the particle-interphase inclusion.

In order to explain the contrast decrease with the addition of matrix layers, the same analysis adopted for a simple nanocomposite applies to a nanodielectric. In fact, the central region of a nanodielectric only differs with the additional layers corresponding to the interphase. At higher depths, the matrix layer in the central region balances out the effective permittivity of this region with that of the matrix at the borders. The decreasing dielectric difference explains the drop in the signal contrast of (B), (C) and (D) compared to (A).

Moreover, the effect of the depth from the upper surface, d_{up}, is also found to be more pronounced than at low effects. The general decreasing intensity of the electric field in the sample depth in an EFM configuration can explain the difference between (B) and (C) cases. Furthermore, since at similar distances from the surface, thicker samples result in lower electric field intensity, the difference between (C) and (D) is understandable.

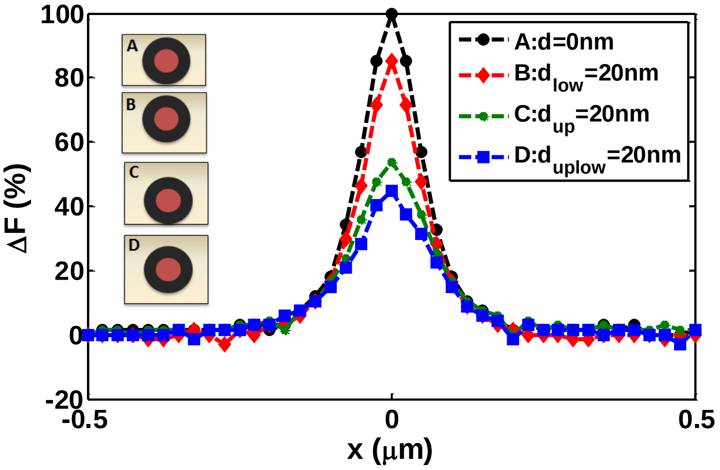

Fig. III - 37 : Simulated 1 μm scans over a nanodielectric with ε_m = 4, ε_p = 10, r_p= 25 nm, ε_i = 2 and t_i = 20 nm at different depths from upper and/or lower surfaces.

b) Critical width of interphase permittivity intervals versus particle-interphase depth

Finally, to complete interphase detection study, we measured the critical width of ε_{ic} intervals for the case of a nonoparticle of 25 nm radius and ε_p = 10, presenting a 20 nm interphase thickness, for several matrix layer depths *d* from lower and upper surfaces. These intervals were calculated following the same procedure explained above (section 5.2.2.1.a). A fast rise in ε_{ic} interval width can be noticed with increasing depth. As examined previously for a nanocomposite, the EFM contrast decreases with increasing particle-interphase assembly depth. The inclusion system becomes more difficult to be detected and thereby, any difference between absence and presence of interphase becomes unnoticeable. For fixed particle and matrix properties, a high dielectric constant interphase is needed to render it detectable. Particularly, at high depths, the ε_{ic} interval width strongly increases, addressing the only possibility of interphases with extremely high permittivity to be detectable. Huge interphase dielectric constants have not been commonly reported in nanodielectrics. This result supposes the impossibility of interphase detection for inclusions deeply embedded in the matrix. We deduce a characteristic thickness of around 70 nm for the detectability depth limit, in the range of our model.

Subsurface imaging has always been a critical issue in scanning probe microscopies [49, 50]. Up to now, researches have only been able to detect metallic nanofillers with EFM, embedded within a limited depth of 40 nm from the matrix upper surface [50]. Thus, one must try to keep a relatively thin matrix layer above the interphase to improve the probability of interphase detection.

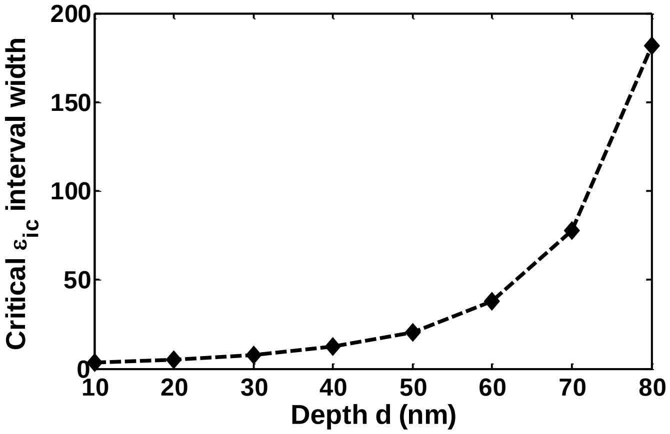

Fig. III - 38 : Width of the critical interphase permittivities interval for 50 nm particle radius, ε_p = 10 and 20 nm interphase thickness calculated at different depths d from upper and lower surfaces.

6. Conclusion

This chapter aimed at improving our understanding of EFM probe response due to several types of dielectric samples. Starting by modeling the specifically chosen sample types and configurations, finally, we were able to interpret the signals over a nanodielectric presenting an interphase with different properties.

A nanodielectric has been electrostatically modeled as an association of three types of dielectric materials differentiated by their dielectric permittivities. The first material type takes the form of a spherical nanoparticle, surrounded by the second material and the resulting system placed into a matrix of the third material.

Based on the configuration of the chosen nanodielectric model, we studied the interaction between the EFM tip and potential sample types and geometries. In particular, we studied the response over bare substrate, planar homogeneous dielectric films, superposed dielectric layers, nanoparticle alone and nanoparticles located within a matrix.

In the absence of a dielectric film, the signal always decreases with the distance between electrodes, and increases with larger tips. Nanometric tip parts have however the greatest impact on force value and sensitivity at low distances.

The signal over homogeneous films rises with the dielectric permittivity of the film and decreases with its thickness. The sensitivity to the dielectric permittivity was found to be favored for materials of low dielectric permittivity and, also, thicker ones. The sensitivity to the film thickness was also proved to be enhanced with a low matrix permittivity and thin films.

For superposed films, the signal detects a general dielectric response from the sample. As a dielectric layer is added on the base matrix, their relative dielectric permittivities will change the signal behavior. When the permittivity of the added layer is higher than the initial layer, it grows the apparent permittivity and thereby, the signal. The latter increases with the added film thickness until reaching saturation of the increasing effective permittivity. The opposite behavior is obtained with the addition of a film with the lowest dielectric permittivity. Care must be taken in the interpretation of EFM experimental results when a possible configuration of the system in the form of superposed layers may be present. Signals might exhibit behaviors in contradiction with conventional ones over homogeneous films.

Next, the response versus a nanoparticle diameter and dielectric permittivity was examined. The signal was found to always rise with the permittivity. On the contrary, the nanoparticle diameter variation exhibits a more complicated effect on the signal. Compared to the response with a matrix possessing similar height, we found that the particle diameter lateral-size, highly affects the physics of the interaction. A certain kind of change in the interaction was found at specific relative values of tip-sample distance, tip radius, particle diameter and permittivity.

For small diameters, the signal starts by decreasing with particle radius. For bigger ones, the interaction keeps on decreasing for low permittivities; whereas for high permittivities, the signal intensifies with the radius. We explained these behaviors with the fact that at low permittivities, the effect of a wider diameter is dominated by the influence on the interelectrode distance, so the signal decreases. Conversely, at higher permittivities, the intrinsic dielectric contribution to the response is more significant, and the broadening of the particle surface with the radius counteracts other effects; hence, increasing the signal. Furthermore, small particles bring the electrodes closer together, thus, the signal is hardly influenced by material polarization contribution. That being so, the increase in tip-substrate distance dominates and explains the drop in these cases, for any permittivity. Nevertheless, we found that particle geometry influence is generally less pronounced either for small particles, or big ones, however, of important permittivities. In conclusion, 3D materials interaction with an EFM probe is difficult to be apprehended intuitively. Several effects co-exist and co-influence the signal. A simulation of the exact geometry of the sample, probe and experimental parameters is then recommended.

The last configuration before directly studying a nanodielectric model sample was a nanocomposite of a homogeneous spherical nanoparticle, introduced into a matrix. We found that the matrix can contribute to the interaction at the middle of the same nanoparticle. Depending on their relative dielectric constants, the matrix affects the effective permittivity of the probed region, and changes the intensity of the signal. Moreover, a high dielectric difference between the inclusion and the matrix proved to enhance EFM contrast and thereby, affect the apparent EFM diameter of the particle. Furthermore, the relative dielectric properties of the nanocomposite can induce either attraction or repulsion in the lateral directions due to normal forces dissymmetry far from the center. We have also brought up the topic of subsurface imaging. Deeply-buried particles were found to exhibit low contrasts and extended EFM apparent diameter. We explained these observations by the effective permittivity of the probed region that gets closer to the matrix alone, decreasing the dielectric contrast, as well as the evanescent electric field in the depth of the sample, reducing the chances of detectability of the buried inclusion. We also showed that EFM lateral resolution is dependent on material properties and the relative dielectric permittivity of its components.

Then, the EFM tip interaction over a nanodielectric material with an interphase was addressed. Although the probe mainly encounters three regions of different capacitances, the signal was found to be only characterized by one maximum and a HWHM. We deduced that the particle-interphase assembly is detected as one apparent particle with one effective permittivity conserving the same diameter of the assembly. The interphase presence is manifested on both signal maximum value in the center and its contrast, and likewise, its HWHM. Thus, certain interphase properties might result in an undetectable signal differences within the sensitivity of the technique. We extracted critical intervals of interphase dielectric constants and permittivities that might show an absence of the interphase, although it is physically present. We found that for a low dielectric permittivity matrix, higher interphase permittivities and thickness, and lower depths, make the interphase more likely to be detectable.

One must note that although we focused exclusively on electrostatic force measurements with EFM, the electrostatic problem can be generalized. In fact, analogous results should hold for force gradient detection and for other scanning probe microscopies such as conductive or scanning microwave microscopy, in which tip and sample geometry and structure influence as well the measured response.

At this stage, we had acquired deeper information about EFM response in front of complex materials, typically, above a nanodielectric. Nevertheless, the study of nanodielectric samples of unknown interphase was considered to be too early. With the very few experimental studies on EFM for interphase characterization, our theoretical simulations become particularly essential to accompany in the following, proper experimental measurements, dedicated to “calibrate” the technique for future interphase study. In this regard, reference materials of relatively known and modifiable composition and shape have been prepared. These reference samples model electrostatically a nanodielectric, since they are made of three dielectric phases, synthesized in a simplified configuration of the particle-interphase-matrix assembly of a nanodielectric. The signature of each dielectric phase is its dielectric permittivity. The following chapter details the choice of constituting materials and preparation methods of these nanodielectric model samples.

7. References

[1] Y. Martin, D. W. Abraham, and H. K. Wickramasinghe, "High ‐ resolution capacitance measurement and potentiometry by force microscopy," *Applied Physics Letters,* vol. 52, pp. 1103-1105, 1988/03/28 1988.

[2] T. Andritsh, "Epoxy based nanocomposites for high voltage DC applications - Synthesis, Dielectric Properties and Space Charge Dynamics," PhD, Technische Universiteit Delft, 2010.

[3] R. Kochetov, "Thermal and Electrical Properties of Nanocomposites, Including Material Processing," PhD, Technische Universiteit Delft, 2012.

[4] I. A. Preda, "Modeling and characterization of nanocomposite materials using dielectric methods," PhD, Université Montpellier 2, 2013.

[5] K. Y. Lau, A. S. Vaughan, and G. Chen, "Nanodielectrics: opportunities and challenges," *IEEE Electrical Insulation Magazine,* vol. 31, pp. 45-54, 2015.

[6] C. Zou, J. C. Fothergill, and S. W. Rowe, "The effect of water absorption on the dielectric properties of epoxy nanocomposites," *IEEE Transactions on Dielectrics and Electrical Insulation,* vol. 15, pp. 106-117, 2008.

[7] T. Tanaka, M. Kozako, N. Fuse, and Y. Ohki, "Proposal of a multi-core model for polymer nanocomposite dielectrics," *IEEE Transactions on Dielectrics and Electrical Insulation,* vol. 12, pp. 669-681, 2005.

[8] J. Seiler and J. Kindersberger, "Insight into the interphase in polymer nanocomposites," *IEEE Transactions on Dielectrics and Electrical Insulation,* vol. 21, pp. 537-547, 2014.

[9] J. C. Pandey and N. Gupta, "Estimation of interphase thickness of epoxy-based nanocomposites," *IEEE Transactions on Dielectrics and Electrical Insulation,* vol. 23, pp. 2747-2756, 2016.

[10] G. M. Sacha, E. Sahagún, and J. J. Sáenz, "A method for calculating capacitances and electrostatic forces in atomic force microscopy," *Journal of Applied Physics,* vol. 101, p. 024310, 2007/01/15 2007.

[11] L. Fumagalli, M. A. Edwards, and G. Gomila, "Quantitative electrostatic force microscopy with sharp silicon tips," *Nanotechnology,* vol. 25, p. 495701, Dec 12 2014.

[12] G. Gomila, J. Toset, and L. Fumagalli, "Nanoscale capacitance microscopy of thin dielectric films," *Journal of Applied Physics,* vol. 104, p. 024315, 2008/07/15 2008.

[13] Y. Yi, C. Jiong, Y. Jingning, X. Dengming, T. Demin, Y. Rui, *et al.*, "Effect of space charge in nanocomposite of LDPE/TiO2," in *Proceedings of the 7th International Conference on Properties and Applications of Dielectric Materials (Cat. No.03CH37417)*, 2003, pp. 913-916 vol.3.

[14] L. Fumagalli, G. Ferrari, M. Sampietro, and G. Gomila, "Dielectric-constant measurement of thin insulating films at low frequency by nanoscale capacitance microscopy," *Applied Physics Letters,* vol. 91, p. 243110, 2007/12/10 2007.

[15] L. Fumagalli, G. Gramse, D. Esteban-Ferrer, M. A. Edwards, and G. Gomila, "Quantifying the dielectric constant of thick insulators using electrostatic force microscopy," *Applied Physics Letters,* vol. 96, p. 183107, 2010/05/03 2010.

[16] C. Riedel, A. Alegria, G. A. Schwartz, J. Colmenero, and J. J. Saenz, "Numerical study of the lateral resolution in electrostatic force microscopy for dielectric samples," *Nanotechnology,* vol. 22, p. 285705, Jul 15 2011.

[17] S. Gómez-Moñivas, L. S. Froufe, R. Carminati, J. J. Greffet, and J. J. Sáenz, "Tip-shape effects on electrostatic force microscopy resolution," *Nanotechnology,* vol. 12, p. 496, 2001.

[18] G. Gomila, G. Gramse, and L. Fumagalli, "Finite-size effects and analytical modeling of electrostatic force microscopy applied to dielectric films," *Nanotechnology,* vol. 25, p. 255702, 2014.

[19] S. Hudlet, M. Saint Jean, C. Guthmann, and J. Berger, "Evaluation of the capacitive force between an atomic force microscopy tip and a metallic surface," *Eur. Phys. J. B,* vol. 2, pp. 5-10, 1998.

[20] E. Castellano-Hernandez and G. M. Sacha, "Finite Conductivity Effects in Electrostatic Force Microscopy on Thin Dielectric Films: A Theoretical Model," *Advances in Condensed Matter Physics,* vol. 2015, p. 6, 2015.

[21] H. W. Hao, A. M. Baró, and J. J. Sáenz, "Electrostatic and contact forces in force microscopy," *Journal of Vacuum Science & Technology B: Microelectronics and Nanometer Structures Processing, Measurement, and Phenomena,* vol. 9, pp. 1323-1328, 1991.

[22] C. Bohm, F. Saurenbach, P. Taschner, C. Roths, and E. Kubalek, "Voltage contrast in integrated circuits with 100 nm spatial resolution by scanning force microscopy," *Journal of Physics D: Applied Physics,* vol. 26, p. 1801, 1993.

[23] L. H. Pan, T. E. Sullivan, V. J. Peridier, P. H. Cutler, and N. M. Miskovsky, "Three‐dimensional electrostatic potential, and potential‐energy barrier, near a tip‐base junction," *Applied Physics Letters,* vol. 65, pp. 2151-2153, 1994/10/24 1994.

[24] J. Hu, X.-D. Xiao, D. F. Ogletree, and M. Salmeron, "Imaging the Condensation and Evaporation of Molecularly Thin Films of Water with Nanometer Resolution," *Science,* vol. 268, pp. 267-269, 1995.

[25] M. S. Lhernould, A. Delchambre, S. Régnier, and P. Lambert, "Electrostatic forces in micromanipulations: Review of analytical models and simulations including roughness," *Applied Surface Science,* vol. 253, pp. 6203-6210, 5/15/ 2007.

[26] W. F. Brown, "Electrostatique et Magnétostatique. Emile Durand. Masson, Paris, 1953, xii - 774 pp. Illus. Paper, 5760 fr., cloth, 6335 fr," *Science,* vol. 120, pp. 62-63, 1954.

[27] G. Mesa, E. Dobado‐Fuentes, and J. J. Sáenz, "Image charge method for electrostatic calculations in field‐emission diodes," *Journal of Applied Physics,* vol. 79, pp. 39-44, 1996/01/01 1996.

[28] S. Belaidi, P. Girard, and G. Leveque, "Electrostatic forces acting on the tip in atomic force microscopy: Modelization and comparison with analytic expressions," *Journal of Applied Physics,* vol. 81, pp. 1023-1030, 1997/02/01 1997.

[29] S. Belaidi, F. Lebon, P. Girard, G. Leveque, and S. Pagano, "Finite element simulations of the resolution in electrostatic force microscopy," *Applied Physics A,* vol. 66, pp. S239-S243, 1998.

[30] C. Riedel, R. Arinero, P. Tordjeman, M. Ramonda, G. Lévêque, G. A. Schwartz*, et al.*, "Dielectric properties of thin insulating layers measured by Electrostatic Force Microscopy," *Eur. Phys. J. Appl. Phys.,* vol. 50, p. 10501, 2010.

[31] Z.-Y. Li, B.-Y. Gu, and G.-Z. Yang, "Scanning-electrostatic-force microscopy: Self-consistent method for mesoscopic surface structures," *Physical Review B,* vol. 57, pp. 9225-9233, 04/15/ 1998.

[32] Z. Jia, S. Ito, K. Hosobuchi, S. Goto, Y. Shimizu, G. He*, et al.*, "Characterization of electrostatic force for scanning electrostatic force microscopy of micro-structured surface," *International Journal of Precision Engineering and Manufacturing,* vol. 14, pp. 1543-1549, 2013.

[33] L. Fumagalli, D. Esteban-Ferrer, A. Cuervo, J. L. Carrascosa, and G. Gomila, "Label-free identification of single dielectric nanoparticles and viruses with ultraweak polarization forces," *Nat Mater,* vol. 11, pp. 808-816, 09//print 2012.

[34] C. T. Dervos, J. A. Mergos, P. D. Skafidas, M. D. Athanassopoulou, and P. Vassiliou, "Effect of water on permittivity of nanodielectrics exposed to the atmosphere," *IEEE Transactions on Dielectrics and Electrical Insulation,* vol. 16, pp. 1558-1565, 2009.

[35] I. Casuso, L. Fumagalli, G. Gomila, and E. Padrós, "Nondestructive thickness measurement of biological layers at the nanoscale by simultaneous topography and capacitance imaging," *Applied Physics Letters,* vol. 91, p. 063111, 2007/08/06 2007.

[36] C. Riedel, R. Arinero, P. Tordjeman, G. Lévêque, G. A. Schwartz, A. Alegria*, et al.*, "Nanodielectric mapping of a model polystyrene-poly(vinyl acetate) blend by electrostatic force microscopy," *Physical Review E,* vol. 81, p. 010801, 01/08/ 2010.

[37] G. Gramse, G. Gomila, and L. Fumagalli, "Quantifying the dielectric constant of thick insulators by electrostatic force microscopy: effects of the microscopic parts of the probe," *Nanotechnology,* vol. 23, p. 205703, 2012.

[38] L. A. Miccio, M. M. Kummali, G. A. Schwartz, Á. Alegría, and J. Colmenero, "Dielectric spectroscopy at the nanoscale by atomic force microscopy: A simple model linking materials properties and experimental response," *Journal of Applied Physics,* vol. 115, p. 184305, 2014.

[39] F. Gao, "Clay/polymer composites: the story," *Materials Today,* vol. 7, pp. 50-55, 2004/11/01/ 2004.

[40] E. Castellano-Hernandez, J. Moreno-Llorena, J. J. Saenz, and G. M. Sacha, "Enhanced dielectric constant resolution of thin insulating films by electrostatic force microscopy," *J Phys Condens Matter,* vol. 24, p. 155303, Apr 18 2012.

[41] C. Riedel, "Dielectric and mechanical properties of polymers and macro and nanoscale," Institut d'électronique et des systèmes, University of Montpellier, 2010.

[42] G. Gomila, D. Esteban-Ferrer, and L. Fumagalli, "Quantification of the dielectric constant of single non-spherical nanoparticles from polarization forces: eccentricity effects," *Nanotechnology,* vol. 24, p. 505713, 2013.

[43] J. A. Stratton and J. A. Stratton, "The Electrostatic Field," in *Electromagnetic Theory*, ed: John Wiley & Sons, Inc., 2015, pp. 160-224.

[44] O. Pfeiffer, R. Bennewitz, A. Baratoff, E. Meyer, and P. Grütter, "Lateral-force measurements in dynamic force microscopy," *Physical Review B,* vol. 65, p. 161403, 04/08/ 2002.

[45] J. Konior, "Vertical and lateral electrostatic forces in a tip-plane system studied with a Green function plus surface charge method," *Journal of Applied Physics,* vol. 101, p. 084907, 2007/04/15 2007.

[46] B. Uluutku and M. Z. Baykara, "Artifacts related to tip asymmetry in high-resolution atomic force microscopy and scanning tunneling microscopy measurements of graphitic surfaces," *Journal of Vacuum Science & Technology B, Nanotechnology and Microelectronics: Materials, Processing, Measurement, and Phenomena,* vol. 33, p. 031802, 2015.

[47] S. Giordano, "Dielectric and elastic characterization of nonlinear heterogeneous materials," *Materials,* vol. 2, pp. 1417-1479, 2009.

[48] R. Arinero, C. Riedel, and C. Guasch, "Numerical simulations of electrostatic interactions between an atomic force microscopy tip and a dielectric sample in presence of buried nano-particles," *Journal of Applied Physics,* vol. 112, p. 114313, 2012/12/01 2012.

[49] H. T. Thompson, F. Barroso-Bujans, J. G. Herrero, R. Reifenberger, and A. Raman, "Subsurface imaging of carbon nanotube networks in polymers with DC-biased multifrequency dynamic atomic force microscopy," *Nanotechnology,* vol. 24, p. 135701, Apr 05 2013.

[50] O. A. Castañeda-Uribe, R. Reifenberger, A. Raman, and A. Avila, "Depth-Sensitive Subsurface Imaging of Polymer Nanocomposites Using Second Harmonic Kelvin Probe Force Microscopy," *ACS Nano,* vol. 9, pp. 2938-2947, 2015/03/24 2015.

Chapter IV

Samples and experiments description

Chapter IV

"The most beautiful experience we can have is the mysterious. It is the fundamental emotion that stands at the cradle of true art and true science." Albert Einstein

1. Introduction

As defined earlier in this thesis, a dielectric model of a nanodielectric possessing an interphase is the association of three materials of different permittivities. The nanodielectric model is constituted by a nanoparticle covered homogeneously by the second material that plays the role of the interphase, and the matrix layer, which is the third material covering all. Moreover, since the dielectric model is used in order to set up an appropriate EFM experimental protocol for interphase detection, a judicious choice of packed materials must be performed. According to Chapter II, samples components must possess appropriate permittivities and geometry/dimensions ratios in order to present sufficient EFM contrast allowing interphase study.

Keeping that in mind, and using some of the most accurate nanomaterials fabrication methods, we designed and prepared samples in the form of a stack of several dielectric materials: spherical nano and mesoparticles (or sub-microparticles) covered by one or two different thin layers of other materials.

Samples description will be presented first, followed by the description of the adopted and developed EFM experimental protocols and the basic principles of the complementary characterization techniques.

2. Samples description

The materials used in this study consist of spherical particles deposited on a metallic substrate and subsequently covered by either one or two shells. Two types of spherical particles were used: silicon dioxide (SiO_2) of 20 nm average diameter and polystyrene (PS) of 250 nm and 380 nm approximate diameter. We mainly utilized 3 types of shells: aluminum oxide (Al_2O_3), silicon dioxide and polyvinyl acetate polymer (PVAc). Note that all of the materials are electrical insulators with different dielectric permittivities. The range of layers thickness is between 20 and 200 nm. Hereafter, particles deposition and preparation methods with layers synthesis and deposition techniques will be detailed.

2.1. EFM substrates

2.1.1. Description

Samples substrates adapted for EFM measurements were based on (100) oriented silicon (Si) single-crystals of high resistivity with a thin native oxide layer (Si-Mat Silicon materials, ref: 1014G1007). A 50 nm gold thin film has been sputtered above a 10 nm chrome fixing layer with plasma sputtering deposition to obtain a conductive substrate surface (see 2.1.2 paragraph). Consequently, a conductive silver paste was sufficient to establish the electrical contact with EFM metallic specimen holders. Silicon based substrates were chosen owing to their very flat surface with low roughness (< 1 nm), much lower than the diameter of the particles to be subsequently deposited [1].

2.1.2. Metallization - Plasma sputtering deposition

Plasma Sputtering Deposition (PSD) is a physical vapor deposition method of thin films in which a high-purity source (or target material) is subjected to a plasma gas. The energetic atoms/ions produced in the plasma gas knock-off source atoms, which then travel and condense into a thin film on the substrate (Fig. IV - 1).

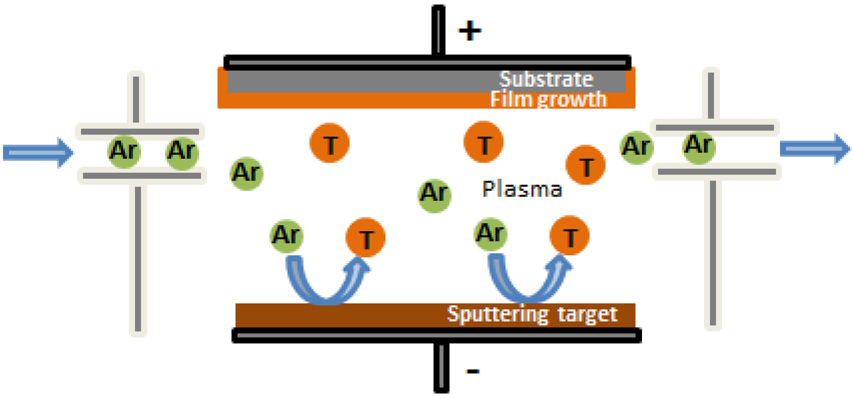

Fig. IV - 1 : Schematic of a plasma sputtering deposition.

Under a vacuum environment, the sample is first screened by a shutter and the sputtering gas is introduced into the chamber until the desired pressure is stably reached. A radio frequency power is applied next to ignite the plasma. Some of the produced ions, electrons and radicals are in high energy states and hence bombard the target material settling the sputtering process [2]. Once the pre-sputter sequence is finished, the shutter opens and the extracted species get then directed ballistically in the deposition chamber, and condense on the entire surface including the substrate. During deposition, substrates are rotated to enhance uniformity. The shutter is timed to close after desired film thickness is achieved. When different types of materials are deposited, shutters are also used to expose the only desired material source. Some of the advantages of PSD are the high purity film and the fact that no additional heating of the substrate is needed.

An Alcatel sputtering plasma argon has been used to deposit a 50 nm gold (99.95 % purity) above a 15 nm chrome (99.95 % purity) fixing layer on the silicon substrates. The process has been performed under 0.03 mbar with 130 W radio frequency power.

2.1.3. Surface activation - O_2 plasma

For subsequent polystyrene spheres deposition, EFM substrates were exposed to oxygen (O_2) plasma and little argon (Ar) percentage for 2 minutes at 50 W and 0.011 mbar to remove organic compounds and enhance hydrophilicity [3-6].

2.2. Particles

2.2.1. Silicon dioxide particles

2.2.1.1. Definition

Silicon dioxide, also known as silica, is an oxide of silicon with the chemical formula: SiO_2. The structure of SiO_2 is sketched on Fig. IV - 2. Silica can come naturally, or synthetically, in a crystalline or amorphous state. However, in nature, SiO_2 is often found as a crystalline solid, with a unit structure like that in Fig. IV - 2b. Each silicon atom is covalently bonded to four oxygen atoms (O) in a tetrahedral way (Fig. IV - 2a.). Although Si is combined to 4 O atoms, the proportion is actually 1:2, which explains the empirical formula: SiO_2. In amorphous SiO_2, no long-range order is present, but there is local ordering with respect to the tetrahedral arrangement of O atoms around Si (Fig. IV - 2c.).

SiO_2 covalent bonds are highly polar. However, due to the symmetry of the tetrahedral molecule geometry, the resulting SiO_2 structure is non-polar. On the other side, SiO_2 nanoparticles for example are often reported as highly attractive centers for water molecules, which are polar molecules. One possible reason behind this attraction is the electrostatic hydrogen bonds that develop between partially positive hydrogen atoms in water and partially negative oxygen in silica. Furthermore, some fabrication techniques introduce polar groups in the lattice or at the surface conferring upon silica network polar properties, e.g, the left hydroxyl groups at the surface of sol-gel synthesized silica gels [7] or water molecules and silane functions with plasma-enhanced chemical vapor deposition [8]. A generally accepted relative dielectric permittivity of SiO_2 is 3.9 [9-11].

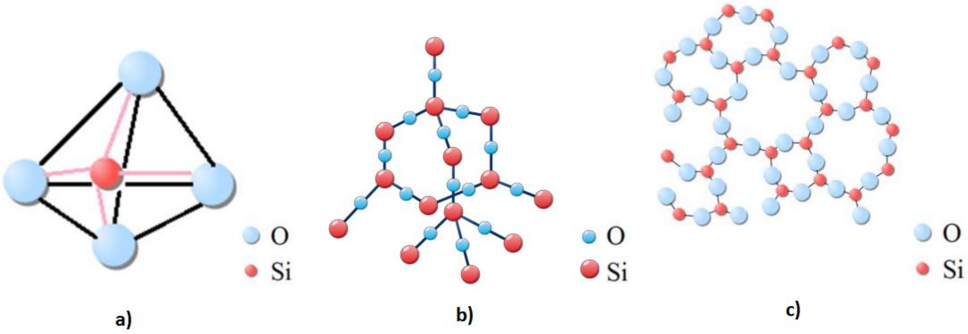

Fig. IV - 2 : Silicon dioxide chemical structure of: a. tetrahedral basic unit, b. quartz like silica crystal and c. amorphous network [12].

2.2.1.2. Silicon dioxide nanoparticles deposition

SiO_2 nanoparticles were used as purchased from Sigma-Aldrich (ref: 791342), possessing a non-crystalline structure with a nominal diameter < 50 nm, 2.3 triethoxylpropylaminosilane functionalized and dispersed in aqueous solution. In order to spread out the nanoparticles on the substrates, 10 µL of SiO_2 solution was first mixed with 200 mL of Milli-Q water (18.5 Ω.m) for 30 min with sonication by a tip (20 %). Then, the same amount of the resulting solution (SiO_2 + Milli-Q water) was mixed with ethanol absolute. For this step, an ultrasonic bath was used for 5 min. Finally, one droplet of the prepared solution was spread on the substrate placed at plane position until the solvent was naturally dried in air, in a partly opened box.

2.2.2. Polystyrene particles

PS has been chosen as a second type of particles to represent the template for our model samples. In fact, PS deposition has been extensively studied in literature for highly organized and controllable structures, thereby, optimal for precise synthesis of model samples.

2.2.2.1. Definition

Polystyrene (PS) is a synthetic, thermoplastic polymer with an aromatic structure. It is formed by the polymerization of the styrene monomer resulting in the chemical formula: $(C_8H_8)_n$ (Fig. IV - 3). Polystyrene is a non-polar polymer with accepted relative permittivity around 2.6 [9, 10]. Moreover, PS dielectric polarization has been already characterized at the nanoscale in the literature [10, 13].

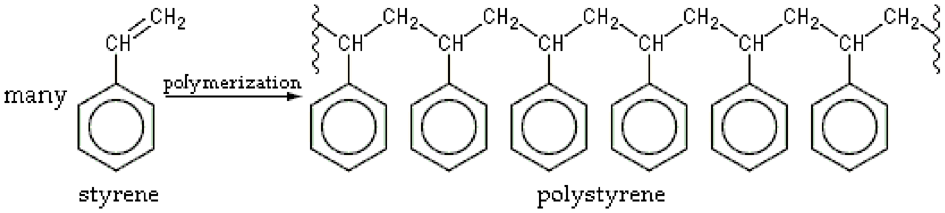

Fig. IV - 3 : Chemical reaction diagram showing polystyrene formed by polymerization of the styrene monomer [14].

2.2.2.2. PS deposition

PS particles of 1 µm initial diameter purchased as a colloidal liquid solution (Sigma-Aldrich, ref: 89904) were deposited on substrates using the self-assembly property of PS spheres (PSS) [15-17]. PSS self-assembly produces periodically organized monolayers tightly adsorbed on the majority of substrate surface.

These monolayers (or multilayers) are usually used as mask/substrates for metal or ceramic deposition for numerous applications. After thin films deposition, the spheres are subsequently removed, keeping special designed structures. This combination of bottom-up and top-down techniques is known as nanosphere lithography. Further information on nanosphere lithography can be found elsewhere [17-19]. However, in our case, PSS were not removed, but used as base particles for ulterior addition of dielectric layers, modeling interphase and matrix. Several methods for PS monolayer deposition have been adopted in literature, each with different degrees of complexity and efficiency [17, 20-23].

In this work, two methods have been developed for PSS deposition based on two techniques: floating-dip and spin-coating.

a) Floating-dip

For the floating-dip method, we dropped 40 µL of the initial solution diluted with equal amount of ethanol, on a glass substrate of 2 × 2.5 cm^2 approximate surface area. Glass substrates were treated with oxygen plasma for 2 minutes in order to increase the hydrophilicity of the surface [3-6]. During deposition, we fixed the substrate at 45 ° approximately from the horizontal. Then, we gently immersed the glass substrate into water as shown in Fig. IV - 4a. A glass vessel of 7 cm diameter and 100 mL capacity filled with 80 mL of Milli-Q water was used. PSS start to organize themselves on the water surface forming a hexagonally close-packed monolayer. A succeeded organization can be directly noticed with bare eyes due to the diffraction of visible light from the formed PSS closely-packed monolayer with periodic nanometric separations (see Fig. IV - 7) [24]. Different orientations of the crystal domains result in different colors at the same white light angle. A drop of sodium dodecyl sulfate (SDS) solution (10 wt. % in water) was subsequently added on the water surface to consolidate the particles (Fig. IV - 4b.). Then, the PSS monolayer was cautiously transferred on the substrates prepared for EFM characterization as shown in Fig. IV - 4c. The substrate was kept to dry in air on an inclined substrate holder, in a partly opened box.

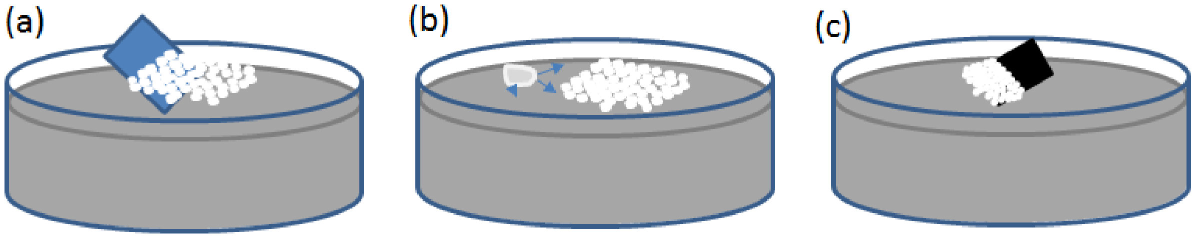

Fig. IV - 4 : PSS deposition process, a. insertion of glass substrates with the solution of PSS (white spheres) organizing on the air-water interface; b. addition of SDS drop, and c. transfer on substrates of PSS monolayer.

Please note that the experimental protocols of SiO_2 nanoparticles deposition and PS floating-dip self-assembly have been mainly developed by the PhD student Viktoriia Fedorenko at the European Institute of Membranes (IEM) in Montpellier, thanks to the collaboration with Dr. Mikhael Bechelany.

b) Spin-coating

Another technique has been investigated in order to deposit PSS in a relatively more reproducible way. In fact, floating-dip method is useful since it can provide a large monolayer out of one deposition. However, many steps are experimentalist controlled, and hence, lack of sufficient precision for reproducible results at any deposition time/conditions.

Similarly to the previous method, we mixed a 1:1 solution of initial PSS solution and ethanol. The resultant diluted solution is kept for 1 min in an ultrasounds bath to ensure that particles had been homogeneously dispersed. EFM substrates have been hydrophilized in O_2 plasma (50 W, 0.001 mBar). 7 µL of the solution was then spread over the whole substrate surface before spinning. We used the following program for the spinning process:

i. 15 s at 100 rpm with a ramp of 2000 rpm
ii. 30 s at 500 rpm with a ramp of 2000 rpm
iii. 60 s at 2000 rpm with a ramp of 2000 rpm

Each spinning step has a great influence on the final result [25, 26], in addition to the influence of substrate surface hydrophilicity and area, solution concentration, solvent used, temperature, humidity etc.

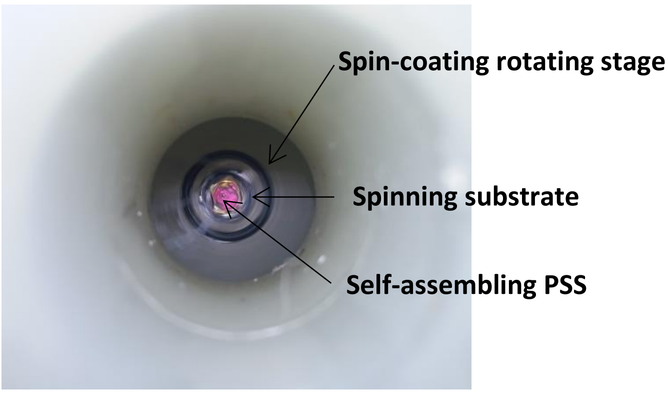

Fig. IV - 5 : Image of spin-coating self-assembly of PSS.

c) Comparison of PS deposition methods

As it has been previously noticed, the transfer of PSS with floating-dip method from the glass substrate to the water-air interface is highly sensitive to any mechanical vibration. Since this step is manually driven, then, in addition to other ambient thermodynamical parameters, this reduces the chances of self-assembly. Moreover, when the assembly has been well established, the extraction of the monolayer to the substrate must also be carefully driven in order to preserve the monolayers at the air-water interface. Furthermore, this transfer can carry an amount of PSS from the water surface that has not been ordered and will overlap on the extracted monolayer, reducing then the percentage of organized regions (Fig. IV - 6a.).

On the other hand, since most spin-coated monolayers procedures are automated, this technique provides relatively more efficient and reproducible results. Nevertheless, the drawbacks are the coverage or the surface density of the periodic monolayers. PSS self-assembly with spin-coating is well known to suffer of holes-like domains in PS monolayers (Fig. IV - 6b.) [25]. Hence, although EFM measurements do not require more than a few microns of ordered domains, the optical positioning of the probe before engage suffers from this level of precise resolution.

Hence, in both methods, either small regions limited by multilayered (or unordered PSS) or small regions limited by void areas, can relatively complicate the positioning for AFM imaging. Therefore, these two methods have been used interchangeably, however preserving one specific synthesis technique for each set of compared samples.

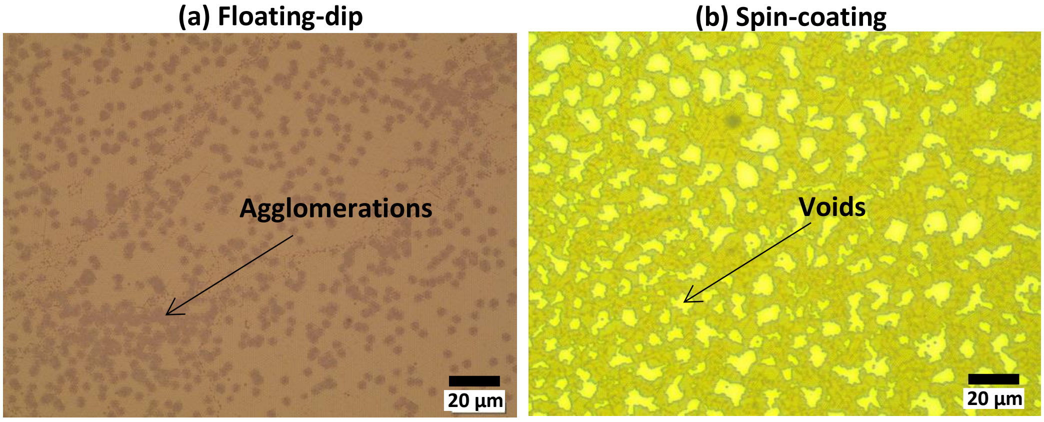

Fig. IV - 6 : Optical microscopy images of PSS deposited with: a. floating-dip method, and b. spin-coating.

2.2.2.3. PSS diameter modification - Dry O_2 plasma etching

As the process of plasma etching has proven to effectively reduce particles size [27, 28], the films of PS particles were radially etched in a plasma reactor with O_2 as a process gas. Since substrates possess a slower etching rate, gold surface topography remained almost unchanged. The samples were inserted into the reactor, and chamber pressure reached $\approx$ 0.011 mbar. Oxygen was introduced using a needle valve, and the pressure was equilibrated to 0.6 mbar by adjusting the valve. After equilibrium pressure is reached, a radio frequency power of 50 W at 0.15 A was applied until obtaining the desired diameter (around 250 nm after 15 min etching) [29]. It must be noted that although particle diameter can be monitored by the amount of removed substance, the distance between particles center is fixed and is determined by the initial diameter of the closely packed particles (spacing ≈ 1 - 1.2 µm).

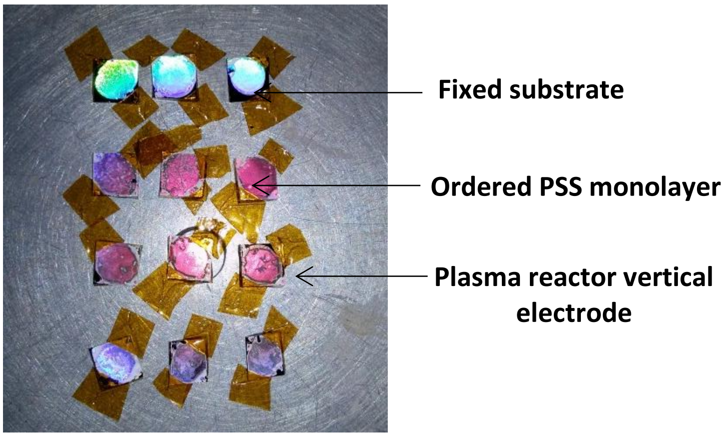

Fig. IV - 7 : Image of substrates with PS self-assembled spheres fixed to one electrode for plasma etching (vertical electrodes).

Concerning the mechanism of dry etching, the latter proceeds in the following four main steps after plasma generation:

i. Reaction species, such as neutral radicals and ions (in the case of O_2 gas), are produced in the plasma;
ii. Those reaction species are transported and adsorbed on the target sample to be etched

iii. Reactions (chemical or physical) take place at the target sample surface, and byproducts are created;
iv. Byproducts desorb from the target sample surface, ending etching procedure.

Etching driven by radicals reaction species proceeds in the three dimensions since resultant species move randomly by Brownian motion [30]. This confers an isotropic etching that is supposed to preserve a spherical shape for PS spheres to a good extent.

In addition to material etching, O_2 plasma activates the surface state of the sample, PSS and gold substrate surface for subsequent thin films deposition. This is due to the creation of hydrophilic surface groups, in addition to the rougher PS surface that results after dry etching [3-6, 31].

2.3. Shells

2.3.1. Alumina thin films

2.3.1.1. Definition

Aluminum oxide, also known as alumina, is a metal-oxide of chemical structure: Al_2O_3. In addition to silica, alumina is, too, among the widely used inorganic compounds in electrical engineering. The generally reported dielectric permittivity of Al_2O_3 is around 9.8 [10, 11].

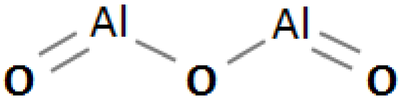

Fig. IV - 8 : Aluminum oxide molecular chemical structure.

The atomic layer deposition method (ALD) was used in order to grow alumina layers above nanoparticles [32, 33].

2.3.1.2. Atomic layer deposition

ALD is a thin film deposition technique where the thickness of the film is precisely controlled at the atomic level. The deposition is based on sequential chemical reactions between gas precursors and the surface of the material. After each cycle of one precursor, an inert gas is introduced to remove the remaining precursor and the resulting byproducts (see Fig. IV - 9).

For alumina deposition, we used trimethylaluminium, (TMA) or (Al $(CH_3)_3$), as an aluminum precursor, H_2O as an oxygen source and argon as an inert gas. The precursor is initially a liquid solution. The evaporated molecules at the surface of the liquid are used at their vapor pressure. The generally accepted and dominant reaction mechanism occurring at steady state (Fig. IV - 9) [34] is:

$$\_OH + Al\,(CH_3)_{3(g)} \rightarrow \_O\_Al\_(CH_3)_2 + CH_{4(g)} \qquad \text{(IV.1)}$$

$$\_CH_3 + H_2O_{(g)} \rightarrow \_OH + CH_{4(g)} \qquad \text{(IV.2)}$$

A custom-made ALD reactor at the European Institute of Membranes (IEM) was used for the synthesis of Al_2O_3 films [35]. ALD was performed using sequential exposures of TMA and H_2O separated by a purge of argon with a flow rate of 100 standard cubic centimeters per minute (sccm). The deposition regime for Al_2O_3 consisted of 0.1 s pulse of TMA, 40 s of exposure, 60 s of purge with argon followed by 2 s pulse of H_2O, 40 s of exposure, and finally 60 s purge with argon. The film thickness was determined by the number of ALD reaction cycles. Thus, 20, 60, 100, 150 and 200 nm thick Al_2O_3

layers were deposited by 100, 300, 500, 750 and 1000 number of ALD cycles, respectively. The deposition was performed at 80 ° C (< glass transition temperature of polystyrene). The typical growth rate for Al_2O_3 coating during these cycles is found to be 0.2 nm per cycle. The final theoretical configuration of the samples is presented in Fig. IV - 10.

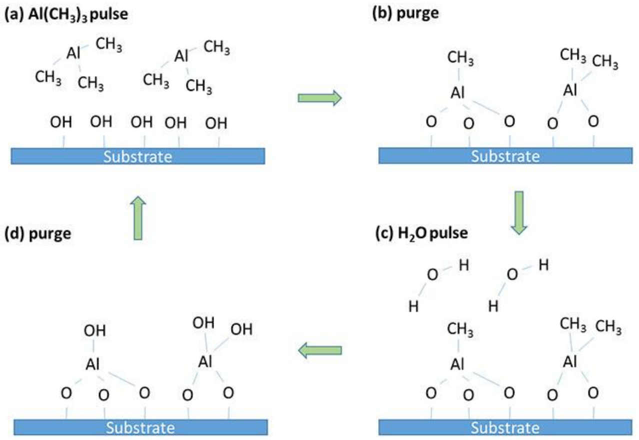

Fig. IV - 9 : Atomic layer deposition cycle showing the formation of Al_2O_3 coating using TMA and water precursors and purge steps that remove byproducts [36].

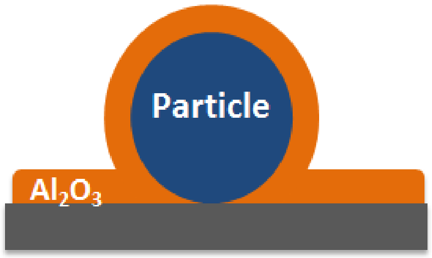

Fig. IV - 10 : Schematic of the resulting sample configuration after ALD.

Since precursors quantity is enough to occupy the whole chamber volume, and hence, cover the whole sample surface, and with the enough chosen exposure time, chemical reactions are supposed to occur evenly on the whole sample surface including the underside of the round beads. The resultant configuration is hence believed to be closely similar to the sketch of Fig. IV - 10. Note that the perfect aspect of film line at particle edges with the substrate is somehow exaggerated. This figure does not also show the relative roughness of PS spheres surface. The characterization of PS+Al_2O_3 samples will be studied in Chapter V.

2.3.2. Polyvinyl acetate thin films

2.3.2.1. Definition

Polyvinyl acetate (PVAc) is a thermoplastic synthetic polymer with the chemical formula: $(C_4H_6O_2)_n$. PVAc is a hydrophobic polymer with a dielectric permittivity of 2.6 at ambient temperature [9, 10].

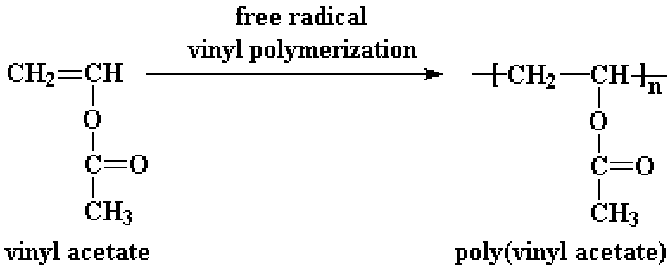

$$CH_2{=}CH{-}O{-}C({=}O){-}CH_3 \xrightarrow{\text{free radical vinyl polymerization}} {-}\!\left[CH_2{-}CH(O{-}C({=}O){-}CH_3)\right]_n\!{-}$$

Fig. IV - 11 : Chemical reaction diagram showing polyvinyl acetate production after polymerization of vinyl acetate monomers [37].

2.3.2.2. Spin-coating

We used spin-coating to deposit PVAc films on the surface of the particles with or without Al_2O_3. A solution of PVAc mixed with a highly evaporating solvent has been used. We mixed 0.25 mg of PVAc with 5 mL toluene and stirred them with magnetic mixing until no visible particulates are visible (around 30 min). The spinning program used for thin film deposition is the following:

i. 15 s at 100 rpm with a ramp of 2000 rpm
ii. 15 s at 500 rpm with a ramp of 2000 rpm
iii. 60 s at 2000 rpm with a ramp of 2000 rpm

Once spin-coated, samples were kept to dry further in ambient conditions. As a first step, films homogeneity and thickness have been verified and monitored upon the deposition of PVAc on bare substrates, with no PS particles. However, since our samples are highly rough due to the sub-micrometric PS spheres, the mechanism of film spreading is not obvious to expect [38]. A detailed discussion on the characteristics of the resulting film over PS+Al_2O_3 templates will be forwarded in Chapter V.

2.3.3. Silicon dioxide thin films - Plasma sputtering deposition

Silicon dioxide layers have been deposited with plasma sputtering in a Plassys 450S reactor using a high purity silicon dioxide target source.

The deposition regime for SiO_2 consisted on a preliminary 20 s exposure to 100 sccm Ar plasma at 50 W while substrates and SiO_2 target sample are screened. Then, the target shutter was opened, and a presputtering step was maintained for 30 s with 15 sccm Ar and 0.8 sccm O_2 plasma gas at 200 W. Next, the planetary rotation of substrates was launched and shutters opened, permitting the deposition of SiO_2 film. The latter thickness was determined by the exposure time to SiO_2 sputtering. The final expected configuration of the samples is likewise similar to Fig. IV - 10. However, in contrary to ALD, it must be noted that although sputtered SiO_2 molecules invade the whole deposition chamber; due to the spherical geometry of PS particles on the surface, a shadowing effect can occur. Then, the final geometry is probable to slightly differ from Fig. IV - 10. In fact, SiO_2 might not cover the very low parts of the particles and the below substrate regions.

3. EFM experiments description

EFM measurements were performed with a commercial AFM (Bruker, previously Veeco, Enviroscope^{TM}). The probe consists of metal covered tips (Budget Sensors: ElectriMulti75-G and µmasch: HQ:NSC18/Pt) supported by a cantilever electrically connected to a metallic sample holder and biased at an electrical potential. Manufacturers claim a radius below 25 nm and an average stiffness of 3 N/m.

In this entire thesis, EFM measurements have been performed in the force gradient detection method. However, both DC and AC electrical excitations were used. Since the basics of EFM experiments have been already described in Chapter II, in the following, each method is briefly reminded with further specification on the adopted experimental protocols.

3.1. DC-force gradient detection

The property of interest in our study is the pure dielectric contribution of each probed region. This particular response lies within the capacitance C of the probe-sample system. As mentioned in Chapter II, the 2ω force-gradient extraction $G_{2\omega}$ accounts to the unique capacitance contribution, contrarily to the DC component G_{DC}, influenced by static surface charges and contact potential. Nevertheless, since DC-biased force gradient detection is usually available in any standard AFM equipped with EFM module, we developped an experimental protocol that permits the study of the pure capacitive contribution from DC component.

During the second scan, the frequency shifts Δf_0 due to the force gradients sensed by the probe can be expressed in the DC excitation mode as a second order polynomial function of the bias voltage V_{DC}. Combining equations II.28 to II.17 of Chapter II, Δf_0 (V_{DC}) writes:

$$\Delta f_0(V_{DC}) \cong \alpha_{DC}\, V_{DC}{}^2 + \beta\, V_{DC} + \gamma \qquad \text{(IV.3)}$$

where $\alpha_{DC} = -(f_0/4K) \times C''$. We remind that C'' is the second derivative of the probe-to-sample capacitance; so it can be deduced that α_{DC} depends solely on the dielectric properties of the probed region. On the other hand, β and γ are the coefficients that depend on local surface charges and contact potential in addition to the capacitance derivatives.

The parabolic dependency of Δf_0 to DC bias voltages has been studied in details in our work published in ref [39]. It has been able to point out the presence of surface charges over epoxy samples without preliminary charge injection. As it can be shown in Fig. IV - 12a. and b., a linear tendency of the curves predominates. β and γ coefficients have been used then to indicate the sign and an order of magnitude of these localized charges. This has been made possible by associating the values of the latter coefficients to numerical and analytical modelling of the probe surface capacitance and the electrostatically coupled area, respectively.

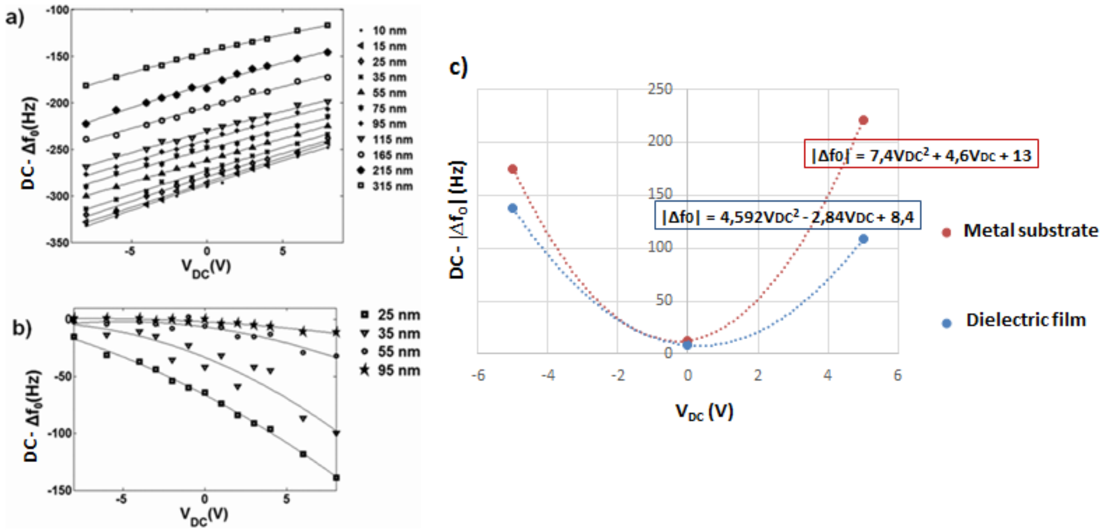

Fig. IV - 12 : a. and b. Experimental DC - Δf_0 curves obtained on epoxy samples at different tip-to-sample distances with a positive charge density and negative charges densities, respectively [39]; c. an example of DC measurements and second order polynomial fitting lines over a bare metallic substrate and a thin aluminum oxide dielectric film.

Consequently, for the DC-adopted protocol, EFM maps were performed at different regions of all samples at V_{DC} = 0, 5 and -5 V. Then, the average Δf_0 on a few number of pixels at the top of the spherical particles has been extracted for each voltage. We fitted Δf_0 (V_{DC}) curves with a polynomial function similar to eq (IV.3) in order to extract α_{DC} coefficient at different tip-sample distances (see Fig. IV - 12c.). This coefficient has been used in ref [40], associated to modeling with the Equivalent Charge Method, in the aim of extracting the dielectric permittivity of PVAc particles placed into a PS matrix.

3.2. AC-force gradient detection

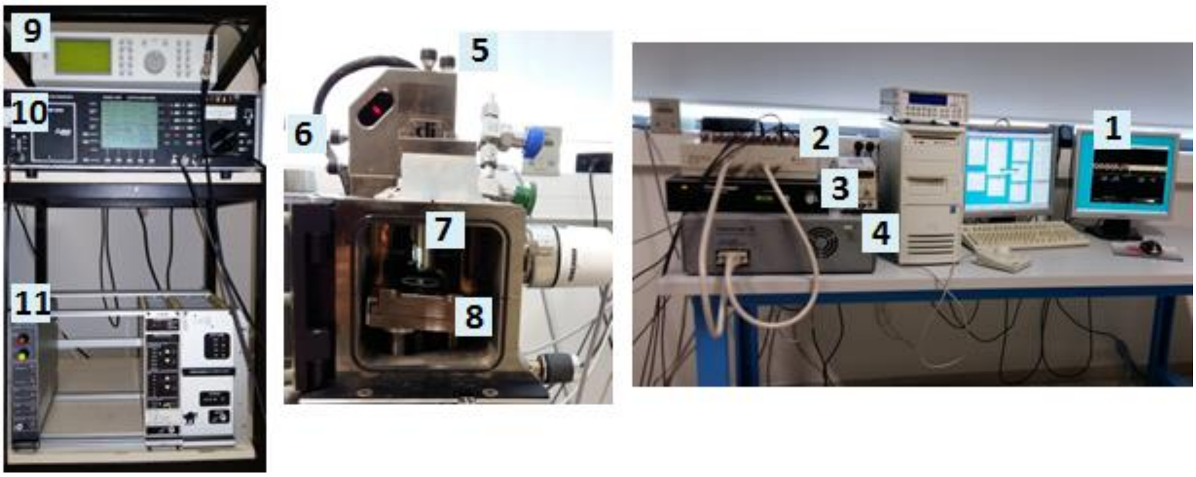

Fig. IV - 13 : EFM apparatus setup including the external modules for AC force gradients measurements: (1) PC, (2) signal access module, (3) Digital Instuments Enviroscope controller, (4) Nanoscope IV controller, (5) laser regulation knobs, (6) photodiode regulation knobs (internal mirror), (7) AFM head, (8) stage, (9) arbitrary function generator, (10) lock-in amplifier, (11) 0-5V switch.

With AC excitation, $G_{2\omega}$ component has been measured with custom-made external installations to the standard EFM apparatus. A NanoScope^{TM} Signal Access Module (SAM) (Fig. IV - 13, (2)) was plugged to both, Digital instruments and Nanoscope IV controllers (Fig. IV - 13, (3) and (4), respectively) in order to get access to their output signals, along with monitoring measurement inputs and feedback controls. An external arbitrary function generator (Sony Tektronic - AFG310) (Fig. IV - 13, (9)) was used to provide the AC excitation signal between the probe and the sample during the second EFM scan. Appropriately collected from the SAM output channels, the measured phase shifts were sent to an external LIA (EG&G Instruments - Model 5302, Fig. IV - 13, (10)), which was used to demodulate the $\Delta\Phi_c$ (2ω) at the second pass. The same AC voltage of the external generator was utilized as the reference signal for the LIA. The internal LIA bandpass filter, set at the double of the electrical excitation reference frequency, gave rise to the RMS of the 2ω demodulated signal. A 0 - 5 V switch (Fig. IV - 13, (11)) was used to monitor the bias so it only gets injected during the interleave mode (the second pass). For that, the switch was biased by the internal interleave channel signal, fixed to 5 V. $\Delta\Phi_c$ (2ω) raw data were finally collected on an EFM image at the computer through an analog-digital converter, with a spatial resolution proportional to the measurement speed, set to 0.1 Hz in the majority of experiments.

The AC electrical pulsation ω must be chosen wisely:

i. Lower than the probe mechanical resonance angular frequency ω_0 of the cantilever in order to avoid interference with the mechanical drive signal that oscillates at ω_0,
ii. lower than the cutoff frequency of the first-order like behavior of phase shifts signals (see Chapter II, paragraph 4.2.2.3.b),
iii. and large enough to minimize lock-in detection noise signal in order to increase the number of demodulation integration cycles.

We used a 100 Hz electrical frequency, much lower than f_0 (60-70 kHz). The cutoff frequency is around 270 Hz. Hence, the reduction due to filtering of the signal was calculated to be around 0.5 (eq (II.34)). Moreover, as we set the LIA to the fast demodulation mode, the time constant of 20 ms is sufficient for accurate measurements.

Raw $\Delta\Phi_{2\omega}$ electrostatic data was acquired on EFM images in Volts. When comparison to simulations was expected, a conversion from Volts to Hz was needed at the first place. Afterwards, since we mainly studied α coefficients, then similarly to DC experiments, $\alpha_{2\omega}$ were measured.

Therefore, the following conversion steps from raw $\Delta\Phi_{2\omega}$ to real $2\omega\text{-}\Delta f_0$, and subsequently real $\alpha_{2\omega}$ coefficients, were adopted (Fig. IV - 14):

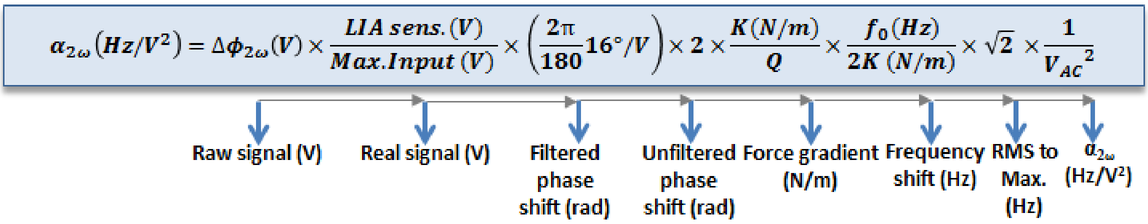

$$\alpha_{2\omega}(Hz/V^2) = \Delta\phi_{2\omega}(V) \times \frac{LIA\ sens.(V)}{Max.Input\ (V)} \times \left(\frac{2\pi}{180} 16°/V\right) \times 2 \times \frac{K(N/m)}{Q} \times \frac{f_0(Hz)}{2K\ (N/m)} \times \sqrt{2} \times \frac{1}{{V_{AC}}^2}$$

Fig. IV - 14 : Conversion coefficients from raw $\Delta\Phi_{2\omega}$ in Volts, to real $\alpha_{2\omega}$ in Hertz per square Volts.

Simulations compute α_{DC}; so in order to correlate AC measurements to simulations, it must be noted that the amplitude of the demodulated 2ω-signal is a DC response, and hence experimental $\alpha_{2\omega}$ are static values. Comparing equations (II.28) and (II.30) of Chapter II, it can be deduced that $\alpha_{2\omega}$ are simply equal to the half of α_{DC} at similar measurement conditions. Hence, α_{DC} simulation values were divided by 2 to get the corresponding simulation-$\alpha_{2\omega}$ and compare to experimental-$\alpha_{2\omega}$values of Fig. IV - 14.

4. Complementary characterization techniques

In addition to the main characterizations with EFM, the following described techniques accompanied EFM measurements for comparisons and complementary informations on our samples. In particular, the elemental chemical composition, thin films thickness and surface composition phases were investigated.

4.1. PeakForce tapping - Quantitative Nanomechanical Mapping

PeakForce tapping-Quantitative Nanomechanical Mapping (PF-QNM) is an easy-to-use, quantitative AFM method to measure materials nanomechanical properties [41]. The principle of PF-QNM lies on the extraction of force-distance curves that are allowed since the probe is slowly oscillating (≈ 1 kHz) [42]. At each probing position, the force is measured regarding the separation between the tip and the sample. Close to the surface, the force highly strengthens, which roughly drags the tip to jump into contact with the surface. As the separation continues to decrease, both bodies stay in contact while repulsion forces between them increase. When the set-point PeakForce is reached, the tip is brought to retract back from the surface. However, when the sample is relatively soft, the tip stays adhered to a certain extent. This is reflected in a hysteresis on the force-distance curve (Fig. IV - 15). The maximum adhesion force with the sample depends on the relative mechanical properties of the tip-sample system. Since the tip is usually sufficiently stiff, a high adhesion force represents a soft specimen, as it retains longer the tip to the surface.

In this work, measurements were performed on a Bruker MultiMode V8 microscope at room temperature. An RTETAP525 cantilever model has been used, supplied by Bruker. On each force curve, the maximum force value corresponds to the peak force and it is used as the feedback signal. The cantilever repeats the cycles from (A) to (E) (Fig. IV - 15) at a fixed frequency, typically 1 kHz. The tapping amplitude was set at a constant value of 250 nm.

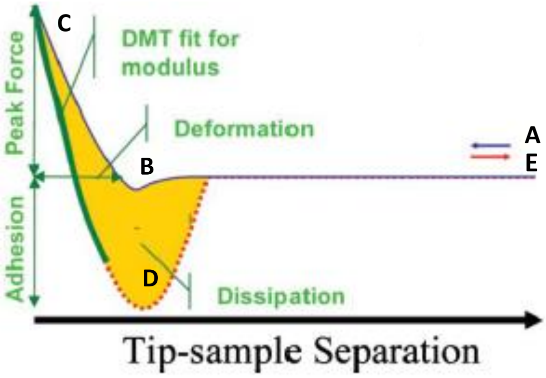

Fig. IV - 15 : Force curve versus tip-sample separation including: (A) approach, (B) jump-to-contact, (C) PeakForce, (D) adhesion and (E) retraction. [41].

4.2. Scanning electron microscopy

Scanning Electron Microscopy (SEM) is a type of electron microscopies, widely applied to the study of nanoparticles and thin films, owing to the high resolutions attainable with an electron-probe and the versatility of acquired informations.

SEM uses a beam of electrons that are accelerated with a high voltage in a vacuum chamber, and focused with electromagnetic or electrostatic lenses [43]. Electron-matter interaction results in several elastic and inelastic phenomena allowing for the derivation of lots of informations on the sample [43, 44]. Fig. IV - 16b. summarizes all possible phenomena and resultant output from the interaction of a high energetic electron beam with a specimen.

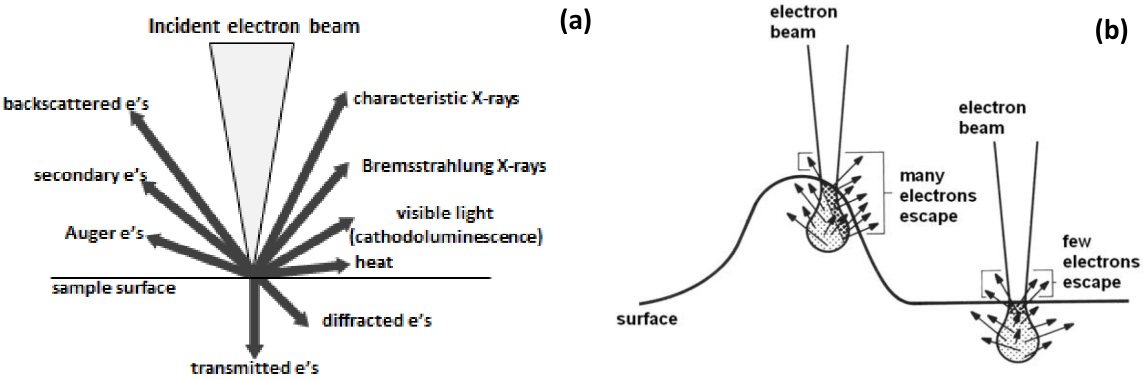

Fig. IV - 16 : a. The different types of interaction between electrons (e's) and a sample, and b. Schematic of secondary-electrons imaging: contrast is dominated by the so-called edge effect, resulting in an image of sample morphology [45].

Typical SEM signals used for imaging include principally secondary electrons (SE). SE result when a primary electron transfers its energy to a bound electron, enough to knock it out of the atom. The extracted electron is the secondary electron. Since SE possess a low-energy, they can get easily scattered and hence, they are usually collected from the first few nanometers of the surface. Consequently, SE contrasts represent the morphology of the specimen (see Fig. IV - 16b.).

Backscattered electrons (BSE) are primarily electrons that, within the specific angle of incidence, have been elastically scattered from the positively charged nucleus, instead of being captured by it. BSE will hence come back out with, optimally, no energy loss. Therefore, BSE contrasts are dependent on the atomic number of the probed region atoms (or on the density).

When the incident electron beam possesses sufficient energy, it can remove a core electron, leaving subsequently a hole. This vacancy is likely to be filled up by an electron from a higher level. The energy released from the recombination can be: either transferred to another electron that gets ejected from the atom, with this second electron called Auger electron, or emitted by a photon. Since the initial vacancy took place in the inner shells, high energy photons get released, typically, X-rays.

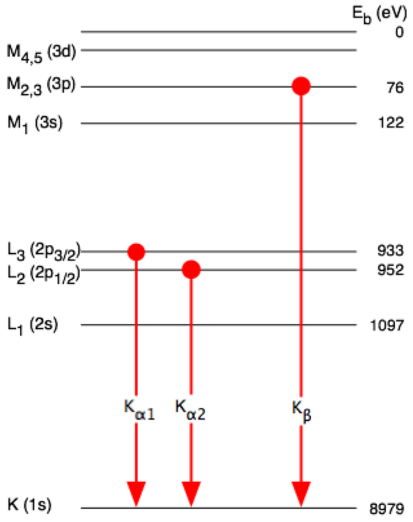

Fig. IV - 17 : Energy levels diagram of copper showing K_α and K_β transitions [44].

Each atom has a set of unique electron energy levels. Consequently, the interpretation of photons and particularly, the X-ray dispersion spectrum is used to analyze the elemental composition of the specimen lines (called Energy Dispersive X-ray Spectrometry or EDS) are commonly identified by two letters and a number (Fig. IV - 17):

i. The first letter indicates the shell containing the initial vacancy (according to Rutherford-Bohr model of an atom: K, L, M…),
ii. the second one specifies the group to which the transition belongs in a decreasing order of importance that filled up the vacancy (α for a L to K or M to L transition, β for a M to K transition…),
iii. and the number denotes the intensity of the line within the group in a decreasing order (1, 2, 3…).

An FEI, INSPECT S50 electron microscope was used, equipped with an EDAx-AMETEK system for EDS measurements. The used acceleration voltage was set to 20 kV, with around 124 eV resolution taken at 10.1 mm from the surface.

4.3. Ellipsometry

Ellipsometry is a highly sensitive optical measurement technique to study the dielectric properties (refractive index, dielectric permittivity tensor), roughness, crystallization and thickness of thin semi-transparent films.

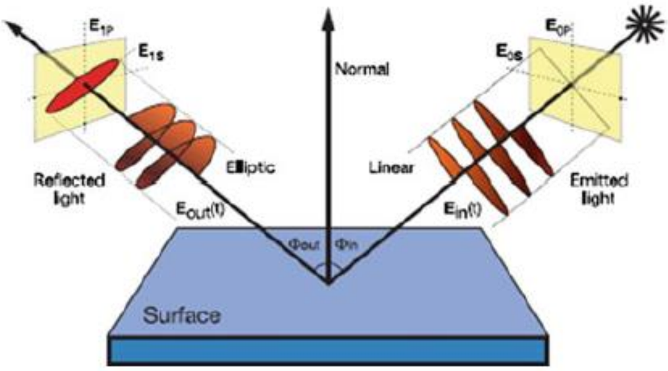

Fig. IV - 18 : Schematic view of an ellipsometry measurement in reflection configuration. The linearly polarized beam is incident on the sample from the right side. After reflection, the beam polarization state becomes elliptical and pursuits its propagation on the left side [46].

The incident light beam is linearly polarized with a polarizer and sent at a fixed angle Φ_{in} to the sample surface. The electromagnetic wave polarization is defined by the direction of its oscillating electric field. The latter can be viewed as the addition of two vectors: one in the plane of incidence (p polarized) and the second normal to the plane of incidence (s polarized). Since the p and s components do not reflect in the same way at the interface of two media of different refractive index, the linearly polarized incident beam becomes elliptical upon reflection [47]. The reflected beam is analyzed, and two quantities are measured denoted by Ψ and Δ, which are related to Fresnel reflectance coefficients by the following [48]:

$$\tan\psi\, e^{i\Delta} = \frac{R_p^*}{R_s^*} = f(n_i, k_i, t_i, \lambda, \Phi_{in}) \qquad \text{(IV.4)}$$

R_p^* and R_s^* are respectively the p polarized and s polarized reflectance Fresnel coefficients. These are complex vectors. Ψ is the ratio of the amplitude of R_p over R_s,and Δ represents the phase lag between the p and s components of the reflected elliptical wave. Ψ and Δ are thus a function of the properties of each layer of the sample: refractive index, absorption coefficient and thickness. λ is the wavelength of the incident light, usually known in addition to Φ_{in}. In order to determine material properties, a spectroscopic measurement is usually performed. Afterwards, the obtained Ψ and Δ spectrum must be inevitably fitted to an appropriate model in order to identify the properties of the sample. A common model used for dielectrics, where there is no need to enter the refractive index of the film, is the dispersion model. Ellipsometry owes its high sensitivity to the measurement of a relative value (ratio of R_p over R_s), unlike absolute light measurements spectroscopies.

4.4. Stylus profilometry

The principle of stylus profiling is at the heart of the operation of first scanning probe microscopies [49]. A stylus profilometer uses a physical probe to directly reproduce the height of a step on the sample surface. While the probe is moving in contact along the surface, a feedback loop monitors the amount of torque acting on the stylus from the pits and valleys of the surface. A set-point force value is thereby maintained by mechanically displacing the *z* position of the probe. Those changes are subsequently used to reconstruct the surface [50].

This technique has proved very good accuracy for thin films measurements. Since it is a contact technique, it is independent of surface reflectance and substrate nature. Moreover, stylus profiling provides direct surface measurements with no need for modeling. Similarly to AFM, the lateral resolution is limited by the probe radius. Nevertheless, as we measure planar thin films on a wide step, there is no special need for high spatial resolution.

A Veeco profilometer, DEKTAK 150 model, has been used with a 5µm stylus radius. Typical set up force was fixed to 5 mg with an approximate 0.1 µm scanning resolution.

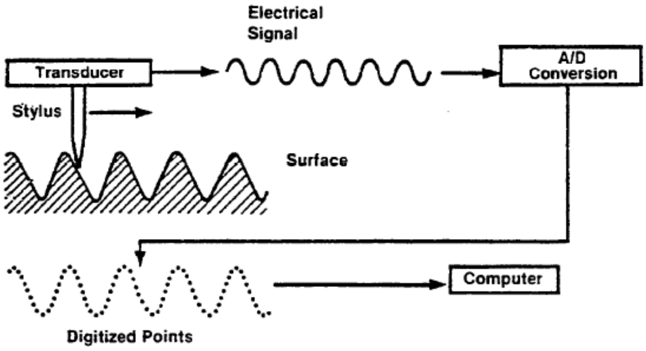

Fig. IV - 19 : Schematic of stylus profilometry operation principle [51].

5. Conclusion

In this Chapter, we defined and described the nanodielectric model samples of this thesis. Nanocomposites model samples are made of nanoparticles of either silicon dioxide or polystyrene. After dispersion on the substrate, SiO_2 were subsequently covered by aluminum oxide. On the other hand, PS microspheres were self-assembled in organized monolayers and etched with oxygen plasma in order to reduce their diameter and produce well organized arrays of nanoparticles with periodic separations. PS nanospheres have been covered by different types of shells, namely, aluminum oxide, silicon dioxide and polyvinyl acetate. Al_2O_3 has been prepared with atomic layer deposition, SiO_2 with plasma sputtering deposition and PVAc films with spin-coating. These shells either model the interphase or the matrix. According to the experimental methods developed in the following chapter, different types of layers assemblies will be utilized.

Next, DC and AC-EFM experimental protocols and set up have been described with the justification of each choice. PeakForce Tapping-Quantitative Nanomechanical Mapping has been described as well, for it has been used later in Chapter V, to distinguish two phases of different stiffness. Morphological and chemical elemental analysis measurements were conducted with scanning electron microscopy. In addition to SEM, thin films height values were also measured with ellipsometry and stylus profilometry. The basic working principles of all these complementary techniques have been reported as well.

6. References

[1] P. W. Natasha Starostina. Part II: Sample Preparation for AFM Particle Characterization [Online]. Available: www.nanoparticles.pacificnanotech.com

[2] A. Kinbara, E. Kusano, and I. Kondo, "Fundamentals of plasma and sputtering processes," *Vacuum,* vol. 51, pp. 475-478, 1998/12/01/ 1998.

[3] S. Y. Kim, K. Hong, K. Kim, H. K. Yu, W.-K. Kim, and J.-L. Lee, "Effect of N2, Ar, and O2 plasma treatments on surface properties of metals," *Journal of Applied Physics,* vol. 103, p. 076101, 2008/04/01 2008.

[4] T. Murakami, S.-i. Kuroda, and Z. Osawa, "Dynamics of Polymeric Solid Surfaces Treated with Oxygen Plasma: Effect of Aging Media after Plasma Treatment," *Journal of Colloid and Interface Science,* vol. 202, pp. 37-44, 1998.

[5] D. Bodas and C. Khan-Malek, "Hydrophilization and hydrophobic recovery of PDMS by oxygen plasma and chemical treatment—An SEM investigation," *Sensors and Actuators B: Chemical,* vol. 123, pp. 368-373, 2007/04/10/ 2007.

[6] V. Jokinen, P. Suvanto, and S. Franssila, "Oxygen and nitrogen plasma hydrophilization and hydrophobic recovery of polymers," *Biomicrofluidics,* vol. 6, pp. 016501-016501-10, 2012.

[7] I. A. Rahman and V. Padavettan, "Synthesis of Silica Nanoparticles by Sol-Gel: Size-Dependent Properties, Surface Modification, and Applications in Silica-Polymer Nanocomposites;A Review," *Journal of Nanomaterials,* vol. 2012, p. 15, 2012.

[8] M. F. Ceiler, P. A. Kohl, and S. A. Bidstrup, "Plasma-Enhanced Chemical Vapor Deposition of Silicon Dioxide Deposited at Low Temperatures," *Journal of The Electrochemical Society,* vol. 142, pp. 2067-2071, June 1, 1995 1995.

[9] Z. Ahmad, "Polymer Dielectric Materials," in *Dielectric Material*, M. A. Silaghi, Ed., ed Rijeka: InTech, 2012, p. Ch. 01.

[10] L. Fumagalli, D. Esteban-Ferrer, A. Cuervo, J. L. Carrascosa, and G. Gomila, "Label-free identification of single dielectric nanoparticles and viruses with ultraweak polarization forces," *Nat Mater,* vol. 11, pp. 808-816, 09//print 2012.

[11] P. Barber, S. Balasubramanian, Y. Anguchamy, S. Gong, A. Wibowo, H. Gao*, et al.*, "Polymer Composite and Nanocomposite Dielectric Materials for Pulse Power Energy Storage," *Materials,* vol. 2, p. 1697, 2009.

[12] I. A. Preda, "Modeling and characterization of nanocomposite materials using dielectric methods," PhD, Université Montpellier 2, 2013.

[13] C. Riedel, R. Arinero, P. Tordjeman, G. Lévêque, G. A. Schwartz, A. Alegria*, et al.*, "Nanodielectric mapping of a model polystyrene-poly(vinyl acetate) blend by electrostatic force microscopy," *Physical Review E,* vol. 81, p. 010801, 01/08/ 2010.

[14] (04/09/2017). *Wikipedia, the free encyclopedia* [Free web image]. Available: https://en.wikipedia.org/wiki/Polystyrene

[15] S. Sakamoto, L. Philippe, M. Bechelany, J. Michler, H. Asoh, and S. Ono, "Ordered hexagonal array of Au nanodots on Si substrate based on colloidal crystal templating," *Nanotechnology,* vol. 19, p. 405304, 2008.

[16] M. Bechelany, P. Brodard, L. Philippe, and J. Michler, "Extended domains of organized nanorings of silver grains as surface-enhanced Raman scattering sensors for molecular detection," *Nanotechnology,* vol. 20, p. 455302, Nov 11 2009.

[17] P. Colson, C. Henrist, and R. Cloots, "Nanosphere Lithography: A Powerful Method for the Controlled Manufacturing of Nanomaterials," *Journal of Nanomaterials,* vol. 2013, p. 19, 2013.

[18] J. Rybczynski, M. Hilgendorff, and M. Giersig, "Nanosphere Lithography — Fabrication of Various Periodic Magnetic Particle Arrays Using Versatile Nanosphere Masks," in *Low-Dimensional Systems: Theory, Preparation, and Some Applications*, L. M. Liz-Marzán and M. Giersig, Eds., ed Dordrecht: Springer Netherlands, 2003, pp. 163-172.

[19] J. Bognár, J. Szűcs, Z. Dorkó, V. Horváth, and R. E. Gyurcsányi, "Nanosphere Lithography as a Versatile Method to Generate Surface-Imprinted Polymer Films for Selective Protein Recognition," *Advanced Functional Materials,* vol. 23, pp. 4703-4709, 2013.

[20] L. S. McCarty, A. Winkleman, and G. M. Whitesides, "Electrostatic Self-Assembly of Polystyrene Microspheres by Using Chemically Directed Contact Electrification," *Angewandte Chemie International Edition,* vol. 46, pp. 206-209, 2007.

[21] S.-K. Wu, T.-P. Tang, and W. J. Tseng, "Self-assembly of polystyrene microspheres within spatially confined rectangular microgrooves," *Journal of Materials Science,* vol. 43, pp. 6453-6458, 2008/10/01 2008.

[22] Y. Fu, Z. Jin, Z. Liu, Y. Liu, and W. Li, "Self-assembly of colloidal crystals from polystyrene emulsion at elevated temperature by dip-drawing method," *Materials Letters,* vol. 62, pp. 4286-4289, 2008/10/31/ 2008.

[23] Y. Wu, C. Zhang, Y. Yuan, Z. Wang, W. Shao, H. Wang*, et al.*, "Fabrication of Wafer-Size Monolayer Close-Packed Colloidal Crystals via Slope Self-Assembly and Thermal Treatment," *Langmuir,* vol. 29, pp. 14017-14023, 2013/11/19 2013.

[24] J. R. Oh, J. H. Moon, H. K. Park, J. H. Park, H. Chung, J. Jeong*, et al.*, "Wafer-scale colloidal lithography based on self-assembly of polystyrene nanospheres and atomic layer deposition," *Journal of Materials Chemistry,* vol. 20, pp. 5025-5029, 2010.

[25] S. S. Shinde and S. Park, "Oriented colloidal-crystal thin films of polystyrene spheres via spin coating," *Journal of Semiconductors,* vol. 36, p. 023001, 2015.

[26] G. Arutinov, S. B. Brichkin, and V. F. Razumov, "Self-Assembling of polystyrene microsphere monolayers by spin-coating," *Nanotechnologies in Russia,* vol. 5, pp. 67-72, 2010/02/01 2010.

[27] C. Haginoya, M. Ishibashi, and K. Koike, "Nanostructure array fabrication with a size-controllable natural lithography," *Applied Physics Letters,* vol. 71, pp. 2934-2936, 1997/11/17 1997.

[28] W. W. Stoffels, E. Stoffels, G. H. P. M. Swinkels, M. Boufnichel, and G. M. W. Kroesen, "Etching a single micrometer-size particle in a plasma," *Physical Review E,* vol. 59, pp. 2302-2304, 02/01/ 1999.

[29] M. Bechelany, E. Berodier, X. Maeder, S. Schmitt, J. Michler, and L. Philippe, "New Silicon Architectures by Gold-Assisted Chemical Etching," *ACS Applied Materials & Interfaces,* vol. 3, pp. 3866-3873, 2011/10/26 2011.

[30] K. Nojiri, "Mechanism of Dry Etching," in *Dry Etching Technology for Semiconductors*, ed Cham: Springer International Publishing, 2015, pp. 11-30.

[31] L. Yan, K. Wang, J. Wu, and L. Ye, "Hydrophobicity of Model Surfaces with Loosely Packed Polystyrene Spheres after Plasma Etching," *The Journal of Physical Chemistry B,* vol. 110, pp. 11241-11246, 2006/06/01 2006.

[32] C. Marichy, M. Bechelany, and N. Pinna, "Atomic Layer Deposition of Nanostructured Materials for Energy and Environmental Applications," *Advanced Materials,* vol. 24, pp. 1017-1032, 2012.

[33] R. Viter, I. Iatsunskyi, V. Fedorenko, S. Tumenas, Z. Balevicius, A. Ramanavicius*, et al.*, "Enhancement of Electronic and Optical Properties of ZnO/Al2O3 Nanolaminate Coated Electrospun Nanofibers," *The Journal of Physical Chemistry C,* vol. 120, pp. 5124-5132, 2016/03/10 2016.

[34] V. Vandalon and W. M. M. Kessels, "What is limiting low-temperature atomic layer deposition of Al2O3? A vibrational sum-frequency generation study," *Applied Physics Letters,* vol. 108, p. 011607, 2016.

[35] M. Baitimirova, R. Viter, J. Andzane, A. van der Lee, D. Voiry, I. Iatsunskyi*, et al.*, "Tuning of Structural and Optical Properties of Graphene/ZnO Nanolaminates," *The Journal of Physical Chemistry C,* vol. 120, pp. 23716-23725, 2016/10/20 2016.

[36] M. Praeger, T. Andritsch, S. G. Swingler, and A. S. Vaughan, "A simple theoretical model for the bulk properties of nanocomposite materials," in *Electrical Insulation and Dielectric Phenomena (CEIDP), 2014 IEEE Conference on*, 2014, pp. 699-702.

[37] M. Fréchette, I. Preda, J. Castellon, A. Krivda, R. Veillette, M. Trudeau*, et al.*, "Polymer composites with a large nanofiller content: a case study involving epoxy," *IEEE Transactions on Dielectrics and Electrical Insulation,* vol. 21, pp. 434-443, 2014.

[38] M. Hershcovitz and I. E. Klein, "Dynamics of spin coating on very rough surfaces," *Microelectronics Reliability,* vol. 33, pp. 869-880, 1993/05/01/ 1993.

[39] D. El Khoury, R. Arinero, J. C. Laurentie, and J. Castellon, "Nanoscale surface charge detection in epoxy resin materials using electrostatic force spectroscopy," *AIP Advances,* vol. 6, p. 035318, 2016.

[40] C. Riedel, R. Arinero, P. Tordjeman, M. Ramonda, G. Lévêque, G. Schwartz*, et al.*, "Determination of the nanoscale dielectric constant by means of a double pass method using electrostatic force microscopy," *Journal of Applied Physics,* vol. 106, p. 024315, 2009.

[41] C. s. Natalia Erina, "Quantitative mechanical property mapping at the nanoscale with PeakForce QNM," Bruker corporation2010.

[42] B. Pittenger, N. Erina, and C. Su, "Mechanical Property Mapping at the Nanoscale Using PeakForce QNM Scanning Probe Technique," in *Nanomechanical Analysis of High Performance Materials*, A. Tiwari, Ed., ed Dordrecht: Springer Netherlands, 2014, pp. 31-51.

[43] L. Reimer, *Scanning Electron Microscopy: Physics of Image Formation and Microanalysis*. Berlin Heidelberg GmbH: Springer-Verlag, 1985.

[44] D. E. N. Joseph Goldstein, David C. Joy, Charles E. Lyman, Patrick Echlin, Eric Lifshin, Linda Sawyer, J.R. Michael, *Scanning Electron Microscopy and X-ray Microanalysis: Third Edition*: Springer Science and Business Media, LLC, 2007.

[45] E. zurich. (21/09/2017). *Electron microscopy* [Web page]. Available: http://www.microscopy.ethz.ch/se.htm

[46] A. laboratory. (27/09/2017). *Spectroscopic Ellipsometry Characterization of Thin Films Used in the Food Packaging Industry* [Web page]. Available: http://www.americanlaboratory.com/914-Application-Notes/138874-Spectroscopic-Ellipsometry-Characterization-of-Thin-Films-Used-in-the-Food-Packaging-Industry/

[47] H. G. Tompkins and E. A. Irene, *Handbook of Ellipsometry*: Springer Berlin Heidelberg, 2005.

[48] M. Losurdo and K. Hingerl, *Ellipsometry at the Nanoscale*: Springer Berlin Heidelberg, 2013.

[49] G. Binnig, H. Rohrer, C. Gerber, and E. Weibel, "Surface Studies by Scanning Tunneling Microscopy," *Physical Review Letters,* vol. 49, pp. 57-61, 07/05/ 1982.

[50] J. Seiler and J. Kindersberger, "Insight into the interphase in polymer nanocomposites," *IEEE Transactions on Dielectrics and Electrical Insulation,* vol. 21, pp. 537-547, 2014.

[51] M. R. Amirzada, "Optimization in the Technological Steps for the Fabrication of Large Area Micromirror Arrays," Doctor of Engineering, Faculty of Electrical Engineering and Informatics, University of Kassel, 2014.

Chapter V

Experimental results

Chapter V

“It is not that I’m so smart; It’s just that I stay with problems longer.”
Albert Einstein

1. Introduction

In this last chapter, EFM characterizations over several types of nanodielectric models have been performed in order to set up correct experimental protocols to investigate the possibility of the technique for detecting interphases in nanocomposites. Model samples, described in Chapter IV, consist on nanoparticles (PS and SiO_2) put on metallized silicon substrates, over which, materials of various permittivities were deposited in thin layers (Al_2O_3, SiO_2 and PVAc). We start by characterizing particles alone, followed by samples combining two materials: nanoparticles covered by a thin shell. The latter configuration can either model a particle with an interphase not covered by a matrix, or a particle with a matrix possessing no interphase. The sensitivity to the top layer above the nanoparticles is examined. Afterwards, we benefit out of two materials results in order to attempt detecting an interfacial effect/layer when three types of materials are combined: particle covered by two different layers. The intermediate material models the interphase. Three methods have been established to address this issue by comparing various types of samples nature and configuration. Most of experimental sections are associated to simulations in order to verify the experimental results, deeper the interpretation of measured signals and get quantitative characterization of materials dielectric permittivities and/or dimensions.

2. Samples substrates

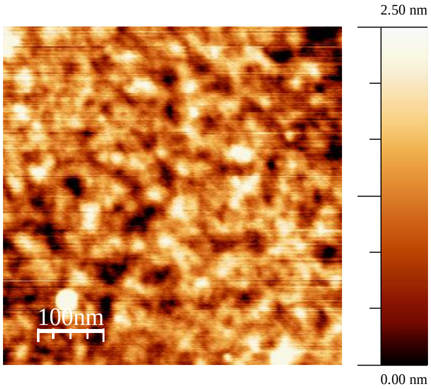

Fig. V - 1 : AFM topography of a 500 × 500 nm^2 region for a typical substrate: 50nm gold / 10nm chrome sputtered films over silicon substrate.

In Fig. V - 1, a typical AFM topography image of samples substrates is presented on a 500 × 500 nm^2 region. The RMS roughness is around 0.6 nm, which is acceptable to base on the deposition of our particles (with diameters of ~ 20 nm for silicon dioxide and ~ 250 – 400 nm for polystyrene particles).

3. Type 1 samples: particle + interphase or particle + matrix

Since our aim is to identify the interphase model, which is the material present above the particle and below the matrix, we started by studying the response over the association of a particle with only one layer. As the first material, SiO_2 nanoparticles and PS nanospheres have been used, and Al_2O_3 shells as the second material. In this configuration, the shell can play two roles: 1) it either represents the interphase model when no matrix covers the system, which can practically occur after cross-sectioning a nanocomposite [1], or 2) it represents the matrix, and the system models a nanodielectric with no remarkable interphase between matrix and filler. Beyond these two cases, the target of this first part is to explore experimentally the response of an inhomogeneous, double layered system of 3D finite size. How will the combination of these two materials affect the signal? How to identify the presence of various stacked materials? How is it possible to identify the intrinsic polarization response of each part? What is the range of sensitivity of EFM?

As described in Chapter IV, samples possess the general configuration sketched in Fig. V - 2. SiO_2 and PS particles were covered by Al_2O_3 of thickness t_i.

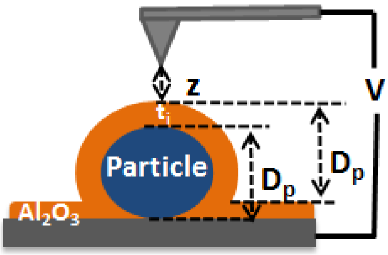

Fig. V - 2 : General configuration of type 1 samples within an EFM set up: particle (diameter D_p) + aluminum oxide shell (thickness t_i), at a z tip-sample surface distance.

3.1. Silicon dioxide particles

3.1.1. Same tip-sample distance

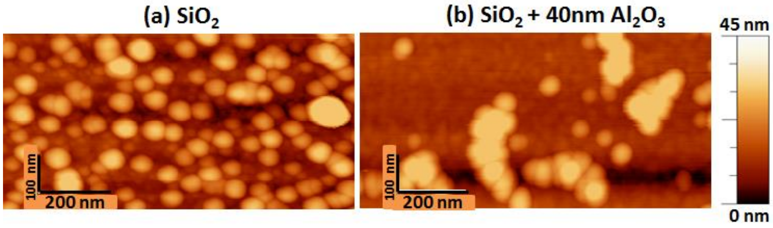

Fig. V - 3 : AFM topography images of silicon dioxide particles, a) without covering, and b) with 40 nm aluminum oxide layer.

The first set of samples is based on SiO_2 nanoparticles of 20 nm approximate diameter. Fig. V - 3 presents the topography over a 1 × 0.5 µm^2 region of SiO_2 particles, and that of 40 nm Al_2O_3 covered particles. It can be first noticed from Fig. V - 3a. that the nanoparticles are relatively well dispersed with little agglomerations. Particles diameter varies as expected from manufacturer (Sigma-Aldrich, ref: 791342). In contrary, Fig. V - 3b. shows little isolated particles, and higher agglomerations size for the covered nanospheres. Consequently, the physisorption of SiO_2 nanoparticles to the surface seems to not be sufficiently stable under the thermodynamical conditions of ALD. Nevertheless, few particles stand still to ALD and can be subsequently compared to bare SiO_2.

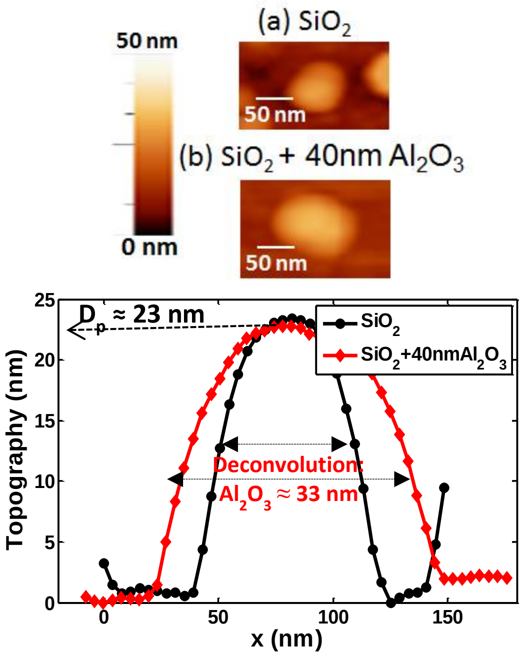

Fig. V - 4 : Cross-sectional topography profiles of SiO_2 nanoparticles placed on bare substrate (inset a.), and SiO_2 with 40 nm Al_2O_3 shell covering the whole sample surface (inset b).

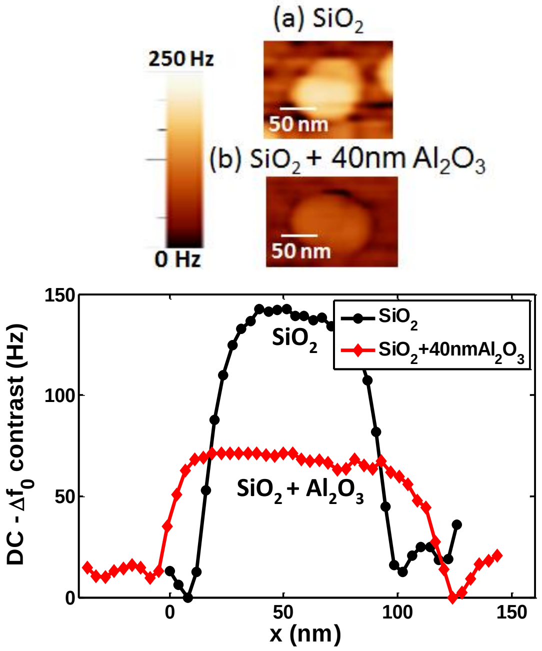

Fig. V - 5 : DC - EFM electrical frequency shifts contrast of SiO_2 nanoparticles placed on bare substrate (inset a.), and SiO_2 with 40 nm Al_2O_3 shell covering the whole surface (inset b.). V_{DC} = 5 V and z = 23 nm.

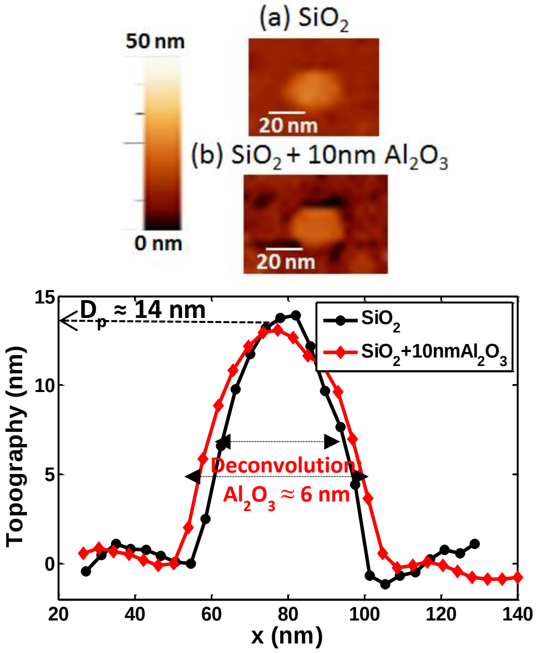

Fig. V - 6 : Cross-sectional topography profiles of SiO_2 nanoparticles placed on bare substrate (inset a.), and SiO_2 with 10 nm Al_2O_3 shell covering the whole sample surface (inset b).

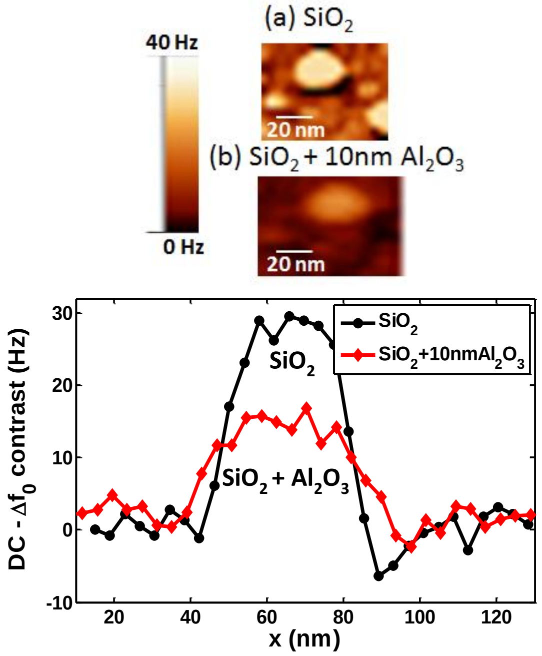

Fig. V - 7 : DC - EFM electrical frequency shifts contrast of SiO_2 nanoparticles placed on bare substrate (inset a.), and SiO_2 with 10 nm Al_2O_3 shell covering the whole surface (inset b.). V_{DC} = 5 V and z = 23 nm.

For this set of samples, DC-EFM frequency shift detection mode at same tip-sample distance has been employed. The above figures present topography images, EFM images and cross-sectional profiles of SiO_2 nanospheres, without Al_2O_3 and with approximately 40 nm (Fig. V - 4 and Fig. V - 5) and 10 nm Al_2O_3 (Fig. V - 6 and Fig. V - 7).

Topography cross-sectional profiles along the main axis at the central region of compared particles show similar heights, around 23 nm and 14 nm for the respective cases of 40 nm and 10 nm Al_2O_3 layers (Fig. V - 4 and Fig. V - 6). This suggests that the initial diameter of compared SiO_2 particles is of the same order, since Al_2O_3 is supposed to equally cover the whole sample as it can be deduced from Fig. V - 2. Note that height profiles, for sufficiently isolated particles, are exempt from Gaussian effect of the tip radius compared to lateral profiles (see Chapter II section 5.1). Al_2O_3 shell thickness is approximately calculated from the deconvoluted particles width profiles before and after ALD. In the present case, where SiO_2 nanoparticles possess a diameter in the same order of tip apex, we referred to eq (II.38) to deduce a layer thickness around 6 nm, and 33 nm from Fig. V - 4 and Fig. V - 6, respectively. Nevertheless, it must be noted that particles do not preserve a completely spherical shape after ALD (particle height: $D_p + t_i$ > particle width: $D_p + 2t_i$, Fig. V - 2). The deconvoluted widths are thereby an underestimation of the real covered spheres because eq (II.38) is appropriate for spherical particles.

For these two couples of particles, their corresponding EFM signals have been compared at the same tip-sample distance (same set-point and lift), and for the same bias voltage. EFM contrast profiles on a cutline at the center of EFM images (Fig. V - 5 and Fig. V - 7) show in addition to the reconstruction of AFM topography width, a remarkable difference in contrast intensity between covered and uncovered particles for both Al_2O_3 thicknesses.

We remind that EFM frequency shift contrasts for SiO_2 nanoparticles without a shell basically result from the difference of the detected electrostatic force gradient between the particle and the metallic substrate. On the other hand, for covered SiO_2 particles, the signal difference comes from the signal over SiO_2+Al_2O_3 compared to Al_2O_3 alone over the substrate. Since the same Al_2O_3 shell is present on the whole surface, at the first sight, the contrasts might be supposed to represent the contribution of the SiO_2 particle under the shell, to the signal.

However, contrasts obtained by the double-pass method, or by retracing sample topography, have been found to be highly influenced by tip-substrate distance, or interelectrode distance change, as the tip is scanning the surface. M. Van Der Hofstadt *et al.* [2] called this effect as topography cross-talk, first introduced by D. Esteban-Ferrer *et al.* [3]. Knowing the thickness of the sample at each position, authors subtracted the measured signal over the sample at a certain distance from the surface, from that over a bare substrate at similar interelectrode distance. This method, also used for other electrical scanning probe microscopies [4], is supposed to extract the so-called intrinsic capacitance of the probed region.

In our case, the bottom of our samples, corresponding to the regions between particles, is covered by Al_2O_3; and for each shell thickness, the composition varies differently among samples. Consequently, although the previously attempted deconvolution from eq (II.38) might give insight into the film thickness when we assume that the shell cover the particles homogeneously, the exact knowledge of our sample depth at each position is not straightforward from AFM topography measurements. The method proposed by D. Esteban-Ferrer and M. Van Der Hofstadt *et al.* cannot be accurately adopted here, nor for any type of specimen with unknown thickness.

The idea behind double-pass cross-talks stems from the irregular dependency of the electrostatic force to tip-sample distance *z* (Chapter III - section 3.2). When a *z* variation over a bare metallic substrate is considered, this is equivalent to the modification of interelectrode distance *Z*. We have verified in Fig. V - 8 the decrease of the force gradient versus *Z* on a metallic substrate, through α_{DC} coefficient extraction, as explained in Chapter IV - section 3.1. The importance of α_{DC} study instead of the raw DC frequency shifts resides in the fact that Δf_0 (*DC*) measurements are sensitive to the sample surface potential and surface space charge, as already explained in previous chapters. On the other hand, α_{DC} separates the pure capacitive response from other electrostatic contributions, and hence, provides the quantity of interest within the framework of our study.

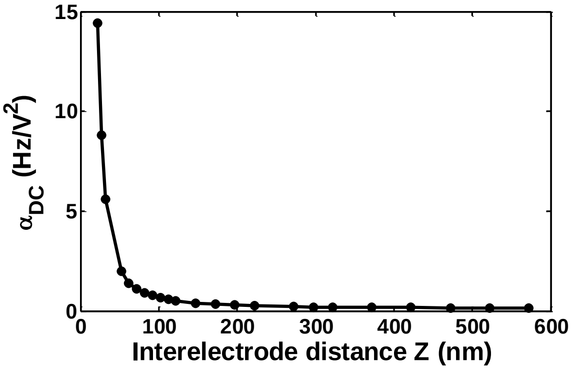

Fig. V - 8 : α_{DC} coefficient vs. interelectrode distance *Z* obtained over a bare metallic substrate.

EFM signal variation is not a monotonous function of *Z*, but it gets steeper at low distances (Fig. V - 8). This changing rate versus *Z* indicates that EFM contrasts with the double-pass method can still be obtained over homogeneous samples when the latter present a rough surface or non-planar features. Nevertheless, these topography cross-talks are more pronounced on thin samples (equivalent to low inter-electrodes distances) and become negligible at thicker ones.

Consequently, the observed decrease in EFM contrasts with Al_2O_3 films can be due to two reasons:

a) Layer addition on the whole surface enlarges interelectrode distance when the tip-sample distance is kept constant during scanning. Hence, for thicker samples, and as the lift is conserved, the same topographical steps will contribute less to EFM contrast (the topography cross-talk decreases);

b) The change in the material dielectric contribution to the signal between particle and sample bottom regions before and after layer addition. Namely, the alumina layer could be screening the electric field from the initial sample: particle and metallic substrate, and thus reducing the contrast.

3.1.2. Same interelectrode distance

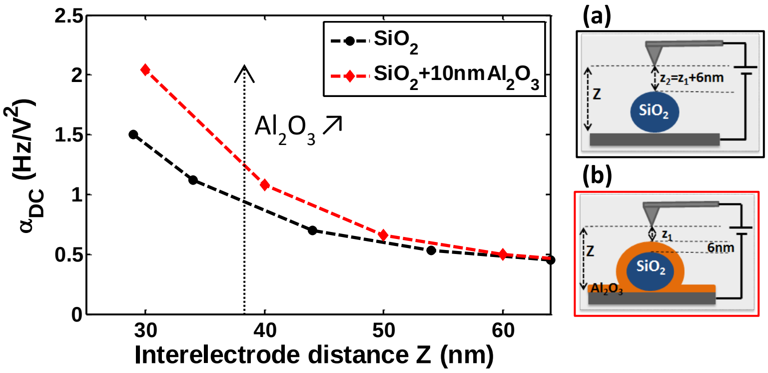

Fig. V - 9 : α_{DC} vs. interelectrode distance *Z* for SiO$_2$ nanoparticles without and with 10 nm Al$_2$O$_3$ layer. Interelectrode distance selection is explained on insets (a) and (b) for SiO$_2$ and SiO$_2$+10nmAl$_2$O$_3$, respectively.

In order to distinguish the two possible effects mentioned previously concerning contrast decrease, we measured the signal at the center of SiO$_2$ without and with 10 nm Al$_2$O$_3$ shell, while keeping this time the same interelectrode distance *Z*, instead of same lift height (Fig. V - 9). Since the same tip is used for measurements (cone height is consequently constant), interelectrode distance *Z* is measured from the end of the tip to the substrate upper surface. Practically, lift heights for SiO$_2$ with and without alumina have been selected based on the following steps, also sketched on insets a. and b. of Fig. V - 9:

In the aim of keeping similar *Z* for both SiO$_2$ (case 1 - inset a) and SiO$_2$+Al$_2$O$_3$ (case 2 – inset b), this relation between experimental parameters for the specific studied particles must be satisfied:

$$D_{p1} + z_{01} + L_1 = D_{p2} + t_i + z_{02} + L_2 \qquad \text{(V-1)}$$

where D_{p1} and D_{p2} are SiO$_2$ particles diameter, associated to AFM measured height. z_0 is the initial distance from the sample surface set at the first scan. L_1 and L_2 are the lift distance chosen at the second scan for case 1 and case 2, respectively; and t_i is the shell thickness.

Since we compare particles with same measured AFM height, then D_{p1} = D_{p2}. z_0 is kept constant by using the same amplitude set-points for tapping, so that z_{01} = z_{02}. Considering with precaution that t_i is equal to the difference of deconvoluted particles widths, then t_i = 6 nm (see section 3.1.1). The final relation between the experimental lifts to be chosen, expressed in nm, becomes:

$$L_1 = L_2 + 6 \qquad \text{(V-2)}$$

We find from the resulting α_{DC} (*Z*) curve of Fig. V - 9 that while keeping the same separation between electrodes, the signal increases with the presence of the dielectric layer. In other words, the signal with an alumina shell over particles is higher than that above the particles with an additional air shell possessing the same thickness as alumina. Thereby, this shows the sensitivity to the dielectric contribution of the material modeling the interphase (or modeling the matrix with no interphase).

Thus, it can be concluded that the EFM contrasts observed in Fig. V - 5 and Fig. V - 7, mainly reflect the polarization response of the material to the EFM signal. The contrast decrease is mostly affected by the dielectric screening of the additional alumina thin film. This result proves the sensitivity of EFM to the presence of an upper dielectric layer via simple comparisons at same tip-sample surface distance, verified for our case of SiO$_2$ nanoparticles covered by Al$_2$O$_3$ shells.

3.2. Polystyrene particles

The second type of particles above which nanodielectric model samples were based is polystyrene particles. For this section, spheres of 230 nm approximate diameter were used to be covered by alumina thin films of several thicknesses: 20, 60, 100 and 200 nm.

It must be noted that although this work is basically meant for common nanocomposites using smaller nanoparticles, the study is equally applied for other purposes. It addresses the issue of setting-up an appropriate experimental protocol and signal analysis in the aim of distinguishing with EFM, the presence of additional layers, or changes in initial ones, of materials with complex shape and finite-size. Nevertheless, the chosen geometry stays appropriate with casual nanocomposites to a certain extent. For instance, the ratio of the model interphase layer thickness (alumina layers: 20 to 200 nm) and particle diameter (polystyrene: 230 nm) goes approximately from 8 % up to 87 %, which satisfies commonly expected ratios in nanocomposites that have been likewise modeled during the simulations of Chapter III [5]. Consequently, polystyrene sub-micrometric particles, or mesoparticles, have been called as nanoparticles in this thesis.

Furthermore, it must be also reminded that although in usual electrical engineering applications, particles are inorganic materials and both interphase and matrix are organic ones, our model only accounts for the permittivity of samples elements. As described previously, materials have been basically chosen according to their relative permittivities, regardless of other properties, as long as they can get appropriately prepared.

3.2.1. Preliminary characterizations

3.2.1.1. PS particles

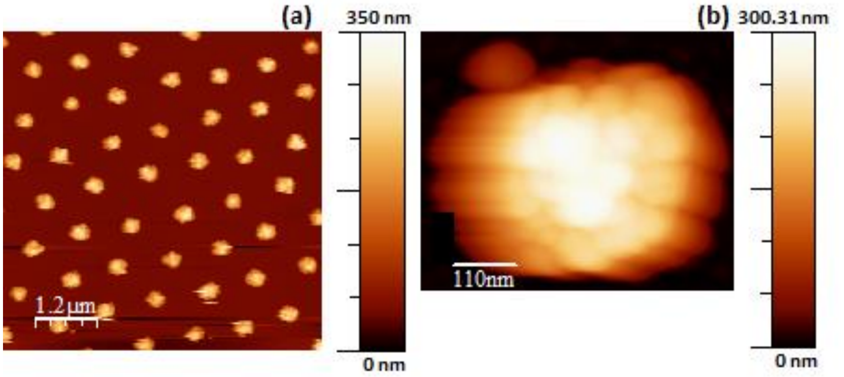

Fig. V - 10 : AFM topography images of a typical PS sample, a. on a 6 × 6 µm² region, the average diameter is around 227 nm ± 16 nm, and b. a zoom around one PS sphere (low gains and drive amplitude cause the expanded PS shape).

The topography of a typical PS sample is presented on Fig. V - 10, proving the periodicity of particles self-assembly and stability after plasma etching. Particle diameter is measured from the relative height between particle center and substrate surface. Then, PS average diameter from Fig. V - 10a. is around 227 nm ± 16 nm. Fig. V - 10b. shows a zoom on one particle indicating a relatively rough surface. This surface state is common for plasma etched PS spheres, especially after ample material extraction (1 µm initial diameter to 227 nm) [6].

Note that topography images of all PS based samples have been flattened after extracting particles from the flattening regions to avoid pits artifacts [7].

3.2.1.2. Aluminum oxide shells

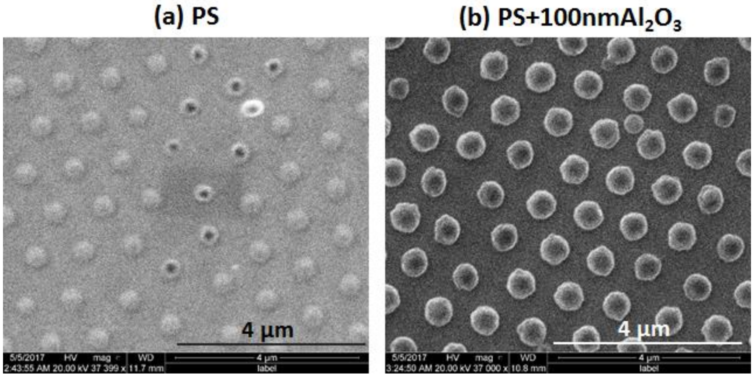

Fig. V - 11 : PS spheres samples, a. without and b. with Al_2O_3, studied on the upper surface with SEM.

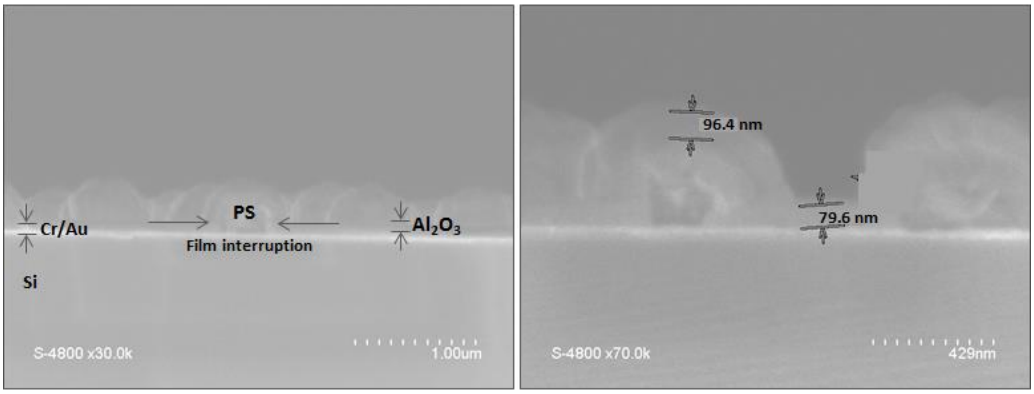

Fig. V - 12 : SEM images of a cross-sectioned region for a 60 nm Al_2O_3 covered PS sample. Right image is a zoom around the particle of left image that shows an interruption of Al_2O_3 film.

The deposition of Al_2O_3 thin films over the whole sample surface, particles and substrate, has been first verified from particles width change using SEM. Contrasts of Fig. V - 11a. and b. reveal the 2D morphology of bare and covered particles, respectively. The particles shape and separation are conserved with notable diameter increase over PS+100nmAl_2O_3 compared to PS alone. This widening following atomic layer deposition has been also recorded on AFM images, as it will be shown in the becoming sections, in addition to particle surface roughness decrease (see Fig. V - 14 and Fig. V - 15). Hence, it can be concluded that alumina must have been successfully grown on the surface of PS particles in a homogeneous way. PS based samples are hence highly controllable, justifying the choice of PS instead of SiO_2 nanoparticles for subsequent measurements.

However, the deposition in the bottom of the substrate, or between particles, cannot be precisely proven by surface imaging. Hence, a cross-section of our samples was necessary. Fig. V - 12 shows an example of SEM images for a PS+60nmAl_2O_3 cross-section specimen. Image contrast is blurred due to the charging of our insulator sample under the electron beam; nevertheless, the thick layer in the region between particles can be clearly distinguished. The range of magnitude of film thickness is around 80 nm. Accounting for the low resolution and the possibility of overestimation due to non-perfect vertical cut and/or vertical inclination of the imaged sample, the measured thickness can be considered as consistent with the theoretical deposited layer of 60 nm. Moreover, we notice an interruption of alumina film at the center of a particle, which can indicate its successful sectioning. Zooming this area shows in Fig. V - 12b. a hollow like region that might refer to the alumina shell of close thickness to that of the film over of the substrate. Nonetheless, during the majority of our preparations, a reference metallic sample was introduced during ALD process to monitor the thickness of the deposited layer. Those reference specimens were characterized with other non-destructive techniques (profilometry, ellipsometry), as it will be described in section 4.3.3.1 of this chapter.

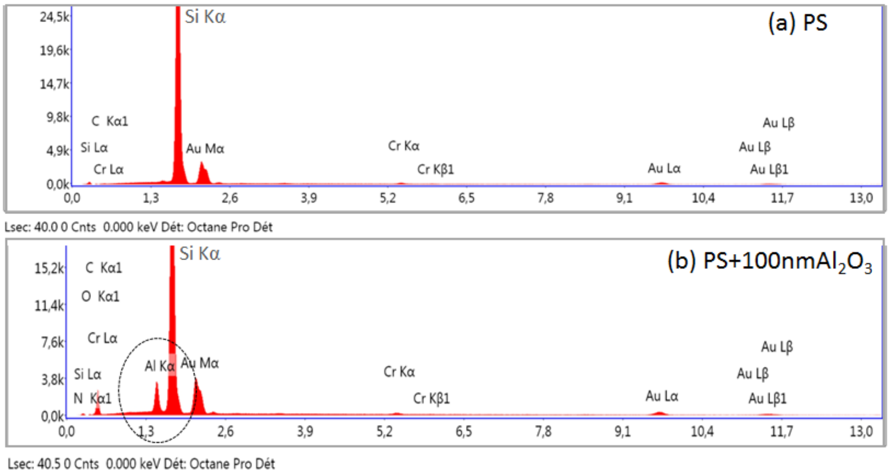

Fig. V - 13 : Energy dispersive X-ray spectrometry spectrum performed over a micrometric region of: a. PS, and b. PS+100nmAl$_2$O$_3$ samples.

In addition to morphological verifications, the chemistry of deposited alumina layers has been verified at the microscale with energy dispersive X-ray spectrometry. The average elemental chemical spectra for bare and alumina covered particles have been compared. As it can be highlighted from Fig. V - 12 a. and b., both samples show the peaks corresponding to silicon, chrome and gold. These elements must be coming from the substrate. A carbon peak is detected as well, which can return to the organic polystyrene particles, or other adsorbed organic molecules at the surface. However, only alumina covered samples show an aluminum peak on the spectrum of Fig. V - 13b. This can prove the consistency of aluminum oxide deposition. Further chemical characterizations could have been forwarded, but we stopped here since ALD alumina films have been already largely studied in the laboratory of ALD preparation (IEM).

3.2.2. DC and AC-2ω force gradient measurements

After showing the sensitivity to the polarization response of thin alumina films over silicon dioxide nanoparticles of 14 and 23 nm diameters, hereafter, we extend the study to EFM force gradient detection in both DC and AC excitation modes. The main objective is to set up appropriate experimental protocols for the detection of alumina shells properties, thickness and dielectric constant, as they cover PS nanoparticles.

3.2.2.1. Signal contrast comparisons

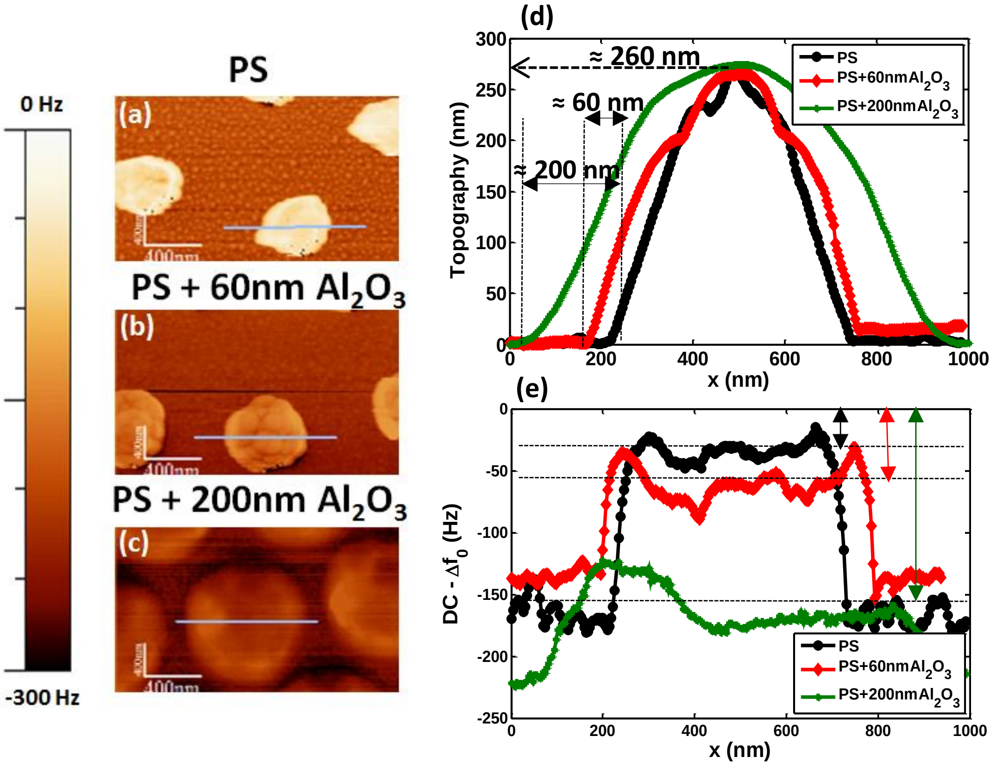

Fig. V - 14 a, b and c: EFM - Δf_0 (*DC*) images for PS, PS with 60 nm and 200 nm Al_2O_3, respectively; d: Cross-sectional topography profiles, and e: the corresponding EFM - Δf_0 (DC) signals for studied PS particles at V_{DC} = 5 V and z = 26 nm.

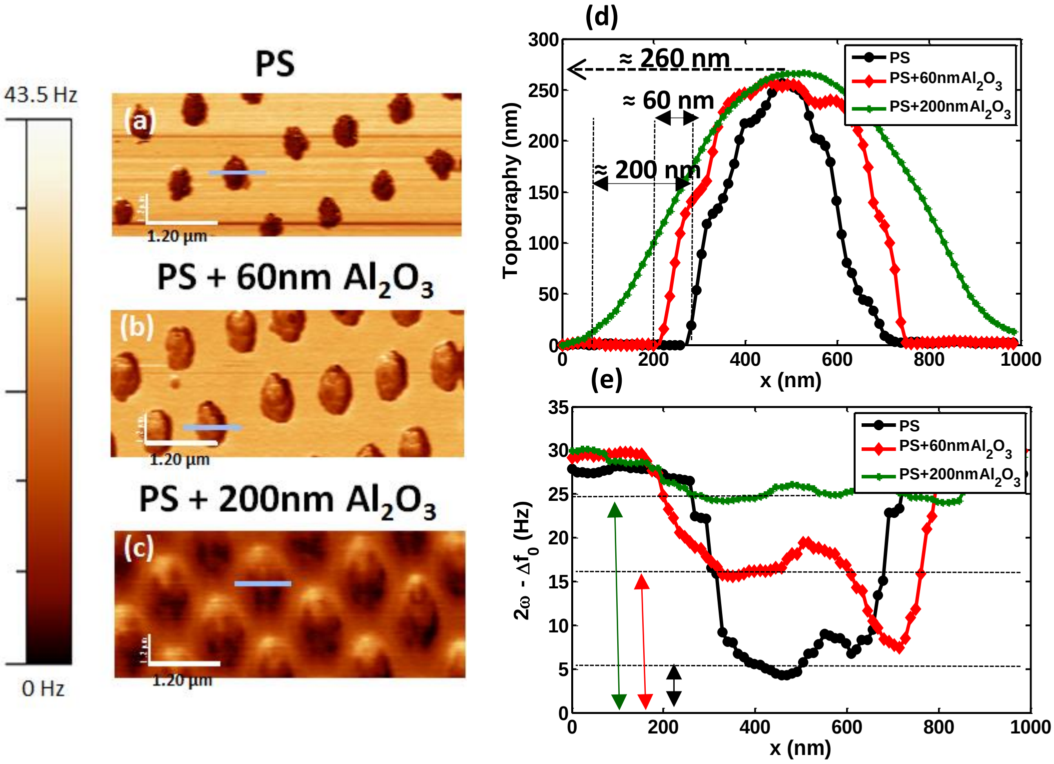

Fig. V - 15 a, b and c: AC - EFM $\Delta f_0 (2\omega)$ images for PS, PS with 60 nm and 200 nm Al_2O_3, respectively; d: cross-sectional topography profiles, and e: the corresponding AC - EFM $\Delta f_0 (2\omega)$ signals for the studied PS particles at V_{AC} = 5 V, ω = 200π rad/s and z = 30 nm.

Fig. V - 14 and Fig. V - 15 show topography and EFM results of PS nanoparticles, without coating (a), with 60 nm (b) and 200 nm alumina coating (c) in DC and AC excitation modes, respectively. Cross-sectional topography profiles of Fig. V - 14d. and Fig. V - 15d. along the main axis of the particles show similar particles height, around 250 nm. Similarly to SiO_2 case, this suggests that the diameter of compared particles without and with alumina is of the same order since alumina is supposed to equally cover the whole sample surface (see Fig. V - 2).

Furthermore, although lateral profiles are not exempt of Gaussian convolution, the measured differences between profiles widths from Fig. V - 14d. and Fig. V - 15d. have been found to be consistent with the theoretical thickness of added alumina layers: 60 and 200 nm approximately. In fact, in this set of samples, particle size is much larger than the tip apex. As we have already seen in Chapter II, in the latter case, the cone angle is the determining factor of tip convolution over AFM profiles. Since the cone angle of the tip is supposed to not change between measurements, according to equation (II.37), the measured lateral profile is directly proportional to the real particle diameter; the difference in AFM profiles becomes thereby directly proportional to real changes in particle width. In other words, for constant tip cone angles, the slope of the tip edge interacting with the surface of the particles is constant, and larger particles will only induce a translational movement of the tip compared to the corresponding position with smaller particles.

Hence, AFM lateral profiles comparison demonstrates with good precision, and in a direct way, the successful deposition of Al_2O_3 with ALD over PS particles. Likewise, it can be noticed from Fig. V - 14d. and Fig. V - 15d. that the roughness of PS spheres decreases with the thickness of deposited Al_2O_3 films. ALD deposition follows the surface of the base material; when the thickness of the deposited layer sufficiently increases, the layers above particles of fixed separations will superimpose, and the void will be filled up after sufficient thin film growth. Hence, since the surface roughness can be viewed as very small PS particles on the surface of the main sphere, then vacant sites can get gradually filled up with thicker Al_2O_3 depositions. PS roughness measurement with AFM can hence also be an indication of a successful ALD growth.

EFM cross-sectional profiles of Fig. V - 14 and Fig. V - 15 a, b and c insets are presented in Fig. V - 14e. and Fig. V - 15e. The latter show raw EFM frequency shifts signals between differently covered PS particles in DC and AC force gradient detection modes, respectively. Measurements have been performed at the same lift height, and hence, same tip-sample distance, since the initial distance at the first scan z_0 has been kept constant too.

For PS nanoparticles without a shell, EFM contrasts result from the difference of the detected electrostatic force gradient between the nanoparticle and the metallic substrate. The signal difference obtained for covered PS particles comes from the difference between the particle and the Al_2O_3 film alone covering the metallic substrate. In addition to the intrinsic capacitive response due to materials permittivity and thickness, interelectrode distance change with prominent topography features adds up to the source of EFM contrasts. As mentioned earlier and further clarified in Fig. V - 8, the topographic cross-talk contrasts are not the same at any separation between electrodes, and consequently, not the same at any Al_2O_3 thickness. However, the comparison at similar electrode separation proved in the first section of this chapter, that EFM is sensitive to the contribution of alumina layers above SiO_2 nanoparticles. This result is directly extended to PS spheres since those particles are bigger, and according to Chapter III, the sensitivity to the intrinsic dielectric response further increases with particles diameter (see Fig. III - 18). Hence, as Fig. V - 14 and Fig. V - 15 still highlight a decreasing contrast with alumina, the comparison of EFM frequency shift contrasts at constant tip-sample distance indicates the sensitivity of EFM to the dielectric contribution of the shell over PS nanospheres. Nevertheless, in order to ensure this sensitivity, and to overcome supposedly topographic contrast artifacts, we adopt next a new comparison method.

In fact, it must be reminded that the bottom of our samples, namely, the areas between particles, do not possess the same composition for different coverage thicknesses. Although for SiO_2 particles (section 3.1), to keep same electrodes separation, we have assumed that the global layer thickness is equal to particles deconvoluted width change; the real thickness of the sample at each position is not straightforward from topography images as it was the case in ref [2, 3]. The lateral profiles consistency with theoretical Al_2O_3 films stays not sufficient to prove the homogeneity of Al_2O_3 on the whole sample surface, including substrate and particles top regions. Consequently, the comparison at similar interelectrode distances is not possible with high precision, neither the method proposed in ref [2, 3] is applicable.

3.2.2.2. Signals comparision at particle center

In the following, a new general method is hence adopted in order to counteract any possible topography cross-talk effects. Instead of comparing EFM image contrasts, we start by confronting raw signals at particles central regions, for similar lift heights. From Fig. V - 14e. and Fig. V - 15e center response, we find that the signal intensity gets amplified with the presence of an alumina shell and further increases with larger alumina thickness for particles of comparable diameters (around 250 nm).

At constant lift heights, when a layer is added above the particles, the resulting increase in the separation between electrodes must decrease the signal. However, we obtained at same tip-sample distance more important signals with thicker alumina. This new method of results interpretation proves in another way, the sensitivity of the electrostatic response in both DC and AC modes to the shell, accounting for topography cross-talks and without further treatments that require quantifying sample thickness.

It must be noted that the signal at the bottom regions between close particles might differ from that above less PS occupied regions, or for instance, over bare substrates with similar Al_2O_3 film thickness. In fact, for a constant electrostatically coupled volume, EFM response between two particles is intensified due to the additional contribution of neighbor particles, when the latter fall within the volume of interaction. For instance, this can explain some inconsistent signals behavior over these regions as noticed in Fig. V - 14e. and Fig. V - 15e: the bottom signal for 200 nm thick Al_2O_3 layer covered samples, where particle separation becomes too narrow, is higher than 60 nm and 0 nm layered samples. In fact, according to the conclusions of Chapter III and the literature [8], the capacitance of the tip-sample system must decrease with the thickness of a dielectric film directly deposited on EFM counter-electrode, contrarily to the observed tendency. Consequently, a precise measurement is mostly directed over the central regions of particles surface, as just presented in above experiments. Readers can refer to "PS+50nmAl_2O_3+50nmSiO_2" inset image of Fig. V - 49 for a direct example of the signal difference, between particles, compared to more isolated bottom regions.

Hence, it can be concluded that the change in both DC and 2ω signals at the center of the particles and for constant tip-sample separations proves the sensitivity of this method to the presence of the shell, without the usage of a precise information on sample thickness.

3.2.3. α_{DC} parabolic coefficient extraction

In this section, we extend DC results to several Al_2O_3 thicknesses, in a further accurate way, allowing comparison of experimental results to simulations.

In fact, as explained in Chapter II and IV, we remind that raw DC measurements are sensitive to the contact potential and surface space charges (see summary of Table II -1). Hence, we studied for several particles, the behavior of the purely capacitive α_{DC} parabolic coefficient parameter, extracted over the central region of the particles, as explained in Chapter IV - section 3.1.

Although 2ω force gradient extraction directly accounts to the unique capacitance contribution of the system, DC-excitation mode measurements are important in the way that they are usually accessible in any standard AFM equipped with EFM module. AC experiments are usually more complicated to perform. Hence, for this section, we investigate DC detection protocols. Nonetheless, both DC and AC measurements have been used interchangeably in this work.

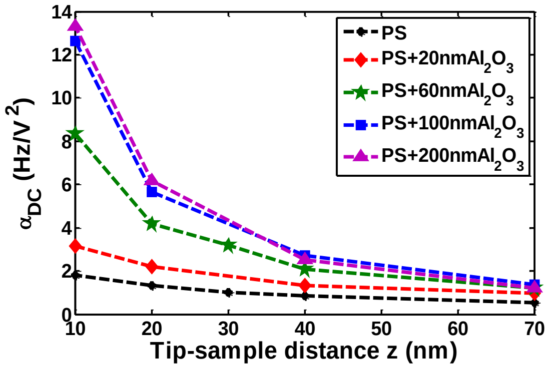

Fig. V - 16 : α_{DC} coefficient vs. tip-sample distance *z* for PS nanoparticles with and without Al_2O_3 shells.

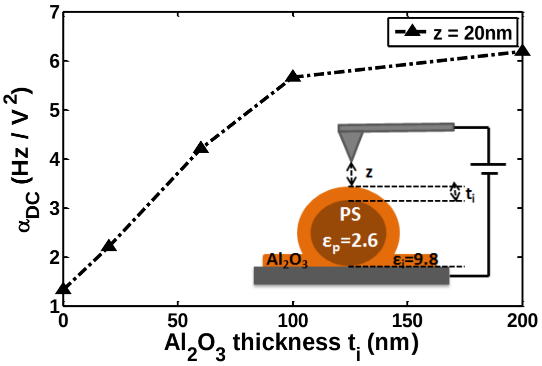

Fig. V - 17 : α_{DC} coefficient for different Al_2O_3 shell thicknesses t_i over PS nanoparticles, measured at a constant tip-sample distance *z* = 20 nm.

Fig. V - 16 presents the curves of the experimental α_{DC} parameter versus tip-sample distance *z* for PS samples covered by different Al_2O_3 shell thicknesses. α_{DC} curves have been obtained by averaging the data on a few pixels over the central region of the particles, and that above several particles of similar height (around 250 nm). Firstly, we notice that α_{DC} decreases with increasing tip-sample distance. This decrease is explained by the proportional dependence of α_{DC} with the electrostatic force gradient, reduced at higher *z* [9]. As a result, measurements at short distances ($\lesssim$ 20 nm) are found to be more sensitive to small variations between samples. Secondly, for the same tip-sample distance, PS nanoparticles with an Al_2O_3 shell exhibit clearly higher α_{DC} values than bare PS nanospheres, and α_{DC} increases with the thickness of the shell.

The difference between the presence and absence of the shell shows the good sensitivity of α_{DC} coefficient extraction to detect the dielectric layer over PS nanoparticles, while removing any ambiguity coming from contact potentials and surface charges. Moreover, the significant increase of α_{DC} with alumina thickness shows that the DC-force gradient extraction method is well adapted to evaluate the thickness of a dielectric alumina layer above PS nanospheres of 250 nm approximate diameter. Detectable thicknesses in our case are comprised in a range between 20 nm and 200 nm. Furthermore, Fig. V - 17 shows the trend observed for α_{DC} coefficient versus alumina shell thickness at a constant tip-sample distance. We notice that the slope of the curve is high up to 100 nm and becomes weaker beyond this value. Thereby, it can be deduced that the sensitivity to alumina thickness is limited to a certain range of thicknesses.

3.2.4. Discussion and determination of shell permittivity relative to particle

In order to interpret previous results summarized in Fig. V - 17, and try to deduce qualitatively an idea about the shell permittivity, we clearly state in the following, the directly observed, and expected to be morphological variations due to shell addition:

1) Interelectrode distance increase:

Changes cannot be the result of enlarged interelectrode separation. In fact, as we compare α_{DC} between PS at z = 76 nm and PS+60nmAl$_2$O$_3$ at z = 16 nm, where both interelectrode distances are supposed to be around 326 nm, we still observe the same signal tendency. As well as, generally, a more important separation between electrodes is expected to decrease the signal (Fig. V - 8 and Fig. V - 9), which is not our case (Fig. V - 17).

2) Total sample thickness increase:

Changes cannot be caused by the greater PS+Al$_2$O$_3$ probed region thickness. We experimentally verified the expected tendency of the signal versus sample thickness, for a homogeneous alumina dielectric film. Fig. V - 18 confirms that an increased thickness of a homogenous dielectric film decreases the signal [8], whereas the opposite behavior is observed over PS spheres (Fig. V - 17).

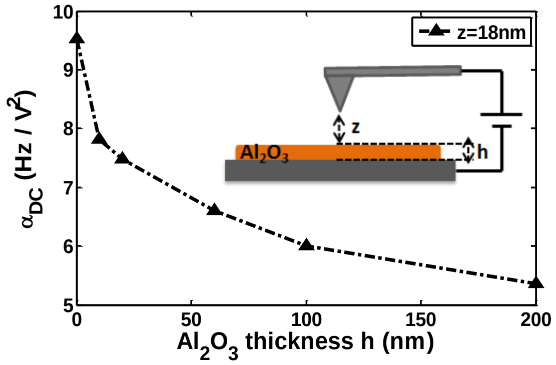

Fig. V - 18 : α_{DC} coefficient for different Al$_2$O$_3$ films thicknesses *h* covering bare metallic substrates at constant tip-sample distance *z* = 18 nm.

3) Particle width increase:

Changes might be attributed to particle width increase, which broadens the surface of interaction of the sample and subsequently, the capacitance of the system. Namely, as reviewed in Chapter III, Z. Y. Li *et al.* studied the size of a squared sample on the signal [10], and G. Gomila *et al.* reported on the eccentricity of a dielectric nanoparticle [11] and the width of a dielectric film [12].

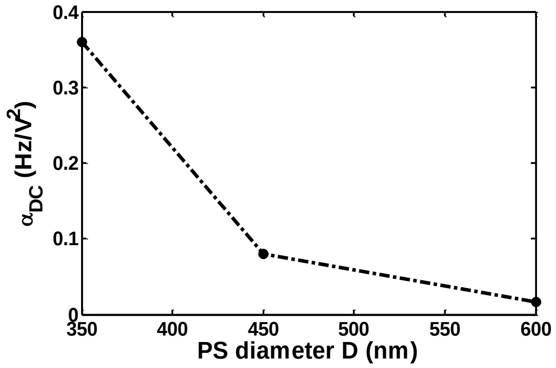

Fig. V - 19: α_{DC} coefficient vs. PS particles diameter *D* measured at *z* =20 nm.

A first attempt for verifying this possibility has been performed by measuring PS particles of different diameters in the range of the previously measured particles with alumina shell. As it can be highlighted from Fig. V - 19, the signal decreases with the diameter, on the contrary to the observed change with Al$_2$O$_3$ covered PS (Fig. V - 17). This is also in accordance with Fig. III - 18a. of Chapter III.

However, it is worth reminding that the size of bigger PS particles grows homogeneously in all directions (1:1 aspect ratio). On the other hand, PS+Al$_2$O$_3$ particles are not fully covered with Al$_2$O$_3$ on their back side in contact with the substrate. Accordingly, an additional layer enlarges particle width, two times faster than its height. For instance, particle + shell width is equal to ($D_p + 2t_i$), compared to the particle + shell height ($D_p + t_i$) (see Fig. V - 2). Therefore, Fig. V - 19 is not sufficient to firmly eliminate the explanation of previous results (Fig. V - 17) by a predominance of particles radius of curvature.

Nevertheless, if the curvature radius is the most influencing parameter, it must satisfy a signal increase for all types of dielectric shells within the studied dimensions. Consequently, at this stage, we are going to consider the last possible parameter, the intrinsic response of the dielectric shell, which will help clarifying this point.

4) Intrinsic shell dielectric response:

The signal is obviously the combination of several parameters effects, each weighting differently on the resulting interaction. However, as we have seen so far, none of them is sufficiently able to explain the increased signal. Actually, the only left possible explanation would be the permittivity increase with the shell that also amplifies the signal. How to relate that to our system?

In the case of a multilayered sample, for instance, a particle + shell, if the added material possesses the same permittivity than the particle, we get a kind of homogeneous material and within this range of morphological changes, the latter will act on the signal in a casual way, enough to understand any signal change. However, since we verified that morphological parameters are not sufficient to explain the obtained results, our material cannot be homogeneous, and the layer cannot be an extension of the particle or a layer with the same dielectric constant. Therefore, based on simulation results of Chapter III concerning superposed dielectric materials, we remind that the assembly of different types of dielectric materials changes the global effective permittivity of the sample, and thereby, presents special behavior regarding geometry modification. In particular, a layer with a lower permittivity than the initial particle decreases the effective permittivity of the resulting particle. In this case, the signal is expected to decay with the layer thickness, even if the radius of curvature rises too. Conversely, a layer with a higher dielectric permittivity than the particle increases the effective permittivity and subsequently, the signal is estimated to become more important with a shell of intermediate thickness.

Therefore, we deduce that EFM is detecting a heterogeneous material. In particular, the added layer over PS particles is extracted owing to EFM sensitivity for the change of the global permittivity, attributed to the intrinsic permittivity of the shell relative to the particle. Consequently, our signal is only explainable if the shell permittivity exceeds the PS one. This is well verified for our case of Al_2O_3 shells, for which the relative permittivity is equal to 9.8, which is indeed, higher than PS permittivity that is equal to 2.6.

3.3. Type 1 samples experiments: conclusions

To conclude, what can be retained from the previous measurements on single layered particles is the following:

a) EFM is able to distinguish homogeneous from heterogeneous materials, in particular, one layered from multilayered materials. Interestingly, this is made possible since heterogeneous samples can present unusual behaviors due to morphology change.
b) The detection of the additional layer (Al_2O_3 shell in our case) is predominated by its dielectric contribution, observed on contrasts decrease at same tip-sample distance (over SiO_2 and PS particles), as well as particles central regions signal change.

c) The distinction of the intrinsic dielectric permittivity of added material (Al_2O_3) relative to the initial material (PS) is possible after precise results interpretation. Morphological changes start reflecting the dielectric identity of the material rather than the casual response for the material alone.

d) Inversely, those results prove at the same time the subsurface sensitivity of EFM (PS below Al_2O_3). Consequently, in the opposite case where the shell is known, the subsurface material properties can be deduced. This latter investigation becomes similar to the work of Fumagalli *et al.,* using AC 2ω-force detection method [13]. The prominent additional information with our results is to benefit out of the geometrical effects on the signal to get direct qualitative insight into the material permittivity. This has been also made possible with DC force gradient measurements.

e) Moreover, an additional contribution of these results is that the adopted experimental and interpretation method (signal study around particle center at constant tip-sample distance vs. layer thickness) provides dielectric information and eliminates topography cross-talks without the mandatory need for sample thickness quantification, in contrary to previous literature [2, 3].

It must be noted that within the dimensions of our PS based samples, the spatial EFM resolution at the top of the particles has been calculated numerically and found to be lower than particles dimensions. In the opposite case (particle diameter > EFM resolution), topographical effects become however more influential, and the intrinsic dielectric response becomes harder to measure.

3.4. Experiments versus simulations

For a further verification and understanding of the previous experimental results, as well as attempting to quantify the supposed-to-be unknown parameters of our reference samples, new numerical simulations have been carried out. We used the same Comsol® model described in Chapter III, however adapted to the used tip and sample characteristics. Moreover, since the software basically calculates electrostatic forces, on the contrary to our EFM experiments that were performed in the force gradient detection mode, we adjusted the simulation procedure in order to provide force gradient values.

3.4.1. Determination of the actual tip-sample distance

The first step towards the quantification of the electrostatic response is determining the actual tip-sample distance during measurements. As already introduced in Chapter II, when the oscillation amplitude during the second scan is relatively small, the tip-sample distance is equal to: $z \approx z_0 + L$. We remind that L is the lift height, and z_0 is the initial distance of the tip during the first scan, that is supposed to be approximately equal to the set-point amplitude of vibration A_{sp} during the topography scan (see Fig. II - 9). z_0 is usually obtained by performing an approach curve of the amplitude of vibration over a stiff sample [14]. An example of an approach curve recorded with one typical probe used for our measurements is presented in Fig. V - 20. The idea behind this method is that as the tip approaches the surface, its oscillation amplitude decreases, and is supposed to nullify once it "touches" the surface of the sample. That being so, the distance traveled from the starting position of A_{sp} to that at zero oscillation represents the tip-sample distance z_0 at the set-point amplitude.

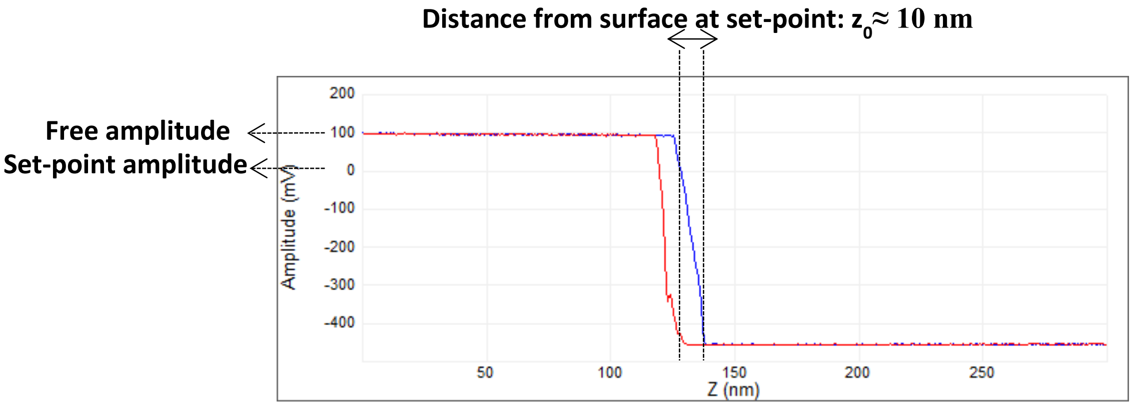

Fig. V - 20 : Typical amplitude vs. distance curve obtained over a stiff substrate for the quantification of tip-sample distance z_0 during tapping mode scanning.

3.4.2. Force gradient calculation

Comsol® software only calculates the interaction force. In order to obtain the force gradient, we calculated the force *F* at different tip-sample distances *z* (10 nm to 90 nm). Then, we deduced the first derivative of the resulting power-law fitting equation of *F* (*z*) to get the gradient *G* (*z*), as shown in Fig. V - 21.

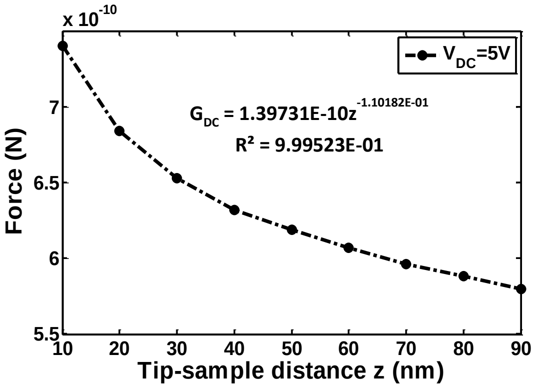

Fig. V - 21 : Typical electrostatic force vs. distance curve computed with our numerical model. Modeling results are fitted to a power-law trendline. The derivative of this equation gives the expression of the force gradient vs. distance.

G (*z*) is calculated at 5 V and 6 V, in order to obtain the first parabolic coefficient α_{DC}, such as:

$$\alpha_{DC}(z) = \frac{f_0}{2K}\left(\frac{G(z)_{6V} - G(z)_{5V}}{6^2 - 5^2}\right) \tag{V-3}$$

3.4.3. Tip calibration

Besides tip-sample distance determination, a precise calibration of the tip size is crucial for the quantification of electrostatic force gradients. Manufacturer only claims that R_0 is less than 25 nm.

Hence, α_{DC} (*z*) curves have been performed on a bare metallic substrate for different tips of the same series and subsequently fitted to simulations [13, 14]. In this case, *z* is known and the tip cone height *H* is fixed to 10 µm. Then, since no dielectric film is present, the only fitting parameters become tip cone half-angle θ and tip radius R_0.

As shown in Fig. V - 22, a tip radius of R_0 = 13 nm and θ = 10 ° fit quite well most experimental curves for the above set of experiments.

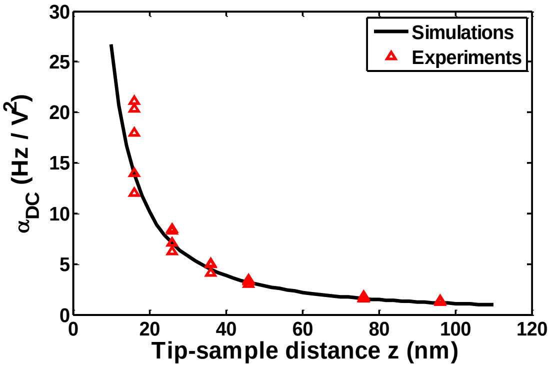

Fig. V - 22 : Best tip geometry fitting curve of experimental results and simulations over a metallic substrate, obtained for tip radius R_0 = 13 nm, half-cone angle θ = 10° and fixed cone height H = 10 µm.

3.4.4. SiO₂ nanoparticles dielectric permittivity quantification

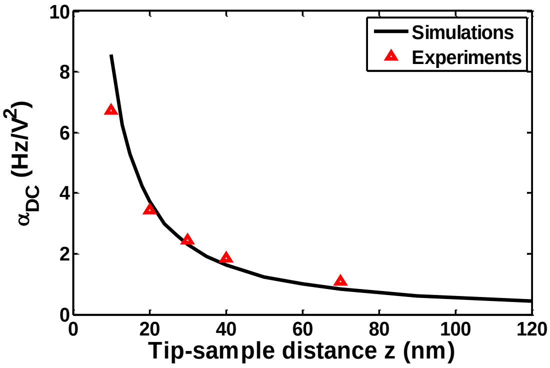

Fig. V - 23 : Experiments and simulation fitting curves of $\alpha_{DC}(z)$ measured over a SiO₂ nanoparticle of approximately 20 nm diameter, obtained for a 3.9 dielectric permittivity.

An example of an $\alpha_{DC}(z)$ curve over a SiO₂ nanoparticle of 20 nm diameter is presented in Fig. V - 23. A dielectric permittivity of 3.9 provides relatively good agreement of experiments to simulation values.

3.4.5. PS nanoparticles dielectric permittivity quantification

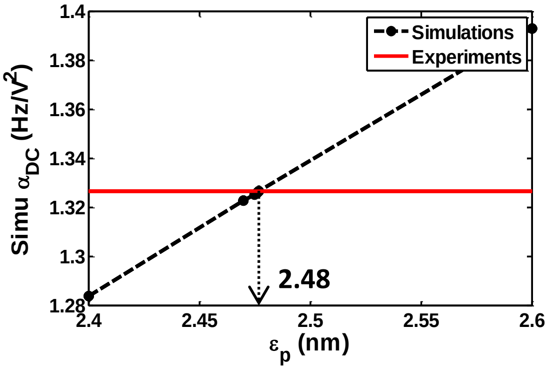

Fig. V - 24 : Best experiment to simulation fit for PS particles of 250 nm diameter at z = 20 nm, obtained for a 2.48 dielectric permittivity.

PS particles dielectric permittivity has been quantified from the fitting of experimental EFM α_{DC} value at z = 20 nm, to simulations with a 250 nm particle diameter, since α_{DC} measurements have been acquired above particles possessing diameters mostly close to 250 nm (Fig. V - 16). Within these conditions, we find 2.48 as the best fit for PS dielectric constant (see Fig. V - 24).

3.4.6. α_{DC} versus alumina thickness

In this paragraph, we confront the results of Fig. V - 17 and Fig. V - 18 to simulations. Our material geometries and permittivities have been modeled as sketched on Fig. V - 2. Polystyrene particles have been implemented as 250 nm diameter particles of a standard dielectric permittivity of 2.6, and the uniform alumina shell over the whole sample surface has been simulated with a 9.8 permittivity.

All parameters have been fixed, while only the thickness of Al_2O_3 layers has been changed. Fig. V - 25 presents experimental and simulation results for PS+Al_2O_3 shells at $z \approx 20$ nm and those for Al_2O_3 films alone at $z \approx 18$ nm (data of Fig. V - 19) for variously thick Al_2O_3. The same trend between simulations and experiments, and a good agreement of α_{DC} values between EFM measurements and our model, can be noticed. However, the fitting is more robust for Al_2O_3 films alone. Over PS+Al_2O_3 assembly, the fitting is less accurate especially at high shell thicknesses.

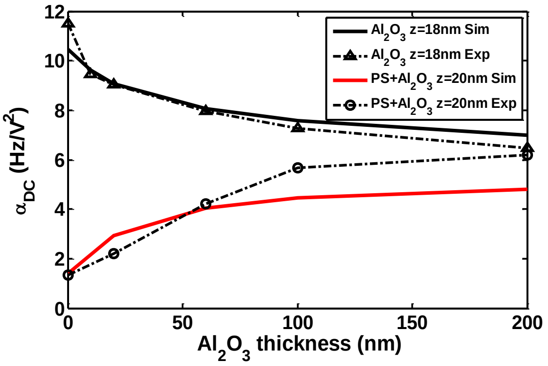

Fig. V - 25 : Experimental vs. simulated α_{DC} values for PS+Al_2O_3 (*z* = 20 nm) and Al_2O_3 films (*z* = 18 nm) for different Al_2O_3 thicknesses.

In order to understand these differences, we review the main experimental features neglected during simulations:

a) Cantilever:

The cantilever arm has not been implemented in our Comsol® model. Although it plays a substantial role over thick samples [15], the cantilever contribution is usually neglected when force gradient detection is used. This can eliminate the effect of this first disregarded experimental parameter.

b) Neighbor particles:

As the shell thickness increases, the separation decreases between the borders of the particles that are placed at fixed positions. The contribution of neighbor particles could justify the important signal increase over thick covered layers. Nevertheless, we verified this influence as we introduced a disk around the particles in our 2D axisymmetric model. The influence of the surroundings on the electrical response has been verified to slightly enhance the overall signal versus t_i, however, keeping a similar slowly increasing trend of α_{DC} versus t_i. This, too, is not sufficient to interpret Fig. V - 25 results.

c) Particles roughness:

Particles surface roughness has been neglected in the simulation model. The approximation of PS to perfect 250 nm diameter spherical shape might either underestimate or overestimate the real amount of PS material in the region probed with EFM. However, both cases result in a relatively small change for any thick layer. Thereby, surface roughness cannot constitute the explanation of the sudden change versus alumina thickness.

d) *z* position uncertainty:

The above results must be due to a certain irregular change with the shell thickness. A possible reason would be the static deflection of the cantilever when the latter undergoes the effect of a force. This deflection is usually neglected, and tip-sample distance is calculated as explained in above paragraphs [16]. However, as it can be noticed from Fig. V - 16, the force gradient slope versus tip-sample distance increases with alumina. Hence, for important t_i, uncertainties on *z* can result in higher errors of the simulated system. In fact, we have verified in simulations that only 3 nm decrease of *z* can afford the good fit with 100 nm and 200 nm thick layers. Furthermore, the static deflection is likely to increase with thicker alumina films as the latter also intensify the attractive electrostatic force.

3.4.7. Alumina shell dielectric permittivity quantification

In order to quantify the dielectric permittivity of alumina shells over PS particles, the EFM experimental value over PS with 60 nm Al_2O_3 has been used as it better agrees with the expected response verified through simulations. Contrarily to the above simulations of α_{DC} (t_i), we used here the exact fitted value of PS permittivity that is equal to 2.48. Within these conditions, we find 10.78 as the best fit for Al_2O_3 shell dielectric permittivity (see Fig. V - 26).

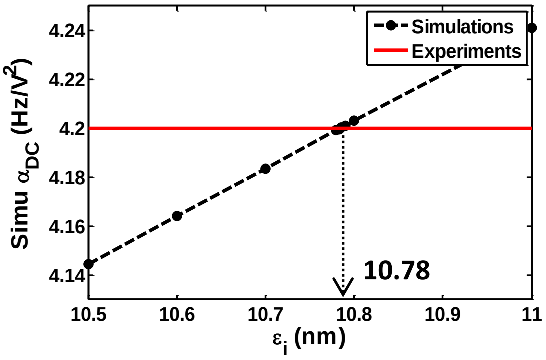

Fig. V - 26 : Best experiment to simulations fit for PS particles of 250 nm diameter with the fitted 2.48 PS permittivity, covered by a 60nm Al_2O_3 shell at *z* = 20 nm, obtained for a 10.78 Al_2O_3 dielectric permittivity.

4. Type 2 samples: particle + interphase + matrix

In the first section of this chapter, EFM capability at distinguishing two superimposed materials with 3D finite-size, mainly in the shape of a nanoparticle (SiO_2 and PS) covered by a thin shell (Al_2O_3), has been addressed. Those samples model either: a) a particle surrounded by an interphase in a thin section of a nanocomposite specimen where the matrix has been removed by the cutting process (particle + interphase), or b) a particle in a nanocomposite covered by the matrix, with no interphase between them (particle + matrix). Developing appropriate experimental protocols and signal analysis, we found that EFM is convenient to detect and characterize the intrinsic permittivity of both, the upper thin layer (Al_2O_3) and the subsurface nanoparticle (PS and SiO_2) of variable dimensions.

In this second section, the experimental results aim at detecting the interphase in a complete nanodielectric model: particle + interphase + matrix. Hence, the goal is now to detect the material embedded between the particle and the upper layer, using an additional dielectric film. This third material (mat3) can be either placed at the top of our initial system: PS+Al_2O_3+(mat3), such as Al_2O_3 becomes the interphase model; or equally, it can be placed between the alumina shell and polystyrene spheres: PS+(mat3)+Al_2O_3, where this third material (mat3) plays the role of the interphase (see Fig. V - 27).

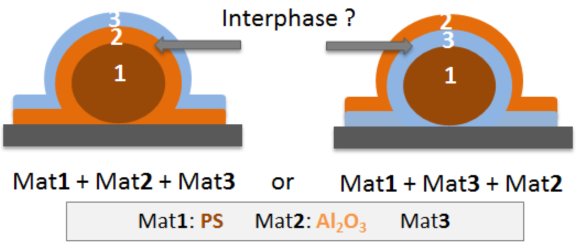

Fig. V - 27 : Simplified configuration of model samples for interphase study: particle + interphase + matrix. Mat3 is either polyvinyl acetate or silicon dioxide. Depending on the deposition method, the geometry could slightly differ from the above sketch.

We note that within all our samples set, particles can be positioned by the topography scan since covering layers have been prepared in an appropriate way to keep the bulge associated to the spheres. Obviously, a more complete study would be performed over totally embedded particles. However, according to our choice of materials, the dielectric contrast is not always sufficient to undertake these measurements. Nevertheless, such configuration, where the particle protrudes from the surface, has been met in previous works studying interphases in “real” nanocomposite systems, either with mechanical scanning probe microscopy techniques [17-19], or with EFM [1, 20-22].

In the following, three main methods have been investigated in order to characterize the interphase model in our samples. PVAc has been used as the third material for method 1, and SiO_2 for methods 2 and 3. PVAc and SiO_2 films deposition has been described in Chapter IV. Henceforth, we will use the denominations: mat1, mat2 and mat3 to designate respectively, PS particles, Al_2O_3 layer and the third material (PVAc or SiO_2).

4.1. Method 1: PS+Al_2O_3 versus PS+Al_2O_3+PVAc

The results of section 3 have been used in order to set up the first method for interphase detection below a matrix. In this first method, we used PS particles of 380 nm approximate diameter covered by 60 nm and 100 nm Al_2O_3 layers. In parallel, a similar set of samples has been covered by an additional layer of PVAc with spin coating as described in Chapter IV.

Fig. V - 28: Interphase detection method 1, left: sketch of the samples to be compared, right: methodology.

The first methodology is based on comparing the signals at same tip-sample distance above PS+60nmAl_2O_3 and PS+100nmAl_2O_3 to PS+60nmAl_2O_3+PVAc and PS+100nmAl_2O_3+PVAc, respectively. As Al_2O_3 is here the interphase model material, PVAc and PS permittivities are then supposed to be the known parameters (Fig. V - 28).

A decrease of EFM response above PVAc covered particles compared to uncovered ones is researched. In fact, since we suppose that PS and PVAc permittivities are given, we know that $\varepsilon_{PVAc} = 3.2 > \varepsilon_{PS} = 2.6$. Therefore, based on the conclusion of section 3.3, the addition of PVAc above PS must increase the signal. Otherwise, a change in particle or matrix permittivities must be the reason for this firm change in the tendency of the signal. Then, since Al_2O_3 is expected to sufficiently enhance the effective permittivity of the covered particle, an additional PVAc layer must decrease the signal, proving that the region below PVAc possesses a higher permittivity than the matrix. This can indicate the presence of a layer above the particle, which possesses a higher permittivity than both, PS and PVAc.

In this section, a statistical study becomes substantial. In fact, spin-coated layers on our rough samples do not necessarily lead to a uniform thick film on the whole surface [23]. Consequently, all information about initial particles diameter is lost with matrix addition.

Therefore, we performed measurements on 12 × 3 μm^2 images that contain 30 complete particles on average. We verified the validity of this choice for the number of particles, by comparing the statistical results on a 12 × 12 μm^2 image to those on its quarter. Calculated values do not significantly change. Moreover, we used AC-2ω force gradient detection in the double-pass method with constant lift distance. A 12 × 3 μm^2 scan with this technique performed at an appropriate resolution takes around 40 minutes. Since a quantitative comparative study is better to be performed with the same tip, a higher imaging duration, for a series of minimum 5 samples, might already wear the tip, in addition to the enhanced probability of breaking and contaminating it, of image drifts etc. For all these reasons, we referred to 12 × 3 μm^2 imaging areas for the rest of experiments.

4.1.1. Reference samples: PS+60nmAl$_2$O$_3$ versus PS+100nmAl$_2$O$_3$

Before matrix addition, we verified that chosen samples possess the usual behavior on which our forthcoming investigation of the interphase could be based. For all next sections, unless otherwise stated, AC excitation has been applied, and the 2ω-frequency shift component has been extracted.

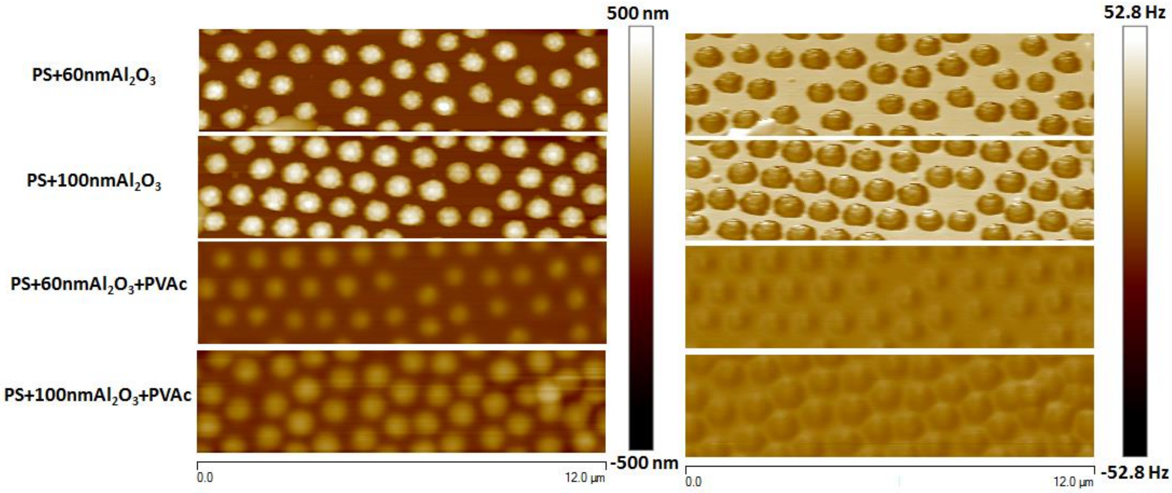

Fig. V - 29 : Topography and EFM AC-2ω frequency shift images of a 12 × 3 μm^2 region of PS+60nmAl$_2$O$_3$, PS+100nmAl$_2$O$_3$, PS+60nmAl$_2$O$_3$+PVAc and PS+100nmAl$_2$O$_3$+PVAc samples, V_{AC} = 5 V and ω = 200π rad/s.

Fig. V - 29 presents respectively topography (left) and EFM images (right) of 12 × 3 μm^2 regions of uncovered and PVAc covered PS, PS+60nmAl$_2$O$_3$ and PS+100nmAl$_2$O$_3$ samples. We have performed a cut-line of around 1.2 μm length in the middle of each particle of Fig. V - 29. The average and the standard deviation of extracted data have been measured at similar x positions. In Fig. V - 30, the resulting averaged topography profiles (Fig. V - 30a.) and their corresponding EFM averaged signals (Fig. V - 30b.) are plotted for the reference samples: PS+60nmAl$_2$O$_3$ versus PS+100nmAl$_2$O$_3$.

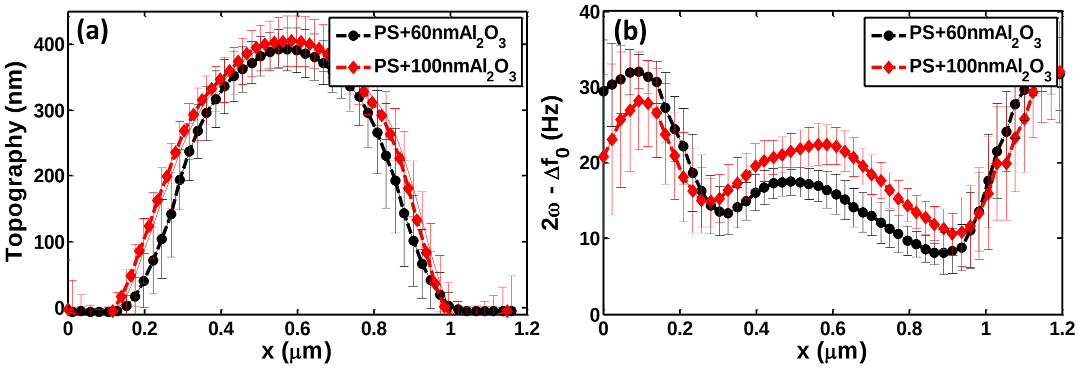

Fig. V - 30 : Average profiles for PS+60nmAl$_2$O$_3$ and PS+100nmAl$_2$O$_3$ samples for a. topography and b. 2ω-frequency shifts results. V_{AC} = 5 V, ω = 200π rad/s and z = 21 nm.

Similarly to the case of 250 nm diameter PS particles (type 1 samples), here too, the average height of covered PS particles superimposes with only 3 % difference. However, the width changes more significantly as it can be directly recorded from Fig. V - 29. The measured difference is around 35 nm, in accordance with the theoretical one of 40 nm. Note that averaging tends to smooth the surface roughness.

Concerning EFM measurements, we have compared the signals at the center of the particles. In order to get a precise, accurate value in the center, without borders effects, we have measured the average EFM signals going from x = 0.45 μm to x = 0.75 μm. One must also note that if lateral forces are influencing the z component, this lateral contribution is expected to be nullified at the center of the particle, where it must exhibit a symmetric behavior from either sides of the center (see Chapter III - Fig. III - 23). Therefore, an averaging around the supposed-to-be center must sufficiently reduce lateral and borders effects.

The EFM average values are around 15.4 ± 2.2 Hz and 20.6 ± 1.9 Hz for PS+60nmAl$_2$O$_3$ and PS+100nmAl$_2$O$_3$, respectively. Then 2ω - Δf$_0$ increases by ~ 34 % with an additional 40 nm Al$_2$O$_3$ layer. The desired tendency observed in section 3.2 is thus verified. This set has been selected to be subsequently compared to the covered ones with PVAc matrix. Note that we have prepared all PS samples within the same experimental conditions, during the same day. Among them, some samples were selected as reference ones, and the others were divided into samples to be covered either with 60 nm or with 100 nm thick Al$_2$O$_3$ layers. Similarly, among PS spheres with Al$_2$O$_3$, we have selected some of them to be covered by PVAc with spin coating. Accordingly, the samples are supposed to be comparable enough.

4.1.2. Spin coated PVAc film characteristics

Topography contrasts of Fig. V - 29 indicate a considerable decrease of particles measured height after coverage with PVAc. Then, this supposes two possible configurations for the film prepared with spin-coating:

a) The film is homogeneously displayed over the core + shell surface, as well as the sample bottom (Fig. V - 31a.).

b) The film is not homogeneously spread over the surface of the sample, comparing particles top regions to substrate surface (Fig. V - 31b.). The film is more likely to accumulate in the deep pits, leaving less solution at the peaks.

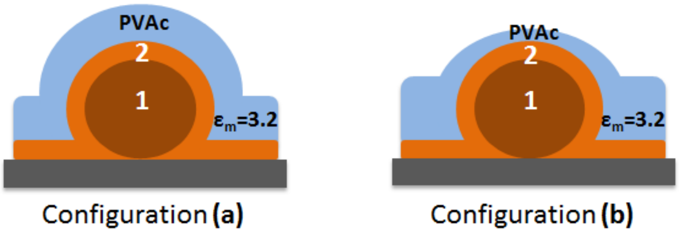

Fig. V - 31 : Possible configurations of PVAc spin-coated films over PS+Al_2O_3 samples: a. film thickness is homogeneous on the whole surface, and b. the film is thicker between the particles.

In order to gain a deeper insight into film configuration and thickness, we performed with a rigid AFM tip, a scratch into the PS+60nmAl_2O_3+PVAc sample with AFM contact mode. Afterwards, the cut has been imaged with a new tip, since scratching breaks the tip. A typical thickness between substrate and film surface between particles is around 120 nm. This value can be roughly supposed to represent PVAc film thickness in the bottom of the sample.

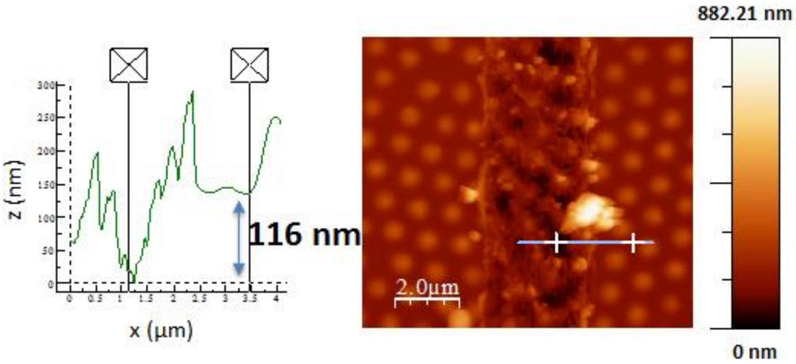

Fig. V - 32: Topography image of a scratched PS+60nmAl_2O_3+PVAc sample with a stiff AFM tip.

Furthermore, since spin-coating of polymer films is not mastered on rough surfaces like other thin film deposition techniques, e.g. ALD, a verification of PVAc sticking to particles surface is needed. In order to do so, and in addition to topography measurements, we combined EFM characterizations to nanomechanical ones with Quantitative nanomechanical measurements, the PeakForce-QNM (see Chapter IV).

Note that all nanomechanical PF-QNM measurements have been performed at LAPLACE laboratory in Toulouse, by the PhD student Mohammed Houssat, thanks to the collaboration with Dr. Nadine Lahoud.

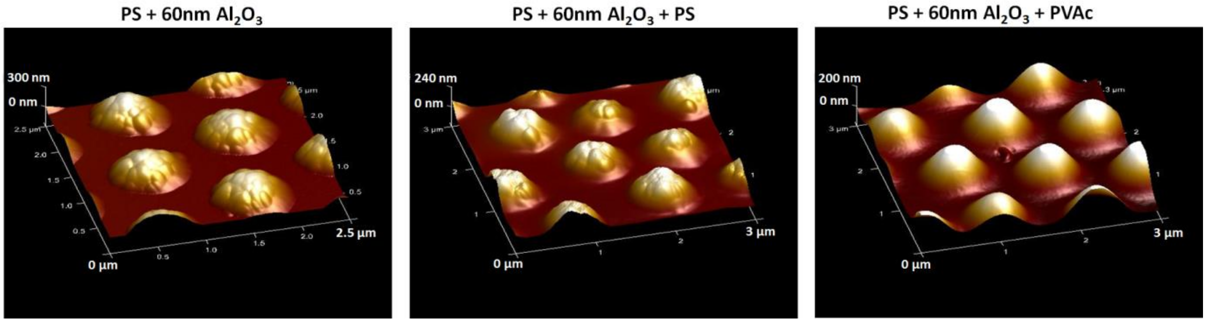

Fig. V - 33 : 3D - topography images obtained with PeakForce-QNM for PS with 60 nm Al_2O_3, PS with 60 nm Al_2O_3 covered by a PS spin-coated film and PS with 60 nm Al_2O_3 covered by a PVAc spin-coated film.

We start by comparing topography images of polystyrene spheres with an alumina layer, before and after the deposition of another material; a polystyrene film and a polyvinyl acetate film (see Fig. V - 33). We observe a decrease in particles height with film deposition, and most interestingly, particles surface gets smoother on the sides for particles with PS film, and on the whole surface for the PVAc film.

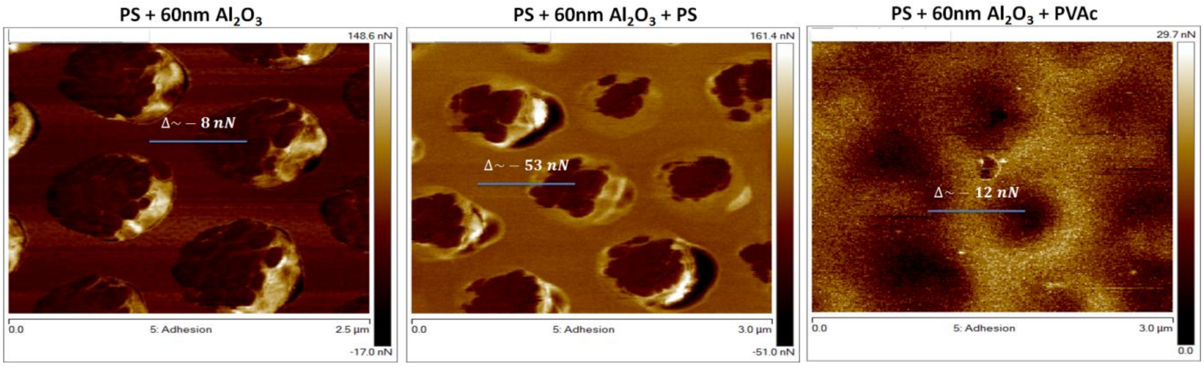

Fig. V - 34 : Adhesion images obtained with PeakForce-QNM for PS with 60nm Al_2O_3, PS with 60nm Al_2O_3 covered by a PS spin-coated film and PS with 60nm Al_2O_3 covered by a PVAc spin-coated film.

On the other hand, the corresponding adhesion images show on Fig. V - 34 noticeable differences in the contrast values: -8 nN, -53 nN and - 12 nN for PS+60nmAl_2O_3, PS+60nmAl_2O_3+PS and PS+60nm Al_2O_3+PVAc, respectively. A high adhesion contrast is known to reveal the detection of two phases, as stiffer regions induce low adhesion forces with the tip compared to smoother ones (Chapter IV - section 4.1) [24]. Since PS+60nmAl_2O_3 and PS+60nmAl_2O_3+PVAc present low contrasts compared to PS+60nmAl_2O_3+PS, this demonstrates that Al_2O_3 and PVAc have successfully covered the whole surface of the sample. Whereas, due to the contrast sign and its important value on PS covered samples, it can be deduced that PS film deposition is not homogeneous on the entire surface; namely, particles top is the least covered, or it might not be even covered at all. We deduce that PS film deposition fills up the regions between particles first.

Furthermore, we confront nanomechanical AFM signals of Fig. V - 34 to EFM ones in Fig. V - 35.

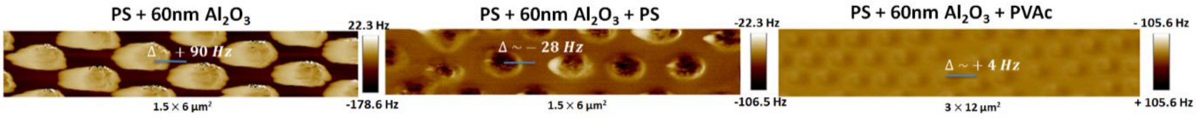

Fig. V - 35 : DC - EFM frequency shift images for PS with 60nm Al_2O_3, PS with 60nm Al_2O_3 covered by a PS spin-coated film and PS with 60nm Al_2O_3 covered by a PVAc spin-coated film (low gains and drive amplitude cause the expanded PS+60nmAl_2O_3 shape).

PS covered samples exhibit EFM contrast inversion in regard to uncovered ones (Fig. V - 35). We remind that EFM images measure the greatest frequency shifts at the regions with the highest capacitance. Consequently, this indicates that the top of PS+Al_2O_3+PS exhibit higher dielectric permittivity than the rest of the sample. Contrariwise, PS+Al_2O_3+PVAc particles present low EFM contrast. Therefore, it can be deduced from EFM images that the PS film partially covers the particles contrarily to PVAc, masking the whole surface. This deduction is supported by the previous results of nanomechanical characterization.

Henceforth, EFM can be used alone to prove the homogeneity of soft films deposition above the stiffer surface. For instance, in Fig. V - 36 we show the signal above a PS+60nmAl_2O_3 covered by a PVAc film from a base PVAc solution of lower concentration (C_2) than the solution of the PVAc covered sample of Fig. V - 35 (C_1). The concentration is related to the thickness t_C of the spin coated film ($t_{C1} < t_{C2}$) [25]. It can be noticed that the sign of EFM contrast for PVAc covered samples of C_2 concentration is similar to that of PS covered samples of Fig. V - 35. This proves that PVAc and PS spin-coating deposition mechanisms are close, and thereby, shows that PVAc additional layer is actually closer to the configuration (b) of Fig. V - 31.

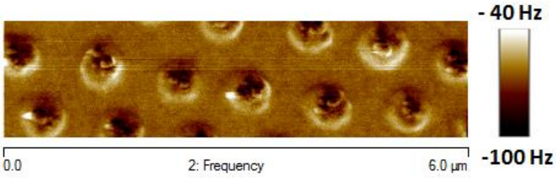

Fig. V - 36 : DC - EFM frequency shift image for PS with 60 nm Al_2O_3 covered by a PVAc spin coated film from a base solution with a lower concentration (*C_2*) than the solution of the PVAc covered sample (*C_1*) of Fig. V - 35.

4.1.3. Results for: PS+60nmAl_2O_3 versus PS+60nmAl_2O_3+PVAc

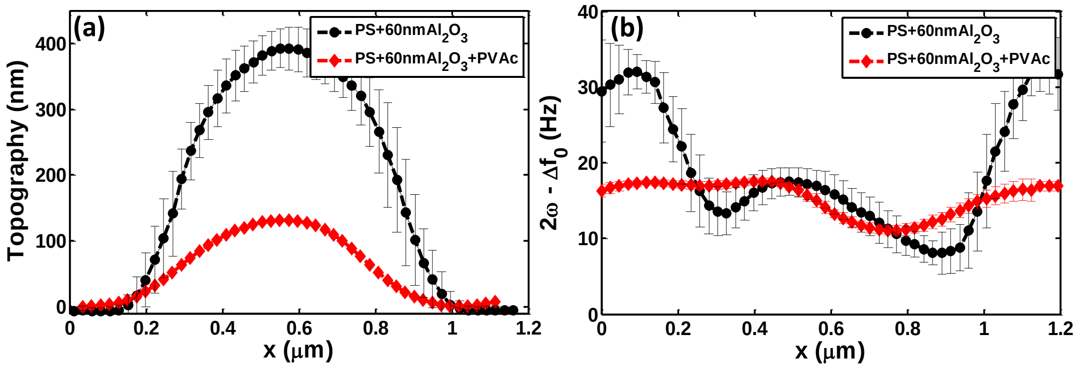

Fig. V - 37 : Average profiles of PS+60nmAl_2O_3 and PS+60nmAl_2O_3+PVAc for a. topography and b. 2ω - frequency shifts results. V_{AC} = 5 V, ω = 200π rad/s and z = 21 nm.

We respectively compare in Fig. V - 37a. and Fig. V - 37b. the average topography and electrical frequency shift profiles, for PS+60nmAl_2O_3 and PS+60nmAl_2O_3+PVAc. Their corresponding mean values calculated around the center give 15.4 ± 2.2 Hz without the matrix compared to 14 ± 2.4 Hz with PVAc. We find that the matrix only slightly decreases the overall center signal over PS+60nmAl_2O_3 (1% ratio). Since this low decrease is confusing and not sufficiently noteworthy, we study in the following paragraph the case of 100 nm alumina layer.

4.1.4. Results for: PS+100nmAl_2O_3 versus PS+100nmAl_2O_3+PVAc

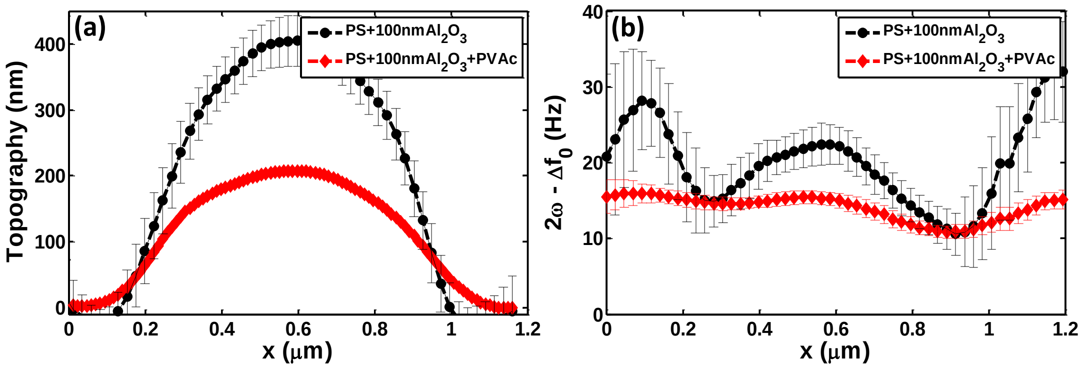

Fig. V - 38 : Average profiles of PS+100nmAl_2O_3 and PS+100nmAl_2O_3+PVAc for a. topography and b. 2ω - frequency shifts results. V_{AC} = 5 V, ω = 200π rad/s and z = 21 nm.

Similarly to 60 nm Al_2O_3 shells, Fig. V - 38a. and b. present respectively the average topography and electrical frequency shift profiles for PS+100nmAl_2O_3 and PS+100nmAl_2O_3+PVAc. Their corresponding average values calculated around the center give 20.6 ± 1.9 Hz without the matrix compared to 14.6 ± 0.95 Hz with PVAc. Hence, it can be noticed in this case that the matrix decreases the overall central signal of PS+100nmAl_2O_3 by ~ 30 % ratio. Contrarily to 60 nm alumina shell case, samples prepared with an interphase model layer of 100 nm meet with a good extent our expectations. In fact, upon the addition of PVAc, the signal has decreased over the PS particle that is considered to be covered by an unknown shell. Since $\varepsilon_{PVAc} > \varepsilon_{PS}$, this supposes that the effective permittivity of PS has changed due to its shell. The latter must possess a higher dielectric permittivity than both PVAc and PS, equal to 3.2 and 2.6, respectively. This is consistent with our case of Al_2O_3 shell, possessing a permittivity of 9.8.

The difference between the two treated cases, 60 nm and 100 nm Al_2O_3 intermediate shells, could be due to:

a) Thinner PVAc film over PS+60nmAl_2O_3 than PS+100nmAl_2O_3: since all experimental conditions are preserved during the deposition of PVAc, the same total volume of the matrix must be left to be dispersed on the surface. Moreover, PS+60nm Al_2O_3 possess larger empty space between two neighbor particles compared to PS+100nmAl_2O_3. As PVAc deposition mechanism has been concluded to start filling up empty cavities before covering the particles, this can suppose that PVAc film thickness is lower over PS+60nmAl_2O_3+PVAc samples. A very thin film can be insufficient to induce a detectable change in the polarization response compared to the base sample (refer to α_{DC} curve versus t_i of Fig. V - 17).

b) Lower effective permittivity of PS+60nmAl_2O_3 compared to PS+100nmAl_2O_3: if the PVAc layer is however supposed to have the same thickness over both covered samples, the lower effective permittivity of the core material with additional 60 nm Al_2O_3 compared to 100 nm Al_2O_3 could explain the low decrease. As the contrast in the permittivities of the core and the matrix is reduced, the risk becomes to be unable detecting an important change in EFM response.

This proves the sensitivity of this first method, within the right geometry and permittivity ratios, to detect the region at the interface between PS particles and the PVAc matrix.

4.1.5. Method 1: limits

The comparison between the associations of mat1+mat2 compared to mat1+mat2+mat3 has shown sensitivity to the effective permittivity of PS particles with 100 nm thick Al_2O_3 film. However, this methodology cannot be adopted as a general method, and in order to extend it, higher precise deposition techniques are needed for the third material, for the two following reasons:

a) The comparison of mat1+mat2 versus mat1+mat2+mat3 is not easily feasible in practice. In fact, such samples confrontation supposes to be able to have the particle with an interphase, alone. Since the creation of the interphase requires the interaction between the particle and the matrix, it cannot be obtained unless after the fabrication of the nanocomposite. Thus, as mentioned earlier, the bulk polymer layer above the particles in a nanocomposite must be extracted to reveal the interphase and obtain a similar association to the model mat1+mat2. However, at which level should matrix etching be stopped? Does it not induce interphase properties changes?

b) Hence, a more realistic method would be to compare the particle + matrix association with and without the interphase. This means to be able to deposit a PVAc film over PS and PS+Al_2O_3 of the same thickness, or at least, with known and accurately controllable thickness. However, as it has been detailed in section 4.1.2 of this chapter, and further investigated in section 4.1.4, spin-coated films are hardly controllable over our substrates since the latter possess rough surfaces.

Therefore, we chose next another alternative method to prove with EFM the existence of an embedded layer between the particle and the surface material.

It must be highlighted that the very low EFM contrasts of PVAc covered samples can lead to suppose that the sublayer is not being detected. However, it may be a wrong interpretation since the bottom of the samples is expected to possess a thicker PVAc film than above the particles. The center and the bottom regions cannot be accurately compared. Nevertheless, this reinforces the need of another method and/or another type of samples to confirm subsurface interphase model detection.

4.2. Method 2: PS+50nmSiO$_2$ versus PS+100nmAl$_2$O$_3$+50nmSiO$_2$

4.2.1. EFM measurements

Fig. V - 39: Interphase detection method 2, left: sketch of the samples to be compared, right: methodology.

As it has been drawn from the conclusion of method 1, a controllable film thickness is needed in order to demonstrate the presence of the interphase layer in samples that model more general nanocomposite configuration. Hence, in the following methods, we used SiO$_2$ instead of PVAc, since it can be deposited with plasma sputtering. The latter is one example of a high precision thin film deposition technique that showed to homogeneously spread SiO$_2$ molecules over the whole sample surface, quite similarly to ALD (see Chapter IV). This allowed us to adopt the second methodology: comparison of mat1+mat3 to mat1+mat2+mat3 at same tip-sample distance. The latter assemblies model in a general way a comparison between a nanocomposite with and without an interphase, respectively. If the signal strengthens with the interphase layer, this shows the detection of an interphase with a permittivity higher than the effective one of particle + matrix association. In fact, according to section 3, when EFM signal increases with a thicker layer at same lift height, this indicates that the added material possesses a dielectric permittivity higher than the effective one of the initial particle + shell assembly. Although in these comparisons the added material is not at the surface, but in the middle, the same analysis holds.

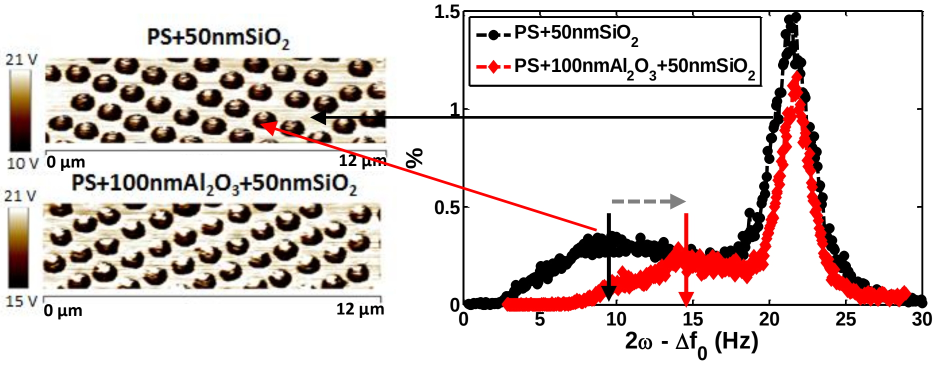

Fig. V - 40 : EFM images of PS+50nmSiO$_2$ and PS+100nmAl$_2$O$_3$+50nmSiO$_2$ samples (left), and their corresponding distribution histogram (right). V_{AC} = 5 V and ω = 200π rad/s.

Fig. V - 40 presents EFM images of PS+50nmSiO_2 and PS+100nmAl_2O_3+50nmSiO_2 along with the histogram illustrating signal distribution of both EFM images. As we set the latter scale to the values of the histogram with the highest percentage, we deduce that the greatest maximum identifies the bottom of the sample and the lowest one goes for the particle center values (see annotations on Fig. V - 40). A shift towards higher Δf_0 is found for particles with an additional intermediate Al_2O_3 layer. This indicates the sensitivity to the embedded Al_2O_3 layer below SiO_2, and corroborates the hypothesis for this method.

4.2.2. [redacted]

The observed shifts are consistent with this method 2 logic, proving that the detected interphase has a higher permittivity than the effective permittivity of PS+50nmSiO_2 ($\varepsilon_i > \varepsilon_{(PS+50nmSiO2)}$). Moreover, since $\varepsilon_{SiO2} > \varepsilon_{PS}$, leading to an $\varepsilon_{(PS+50nmSiO2)} > \varepsilon_{PS}$ according to section 3 conclusions, this shows that $\varepsilon_i > \varepsilon_{PS}$. However, no information can be drawn about the relative permittivity of the interphase compared to the matrix (ε_i versus ε_{SiO2}).

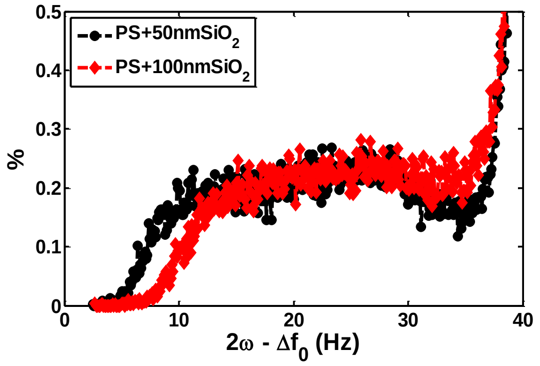

Fig. V - 41 : EFM histogram of distribution of PS+50nmSiO_2 and PS+100nmSiO_2 samples. V_{AC} = 5 V, ω = 200π rad/s.

For instance, an additional SiO_2 layer, representing a thicker matrix layer above the particles, would have also raised the signal, since the matrix possesses a higher permittivity than the particles (Fig. V - 41). This method could be important when information about the interphase compared to the particle is researched, while an approximate notion compared to the matrix one is enough. Certainly, once associated to simulations, signal change ratio can quantify the sublayer permittivity. However, a straightforward method would be to gain insight into the relative permittivity of the interphase layer model regarding both, matrix and particle, before verification with simulations. Consequently, we propose in method 3 a comparison procedure sufficient to draw direct information of the interlayer properties.

4.3. Method 3: comparisons of samples with similar dimensions

The above adopted comparison methodology has shown sensitivity to the interlayer. Nevertheless, these methods have shown limitations: either the compared samples are not so much feasible for a real application to nanocomposites (method 1), or the information about the relative identity of the interphase to particle and matrix is not complete (method 2). Moreover, the total thickness of confronted samples was not the same. Confusions due to the topography can be always considered as misleading, even if we have proved the predominance of the intrinsic response of the layers. Consequently, in this last method, we have compared samples possessing similar total height and stacked model layers shape. Sketch of Fig. V - 42 details the respective steps adopted in order to cautiously show the presence of the material between PS particles and the surface material.

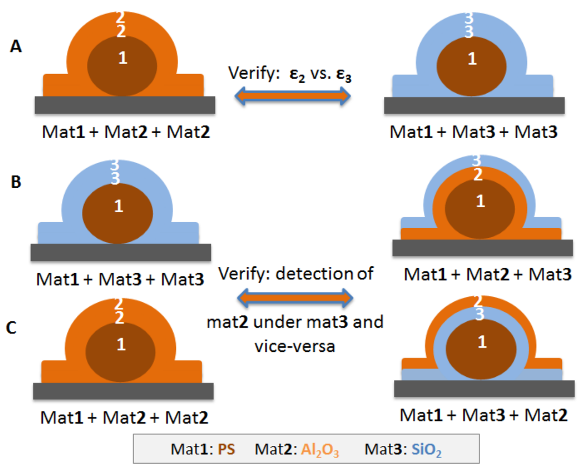

Fig. V - 42 : The main three steps of samples comparisons for method 3: comparisons of samples with similar dimensions.

In this last method too, PS spheres, Al_2O_3 layers and SiO_2 have been deposited with the same adopted methods for previous samples: self-assembling + plasma etching, ALD and PSD, respectively (Chapter IV). EFM measurements have been acquired in the AC-force gradient detection mode, with the extraction of the 2ω component. AC-$\alpha_{2\omega}$ coefficient values have been calculated according to the conversion steps explained in Chapter IV (Fig. IV - 13). For this set of measurements, α was used as an independent coefficient from the applied voltage, contrarily to section 3.2.3 where it was especially used to remove the effect of surface contact potential and charges. In fact, 2ω-Δf_0 is naturally independent of those parameters. A tip-sample distance of around 30.14 nm has been conserved for all of the coming up measurements, unless otherwise stated.

The reproducibility of the following results has been always verified at several sample regions and most of the times, for several comparable samples, measured with different probes. However, since in this section we correlate experiments to simulations for a large set of samples, we present results obtained with a specific probe for all measurements.

4.3.1. [redacted]

The first step in order to confront experiments to simulations is always the calibration of the tip geometry. We performed one-point $\alpha_{2\omega}(z)$ curves over a metallic sample at a limited region (10 nm × 2.5 nm). Using the truncated conical tip with the same numerical model parameters as Chapter III, and extending to force gradient measurements, we obtain a tip radius of 28 nm and cone half-angle of 15 ° that best fit experiments with a 4.6 % total error. Errors have been measured by:

$$error = 100 \times \left| \frac{\alpha_{exp} - \alpha_{sim}}{\alpha_{exp}} \right| \quad \text{(V-4)}$$

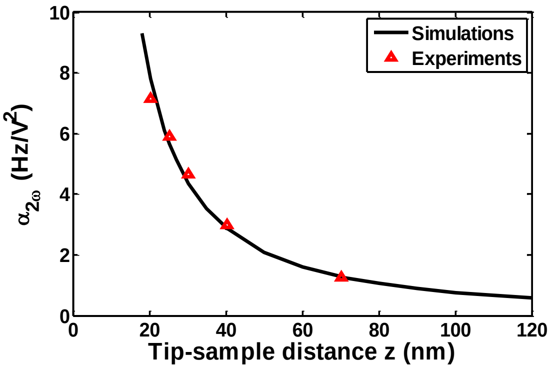

Fig. V - 43 : Tip calibration: experimental measurements fit simulations for a tip of (R_0, θ) = (29 nm, 15 °) with 4.6 % total error.

[redacted]

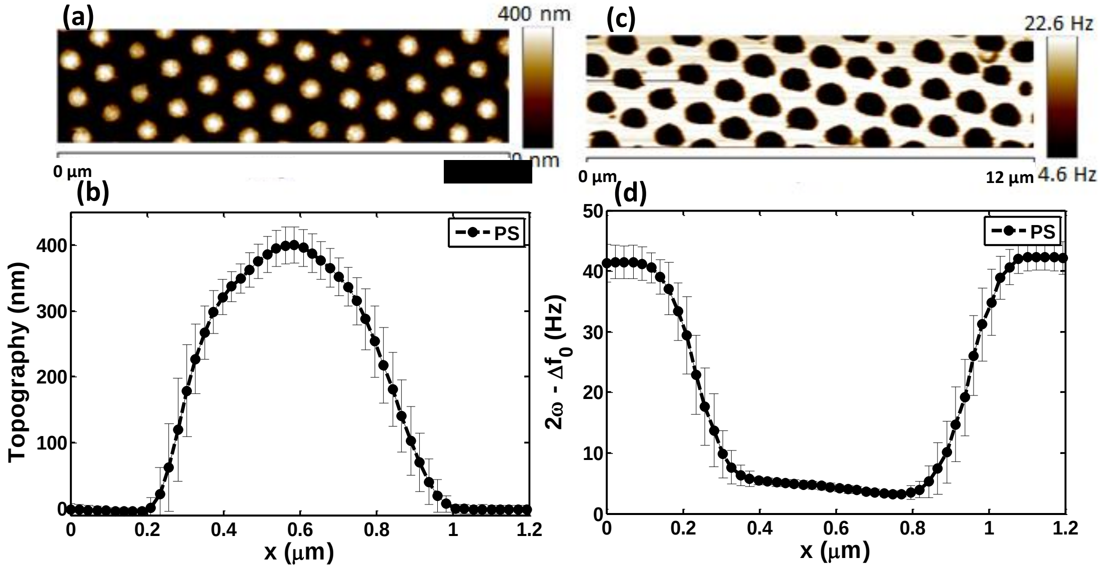

Fig. V - 44 : AFM images and average cross-sectional profiles for PS reference sample, of its corresponding topography (a. and b. respectively), and EFM response (c. and d. respectively). V_{AC} = 5 V, ω = 200π rad/s, z = 30.14 nm.

Topography and EFM images of the polystyrene reference sample of this section are presented in Fig. V - 44a. and c., respectively. The corresponding average topography and EFM profiles of the cross-sections extracted over the particles of Fig. V - 44a. and c. images, are respectively plotted in Fig. V - 44b. and d. Furthermore, we have measured the average value of both profiles around their center. Particles average height is 383 nm ± 29 nm and $\alpha_{2\omega}$ is 0.489 ± 0.07 Hz/V^2. Implementing the present PS geometry and experimental parameters to our model, a PS dielectric permittivity of 2.6 has been found to agree with experiments with 0.80 % error (Table V - 1).

Table V - 1 : Summary of the obtained experimental topography and EFM results over PS reference sample, compared to simulations. Tip-sample distance z = 30.14 nm, tip-calibration parameters (28 nm, 15 °) and average particles diameter experimental value (382 nm) are used. A particle permittivity of 2.6 fits simulations with 0.8 % error.

Experiments- PS Height (nm)	Experiments- $\alpha_{2\omega}$ (Hz/V^2)	Simulations - $\alpha_{2\omega}$ (Hz/V^2)	Error (%)	Permittivity
383 ± 29	0.489 ± 0.07	0.493	0.80	ε_{PS} = **2.6**

[redacted] [redacted]

As it has been sketched in Fig. V - 42, we compare in the first place (step A) for method 3 the signals over uniformly covered particles of 100 nm Al_2O_3 versus 100 nm SiO_2. In order to verify the uniformity of layers thickness prepared with ALD and PSD, we added during the deposition process, reference samples of silicon and gold-covered bare Si substrates. Ellipsometry has been used to characterize Al_2O_3 and SiO_2 layers that have been grown and deposited on Si substrates, and profilometry to study the films over gold-covered substrates. This choice has been adopted since ellipsometry uses a theoretical model to calculate samples thickness (Chapter IV). Then, the fitting process becomes complicated when measurements are performed over multi-layered samples, which is the case for our gold-sputtered substrates: silicon + native oxide layer + chrome + gold, compared to silicon + native oxide layer for unmodified silicon substrates.

4.3.3.1. Films thickness uniformity characterization

a) Ellipsometry

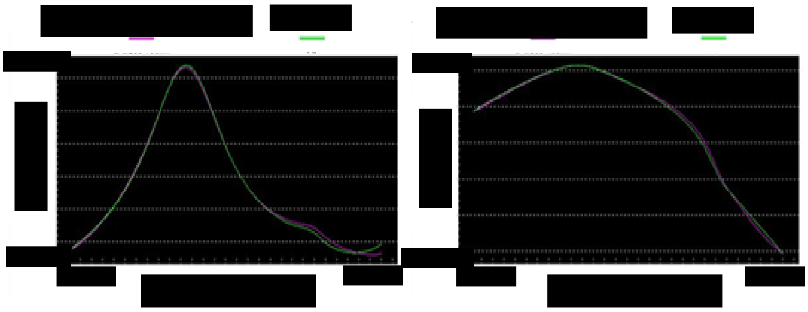

Fig. V - 45 : Ellipsometry results for 100 nm Al_2O_3 covered PS spheres. A 101 nm thickness is obtained with a good regression value of 0.998.

Clean dispersion spectrum have been collected over 100 nm Al_2O_3 (Fig. V - 45) and SiO_2 layers (not shown here). Fitting indicates an approximation of Al_2O_3 layer thickness of ~ 101 nm and SiO_2 of ~ 115 nm.

b) Profilometry

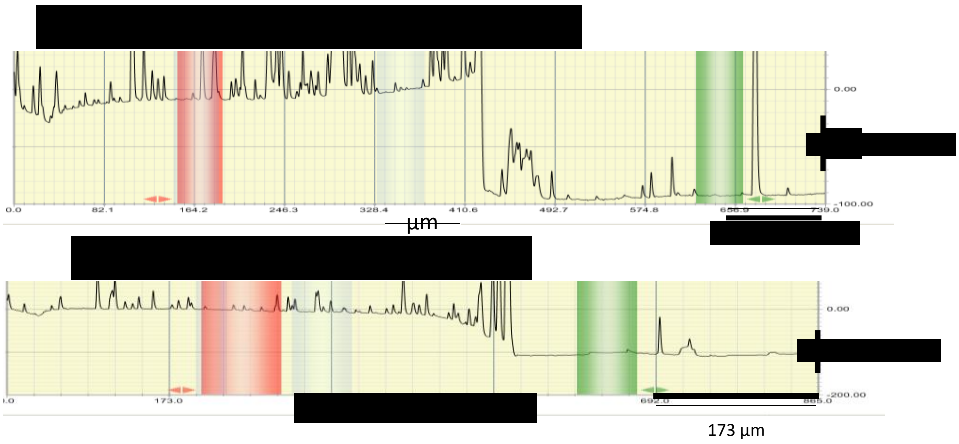

Fig. V - 46 : Typical profilometry results on a step of: a. 100nm Al_2O_3, and b. 100nm SiO_2 planar films. Measured thicknesses are around 93 nm and 98 nm, respectively.

Typical profilometry results over a step of 100 nm Al_2O_3 and SiO_2 films are presented in Fig. V - 46, showing 93 nm and 98 nm heights for Al_2O_3 and SiO_2, respectively. Combining both characterization methods results, it can be concluded that within the measurement techniques accuracy, the films exhibit relatively similar thicknesses. This result is extrapolated to PS covered samples: as PS reference samples present similar diameter, Al_2O_3 and SiO_2 layers are supposed to give similar shells thicknesses once deposited over PS.

4.3.3.2. EFM measurements

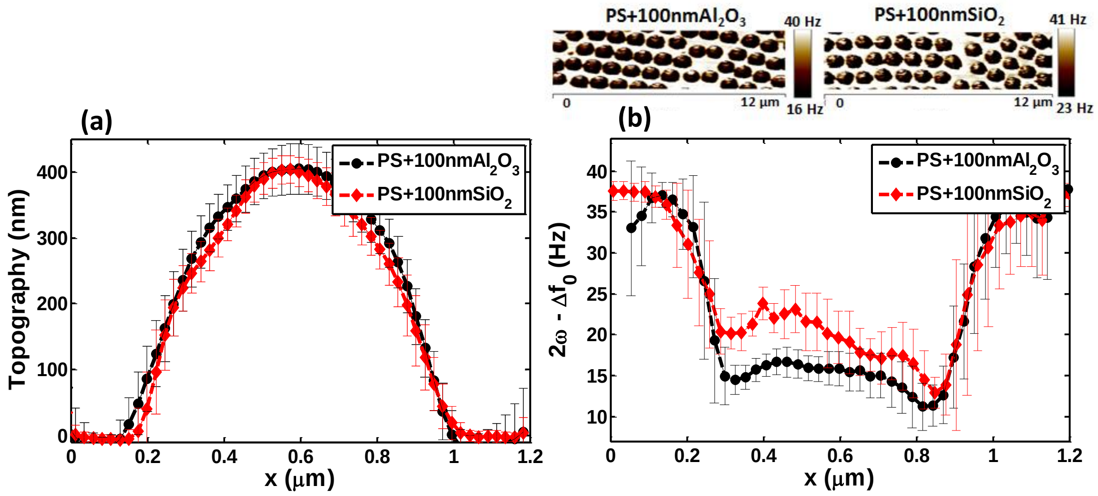

Fig. V - 47 : PS+100nmAl_2O_3 and PS+100nmSiO_2 samples: a. average topography profiles, b. average EFM signal profiles, and their corresponding EFM images (insets). V_{AC} = 5 V, ω = 200π rad/s.

Fig. V - 47 presents topography and EFM results of PS+100nmAl_2O_3 and PS+100nmSiO_2 samples. Average topography profiles of all AFM image spheres (around 25 particles) show interestingly similar topography profiles as expected from the calibrated preparation process. Although topography profiles sharply match, their corresponding EFM profiles are distinctly different in terms of signal magnitude at both the center of the particles as well as sample bottom regions. As SiO_2 and Al_2O_3 possess different dielectric permittivities, in the hypothesis of similar thicknesses, signal change becomes explainable. However, surprisingly, the EFM response increases with SiO_2 as covering layer compared to Al_2O_3, although SiO_2 is known to possess a lower permittivity than Al_2O_3 (3.9 for SiO_2 compared to 9.8 for Al_2O_3). Since Al_2O_3 shells have been already characterized in the above sections showing predictable performances, this odd dielectric response is attributed to SiO_2.

Hence, in order to explain this apparently higher dielectric response of SiO_2 compared to Al_2O_3, we suppose that SiO_2 layers are prompt to retain at their surface water molecules from the environment more than Al_2O_3, although both materials are usually reported as highly hydrophilic [26, 27]. In fact, compared to the smooth chemical vapor ALD technique, SiO_2 physical deposition with plasma sputtering could be producing a more developed ionic surface state, creating favorable sites for water attraction. This could be particularly caused by the little percentage of reactive O_2 gas that was added to the neutral Ar gas during sputtering (see Chapter IV). Typically, O^- and O_2^- could be introduced, attracting the hydrogen ends of water molecules [28].

A test in a highly humid environment has been performed over each of those samples. Both topography (not shown here) and EFM imaging have not been possible on SiO_2 covered spheres, contrarily to Al_2O_3 that presented no problem (see Fig. V - 48). All used probes have been stuck to the surface, and consequently, got crushed or polluted, requiring tip change. Since a water meniscus created between the tip and the surface in air environment can be responsible for sticking of the tip to the surface at low distances, greater water molecules adsorption layers are supposed to be responsible of greater attraction forces. Consequently, water meniscus can be responsible for dynamic imaging instabilities [29], and an important water adsorption/absorption can then explain surface states difference between Al_2O_3 and SiO_2.

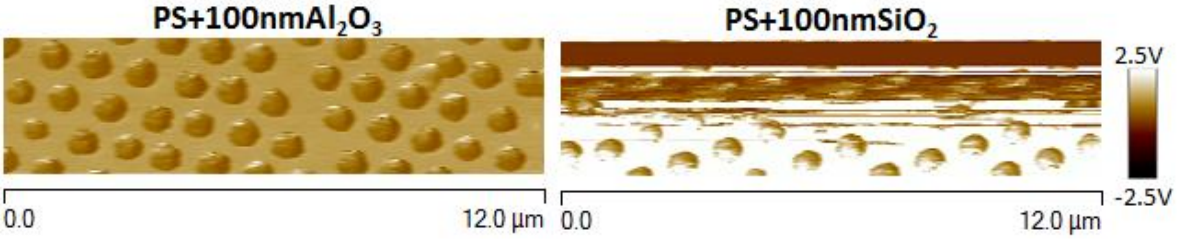

Fig. V - 48 : EFM images of PS+100nmAl_2O_3 (left) and PS+100nmSiO_2 (right) in a highly humid environment. Imaging process is not stable over silicon dioxide covered samples. V_{AC} = 5 V, ω = 200π rad/s and z = 30.14 nm.

We correlate experimental results to simulations in order to calculate the apparent permittivity of the SiO_2 layer over PS spheres. An apparent permittivity of $\varepsilon_{app} = 17$ is found to fit experiments with 0.6 % error. This permittivity is certainly much higher than the usual SiO_2 value around 3.9. On the other hand, a 9.8 dielectric permittivity for 100 nm alumina covered PS spheres agrees with experiments with only 3.2 % error. Hence, within the same hypothesis of the above paragraph, we simulate the presence of a water layer above the samples of PS+100nmSiO_2. While water is simulated with a dielectric permittivity of 80, calculations give an adsorption layer of 14 nm, capable of resulting in a similar EFM response as experiments with 0.9 % error. Since 14 nm water layer is relatively large for an adsorption layer [30], it must be noted that water molecules can also diffuse in the material at the interface with air [29], which creates a region possessing an average permittivity between 3.9 and 80. The latter region is a “real” interphase region that seems to dominate in this type of samples.

Nevertheless, the high signal could be due as well to a thin water layer, however, resulting in a developed nanomeniscus that modifies the intensity of interaction [31].

Our hypothesis of external conditions changing the apparent dielectric response of SiO_2 at the surface will be further investigated in the following sections.

[redacted] [redacted]

At this stage, since the deposition of similarly thick layers with ALD and PSD has been verified, and the relative difference between SiO_2 and Al_2O_3 layers have been calibrated, stacking different layers of SiO_2 and Al_2O_3 over PS for detecting the intermediate material becomes meaningful.

The second main step in order to test the interphase model detection with this third method has been addressed by comparing EFM response over PS+50nmAl_2O_3+50nmSiO_2 with PS+100nmSiO_2. The interphase model layer is hence the 50 nm Al_2O_3 intermediate layer (see step B in the sketch of Fig. V - 42).

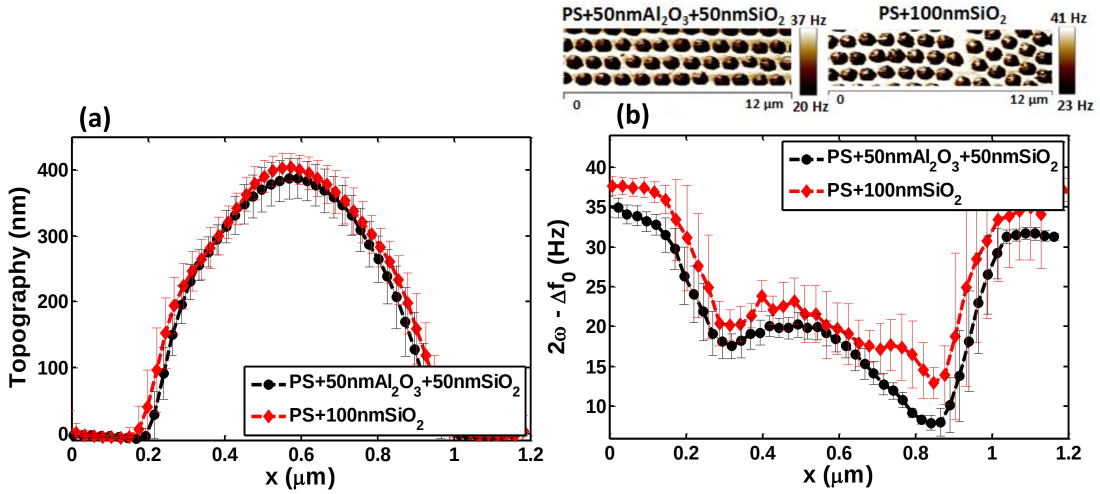

Fig. V - 49 : PS+50nmAl$_2$O$_3$+50nmSiO$_2$ and PS+100nmSiO$_2$ samples: a. average topography profiles, b. average EFM signal profiles and their corresponding EFM images (insets). V_{AC} = 5 V, ω = 200π rad/s and z = 30.14 nm.

Fig. V - 49 shows topography and EFM signals of PS+50nmAl$_2$O$_3$+50nmSiO$_2$ and PS+100nmSiO$_2$ samples. For this set of samples too, the average topography profiles match to a good extent (Fig. V - 49a.). On the other hand, EFM average response is not conserved, the signal around the center decreases with a 50 nm Al$_2$O$_3$ shell below the 50 nm SiO$_2$ layer compared to 100 nm SiO$_2$ unique covering material (see Table V - 2). Based on the measurements of section 4.3.3, surface SiO$_2$ layer has shown to present a higher permittivity than Al$_2$O$_3$. The exchange of 50 nm SiO$_2$ (ε_{app} = 17) above the particles with 50 nm Al$_2$O$_3$ (ε_{Al2O3} = 9.8) becomes thereby reasonable to decrease the signal at both particles center as well as bare substrates regions. Please note that EFM cross-sections have been collected slightly far from the center to avoid borders effects, which is reflected in a change of apparent particles width on EFM average profiles.

Signal decrease suggests both, the detection with EFM double-pass method of the interphase represented by the 50 nm Al$_2$O$_3$ layer, and the sensitivity to its relative permittivity regarding the matrix.

Nevertheless, the difference between the signals is relatively small. This can be justified since the upper layer is already 50 nm thick; due to electric field penetration limits, the subsurface layer is prone to only lightly modify it (see Chapter II – section 4.3.3.3) [32]. Moreover, the surface material presents a high dielectric polarization response, which further screens the one from the deeper parts. Besides, the difference between the deduced SiO$_2$ apparent permittivity (ε_{app} = 17) and that of Al$_2$O$_3$ (ε_{Al2O3} = 9.8) is relatively low. Namely, high dielectric permittivity materials are difficult to be distinguished [33], even if their effective permittivity decreases since they are placed on a material of lower permittivity (ε_{PS} = 2.6 < 9.8 and 17). We remind that a reduction in sample effective permittivity enhances the sensitivity to the top film. This latter remark can be either understood from section 3 conclusions of this chapter, or from Chapter III - section 4.2.

In order to further verify this result, as well as the quantification of the interphase permittivity, we corroborate experimental results with numerical simulations. We also used for the upcoming simulations the appropriate fitting parameters of section 4.3.1 for tip geometry, and section 4.3.2 for PS particles geometry and dielectric permittivity, in addition to ε_{app} = 17 for SiO$_2$ as derived from experiments to simulations fitting of section 4.3.3.2. An adequate match of experiments to simulations can be clearly noticed. The resultant dielectric permittivity of Al$_2$O$_3$ is fitted to 9.8 with 5 % error (see Table V - 2). Errors below 5 % are widely acceptable considering the errors on tip and spheres calibration, films thickness and the technique inherent experimental errors.

Table V - 2 : Experiments to simulations comparison for PS+50nmAl$_2$O$_3$+50nmSiO$_2$ vs. PS+100nmSiO$_2$ samples. Al$_2$O$_3$ subsurface layer presents a 9.8 dielectric permittivity with 5 % error for a calibrated SiO$_2$ upper layer with a 17 permittivity value, z = 30.14 nm.

	Experiments- $\alpha_{2\omega}$ (Hz/V^2)	Simulations- $\alpha_{2\omega}$ (Hz/V^2)	Error (%)	Interphase	Matrix
PS+100nmSiO$_2$	2.285 ± 0.33	2.271	0.60	ε_{SiO2} = 17	ε_{SiO2} = 17
PS+50nmAl$_2$O$_3$+50nmSiO$_2$	2.011 ± 0.18	2.113	5.1	**ε_{Al2O3} = 9.8**	ε_{SiO2} = 17

[redacted] [redacted]

In this last set of experiments, for the third main step for interphase model detection with method 3, we compare the signal over the reversed system of the above section: PS+50nmSiO$_2$+50nmAl$_2$O$_3$ is compared to PS+100nmAl$_2$O$_3$ (step C of Fig. V - 42).

The total thickness of 100nmSiO$_2$+50nmAl$_2$O$_3$ and that of 150nmAl$_2$O$_3$ reference films over gold sputtered substrates have been verified with profilometry. Here also, measured heights closely equate to the theoretical thickness (159 nm and 154 nm, Fig. V - 50).

[redacted]

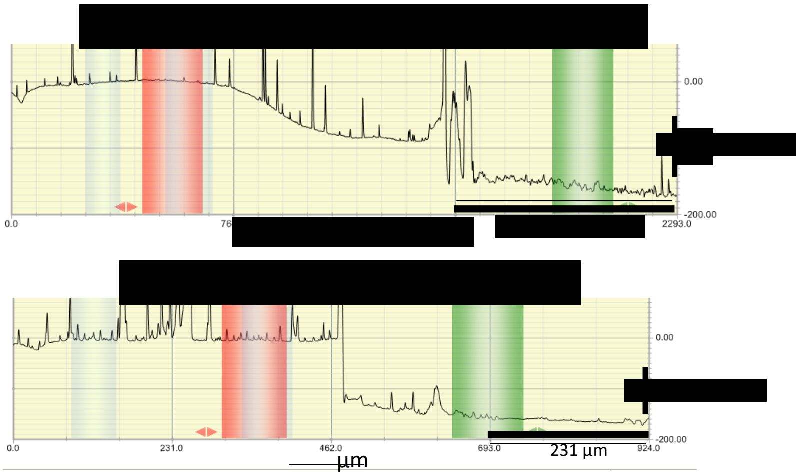

[redacted] [redacted] [redacted] [redacted] [redacted] [redacted]

Fig. V - 50 : Typical profilometry results on a step over: a. 100nmSiO$_2$+50nmAl$_2$O$_3$, and b. 150nmAl$_2$O$_3$ planar films. Measured thicknesses are around 159 nm and 154 nm, respectively.

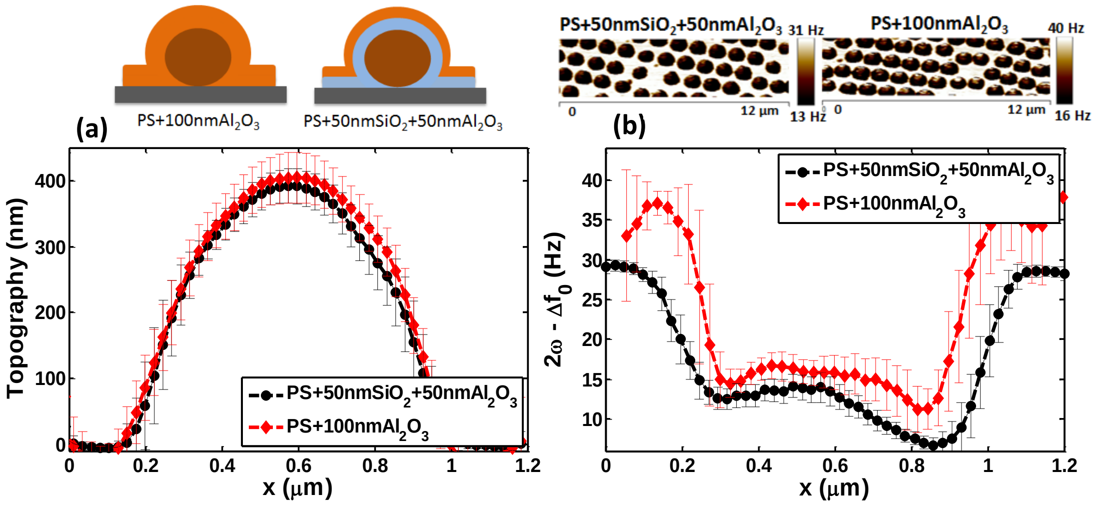

Fig. V - 51 : PS+50nmSiO$_2$+50nmAl$_2$O$_3$ and PS+100nmAl$_2$O$_3$ samples: a. average topography profiles, b. average EFM signal profiles and their corresponding EFM images (insets). V_{AC} = 5 V, ω = 200π rad/s and z = 30.14 nm.

Fig. V - 51 presents topography and EFM signals obtained above PS+50nmSiO$_2$+50nmAl$_2$O$_3$ and PS+100nmAl$_2$O$_3$ samples. In accordance with above comparisons, the average topography profiles for this set of samples closely match, on the contrary to EFM responses. The average electrical signal clearly decreases with 50 nm SiO$_2$ below the 50 nm Al$_2$O$_3$ upper layer, compared to the full 100 nm Al$_2$O$_3$ covering material, at both, particles center and bare substrate regions.

From the previous two last sections, an apparent dielectric permittivity of 17 has been calculated for SiO$_2$ layer. If this latter permittivity holds for SiO$_2$ when it is placed as the interphase layer, the signal above SiO$_2$ filled samples must exceed Al$_2$O$_3$ one, which contradicts the results of Fig. V - 51. However, if one considers the nominal intrinsic bulk permittivity of SiO$_2$ that is around 3.9, lower than Al$_2$O$_3$ permittivity (ε_{Al2O3} = 9.8), these results become reasonable.

It must be noted that in all cases (A, B and C), SiO$_2$ has been deposited with the same technique. Thereby, intrinsic material changes (bulk SiO$_2$) must not be the reason for the apparent permittivity change of SiO$_2$ among samples. Hence, in order to interpret those changes, it can be noted from the above section that the amplified signal has been attributed to adsorbed/absorbed water molecules at the interface of SiO$_2$ with the air. Since measurements were performed in air, this effect has been widely noticed when SiO$_2$ was the upper layer. However, in the present set of samples, SiO$_2$ layer is below Al$_2$O$_3$.

If Al$_2$O$_3$ deposition had been performed in air, the surface state of SiO$_2$ would have been probably preserved, and SiO$_2$ dielectric response would have still exceeded Al$_2$O$_3$ one in Fig. V - 51. Yet, this is not the case. We remind that ALD is performed under vacuum (0.01 mbar) at 80 ° C. Samples were left for at least 40 min before launching the deposition process, in order to acquire vacuum and temperature stability. At these pressure and temperature conditions, water molecules can get evaporated, and within the 40 min delay time, we suppose that relatively enough time has been conferred for H$_2$O desorption [34]. Consequently, this could explain the return of SiO$_2$ to its initial properties when Al$_2$O$_3$ is grown above it.

In all cases, from the comparison of topography to EFM response, the detection of the interphase represented by the 50 nm SiO$_2$ layer can be clearly identified.

This result is verified as well for superimposed planar films, as deduced from the bottom regions of the sample on Fig. V - 51b. We demonstrate these results on entirely planar samples too. As presented in Fig. V - 52, $\alpha_{2\omega}(z)$ curve, with SiO$_2$ in the sublayer, lies below the homogeneous Al$_2$O$_3$ film curve. This result closely matches numerical simulations of the corresponding system with ε_{SiO2} = 3.9 and ε_{Al2O3} = 9.8.

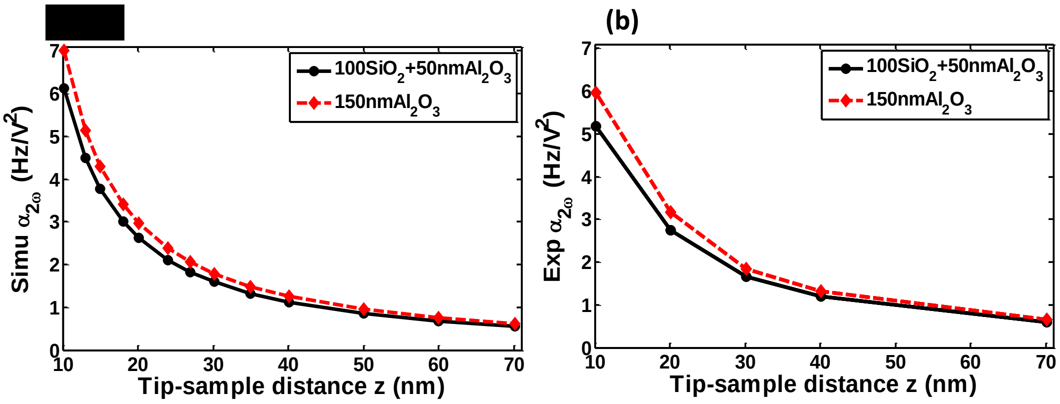

Fig. V - 52 : $\alpha_{2\omega}$ vs. z curves for planar SiO$_2$ and Al$_2$O$_3$ films obtained with a. AC - EFM experiments, b. simulations. The SiO$_2$ sublayer decreases the signal, with close match to simulations. V_{AC} = 5 V, ω = 200π rad/s.

Furthermore, in order to prove the proper sensitivity to the dielectric constant of the interphase over PS spheres, here also, we extend the above PS results (Fig. V - 51) to simulations. Similarly to Fig. V - 52a., we used in these simulations a permittivity of 3.9 for SiO_2. Experiments and simulations are closely equivalent, using ε_{Al2O3} = 9.8 and ε_{SiO2} = 3.9, with only 0.2 % error (see Table V - 3).

Table V - 3 : Experiments to simulations comparison for PS+50nmSiO_2+50nmAl_2O_3 vs. PS+100nmAl_2O_3 samples. Subsurface SiO_2 layer presents a 3.9 dielectric permittivity with 0.3 % error, *z* = 30.14 nm.

	Experiments- $\alpha_{2\omega}$ (Hz/V^2)	**Simulations - $\alpha_{2\omega}$ (Hz/V^2)**	**Error (%)**	**Interphase**	**Matrix**
PS+100nmAl_2O_3	1.709 ± 0.26	1.653	3.24	ε_{Al2O3} = 9.8	ε_{Al2O3} = 9.8
PS+50nmSiO_2+50nmAl_2O_3	1.478 ± 0.17	1.475	0.27	**ε_{SiO2} = 3.9**	ε_{Al2O3} = 9.8

4.3.6. [redacted]

Method 3 showed the possibility of detecting the interphase model layer with EFM-force gradient measurements performed in the double pass method and at constant tip-sample distance, by comparing samples with similar dimensions.

After calibration of matrix permittivity, direct EFM results showed to allow distinguishing the relative dielectric permittivity of the interphase model layer. For instance, in the case of a calibrated 50 nm thick SiO_2 matrix, and an unknown 50 nm Al_2O_3 interphase, the quantification of Al_2O_3 permittivity matched the casual one of 9.8 with acceptable error (5 %). In the opposite case, for a 50 nm Al_2O_3 calibrated matrix, and 50 nm SiO_2 as the unknown interphase, a 3.9 permittivity also agreed with simulations with only 0.3 % error.

In practice, this type of study can be practically transposed to comparisons between particles in a nanocomposite that show similar bulge shape (height and width). In the assumption that filler particles possess similar size, the same shape returns to particles with equally thick covering layers. The latter may be the matrix alone or both, matrix and interphase. Moreover, with this methodology, the interphase permittivity can be directly compared to the matrix one; and knowing particle permittivity, it can be stated regarding the particle one.

5. Conclusion

In conclusion, this last thesis chapter has been dedicated to assess experimentally the capabilities of EFM for interphase detection with the samples prepared as electrostatic model of nanodielectrics. An association of 3 materials of different dielectric permittivities has been used such as the first has the shape of a nanoparticle, covered homogeneously by the second material, being the interphase model, and subsequently, by the third material for the matrix model.

As a preliminary basic study, the association of two materials has been investigated. This association can represent the particle with an interphase where the matrix has been removed, or the particle with the matrix with no interphase. Paramount conclusions on suitable experimental protocols and signal analysis have been deduced. For instance, for the studied samples, SiO_2 nanoparticles (20 nm diameter) and PS spheres (250 and 350 nm diameter) covered by Al_2O_3 shells (from 10 to 200 nm thickness), EFM showed a special sensitivity to the shell intrinsic dielectric permittivity relative to the particle. An appropriate detection method is to compare signals at the center of the particles at similar tip-sample distance. Unusual morphological effects on EFM responses are used to extract the dielectric information about the shell, when the particle is known, and vice versa, when the shell is known, all with no need for sample thickness quantification. Namely, as the increase of the additional layer thickness intensifies EFM response, this reflects a material with higher dielectric permittivity than base particle, which enhances the effective permittivity of the particle-shell association. Experiments showed good agreement with simulations allowing for an approximate fitting of PS spheres permittivity to 2.48 and Al_2O_3 to 10.78.

Next, the interphase investigation in a three-layered material: particle + interphase + matrix, has been attempted by three methods. The first method consisted in comparing the signal between the system particle + interphase to that of particle + interphase + matrix. Since the interphase layer is always the unknown material, and based on above section conclusions, a 100 nm Al_2O_3 interphase has provoked signal changes between a PS particle and a PVAc spin coated matrix that were interpreted to prove its detectability, as well as the sensitivity to its intrinsic permittivity, lower than both particle and matrix. This method represents the comparison between the signals above a particle covered by an interphase with no matrix to those above the same system, however with the matrix layer. This comparison is delicate since matrix etching without affecting the interphase is not straightforward.

A more realistic comparison has been then forwarded by studying particle + matrix compared to particle + interphase + matrix, such as matrix layers possess controlled thicknesses. This has been possible with the use of SiO_2 layers deposited with controlled sputtering method adapted to our samples with rough surfaces. Signal comparison of PS+50nmSiO_2 versus PS+100nmAl_2O_3+50nmSiO_2 also showed consistent results with the characteristics of our materials. However, the conclusion on the interphase layer was limited to its relative dielectric permittivity regarding the effective one of particle and matrix association, and that of the particle, but not matrix alone.

Hence, a third more direct method for interphase detection has been attempted via comparisons of carefully prepared samples, possessing similar shape and dimensions. Having removed any topographical ambiguity, interphase detection has been studied after a preliminary step: quantification of matrix dielectric permittivity when the latter is deposited first over the particles, without the interphase layer. Once the SiO_2 matrix has been calibrated, the dielectric permittivity of 50 nm Al_2O_3 interphase below a 50 nm SiO_2 matrix has shown to match the expected permittivity of 9.8 with 5 % error compared to simulations. As well as, in the inversed system, the permittivity of the Al_2O_3 matrix layer has been first verified. Then, in this case, the permittivity of SiO_2 as the interphase shell agreed well with the casual reported SiO_2 permittivity of 3.9, with 0.3 % error from simulations.

Moreover, we have also noted a higher polarization response provoked by SiO_2 when this material is grown on the top surface than in the bulk. This result has been attributed to the surface state of SiO_2 with air that seems to develop a water adsorption/absorption layer. This layer is probably removed when Al_2O_3 is grown on its surface, due to Al_2O_3 film deposition thermodynamical conditions. Nevertheless, surface to bulk SiO_2 properties change must be further investigated.

This third method can be practically adopted with the comparison of thin cross-sectioned nanocomposite specimens showing bulges of the same dimensions. Differently prepared nanocomposites can be compared at the regions of same bulges shape; in the assumption of equal fillers dimensions, signal changes must reflect an interphase contribution.

The general conclusion states the capabilities of EFM to detect subsurface multilayered materials of 3D finite-size with very good sensitivity and resolution, namely, for interphase detection in nanodielectrics. Several methods can be adopted to draw information about those layers. Nevertheless, as detailed in this chapter, each experimental parameter and material property must be kept in mind, similarly to our developed methods, in order to forward accurate analysis and appropriate conclusions on the intrinsic dielectric response of studied layers.

6. References

[1] S. Peng, Q. Zeng, X. Yang, J. Hu, X. Qiu, and J. He, "Local Dielectric Property Detection of the Interface between Nanoparticle and Polymer in Nanocomposite Dielectrics," *Sci Rep,* vol. 6, p. 38978, Dec 13 2016.

[2] M. V. D. Hofstadt, R. Fabregas, M. C. Biagi, L. Fumagalli, and G. Gomila, "Nanoscale dielectric microscopy of non-planar samples by lift-mode electrostatic force microscopy," *Nanotechnology,* vol. 27, p. 405706, 2016.

[3] D. Esteban-Ferrer, M. A. Edwards, L. Fumagalli, A. Juárez, and G. Gomila, "Electric Polarization Properties of Single Bacteria Measured with Electrostatic Force Microscopy," *ACS Nano,* vol. 8, pp. 9843-9849, 2014/10/28 2014.

[4] G. Gramse, M. Kasper, L. Fumagalli, G. Gomila, P. Hinterdorfer, and F. Kienberger, "Calibrated complex impedance and permittivity measurements with scanning microwave microscopy," *Nanotechnology,* vol. 25, p. 145703, 2014.

[5] Ashish S. Paramane and K. S. Kumar, "A Review on Nanocomposite Based Electrical Insulations," *Transactions on electrical and electronic materials,* vol. 17, pp. 239-251, October 25, 2016 2016.

[6] E. M. Akinoglu, A. J. Morfa, and M. Giersig, "Understanding Anisotropic Plasma Etching of Two-Dimensional Polystyrene Opals for Advanced Materials Fabrication," *Langmuir,* vol. 30, pp. 12354-12361, 2014/10/21 2014.

[7] A. L. Tolstikhina, R. V. Gaĭnutdinov, M. L. Zanaveskin, K. L. Sorokina, N. V. Belugina, and Y. V. Grishchenko, "Particular artifacts of topographic images of dielectrics in atomic-force microscopy," *Crystallography Reports,* vol. 52, pp. 894-900, 2007/09/01 2007.

[8] I. Casuso, L. Fumagalli, G. Gomila, and E. Padrós, "Nondestructive thickness measurement of biological layers at the nanoscale by simultaneous topography and capacitance imaging," *Applied Physics Letters,* vol. 91, p. 063111, 2007/08/06 2007.

[9] C. Riedel, "Dielectric and Mechanical Properties of Polymers at Macro and Nanoscale " PhD, Université Montpellier 2, 2010.

[10] Z.-Y. Li, B.-Y. Gu, and G.-Z. Yang, "Scanning-electrostatic-force microscopy: Self-consistent method for mesoscopic surface structures," *Physical Review B,* vol. 57, pp. 9225-9233, 04/15/ 1998.

[11] G. Gomila, D. Esteban-Ferrer, and L. Fumagalli, "Quantification of the dielectric constant of single non-spherical nanoparticles from polarization forces: eccentricity effects," *Nanotechnology,* vol. 24, p. 505713, 2013.

[12] G. Gomila, G. Gramse, and L. Fumagalli, "Finite-size effects and analytical modeling of electrostatic force microscopy applied to dielectric films," *Nanotechnology,* vol. 25, p. 255702, 2014.

[13] L. Fumagalli, D. Esteban-Ferrer, A. Cuervo, J. L. Carrascosa, and G. Gomila, "Label-free identification of single dielectric nanoparticles and viruses with ultraweak polarization forces," *Nat Mater,* vol. 11, pp. 808-816, 2012.

[14] C. Riedel, "Dielectric and mechanical properties of polymers at macro and nanoscale," PhD, Institut d'électronique et des systèmes, University of Montpellier, 2010.

[15] L. Fumagalli, G. Gramse, D. Esteban-Ferrer, M. A. Edwards, and G. Gomila, "Quantifying the dielectric constant of thick insulators using electrostatic force microscopy," *Applied Physics Letters,* vol. 96, p. 183107, 2010/05/03 2010.

[16] L. Portes, M. Ramonda, R. Arinero, and P. Girard, "New method for electrostatic force gradient microscopy observations and Kelvin measurements under vacuum," *Ultramicroscopy,* vol. 107, pp. 1027-1032, 2007/10/01/ 2007.

[17] S. Cheng, V. Bocharova, A. Belianinov, S. Xiong, A. Kisliuk, S. Somnath*, et al.*, "Unraveling the Mechanism of Nanoscale Mechanical Reinforcement in Glassy Polymer Nanocomposites," *Nano Letters,* vol. 16, pp. 3630-3637, 2016/06/08 2016.

[18] N. Lahoud-Dignat, M. N. Hidayatullah, F. Saysouk, M. L. Locatelli, and S. Diaham, "Using the Atomic Force Microscopy for nanocomposites local mechanical characterization: Towards the interphase measurement," in *2016 IEEE International Conference on Dielectrics (ICD)*, 2016, pp. 64-67.

[19] H. Huang, I. Dobryden, N. Ihrner, M. Johansson, H. Ma, J. Pan*, et al.*, "Temperature-dependent surface nanomechanical properties of a thermoplastic nanocomposite," *Journal of Colloid and Interface Science,* vol. 494, pp. 204-214, 5/15/ 2017.

[20] J. Seiler and J. Kindersberger, "Insight into the interphase in polymer nanocomposites," *IEEE Transactions on Dielectrics and Electrical Insulation,* vol. 21, pp. 537-547, 2014.

[21] J. Deschler, J. Seiler, and J. Kindersberger, "Detection of charges at the interphase of polymeric nanocomposites," *IEEE Transactions on Dielectrics and Electrical Insulation,* vol. 24, pp. 1027-1037, 2017.

[22] R. Borgani, L. K. H. Pallon, M. S. Hedenqvist, U. W. Gedde, and D. B. Haviland, "Local Charge Injection and Extraction on Surface-Modified Al2O3 Nanoparticles in LDPE," *Nano Letters,* vol. 16, pp. 5934-5937, 2016/09/14 2016.

[23] M. Hershcovitz and I. E. Klein, "Dynamics of spin coating on very rough surfaces," *Microelectronics Reliability,* vol. 33, pp. 869-880, 1993/05/01/ 1993.

[24] N. E. Bede Pittenger, Chanmin Su, "Quantitative mechanical property mapping at the nanoscale with PeakForce QNM," *Application Note Veeco Instruments Inc,* pp. 1-12, 2010.

[25] T. G. Stange, R. Mathew, D. F. Evans, and W. A. Hendrickson, "Scanning tunneling microscopy and atomic force microscopy characterization of polystyrene spin-coated onto silicon surfaces," *Langmuir,* vol. 8, pp. 920-926, 1992/03/01 1992.

[26] I. L. Hosier, M. Praeger, A. S. Vaughan, and S. G. Swingler, "The Effects of Water on the Dielectric Properties of Aluminum-Based Nanocomposites," *IEEE Transactions on Nanotechnology,* vol. 16, pp. 667-676, 2017.

[27] C. Zou, J. C. Fothergill, and S. W. Rowe, "The effect of water absorption on the dielectric properties of epoxy nanocomposites," *IEEE Transactions on Dielectrics and Electrical Insulation,* vol. 15, pp. 106-117, 2008.

[28] J. W. Bradley and T. Welzel, "Process Diagnostics," in *Reactive Sputter Deposition*, D. Depla and S. Mahieu, Eds., ed Berlin, Heidelberg: Springer Berlin Heidelberg, 2008, pp. 255-300.

[29] T. O. u. JP. Aim, R. Boisgard,L. Fabi, M. Delmas, C. Fouch, "Nanomeniscus Mechanical Properties," in *Nanoscale Liquid Interfaces Wetting, Patterning and Force Microscopy at the Molecular Scale*, ed: Pan Stanford Publishing, 2013.

[30] S. Santos and A. Verdaguer, "Imaging Water Thin Films in Ambient Conditions Using Atomic Force Microscopy," *Materials,* vol. 9, p. 182, 2016.

[31] D. T. Lee, J. P. Pelz, and B. Bharat, "Scanning capacitance microscopy for thin film measurements," *Nanotechnology,* vol. 17, p. 1484, 2006.

[32] D. Ebeling, B. Eslami, and S. D. J. Solares, "Visualizing the Subsurface of Soft Matter: Simultaneous Topographical Imaging, Depth Modulation, and Compositional Mapping with Triple Frequency Atomic Force Microscopy," *ACS Nano,* vol. 7, pp. 10387-10396, 2013/11/26 2013.

[33] E. Castellano-Hernández and G. M. Sacha, "Ultrahigh dielectric constant of thin films obtained by electrostatic force microscopy and artificial neural networks," *Applied Physics Letters,* vol. 100, p. 023101, 2012/01/09 2012.

[34] H. Yanagihara, K. Yamashita, A. Endo, and H. Daiguji, "Adsorption–Desorption and Transport of Water in Two-Dimensional Hexagonal Mesoporous Silica," *The Journal of Physical Chemistry C,* vol. 117, pp. 21795-21802, 2013/10/24 2013.

Conclusions and Future works

> "I would rather have questions that can't be answered than answers that can't be questioned."
> Richard Feymann

Since interphases have long been considered to be responsible for the improved, or at least, unique properties of nanocomposites compared to their microcomposite counterparts and to the base polymer, a serious need for their local characterization has arisen. Among possible high resolution microscopic techniques, the Electrostatic Force Microscope (EFM) has been selected as a potential method to locally study nanodielectrics owing to the contrasts in the dielectric properties of the different nanocomposite components.

Little fundamental work of EFM response to polymeric dielectric nanocomposites has been investigated. Hence, the aim of this work was to explore the capabilities of EFM to locally study interphases in nanodielectric materials.

1. Conclusions

In order to do so, we developed first a model for a nanodielectric sample within the frame of an EFM measurement. Based on the literature review, this type of nanocomposites can be simplified as an association of three materials, characterized by their dielectric permittivity: the first one is a nanoparticle, covered by a shell of the second material that models the interphase, and the third material covering the particle-interphase assembly, modeling the polymeric matrix.

As a nanodielectric sample is a relatively complicated system for casual EFM measurements, we have resorted to numerical simulations to deeper our understanding of the physics behind the interaction of an EFM probe and dielectric samples of several types and configurations, allowing at the end to simulate the specific interaction with a nanodielectric model. Numerical simulations proved that the electrical signal in an EFM is a mix result of several parameters effect, each weighing differently on the final response. The intensity of each parameter depends on the specific type, geometry and dimensions of the sample, as well as tip geometry, measurement parameters etc. Nevertheless, some global and salient conclusions could be drawn:

1) As expected, in the absence of a dielectric film, the signal always decreases with the distance between electrodes, and increases with larger tips. The sensitivity to distance change is higher at low electrodes spacing where the nanometric tip parts dominate over probe micrometric parts.

2) Within the electrostatically coupled region, and for fixed tip-sample distance, a homogeneous material intensifies the tip-sample interaction when it possesses a high dielectric permittivity and/or reduced thickness. The improved polarization with higher permittivities clarifies the stronger electrostatic force. On the other hand, thinner homogeneous films bring electrodes closer together, which is responsible for the improved capacitance.
   Nevertheless, the sensitivity to the permittivity decreases for important permittivities and/or thin films. This sensitivity can be relatively restored with thicker films. On the other hand, the sensitivity to the thickness is higher for thin films. Thick samples of high dielectric constant can also relatively restore the sensitivity to the film thickness.

3) Multilayered planar films of different permittivities are detected as one global material with an effective permittivity comprised between the minimal and maximal permittivities of involved materials.

The effective dielectric constant is affected by the percentage of occupation of each component. Consequently, dimension changes might induce signal variations inconsistent with casual ones that are appropriate to homogeneous films. For instance, increasing the thickness of the layer with the highest permittivity can rise the signal to a certain extent, contrarily to homogeneous planar films where thicker films always reduce the interaction.

4) Finite-sized samples, typically in the form of a nanoparticle, present a relatively complicated behavior regarding particle radius change. As a summary, for small particles, the signal decays with increasing particle size. In fact, in this case the tip and the substrate are very close, the sensitivity to interelectrode distance change with particle size dominates, and explains signal decay. However, exceeding a certain particle size, the smoothly reduced interaction due to the spacing between electrodes can be partially compensated by the polarization response of high dielectric materials. Bigger particles start to intensify the interaction owing to the contribution of the width increase.

5) In a nanocomposite, finite-size effects can also be noticed as the matrix permittivity affects signal intensity contrast and the half-width at half-maximum of the inclusion. The spatial resolution in EFM was then found to depend on the permittivity ratio of sample components.
   The depth of the inclusion in the matrix equally affects electrical signal maximum and the apparent diameter. In fact, spatial resolution decrease is due to the effective permittivity of the probed region that gets closer to the matrix alone. Moreover, the limited penetration depth of the electric field reduces the detectability chances of deeply buried inclusions.

6) Finally, for the specific case of a nanodielectric material, the particle-interphase assembly was found to be approximated to a particle of similar global dimensions, with an effective apparent permittivity. The same conclusions drawn for a simple nanocomposite system thereby hold for a nanodielectric. An insight into the detectability limits of the interphase in several common nanodielectric configurations has been established. In general, we found that a low dielectric permittivity matrix, higher interphase permittivities and thickness, and lower depths, make the interphase more likely to be detectable.

Subsequently, we designed and synthesized samples of known and mastered properties to play the role of an electrostatic model of a nanodielectric material (particle + interphase + matrix) making use of most recent nanotechnology preparation methods. In particular, silicon dioxide (~ 20 nm diameter) and polystyrene nanoparticles (~ 250 - 380 nm diameter) were placed on metallic substrates and aluminum oxide, polyvinyl acetate and silicon dioxide thin shells deposited on samples surface (particle and substrate). The shells can either model the interphase or the matrix depending on the adopted order of shells deposition.

Based on the theoretical background gained through our simulations, and making use of the model samples as reference samples, EFM measurements were performed in order to assess experimentally the ability to characterize interphases with EFM. Several experimental protocols and comparison methods were developed for this issue:

7) The association of a particle with one shell was first studied, representing either a particle + interphase model, or a particle + matrix model.
   EFM showed a special sensitivity to both particle and shell intrinsic dielectric permittivities, relatively to each other. We deduced that the comparison of EFM signals at the center of the

particles at similar tip-sample distance is an appropriate detection method with no special need for thickness measurements compared to literature previous studies. This was proved in both the simple DC as well as the AC (2ω) excitation methods of force gradient detection.

In accordance with simulation results, unusual morphological effects on EFM signals are found to be useful to extract dielectric information about similar 3D multilayered materials.

Experiments showed good agreement with simulations allowing for an approximate fitting of PS spheres permittivity to 2.48 and Al_2O_3 one 10.78.

The study of the interphase model layer embedded between the particle and the matrix has been attempted by three methods.

8) In the first one, we compared the system particle + interphase to that of particle + interphase + matrix. This method represents the comparison between the signals above a particle with an interphase with removed matrix (e.g. by etching) to those above the same system, however with the matrix layer.

   Owing to the previous experimental conclusions, we were able to analyze the signal and prove an acceptable sensitivity to a 100 nm Al_2O_3 thick interphase between a PS particle and a PVAc matrix. However, this type of material comparison is delicate in practice since matrix etching without affecting the interphase is not straightforward.

9) A more realistic comparison was forwarded by comparing: particle + matrix to particle + interphase + matrix, such as the matrix layers possess equal thicknesses. Signal comparison of PS with 50nmSiO_2 vs. PS+100nmAl_2O_3+50nmSiO_2 also showed consistent results with the 100nm Al_2O_3 interphase layer characteristics. The conclusion on the interphase layer was however limited to its relative dielectric constant compared to the association of particle and matrix effective permittivity, and that of the matrix but not particle alone.

10) Hence, the third method investigated the comparison of carefully prepared samples possessing similar shape and dimensions to remove any topographical ambiguity. This third method can be practically adopted by comparing thin cross-sectioned nanocomposite specimens showing bulges of same dimensions.

    After the calibration of matrix dielectric constant when it is deposited first over the particles without the interphase layer, the dielectric constant of 50 nm Al_2O_3 interphase below a 50 nm SiO_2 matrix was estimated and shown to match the expected permittivity for Al_2O_3 of 9.8 with 5 % error regarding simulations results.

    As well as, in the inversed system, the dielectric constant of SiO_2 as the interphase shell below a calibrated Al_2O_3 matrix layer agreed with the expected bulk permittivity of SiO_2 of 3.9 with 0.3 % error regarding simulations.

    Surprisingly, due to matrix calibration measurements, we noted a higher apparent dielectric permittivity for SiO_2 when grown on the upper surface compared to the bulk one. This result has been attributed to the surface state of SiO_2 that seems to develop a water adsorption/absorption layer, related to the deposition technique of SiO_2. This layer was supposed to be probably removed when Al_2O_3 is grown on its surface, due to Al_2O_3 deposition thermodynamical conditions.

Altogether, the results of this thesis demonstrate the potential of EFM to study subsurface multilayered dielectric materials of 3D finite-size, namely, to study interphases in nanodielectrics.

Quantitative characterizations can be obtained too by correlating to numerical simulations; nevertheless, accurate analysis of all influencing parameters must be kept in mind.

2. Future works

The first straightforward recommendation to confirm the third methodology for interphase measurement would be to examine other types of SiO_2 thin film deposition methods. EFM measurements could also be tested under vacuum, after in-situ samples heating to remove water. A broadband nanoscopic Dielectric Spectroscopy (nDS) could be adapted to investigate surface molecules dynamics.

Various types of ceramics could be tested too as covering shells like titanium dioxide, boron nitride, zinc oxide etc.

An extension of this work towards closer configurations to practically used nanodielectrics would be to:

a) Disperse PS particles of lower initial size (< 1 µm), etch to smaller diameters and grow lower layer thicknesses in order to test EFM developed protocols over lower dimension samples.
b) Evenly disperse inorganic particles instead of organic ones, which was the case of our PS particles and subsequently, deposit polymeric shells instead of ceramic ones. The latter could be prepared with either chemical vapor or physical vapor deposition methods, in order to model the interphase and the matrix. A broadband nDS measurement becomes interesting over this latter type of model samples.

Intrinsic space charge measurements (when they exist) and injected charges propagation could be also envisaged with EFM on both model samples configurations: organic particle + inorganic shells, and vice-versa. Either appropriate DC-force gradient measurements or casual AC-ω component measurements could be used.

Since analytical methods have been limited to the calculus of the interaction of EFM probe with simple geometries, some attempts to develop these models for complicated configurations must start in the future in order to master the interpretation of EFM signals.

Finally, the ultimate recommendation would be to evaluate these developed methods over "real" (industrial) nanodielectric materials, where only filler and matrix are the known parameters. Testing must obviously begin with materials exhibiting at the macroscale non-common behaviors, either in the real dielectric permittivity or other dielectric properties. In the meantime, several types of EFM specimen preparation methods must be also tested. Numerical modeling could always come in handy to verify, understand and quantify EFM results.

It must be noted that the electrostatic problem of our work could be equally generalized and adapted to other types of electrical scanning probe microscopies such as KPFM, SMM, C-AFM etc. Moreover, the application of the developed experimental protocols could also be applied to other types of nanometric heterogeneous materials, such as the wide types of synthesized core-shell materials and core-shell filled composites, as well as natural core-shell like structures such as viruses and bacteria.

Consequently, some reflections remain to wonder: how far could we reach with electrical scanning probe microscopies? Could direct tomography of complex nanomaterials be possible one day? What are the missing parts to reach this level of 3D unambiguous nanometric-resolution with AFM? Meanwhile, how could we confirm the nature of interphases?

Résumé

Les matériaux polymères composites ont longtemps révélé des propriétés physiques améliorées en raison du mélange des caractéristiques de leurs constituants. Par conséquent, les lois conventionnelles de mélange de deux phases sont généralement suffisantes pour clarifier et prévoir la réponse des microcomposites à un stimulus externe. Cependant, pour une concentration donnée, lorsque la taille de la charge est réduite à l'échelle nanométrique, les nanocomposites présentent des changements de propriétés inattendues. A titre d'exemple, J.K. Nelson et J.C. Fothergill ont remarqué pour la première fois en 2004, une diminution de la permittivité diélectrique de la résine de base (de 9.99 à 8.49 à 1 kHz par exemple) avec l'ajout de nanoparticules de dioxyde de titane, bien que celles-ci possèdent une permittivité beaucoup plus élevée que la matrice polymère [1].

Le comportement singulier des nanocomposites diélectriques, constitués d'un mélange de particules dans une matrice, appelé également nanodiélectriques [2], a été attribué à la taille nanométrique des particules qui les constituent [3]. À cette échelle, et à masse équivalente de matériau, le rapport des atomes et des molécules présents à la surface des particules à l'égard de ceux présents dans le volume, augmente de façon exponentielle, comparé à des microparticules. En outre, la réactivité des molécules de surface d'une phase condensée est élevée. Au contact d'une autre phase, une série d'interactions se produit sur leur interface mutuelle afin d'établir un équilibre thermodynamique. Ces interactions sont susceptibles de favoriser l'apparition d'une région aux propriétés uniques, différentes de celles des phases impliquées. Ainsi, et à titre d'exemple, il est généralement signalé que, dans un nanocomposite, les chaînes de polymères se réorganisent à l'interface avec les nanoparticules créant une couche immobilisée, et plus ordonnée [4]. L'ordre de cette dernière est surtout élevé à la surface de la particule et diminue à mesure qu'on s'approche du volume du polymère. Cette région, aux propriétés modifiées, est communément appelée ''interphase''. Celle-ci occupe ainsi un pourcentage considérable en volume dans les nanodiélectriques, s'étendant de quelques angströms jusqu'à quelques centaines de nanomètres d'épaisseur. L'interphase pourrait donc posséder une permittivité inférieure à celle du polymère en volume, ce qui explique la réponse diélectrique exceptionnelle observée dans les nanodiélectriques. De surcroit, de nombreuses propriétés d'isolation électrique, telles que la formation de charges d'espace, la propagation des arborescences, la résistance aux décharges électriques, etc., ont également été améliorées avec l'addition de nanoparticules par rapport au même diélectrique non chargé, aussi bien que leurs équivalents chargés avec des particules micrométriques [5-7].

Par conséquent, à cette échelle, du fait que les interphases commencent à contrôler les propriétés finales du matériau, la caractérisation locale de ces régions nanométriques devient incontestablement fondamentale. De quoi sont-elles faites ? Où sont-elles vraiment situées dans le matériau ? Quelles sont leurs propriétés ? Quelle est leur étendue ?

Afin de répondre à toutes ces interrogations, les techniques d'imagerie à haute résolution s'avèrent potentiellement aptes à offrir des solutions.

De nos jours, les deux méthodes d'imagerie à haute résolution les plus développées sont les microscopies électroniques et les microscopies à sondes locale, en anglais, Scanning Probe Microscopy (SPM). Contrairement aux microscopies électroniques, les techniques SPM et en particulier les techniques de Microscopie à Force Atomique (AFM) sont des méthodes polyvalentes et relativement faciles à utiliser, particulièrement adaptées à l'étude des isolants électriques [8]. Pour la définir simplement, l'AFM utilise une sonde physique comportant une pointe à son extrémité, d'apex nanométrique, dont dépend la haute résolution spatiale. La sonde détecte, avec une grande précision, le champ d'interaction avec l'échantillon, de façon analogue à une main qui effleure une surface avec les yeux fermés. Lorsque des forces électrostatiques sont à l'origine de l'interaction, nous parlons alors de Microscopie à Force Electrostatique (EFM) [9].

L'EFM est une des méthodes dérivées de l'AFM, prometteuse pour caractériser localement les interphases, en raison de sa sensibilité à la réponse capacitive en présence de l'échantillon [10].

Cependant, compte tenu de la géométrie de la sonde et de la nature des forces électrostatiques à longue portée, la région réellement sondée de l'échantillon devient très complexe à définir, et les signaux EFM deviennent souvent mal interprétés.

Par conséquent, le but de ce travail de recherche est de déterminer si l'EFM est capable de détecter et caractériser les interphases dans les nanodiélectriques. En d'autres termes, les questions qui se posent sont les suivantes : Comment la présence ou l'absence d'une interphase se manifeste-t-elle sur les signaux EFM ? Comment est-il possible de mesurer sa permittivité diélectrique et /ou ses dimensions ? Quels sont les protocoles expérimentaux et les analyses des signaux qui permettent d'interpréter la réponse intrinsèque aux interphases sans artéfacts ?

Pour répondre à ces questions, nous avons choisi, dans un premier temps, de simuler numériquement l'interaction de la pointe EFM avec plusieurs types d'échantillons nanostructurés, pour combler les lacunes dans la littérature concernant la réponse EFM à de tels matériaux aux géométries et aux compositions complexes. Par la suite, l'impact de l'interphase sur les signaux EFM a été simulé pour des matériaux nanodiélectriques aux diverses propriétés et dimensions. Néanmoins, cette approche théorique n'était pas suffisante pour nous permettre, à ce stade, de mesurer les propriétés diélectriques par EFM de nanodiélectriques "réels", aux interphases inconnues. Des mesures expérimentales sur des échantillons de référence se sont rapidement avérées essentielles au développement des méthodes EFM appropriées en vue d'une caractérisation future des nanodiélectriques "réels". Des matériaux comportant trois phases diélectriques distinctes ont été conçus et synthétisés pour modéliser un matériau nanodiélectrique. Des tests expérimentaux ont donc été effectués sur ces échantillons pour adapter l'EFM à l'étude de l'interphase. De ce fait, plusieurs méthodes ont été développées.

Ainsi, après l'introduction dans les Chapitres I et II des notions de base des matériaux diélectriques soumis à un champ électrique, des nanodiélectriques, des interphases d'un point de vue électrochimique, des modes de fonctionnement de l'EFM et leurs spécificités, ainsi qu'un état de l'art des avancées générales concernant les mesures locales des interphases, et ensuite par EFM en particulier, les premiers résultats sont traitées dans le Chapitre III.

Modèle d'un nanodiélectrique:

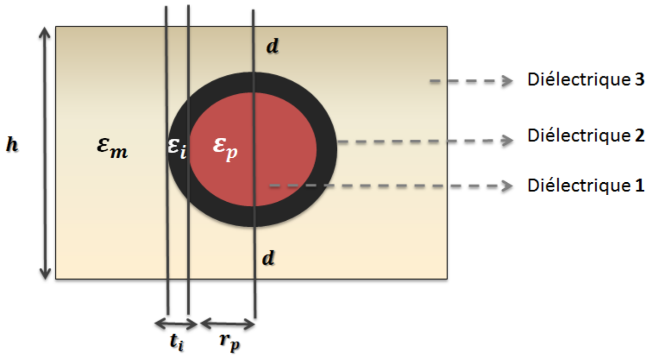

Fig. 1 : Modèle diélectrique adopté pour modéliser les nanodiélectriques, dans le cadre d'une mesure EFM : l'association de particule + couche interphase + matrice représente trois matériaux identifiés par leur permittivité diélectrique, géométrie, dimensions et disposition. ε_p, ε_i et ε_m représentent respectivement les permittivités diélectriques de la particule, de l'interphase et de la matrice. r_p est le rayon de la particule, t_i est l'épaisseur de l'interphase, h l'épaisseur de la matrice et d, la séparation de l'interphase par rapport à la matrice.

Au cours d'une mesure EFM, un nanodiélectrique possédant une interphase a été modélisé comme étant constitué de trois phases diélectriques, caractérisées par leur permittivité diélectrique et disposées dans la configuration suivante : une nanoparticule constituant la première phase, enrobée d'une couche d'un deuxième matériau, illustrant l'interphase, et le tout recouvert par un troisième matériau modélisant la matrice (voir Fig. 1).

Dans le Chapitre III, nous discutons au travers de simulations par éléments-finis, la physique relative à l'interaction entre une sonde EFM et plusieurs types d'échantillons diélectriques nanostructurés. En particulier, nous étudions l'effet de l'association de multicouches diélectriques sur le signal, ainsi que l'effet des dimensions nanométriques des particules, enfouies ou pas dans une matrice, pour pouvoir enfin étudier le cas particulier d'un nanodiélectrique.

La réponse EFM est affectée en premier lieu par la géométrie de la pointe, la séparation entre les électrodes, la permittivité diélectrique et la profondeur du matériau dans le volume d'interaction avec la pointe. Ainsi, nous avons pu montrer que la réponse d'un matériau hétérogène, structuré par multicouche, dépend des ratios permittivité/hauteur de chaque couche. Le signal est une réponse globale, que l'on illustre par une permittivité effective du système.

On montre qu'il est possible de mettre en évidence l'hétérogénéité diélectrique du matériau du fait que ce dernier montre des variations consécutives à des modifications de la géométrie du matériau, incompatibles avec des échantillons homogènes. Le changement du rayon d'une nanoparticule, quand à lui, peut potentiellement faire intervenir tous les paramètres désignés ci-dessus. Une combinaison critique de tous ces paramètres peut ainsi changer les tendances classiquement obtenues en présence d'un diélectrique plan homogène. Ainsi, un nanocomposite, avec et sans interphase, combine à la fois les effets de taille et les effets de multicouche. L'ensemble particule + interphase est ainsi détecté comme une particule globale, ayant une permittivité effective. L'interphase agit alors sur le maximum, le contraste et la largeur à mi-hauteur du signal (voir Fig. 2). En conclusion, nous avons constaté qu'une matrice de faible permittivité diélectrique, qu'une interphase de permittivité et d'épaisseur élevées, et qu'un couple particule + matrice de permittivités comparables avec particule proche de la surface extérieure, rendent l'interphase plus susceptible d'être détectable.

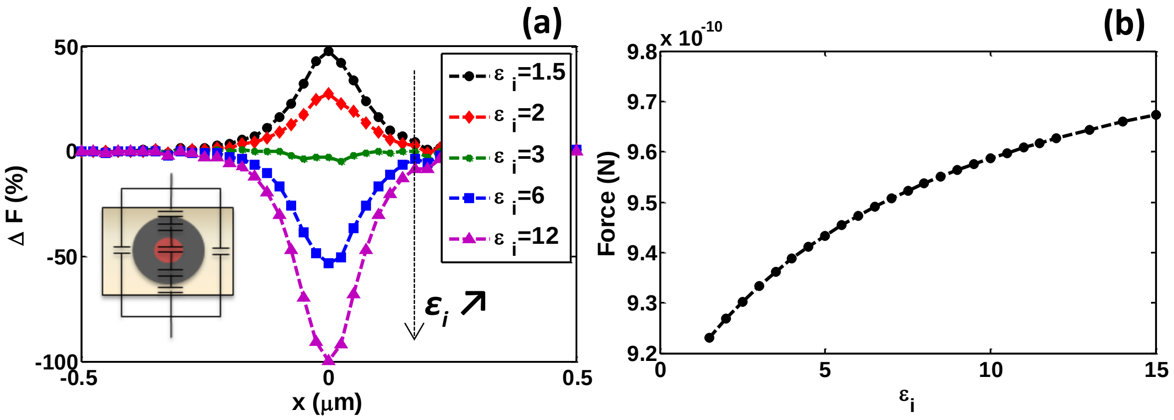

Fig. 2 : Simulations numériques de l'interaction pointe EFM avec un nanodiélectrique: a. Contraste EFM normalisé, sur un scan de 1 µm d'un nanodiélectrique ayant $\varepsilon_m = 4$, $\varepsilon_p = 10$, $r_p = 25$ nm, $t_i = 20$ nm, $d = 20$ nm à 20 nm de la surface, encart: modèle de condensateurs en permettant de comparer le signal au centre à celui obtenu aux bords de la particule; b. valeurs absolues brutes de la force, obtenues au centre des particules ($x = 0$ µm) pour différentes ε_i.

Ainsi, après avoir identifié la réponse EFM liée à une interphase, et souligné certaines gammes de validité de l'EFM pour ce problème, l'étude expérimentale directe d'échantillons nanodiélectriques ayant une interphase inconnue a été jugée encore précoce à ce stade. Les études théoriques deviennent particulièrement essentielles pour accompagner des mesures expérimentales appropriées, dédiées à "étalonner" la technique de mesure pour de futurs études de l'interphase.

À cet égard, des matériaux de référence de composition et de forme relativement connues et modifiables ont été préparés. Ces échantillons modélisent diélectriquement un nanodiélectrique (particule + interphase + matrice) utilisant les méthodes de préparation en nanotechnologie les plus récentes.

Dans le Chapitre IV, nous détaillons le choix des matériaux composants ces échantillons modèles ainsi que leurs méthodes de préparation. Des nanoparticules de polystyrène (PS ~ 250 - 380 nm de diamètre) et de dioxyde de silicium (SiO_2 ~ 20 nm de diamètre) ont été placées sur des substrats métalliques, et de couches minces de dioxyde d'aluminium (Al_2O_3), de polyvinyl acétate (PVAc) et de dioxyde de silicium ont été déposées à la surface des échantillons (particules et substrat). Les couches minces ont été utilisées pour modéliser soit l'interphase, soit la matrice, ceci en fonction de l'ordre adopté pour la croissance des couches.

En se basant sur les constats théoriques obtenus grâce à nos simulations, et en utilisant les échantillons modèles comme échantillons de référence, des mesures EFM ont été effectuées afin d'évaluer expérimentalement la capacité avec cette technique de caractériser les interphases. Ces résultats sont détaillés dans le Chapitre V du mémoire.

Divers protocoles expérimentaux et méthodes de comparaison ont été développés dans l'optique de répondre à notre problématique. Dans un premier temps, l'association du système particule avec une seule couche a été étudiée, représentant soit un modèle de particule + interphase, soit un modèle de particule + matrice sans interphase.

L'EFM a montré une sensibilité particulière à l'épaisseur et aux permittivités diélectriques intrinsèques des particules et des films déposés dessus, les unes par rapport aux autres. Nous avons déduit que la comparaison des signaux EFM au centre des particules, avec une même distance pointe-échantillon, est une méthode de détection appropriée, sans le besoin particulier de mesurer l'épaisseur du matériau (voir Fig. 3). Ce résultat est une avancée comparé aux études antérieures de la littérature. Ceci a été prouvé pour la détection de gradient de force électrostatique à la fois, avec une excitation DC ainsi qu'une excitation AC. Pour le mode DC, un protocole de mesure particulier a été adapté afin de sélectionner la réponse purement capacitive du signal. Alors qu'en AC, un banc de mesure supplémentaire a été mis en place. Dans ce cas, la composante qui varie avec le double de la fréquence du potentiel électrique a été démodulée, permettant de mesurer directement la réponse capacitive propre de l'échantillon.

Conformément aux résultats des simulations, des effets morphologiques inhabituels sur les signaux EFM obtenus se sont avérés utiles pour extraire des informations sur les grandeurs diélectriques des matériaux multicouches 3D étudiés.

Les expériences ont montré un bon accord avec les simulations permettant une quantification approximative de la permittivité relative des sphères de PS, de SiO_2 et d'Al_2O_3 respectivement égales à 2.48, 3.9 et 10.78.

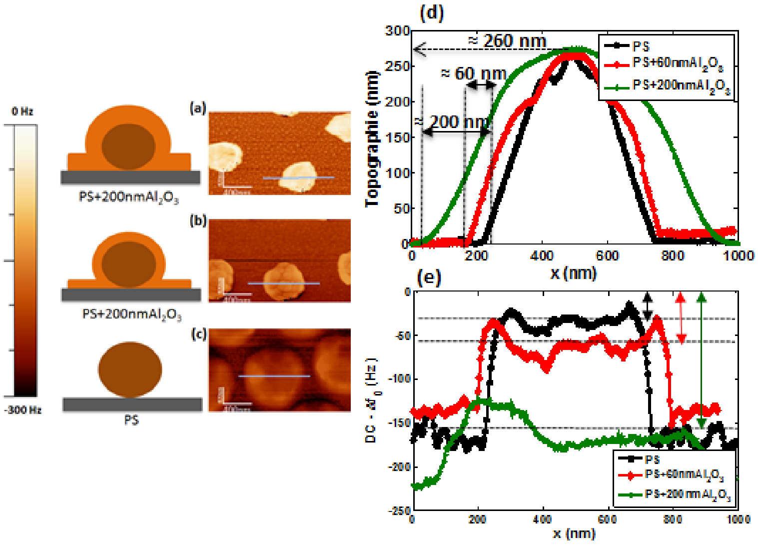

Fig. 3a, b et c: (gauche) Représentation de la structure des échantillons et (droite) images du signal EFM en excitation DC : modification de la fréquence de résonance de la pointe (Δf_0 (Hz)) liée aux gradients de forces électrostatiques, pour des échantillons de PS, PS+60nmAl_2O_3 et PS+200nmAl_2O_3 ; d. et e. profils de coupes au centre, de la topographie (d.) et du signal EFM à potentiel et distance-pointe échantillon constantes(e.). La chute du contraste et l'augmentation du signal au centre montre la sensibilité à l'épaisseur et à la permittivité de l'Al_2O_3, supérieure au PS.

Ensuite, l'étude de la couche modèle de l'interphase, placée entre la particule et la matrice, a été réalisée par trois méthodes.

La première méthode a consisté à comparer la réponse à un système particule + interphase à celle d'un système de particule + interphase + matrice. Cette méthode représente en pratique, la comparaison entre les signaux obtenus face à une particule possédant une interphase, dont la matrice aurait été éliminée (par exemple par gravure), à ceux obtenus au-dessus du même système, conservant la couche matricielle cette fois-ci.

Suite aux conclusions de la partie traitant le système particule + couche unique, nous avons pu analyser la réponse EFM et prouver une sensibilité acceptable à une interphase modèle de 100 nm d'Al_2O_3 entre une particule PS et une matrice de PVAc. Cependant, ce type de comparaison de matériau est délicat en pratique. En effet, le prélèvement de la matrice (particule + interphase) sans affecter l'interphase n'est pas évident.

Une comparaison plus réaliste a été ainsi réalisée par une deuxième méthode, en comparant le système particule + interphase + matrice à celui particule + matrice, tout en gardant une même épaisseur de la couche de matrice modèle. La comparaison du signal obtenu pour le PS avec un enrobage de 50 nm de SiO_2 par rapport à celui obtenu pour le PS + 100nmAl_2O_3 + 50nmSiO_2, a également montré des résultats cohérents avec les caractéristiques de la couche modèle d'interphase (100 nm d'Al_2O_3). Cependant, la conclusion sur cette dernière couche a été limitée à sa constante diélectrique relative par rapport à la permittivité efficace de l'association particule + matrice, et non à celle de la matrice ou de la particule, seules.

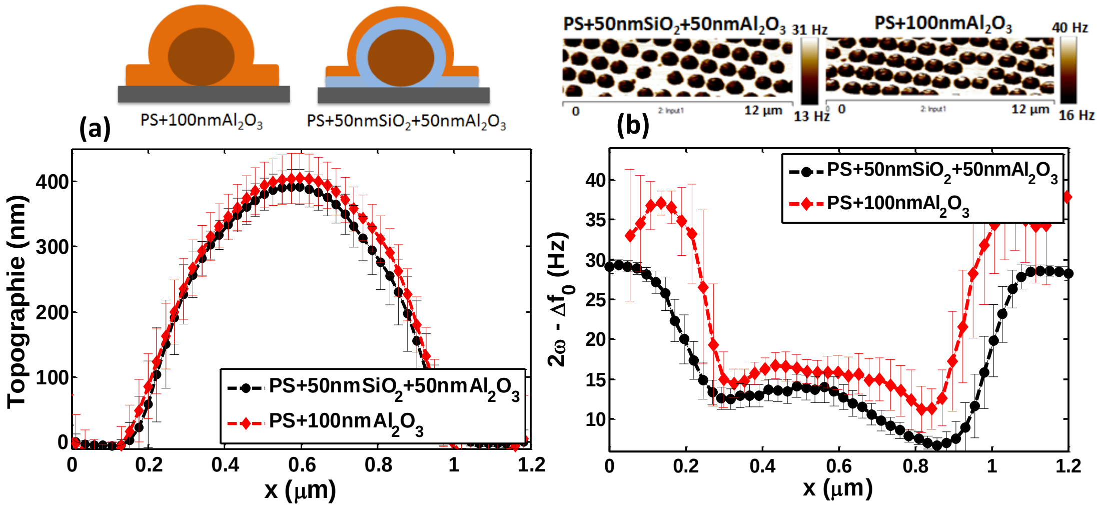

Fig. 4 : Détection de la couche modèle d'interphase - Méthode 3 : échantillons de PS+50nmAl_2O_3+50nmSiO_2 comparés à PS+100nmAl_2O_3: a. profil moyen de la topographie (encart : dessin représentatif de la configuration des matériaux) ; b. profil moyen du signal EFM et images EFM correspondantes (encart), à pulsation (ω) et amplitude du potentiel AC et distance constantes. Une superposition de la topographie est notée, à l'inverse de la réponse EFM montrant en moyenne une diminution du signal au centre avec une interphase de SiO_2, en accord avec les permittivités relatives du SiO_2 par rapport à Al_2O_3.

Par conséquent, une troisième méthode a consisté à comparer la réponse d'échantillons soigneusement préparés, possédant des géométries et des dimensions similaires, afin de supprimer toute ambiguïté liée à la topographie et acquérir une information directe sur l'interphase modèle. Cette troisième méthode pourrait être adoptée en pratique pour la comparaison de spécimens d'un nanocomposite présentant des protrusions, liées aux inclusions, et qui possèdent les mêmes dimensions.

Après un étalonnage de la constante diélectrique de la matrice, déposée d'abord sur les particules sans la présence de la couche modèle d'interphase, la constante diélectrique d'une couche de 50 nm d'Al_2O_3, au-dessous de 50 nm d'une matrice de SiO_2, a été estimée (voir Fig. 4). La quantification des résultats montrent une correspondance avec la permittivité relative prévue pour l'Al_2O_3 de 9,8 avec une erreur de 5 % par rapport aux résultats de simulations.

De même, pour le système inversé, la constante diélectrique du SiO_2 en tant que couche modèle d'interphase sous une couche de matrice d'Al_2O_3 calibrée, coïncide avec la permittivité attendue du SiO_2 de 3.9 avec une erreur de 0,3 % par rapport à la simulation.

En outre, suite aux mesures d'étalonnage de la matrice, nous avons noté une permittivité apparente de la couche de SiO_2, lorsque cette dernière est déposée à la surface libre du matériau, beaucoup plus élevée que celle mesurée en volume du matériau. Cette différence a été attribuée à l'état de surface du SiO_2 qui semble développer une couche d'adsorption / absorption d'eau, liée à la technique de préparation du SiO_2. Cette couche a été supposée être éliminée lorsque l'Al_2O_3 est déposé à la surface du SiO_2, ceci en raison des conditions thermodynamiques spécifiques du dépôt d'Al_2O_3.

L'ensemble des résultats de cette thèse démontre la capacité de l'EFM à étudier des matériaux diélectriques multicouches, de tailles nanométriques en 3D ; elle permet en particulier d'étudier l'interphase dans les nanodiélectriques. Des caractérisations quantitatives peuvent également être offertes en corrélant l'expérience aux résultats obtenus en simulations numériques. Néanmoins, une analyse précise de tous les paramètres d'influence doit être effectuée.

Le dernier chapitre de ce mémoire regroupe les résultats clés, et propose des perspectives de travail afin d'appuyer les hypothèses dégagées dans ce travail qui n'ont pas pu être approfondies. Ces travaux permettront ainsi d'étendre l'application pour aller encore plus loin avec l'EFM.

Notamment, nos travaux théoriques et expérimentaux pourraient s'appliquer également à d'autres techniques de caractérisation électriques avec l'AFM. (Scanning Microwave Microscopy, Conductive-Microscopy). En plus, l'étude de nos échantillons, à composition et géométrie relativement complexes, pourrait s'avérer transposable à d'autres types de nanomatériaux ; on peut citer par exemple les particules type core-shell, pour les applications pharmaceutiques, biologiques, et même énergétique; ainsi que des structures similaires mais naturelles telles que les virus et les bactéries...

Références

[1] J. K. Nelson and J. C. Fothergill, "Internal charge behaviour of nanocomposites," *Nanotechnology,* vol. 15, p. 586, 2004.

[2] M. F. Frechette, M. L. Trudeau, H. D. Alamdar, and S. Boily, "Introductory remarks on nanodielectrics," *Dielectrics and Electrical Insulation, IEEE Transactions on,* vol. 11, pp. 808-818, 2004.

[3] T. J. Lewis, "Nanometric dielectrics," *Dielectrics and Electrical Insulation, IEEE Transactions on,* vol. 1, pp. 812-825, 1994.

[4] T. Andritsch, R. Kochetov, P. H. F. Morshuis, and J. J. Smit, "Proposal of the polymer chain alignment model," in *Electrical Insulation and Dielectric Phenomena (CEIDP), 2011 Annual Report Conference on*, 2011, pp. 624-627.

[5] J. K. Nelson, J. C. Fothergill, L. A. Dissado, and W. Peasgood, "Towards an understanding of nanometric dielectrics," in *Annual Report Conference on Electrical Insulation and Dielectric Phenomena*, 2002, pp. 295-298.

[6] Y. Yi, C. Jiong, Y. Jingning, X. Dengming, T. Demin, Y. Rui*, et al.*, "Effect of space charge in nanocomposite of LDPE/TiO2," in *Proceedings of the 7th International Conference on Properties and Applications of Dielectric Materials (Cat. No.03CH37417)*, 2003, pp. 913-916 vol.3.

[7] K. Y. Lau, A. S. Vaughan, and G. Chen, "Nanodielectrics: opportunities and challenges," *IEEE Electrical Insulation Magazine,* vol. 31, pp. 45-54, 2015.

[8] G. Binnig, C. F. Quate, and C. Gerber, "Atomic Force Microscope," *Physical Review Letters,* vol. 56, pp. 930-933, 03/03/ 1986.

[9] Y. Martin, C. C. Williams, and H. K. Wickramasinghe, "Atomic force microscope–force mapping and profiling on a sub 100 ‐ Å scale," *Journal of Applied Physics,* vol. 61, pp. 4723-4729, 1987/05/15 1987.

[10] S. Peng, Q. Zeng, X. Yang, J. Hu, X. Qiu, and J. He, "Local Dielectric Property Detection of the Interface between Nanoparticle and Polymer in Nanocomposite Dielectrics," *Sci Rep,* vol. 6, p. 38978, Dec 13 2016.

List of publications

---

1. D. El Khoury, R. Arinero, J-C. Laurentie, M. Bechelany, M. Ramonda, J. Castellon,"Novel approaches towards detecting interphases with Electrostatic Force Microscopy", 2018 (submitted).
2. D. El Khoury, R. Arinero, J-C. Laurentie, M. Bechelany, J. Castellon, "Nanodielectric model samples to access the detectability of interphases with Electrostatic Force Microscopy", *2018 IEEE International Conference on Dielectrics (ICD)*, Budapest, 2018 (to come).
3. D. El Khoury, V. Fedorenko, J. Castellon, M. Bechelany, J-C. Laurentie, S. Balme, M. Fréchette, M. Ramonda, R. Arinero, "Characterization of dielectric nanocomposites with electrostatic force microscopy": Scanning, vol. 2017 (2017), Article ID 4198519, https://doi.org/10.1155/2017/4198519
4. D. El Khoury, R. Arinero, J-C. Laurentie , V. Fedorenko, M. Bechelany, S. Balme, M. Fréchette, J. Castellon, "Detection of shell coatings from core-shell like dielectric nanoparticles with electrostatic force microscopy," *2016 IEEE Conference on Electrical Insulation and Dielectric Phenomena (CEIDP)*, Toronto, ON, 2016, pp. 755-758. doi: 10.1109/CEIDP.2016.7785549
5. D. El Khoury, R. Arinero, J-C. Laurentie, M. Fréchette, J. Castellon, "Investigation of EFM capabilities for probing interphases in nanodielectric materials: A numerical study," *2016 IEEE International Conference on Dielectrics (ICD)*, Montpellier, 2016, pp. 800-803. doi: 10.1109/ICD.2016.7547737
6. D. El Khoury, R. Arinero, J-C. Laurentie, J. Castellon,"Nanoscale surface charge detection in epoxy resin materials using electrostatic force spectroscopy," *AIP Advances,* vol. 6, p. 035318, 2016. doi.org/10.1063/1.4944953

Towards the use of Electrostatic Force Microscopy to study interphases in nanodielectric materials

Abstract: Interphases are usually considered to be responsible for the physical properties of nanodielectrics unexplainable by general mixture laws. The prediction of the effective dielectric permittivity of these materials needs to reconsider the intrinsic permittivity and the volume of the interphase. Despite the urge for a local characterization of these nanometric interfacial regions, no reliable experimental method has been developed yet. The Electrostatic Force Microscope (EFM) constitutes a promising technique to fulfill this objective. The aim of this thesis is to develop appropriate experimental protocols and signal analysis to explore the ability of EFM to the study of interphases in nanodielectrics. We first resorted to finite-element numerical simulations in order to deeper our understanding of the interaction between an EFM probe and several types of nanostructured samples, allowing to simulate afterwards the specific response to a nanocomposite possessing an interphase. We proposed a three-phase electrostatic model of a nanodielectric, upon which, we designed and synthesized model samples of known properties to play the role of a reference nanodielectric material for EFM measurements. Consequently, we were able to develop several experimental protocols and signal analysis with both DC and AC force gradient EFM modes. These techniques offer versatile methods to characterize interphases with reduced impact of the parasitic effects commonly convoluted within EFM signals. Finally, a quantification of the interphase in our nanodielectric model samples was possible thanks to correlation with our numerical simulations.

Key-words: Interphases, Nanocomposites, Nanodielectrics, Dielectric permittivity, Atomic force microscopy, Electrostatic force microscopy, Finite-elements.

Vers l'utilisation du Microscope à *Force Electrostatique pour l'étude des interphases dans les matériaux nanodiélectriques*

Résumé: Les interphases sont souvent considérées comme responsables des propriétés physiques des nanodiélectriques inexplicables par les lois de mélange. La prédiction de la permittivité diélectrique des nanodiélectriques nécessite de reconsidérer la permittivité intrinsèque et le volume de l'interphase. Malgré le besoin d'une caractérisation locale de ces régions interfaciales nanométriques, aucune méthode expérimentale fiable n'a encore été développée. La Microscopie à Force Electrostatique (EFM) constitue une technique prometteuse pour atteindre ce but. L'objectif de cette thèse est de développer des protocoles expérimentaux et des méthodes d'interprétations du signal appropriés pour évaluer l'aptitude de l'EFM à l'étude des interphases dans les nanodiélectriques. Nous avons eu recours d'abord à des simulations numériques par éléments-finis pour approfondir notre compréhension de l'interaction entre une sonde EFM et plusieurs types d'échantillons nanostructurés, permettant par la suite de simuler la réponse spécifique face à un nanocomposite possédant une interphase. Nous avons proposé un modèle électrostatique de nanodiélectrique possédant trois phases, selon lequel, nous avons conçu et synthétisé des échantillons modèles aux propriétés connues afin de jouer le rôle de matériaux nanodiélectriques de référence pour les mesures EFM. Par conséquent, nous avons pu développer plusieurs protocoles expérimentaux et d'analyses du signal utilisant des modes DC et AC de détection du gradient de force pour caractériser les interphases dans des nanocomposites. Ces techniques constituent un ensemble polyvalent de méthodes d'étude des interphases avec un impact réduit des effets parasites communément convolués dans les signaux EFM. Enfin, une quantification de la permittivité de l'interphase de nos échantillons modèles a été possible par corrélation avec nos simulations numériques.

Mots-clés: Interphases, Nanocomposites, Nanodiélectriques, Permittivité diélectrique, Microscopie à force atomique, Microscopie à force électrostatique, Eléments-finis.